DOCTORAL THESIS IN

Advances In Modelling, Health-Monitoring, Infrastructures, Geomatics, Geotechnics, Hazards, Engineering Structures, Transportation (AIM HIGHEST)

Curriculum: Structural and Geotechnical Engineering

Reliability-Based Structural Assessment of Monumental Heritage Structures: Application to St. Peter's Basilica in Vatican City

Ph.D. CANDIDATE
Engr. Giuseppe Rusticano

COORDINATOR
Prof. Engr. Dr. Piero Colajanni

SUPERVISORS
Prof. Engr. Dr. Lidia La Mendola
UniPa, Italy
Prof. Engr. Dr. Giuseppe Mancini
Sacertis Ingegneria S.r.l., Italy

CO-SUPERVISORS
Prof. Engr. Dr. Liborio Cavaleri
UniPa, Italy
Prof. Engr. Dr. Robby Caspeele
UGent, Belgium

XXXVIII CYCLE
University of Palermo, Italy

Finanziato dall'Unione europea NextGenerationEU
Ministero dell'Università e della Ricerca
Italiadomani
PIANO NAZIONALE DI RIPRESA E RESILIENZA

This page intentionally left blank.

UNIVERSITÀ DEGLI STUDI DI PALERMO

dipartimento di ingegneria unipa

DOCTORAL THESIS IN

Advances In Modelling, Health-Monitoring, Infrastructures, Geomatics, Geotechnics, Hazards, Engineering Structures, Transportation (AIM HIGHEST)

Curriculum: Structural and Geotechnical Engineering

CEAR 07/A (ICAR 09)

Scholarship: DM 352/2022 (PNRR - SACERTIS)

Reliability-Based Structural Assessment of Monumental Heritage Structures: Application to St. Peter's Basilica in Vatican City

Ph.D. CANDIDATE

Engr. Giuseppe Rusticano

COORDINATOR

Prof. Engr. Dr. Piero Colajanni

SUPERVISORS

Prof. Engr. Dr. Lidia La Mendola
UniPa, Italy

Prof. Engr. Dr. Giuseppe Mancini
Sacertis Ingegneria S.r.l., Italy

CO-SUPERVISORS

Prof. Engr. Dr. Liborio Cavaleri
UniPa, Italy

Prof. Engr. Dr. Robby Caspeele
UGent, Belgium

XXXVIII CYCLE, ACADEMIC YEAR 2024/2025

University of Palermo, Italy

Finanziato dall'Unione europea NextGenerationEU

Ministero dell'Università e della Ricerca

Italiadomani PIANO NAZIONALE DI RIPRESA E RESILIENZA

For Valeria

This page intentionally left blank.

Declaration

. . . . . .

Giuseppe Rusticano

Palermo, December 15, 2025

This page intentionally left blank.

Acknowledgements

A Ph.D. is more than just a way to learn; it is a combination of experiences, people, and feelings that are exceptional because of the people who share them. Thanks to everyone I have been fortunate enough to meet, talk with, and learn from.

I am deeply grateful to my supervisors for their mentoring throughout this journey. In particular, to Prof. Giuseppe Mancini for his invaluable support and expertise, for gently leading this effort when decisions were difficult, and for giving me the opportunity to collaborate on this important and prestigious project. Many thanks to Prof. Lidia La Mendola, for patient guidance, and the many line-by-line comments that made the text clearer and the arguments tighter. To Prof. Liborio Cavaleri, for trusting in me and for his persistent support. To Prof. Robby Caspeele who supervised me at Ghent University for always keeping his door open, offering constructive feedback, and encouraging genuine interaction with international students and researchers.

I also carry with me the memory of Prof. Giovanni Minafò: your clarity, kindness, and example as a teacher remain a compass for my work and life. This dissertation is also a tribute to your memory.

Working inside St. Peter's Basilica was a privilege I will never forget. Walking under its immense vaults, masonry walls, and piers, and sensing the peaceful rhythm of a living monument changed the way I look at structures. It was a daily reminder that engineering is a dialogue across centuries between builders and materials, memory and matter, calculation and care and of our responsibility to help preserve a treasure of universal heritage for future generations.

I would also like to express my sincere gratitude to the *Fabbrica di San Pietro*, a centuries-old institution that harmoniously combines heritage and progress in its distinctive conservation mission. In particular, my thanks go to Eng. Alberto Capitanucci, Director of the Fabbrica's Technical Division, and Cardinal Mauro Gambetti, Archpriest of the Papal Basilica of St. Peter and President of the Fabbrica di San Pietro for their assistance and contributions to this project.

Similarly, a special note of gratitude to SACERTIS INGEGNERIA S.R.L.: my time in Turin was as human as it was technical. Thank you to all my colleagues there for the warmth and affection you showed me every day; your trust and friendship made this work possible. I am especially grateful to Eng. Lavinia Coraci for the many hours spent side by side on finite element modeling; to Eng. Gianni Croce for his constant and practical support; and to Eng. Paola Darò and Eng. Dario La Mazza for their help and insight.

None of this would have been possible without my family, my mother, my father, and my brother Alessandro whose steady support and trust sustained me throughout. And Valeria, thank you for your patience and love, and for opening your home in Uruguay and your family to me. You transformed geographical separation into belonging and showed me, in good days and hard ones, that life is always larger than any deadline.

Giuseppe Rusticano, December 2025

Table of contents

List of symbols

Roman symbols

E_h	Equivalent homogenized elastic modulus of the multi-leaf masonry wall (Chapter VII & VIII)
E_{sec}	Secant modulus at peak compressive strength (Chapter VII)
$f_{c,h}$	Equivalent homogenized compressive strength of the multi-leaf masonry wall (Chapter VII)
a	Geometrical factor (Chapter II)
a	Thickness of each external brickwork masonry leaf in the multi-leaf wall specimen (Chapter VII)
A_C	Cutting area of the flat-jack slot (Chapter V)
A_d	Ductility parameter governing the post-peak softening branch in compression (Chapter VII)
A_{eff}	Effective bearing area of the drilling/penetration tool (Chapter III)
A_J	Nominal area of the flat-jack (Chapter V)
b	Thickness of the internal Ancient Roman Concrete core in the multi-leaf wall specimen (Chapter VII)
c	Cohesion parameter of the Drucker–Prager failure criterion (Chapter VI)
D	Diameter of cylindrical specimen (Chapter V)
d_c	Compressive damage variable in the Concrete Damage Plasticity model (Chapter VII)
D_h	Representative thickness of the homogenized multi-leaf masonry wall (Chapter VIII)
D_s	Total depth of multi-leaf specimen (Chapter VII)
D_t	Mean thickness of the travertine masonry layer (Chapter VIII)
d_t	Tensile damage variable in the Concrete Damage Plasticity model (Chapter VII)
E	Effect of actions (Chapter II & IX)
E	Elastic Young's modulus (Chapter III, V, VI, VIII & VII)
E_{dyn}	Dynamic Young's modulus (Chapter V)

E_{stat}	Static Young's modulus (Chapter V)
E_t	Elastic modulus of the travertine masonry (Chapter VII & VIII)
E_t	Tangent stiffness modulus (Chapter V)
$E(X)$	Effect of actions (Chapter II)
f	Generic material strength (Chapter II)
f_c	Cylindrical compressive strength (Chapter III, V & VII)
$f_{c,d}$	Design compressive strength (Chapter IX)
f_{CSD}	Natural frequency identified from experimental Cross Spectral Density (Chapter VIII)
f_d	Design material strength (Chapter II & IX)
F_d	Design value of the resultant external action (Chapter IX)
f_{DPT}	Equivalent strength indicator from drilling penetrometer tests (Chapter III)
f_{FEM}	Natural frequency from the Finite Element model (Chapter VIII)
f_k	Characteristic material strength (Chapter II)
f_m	Representative mean material strength (compression or tension) (Chapter II & IX)
f_{rep}	Representative material strengths used in the Global Resistance Factor method (Chapter II)
$f_{t,d}$	Design tensile strength (Chapter IX)
$F_{X_i}(x_i)$	Cumulative distribution function (Chapter II)
$f_X(x)$	Probability density function (Chapter II)
f_y	Yield stress of steel tie-rods (Chapter VIII)
G	Permanent action (gravity load) (Chapter IX)
G_d	Design value of Permanent action (Chapter IX)
G_k	Characteristic value of a permanent action (Chapter II & IX)
$G(U)$	Limit-state function expressed in the standard normal space (Chapter II)
$g(X)$	Limit-state function (Chapter II & IX)
$g(Z)$	Performance function expressed in terms of the random vector Z (Chapter II)
h	Height of cylindrical specimen (Chapter V)
h_{mesh}	Average mesh element size (Chapter VIII)
H_s	Total height of multi-leaf specimen (Chapter VII)

k	Empirical coefficient relating the ratio between the Young's modulus and the mean value of compressive strength of brickwork masonry (Chapter VII)
k_n	Fractile factor for the 5% lower fractile of a lognormal variable (Chapter II)
K_a	Area correction factor for flat-jack tests (Chapter V)
k_i	Principal curvatures of the limit state surface at the design point (Chapter II)
K_m	Calibration factor for flat-jack tests (Chapter V)
k_n	Normal stiffness of the zero-thickness interface elements (Chapter VIII)
k_t	Tangential stiffness of the zero-thickness interface elements (Chapter VIII)
K_x	Translational spring stiffness in the global x direction (Chapter VIII)
K_y	Translational spring stiffness in the global y direction (Chapter VIII)
K_z	Translational spring stiffness in the global z direction (Chapter VIII)
L	Path length between source and receiver in stress-wave transmission tests (Chapter III)
L_s	Total length of multi-leaf specimen (Chapter VII)
V	Coefficient of Variation (Chapter VII)
n	Number of years in the reference period or number of simulations (Chapter II)
N	Number of sampling points along the loading branch (Chapter VI)
N_f	Number of failure realizations in a set of simulations (Chapter II)
N	Number of basic random variables or number of simulations (Chapter II)
p_{jack}	Applied flat-jack pressure (Chapter III & V)
P_f	Probability of failure (Chapter II & IX)
P_f^{FORM}	Approximate failure probability obtained with the First-Order Reliability Method (Chapter II)
P_f^{SORM}	Approximate failure probability obtained with the Second-Order Reliability Method (Chapter II)
$p_{f,t}$	Target failure probability (Chapter II & IX)
$\hat{P}_f$	Estimated failure probability from simulation (Chapter II)
$P_{\max}$	Maximum penetration force recorded during drilling/penetration tests (Chapter III)

Q_k	Characteristic value of a variable action (Chapter II)
R	Structural resistance (Chapter II & IX)
r	Residual stress ratio at ultimate compressive strain (Chapter VII)
R_c	Cubic compressive strength (Chapter V)
R_d	Design resistance (Chapter II & IX)
R_f	Failure domain (Chapter II)
R_k	Global resistance from non-linear finite element analysis with characteristic strengths f_k (Chapter II)
R_m	Global resistance from non-linear finite element analysis with mean strengths f_m (Chapter II)
R_{NLFEA}	Global structural resistance computed by a non-linear finite element analysis (Chapter II & IX)
R_{rep}	Global resistance from non-linear finite element analysis with representative strengths f_{rep} (Chapter II)
R_s	Safe domain (Chapter II)
$\{R^{(i)}\}$	Sample of global resistance values obtained from probabilistic non-linear finite element analyses (Chapter II)
$R(X)$	Structural resistance (Chapter II)
$R(X,Y)$	Actual (unknown) structural resistance (Chapter II)
$R(z)$	Drilling resistance profile (Chapter III)
S	Effect of actions (Chapter IX)
$T(x,y,t)$	Measured surface temperature field in infrared thermography (Chapter III)
T_{n}	Reference period (in years) (Chapter II)
$T_{\mathrm{ref}}(x,y,t)$	Reference or background temperature field n infrared thermography (Chapter III)
t	Time of flight of the sonic/ultrasonic pulse along the path L (Chapter III)
$T(z)$	Torque transmitted to the drilling tool (Chapter III)
U	Vector of independent standard normal random variables (Chapter II)
u	Generic point in the standard normal space (Chapter II)
U_i	i-th component of the standard normal vector U (Chapter II)
u^*	Design point or most probable point of failure in the standard normal space (Chapter II)
V_a	Coefficient of variation of the geometrical factor a (Chapter II)

V_η	Coefficient of variation of the conversion factor η (Chapter II)
V_f	Coefficient of variation of the material strength f (Chapter II)
V_g	Coefficient of variation of the permanent action G (Chapter IX)
V_{g1}	Coefficient of variation of self–weight (Chapter IX)
V_{g2}	Coefficient of variation of other permanent non-structural loads (Chapter IX)
V_{hom}	Coefficient of variation of homogenized multi-leaf masonry strength (Chapter IX)
V_p	Ultrasonic P-wave velocity (Chapter III & V)
V_R	Coefficient of variation of the global resistance R (Chapter II)
V_{θ_R}	Coefficient of variation of the resistance model factor θ_R (Chapter II & Chapter IX)
V_{θ_E}	Coefficient of variation of the load–effect model (Chapter IX)
V_{trav}	Coefficient of variation of travertine strength (Chapter IX)
V_X	Coefficient of variation (CoV) of the random variable X (Chapter II & IX)
$V_{X,\text{ex}}$	Coefficient of variation of X in the assessment of an existing structure (Chapter II)
$V_{X,\text{new}}$	Coefficient of variation of X in the design of new structures (Chapter II)
w_y	Adjustment factor for partial safety factors in the Adjusted Partial Factor Method (Chapter II)
X	Vector of random variable (Chapter II & IX)
x	Non-dimensional strain ratio, $x = \varepsilon/\varepsilon_c$ (Chapter VII)
X_d	Design value of a basic random variable X (Chapter II & IX)
X_i	i-th component of the basic random variable vector X (Chapter II)
X_k	Characteristic value of a basic random variable X (Chapter II & IX)
x_u	Ultimate non-dimensional strain ratio, $x_u = \varepsilon_{cu}/\varepsilon_c$ (Chapter VII)
Z	Vector of random variables used in the Probabilistic Method (Chapter II)

Greek symbols

α_E	Load–effect sensitivity factor (Chapter II & IX)
α_R	Resistance sensitivity factor (Chapter II & IX)
$\tilde{\alpha}_R$	Effective resistance sensitivity factor for a one-year reference period (Chapter IX)

β	Reliability index (Chapter II & IX)
β_{ex}	Target reliability index adopted for an existing structure (Chapter II)
β_{new}	Target reliability index used for calibration of new structures (Chapter II)
$\beta_{\text{assessment}}$	Estimated reliability index from the global non-linear finite element analysis (Chapter IX)
$\hat{\beta}$	Estimated reliability index from full-probabilistic method (Chapter II)
β_{t}	Target reliability index (Chapter II & IX)
δ_R	Bias factor between probabilistic mean resistance and deterministic R_m (Chapter II)
$\Delta T(x,y,t)$	Thermal contrast field in infrared thermography (Chapter III)
δ_v	Vertical displacement at the control node (Chapter IX)
ε_c	Peak compressive strain (Chapter VII)
ε_{cu}	Ultimate compressive strain (Chapter VII)
$\varepsilon_c^{\text{inel}}$	Inelastic strain in compression used in the Concrete Damage Plasticity model (Chapter VII)
$\varepsilon_t^{\text{inel}}$	Inelastic strain in tension used in the Concrete Damage Plasticity model (Chapter VII)
ε_t	Cracking strain in uniaxial tension (Chapter VII)
ε_{tu}	Ultimate tensile strain (Chapter VII)
ε_v	Vertical strain (Chapter V)
η	Conversion factor between test and in-situ conditions (Chapter II)
γ	Unit weight (Chapter V & VIII)
γ_c	Unit weight of Ancient Roman Concrete (Chapter VII)
γ_m	Unit weight of brickwork masonry (Chapter VII)
γ_G	Partial safety factor for permanent actions (Chapter II & IX)
γ_m	Partial safety factor accounting for material strength variability (Chapter II)
γ_Q	Partial safety factor for variable actions (Chapter II)
γ_R	Global resistance factor associated with the variability of R (Chapter II)
$\gamma_{Rd,1}$	Partial safety factor for resistance model uncertainty (Chapter II)
$\gamma_{Rd,2}$	Partial safety factor for geometrical deviations (Chapter II)
γ_X	Generic partial safety factor for action or resistance X (Chapter II)
$\gamma_{X,\text{new}}$	Partial safety factor for X used for new structures (Chapter II)

$\gamma_{Ed,G}$	Partial safety factor for the modeling of load effects due to permanent actions (Chapter IX)
γ_{G_1}	Combined partial safety factor for permanent actions (self-weight) (Chapter IX)
γ_{G_2}	Combined partial safety factor for permanent actions (other type of load) (Chapter IX)
γ_g	Partial safety factor for permanent actions (Chapter IX)
γ_M	Combined material partial safety factor for non-linear finite element analysis resistance (Chapter II & IX)
γ_m	Partial safety factor for material properties (Chapter IX)
γ_{Rd}	Partial safety factor for resistance model uncertainties (Chapter II & IX)
μ	Mean value
μ_c	Friction coefficient (Chapter VI)
μ_a	Mean value of the geometrical factor a (Chapter II)
μ_η	Mean value of the conversion factor η (Chapter II)
μ_{θ_R}	Mean value of the resistance model factor θ_R (Chapter II)
μ_g	Mean value of the permanent action G (Chapter IX)
μ_R	Mean global resistance (Chapter II)
μ_{θ_E}	Mean value of the load–effect model (Chapter IX)
μ_X	Mean value of the random variable X (Chapter II & IX)
ν_c	Poisson's ratio of Ancient Roman Concrete (Chapter VII)
ν_m	Poisson's ratio of brickwork masonry (Chapter VII)
ν_t	Poisson's ratio of travertine (Chapter VII)
ν	Poisson's ratio (Chapter V, VI & VIII)
ω	Angular rotation speed of the drilling/penetration tool (Chapter III)
Ω_f	Non-admissible domain of Concrete Damage Plasticity parameter triplets (Chapter VII)
Ω_s	Admissible domain of Concrete Damage Plasticity parameter triplets (Chapter VII)
$\Phi(\cdot)$	Cumulative distribution function of the standard normal distribution (Chapter II)
$\varphi(\cdot)$	Probability density function of the standard normal distribution (Chapter II)
ϕ	Internal friction angle of the Drucker-Prager model (Chapter VI)

Φ^{-1}	Inverse standard normal cumulative distribution function (Chapter IX)
ψ_0	Combination factor for variable actions (Chapter II)
ψ	Dilation angle of the Drucker-Prager model (Chapter VI)
σ_c	Nominal compressive stress in the uniaxial stress–strain law (Chapter VII)
σ	Stress in the original stress–strain law (Chapter IX)
σ_d	Design stress (in the design stress–strain law) (Chapter IX)
σ_g	Standard deviation of permanent load (Chapter IX)
$\sigma_{\text{in-situ}}$	Average compressive stress in masonry from single flat-jack tests (Chapter III & V)
σ_t	Nominal tensile stress in the uniaxial stress–strain law (Chapter VII)
σ_{zz}	Vertical normal stress component in the z-direction (Chapter VI)
σ_R	Standard deviation of the global resistance R (Chapter II)
Θ	Random model uncertainty factor relating actual and model resistance (Chapter II)
θ	Vector of model parameters in the calibration procedure (Chapter VI)
θ_E	Load–effect model factor (Chapter IX)
θ_R	Resistance model factor (Chapter II & IX)
θ_{Rd}	Design value of the resistance model factor (Chapter IX)

Abbreviations

1D	One-Dimensional
2D	Two-Dimensional
3D	Three-Dimensional
APFM	Adjusted Partial Factor Method
ARC	Ancient Roman Concrete
AVT	Ambient Vibration Tests
CC	Consequence Class
CDF	Cumulative Distribution Function
CDP	Concrete Damage Plasticity
CSD	Cross Spectral Density
D-P	Drucker–Prager (failure criterion)
DPT	Drilling Penetrometer Test

DT	Destructive Test
DVM	Design Value Method
ECoV	Estimation Coefficient of Variation method
FEA	Finite Element Analysis
FE	Finite Element
fib	International Federation for Structural Concrete
FORM	First-Order Reliability Method
GPR	Ground-Penetrating Radar
GRF	Global Resistance Factor method
GSF	Global Safety Format
H-BIM	Heritage Building Information Model
HPT	Helix Pull-out Test
ICCROM	International Centre for the Study of the Preservation and Restoration of Cultural Property
ICOMOS	International Council on Monuments and Sites
ISCARSAH	International Scientific Committee for Analysis and Restoration of Structures of Architectural Heritage
ISO	International Organization for Standardization
JCSS	Joint Committee on Structural Safety
LE	Linear Elastic
LHS	Latin Hypercube Sampling
LoA	Levels of Approximation
LWIR	Long-Wave Infrared
MCMC	Markov Chain Monte Carlo
MDT	Minor-Destructive Test
MSE	Mean Squared Error
MWIR	Mid-Wave Infrared
NDT	Non-Destructive Test
NLFEA	Non-Linear Finite Element Analysis
NLFE	Non-Linear Finite Element
NLSA	Non-Linear Static Analysis
OMA	Operational Modal Analysis
PDF	Probability Density Function

PFM	Partial Factor Method
PM	Probabilistic Method
PP	Perfectly Plastic
PPT	Penetration Resistance Test
PSF	Partial Safety Factor
RMS	Root Mean Square
SHM	Structural Health Monitoring
SLS	Serviceability Limit State(s)
S-NLFEA	Stochastic Non-Linear Finite Element Analysis
SORM	Second-Order Reliability Method
ULS	Ultimate Limit State(s)
UNESCO	United Nations Educational, Scientific and Cultural Organization
UPV	Ultrasonic Pulse Velocity

Summary

Monumental masonry buildings such as cathedrals and basilicas are characterized by complex structural systems, multi-leaf walls and large-span vaulted elements, often built with heterogeneous materials whose properties are only partially known. At the same time, modern structural design is increasingly taking basis in probabilistic concepts, target reliability indices and safety formats formalized in international standards. Over the past decades, a substantial body of research has been developed in this direction for other classes of existing structures, such as bridges, offshore platforms and modern reinforced concrete buildings, and several studies have already demonstrated the potential of probabilistic methods, Bayesian model updating and reliability analysis for historic towers, churches and bridges. However, the practical application of structural reliability concepts to monumental masonry heritage remains relatively limited compared with these other areas of civil engineering. This thesis provides a first step toward connecting these two worlds by developing and implementing an integrated framework for the reliability-based structural assessment of monumental heritage buildings. The framework is implemented for the 17th-century body of St. Peter's Basilica in Vatican City, the most important church in Western Christianity, which serves as a reference case study for massive multi-leaf masonry churches.

In order to provide a theoretical background of the proposed framework, the dissertation begins with an overview of the basic concepts of structural reliability and the most common safety formats used today for both new and existing structures. Building on this basis, a research strategy is formulated that integrates historical and construction knowledge, the extensive experimental diagnostic campaign carried out in 2023 inside the Basilica by SACERTIS INGEGNERIA S.R.L., hierarchical numerical modeling at material, wall, and global scales, and probabilistic calculations that take into account uncertainties and allow the calibration of partial safety factors.

An important component of the thesis is the material characterization of the different layers forming the multi-leaf masonry walls of St. Peter's Basilica, known as *Opus Caementicium*, in which the Ancient Roman construction technique includes

an Ancient Roman Concrete core between two brickwork leaves, and finally covered with an external travertine stone masonry. In-situ testing (i.e., ultrasonic pulse velocity, dynamic identification, endoscopic surveys and flat-jack tests) and laboratory tests on extracted cores are interpreted with the help of three-dimensional finite element analyses. A preliminary Drucker–Prager elasto-plastic failure criterion is calibrated in order to simulate the behavior of brickwork masonry panels and cylindrical Ancient Roman Concrete specimens under uniaxial compression. These studies provide a set of mechanical characteristics and enable a possible homogenization of the multi-leaf walls into an equivalent single-layer material appropriate for global non-linear finite element analyses.

Further, this thesis aims at extending the material modeling within a probabilistic framework based on the concrete damage plasticity model, in which three main parameters governing the compressive and tensile stress–strain response are treated as random variables, while others remain deterministic. Prior probabilistic models are formulated from literature and standards, and are then updated using the results of the diagnostic experimental campaign through Bayesian inference. In this way, are determined posterior distributions for the key material parameters, taking into account experimental variability and model uncertainty, while showing how these factors influence the final estimates. In addition, stochastic three-dimensional non-linear finite element analyses are performed on multi-leaf masonry walls in order to explore the variability of homogenized properties induced by the random parameters of the constitutive model adopted.

On this basis, a detailed three-dimensional global non-linear finite element model of the 17th-century body of St. Peter's Basilica in Vatican City is developed. The model involves the main structural components (i.e., multi-leaf walls, piers, barrel and groin vaults, secondary domes and foundations) using the homogenized material and calibrated constitutive parameters. Boundary and load conditions are defined on the basis of historical and structural knowledge, and the model is calibrated on the basis of the available dynamic identification data. Then, non-linear static analyses under gravity loads are performed to evaluate the main stress paths and identify potential damage and critical zones in the Basilica, as well as to quantify the global safety levels.

Finally, the probabilistic material models and the global finite element simulations are embedded in a reliability-based safety format tailored to monumental masonry structures. Partial safety factors for material properties and for effects of actions are

calibrated by relating them to target reliability indices adopted from international documents. The resulting safety format is applied to the structural members of St. Peter's Basilica, enabling the evaluation of reliability indices and probabilities of failure for the ultimate limit state under gravity loading. The analysis shows how the calibrated partial factors for existing structures differ from those commonly used for ordinary structures in the design formulation and highlights the influence of epistemic and aleatory uncertainties on the assessed safety levels.

The main contributions of this thesis are: (i) the development of a coherent workflow that links diagnostic campaigns, advanced constitutive modeling and homogenization for multi-leaf masonry; (ii) the formulation and Bayesian updating of a non-linear probabilistic concrete damage plasticity material model specific to a monumental masonry case study; (iii) the develop and calibration of a complex three-dimensional non-linear finite element model of St. Peter's Basilica; and (iv) the application of a reliability-based global safety format based on the semi-probabilistic partial factor method, including the calibration of the partial safety factors. Although the framework is demonstrated on St. Peter's Basilica, it is designed to be applicable, subjected to appropriate adaptations, to other complex heritage structures. As such, it provides a rational basis for integrating probabilistic thinking into the assessment and conservation of monumental masonry buildings, supporting informed decision-making and the long-term preservation of cultural heritage. In addition, the framework could be further extended to support continuous structural health monitoring, both for exploring possible damage scenarios and for optimizing the layout of the sensor system within the structure.

This page intentionally left blank.

CHAPTER I

General introduction

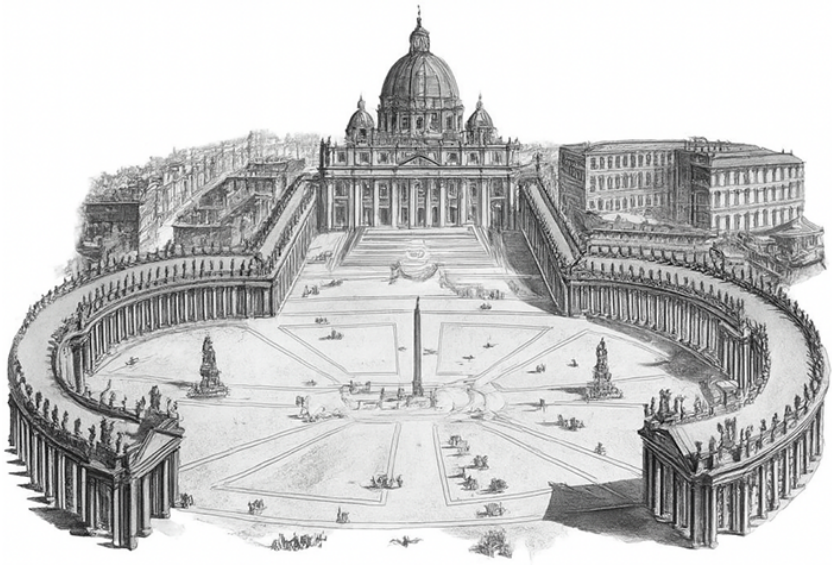

"Poiché San Pietro è quasi la madre di tutte le chiese, era necessario dotarla di un portico che mostrasse un'accoglienza materna a braccia aperte."

("Since St. Peter's is almost the mother of all churches, it needed a portico showing a maternal open-armed welcome.")

– Gian Lorenzo Bernini

I.1 Introduction

I.1.1 Context of the research topic

Monumental churches, cathedrals, and palaces are not only architectural masterpieces, but also buildings with complex structural systems. Built centuries ago with different construction techniques different from those we use today, they continue to host millions of visitors and liturgical activities each year. Preserving their safety and serviceability while keeping their authenticity and sustaining exceptional universal value is a challenging task that combines structural engineering, conservation science, and art history.

From the point of view of structural safety, monumental masonry buildings are characterized by massive but heterogeneous walls, slender piers, large-span vaults and domes, and by materials whose mechanical properties are often only partially known. At the same time, modern design philosophies for new structures are deeply rooted in structural reliability theory and in codified safety formats based on probability of failure and target reliability indices, as formalized for example in ISO 2394, ISO 13822, EN 1990 the JCSS Probabilistic Model Code and the *fib* Model Code 2020 [5, 6, 10–12]. In contrast, the assessment of existing monumental heritage structures is still mostly based on linear-elastic studies followed by local checks, with fixed Partial Safety Factors (PSFs) required for the design of ordinary buildings and modern materials.

The United Nations Educational, Scientific and Cultural Organization (UNESCO) World Heritage Convention identifies cultural heritage as monuments, buildings, and sites with great universal importance in history, art, or science. As of 2025, the World Heritage list has 1,248 sites throughout 170 states, with 972 categorized as cultural sites [16, 17]. Although not exhaustive, the list represents the most generally used global inventory of heritage assets, with monumental masonry architecture (e.g., churches, cathedrals, basilicas, palaces, towers, defensive systems, and other significant historic structures) playing an essential role.

World Heritage cultural sites are primarily located in Europe and North America, with a growing number in Asia and the Pacific region [3, 16]. Countries such as Italy (61), China (60), Germany (55), France (54) and Spain (50) currently have the most listed World cultural heritage sites, indicating a high concentration of heritage assets with developed national conservation systems of preservation.

To contextualize the present case study within this global context, Figure I.1 shows a world map based on the official UNESCO World Heritage list dataset, where all cultural heritage sites are highlighted.

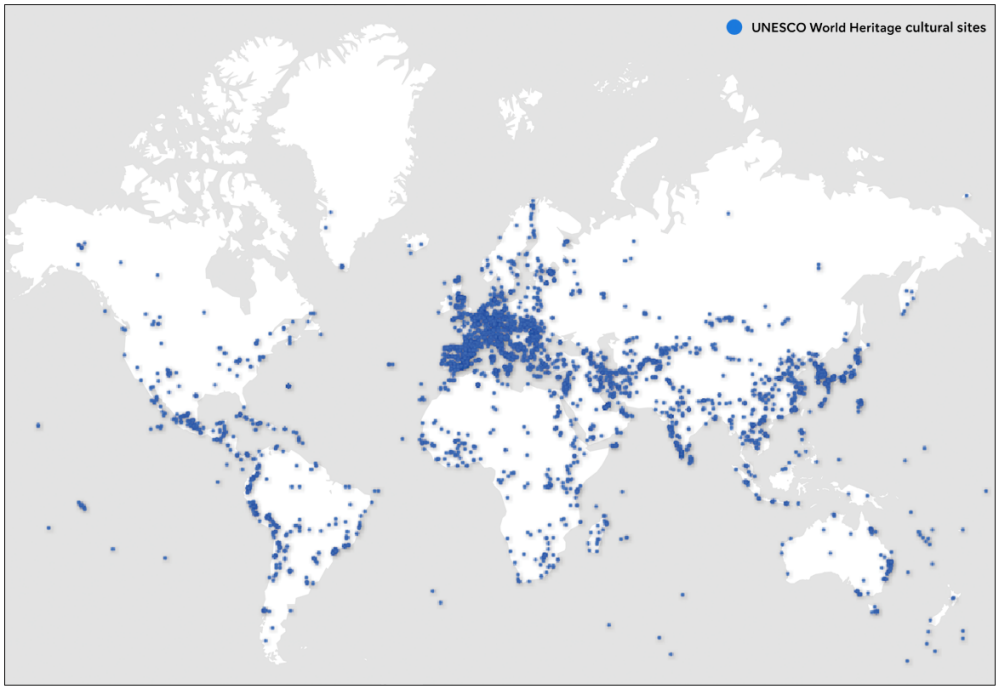

Figure I.1: Global map showing the distribution of UNESCO World cultural heritage sites. Data source: UNESCO World Heritage list (accessed November 2025).

The map shows a high concentration of UNESCO World Heritage sites in several regions of the world, with Europe alone accounting for 570 sites. The bar chart shown in Figure I.2 highlights the geographical imbalance in the distribution of heritage sites by continent.

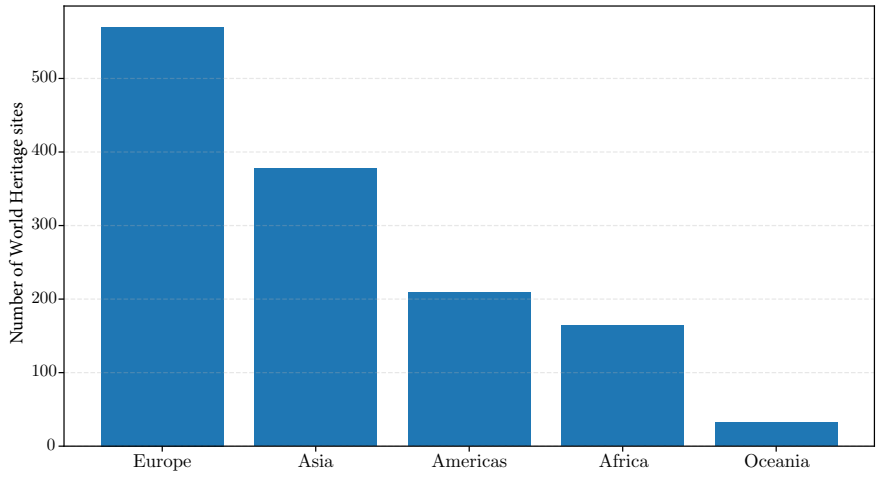

Figure I.2: Bar charts showing the number of UNESCO World Heritage properties by continent. Data source: UNESCO World Heritage List (accessed November 2025).

Thousands of monuments and protected buildings worldwide are classified in national and regional inventory, in addition to World Heritage sites. These constructions are often located in highly populated urban areas and areas vulnerable to natural disasters like earthquakes, floods, windstorms, and climate change-induced catastrophic events. Recent earthquakes in Italy and other Mediterranean countries have once again highlighted the vulnerability of heritage masonry buildings. Local failures or progressive collapse can lead to significant human and cultural loss [15].

The structural response of monumental masonry buildings is governed by several features that differentiate them from ordinary contemporary structures. Multi-leaf masonry walls with thick joints and internal cores of ancient conglomerates, such as those found in St. Peter's Basilica (which forms part of the Vatican City World Heritage site) exhibit anisotropic and highly heterogeneous behavior, where the mechanical properties of brickwork leaves, Ancient Roman Concrete (ARC) and stone facing interact at different scales. Large-span barrel and groin vaults, domes and massive piers lead to complex Three-Dimensional (3D) stress paths, while previous damage, hidden cavities and undocumented interventions add further uncertainty [7, 15]. These features require advanced modeling methodologies, beyond simple One-Dimensional (1D) equivalent-frame or Two-Dimensional (2D) macro-element models. Specific nonlinear constitutive models should be calibrated based on structure-specific diagnostic tests.

In the last two decades, international documents have progressively recognized the need for rigorous structural analysis and assessment methods tailored to cultural heritage. The ICOMOS recommendations on the analysis, conservation and structural restoration of architectural heritage, together with the guidelines developed by the ICOMOS/ISCARSAH committee, emphasize the combined use of historical research, in-situ investigation, monitoring and numerical modeling within an iterative, knowledge-based process [9, 14]. More recent ICOMOS and ICCROM documents on post-disaster recovery underscore the importance of quantifying safety levels and residual capacity when planning interventions on damaged monuments [8]. In parallel, the *fib* Model Code 2020 and ISO 13822 extend reliability concepts to the assessment of existing structures, advocating performance-based approaches and explicit consideration of uncertainties in material properties, actions and modeling [6, 10].

Despite these developments, the practical application of structural reliability concepts to monumental masonry heritage is still relatively limited compared with other areas of civil engineering (e.g., bridges, offshore platforms, or modern reinforced concrete structures). Several studies have demonstrated the potential of probabilistic methods, Bayesian model updating and reliability analysis for historic towers, churches

and bridges [4]. For example, Bayesian updating of finite element models using dynamic monitoring data has been used to identify damage and refine mechanical parameters in heritage towers and palaces, while probabilistic seismic fragility analyses have been carried out for masonry churches based on macro- or micro-models [13, 18]. However, most existing applications focus on specific structural typologies or local components and rarely integrate: (i) a comprehensive experimental characterization of multi-leaf masonry, (ii) advanced 3D Non-Linear Finite Element (NLFE) models of entire monumental complexes and (iii) a reliability-based global safety format based on modern codes.

St. Peter's Basilica in Vatican City offers a unique opportunity to address this gap. The Basilica is a monumental masonry complex of exceptional size and complexity, built between the sixteenth and seventeenth centuries, with a central dome by Michelangelo resting on massive piers and surrounded by an extensive system of barrel vaults, secondary domes and multi-leaf walls. Recent diagnostic campaigns and monitoring programs, including the one conducted in 2023 by SACERTIS INGEGNERIA S.R.L. (Turin, Italy), have provided unprecedented information on the mechanical properties of the constituent materials and the current structural condition. Building upon this rich body of data, the present thesis proposes a reliability-based assessment framework that can serve as a prototype for similar monumental masonry structures, combining state-of-the-art probabilistic tools with the constraints and opportunities of heritage conservation practice.

I.2 Research scope and methodology

I.2.1 Research scope

The aim of this thesis is to develop, implement and critically evaluate an integrated framework for the probabilistic reliability assessment of complex monumental masonry buildings, with a specific application to the 17th-century body of St. Peter's Basilica in Vatican City. Within this general objective, the research focuses on four main points:

1. The first objective is to derive a consistent set of mechanical parameters for the different materials composing the multi-leaf masonry walls of St. Peter's Basilica (brickwork leaves, ARC core, travertine stone facing) and to convert them into an equivalent single-layer representation for global 3D Non-Linear Finite Element Analyses (NLFEAs). This involves combining experimental in-situ and laboratory

testing with non-linear constitutive models such as Drucker–Prager (D-P) and Concrete Damage Plasticity (CDP) [7, 15].

2. A second objective is to identify which CDP parameters can and should be treated as random variables, to formulate prior probabilistic models informed by literature and standards, and to update these priors using the results of the diagnostic campaign through Bayesian inference. Particular attention is given to modeling uncertainties, correlation structures and the definition of appropriate likelihood functions [1, 2, 4].

3. A third objective is to develop and calibrate a 3D NLFE model of the the 17th-century body of St. Peter's Basilica, capable of reproducing the main structural elements (vaults, multi-leaf walls, foundations) and of capturing the non-linear response under gravity load, using the homogenized material models developed in the previous stages.

4. Finally, the thesis proposes to integrate the stochastic material models and global NLFEAs within a reliability-based safety format tailored to monumental masonry structures. This includes the calibration of (PSFs) for material properties and effects of actions, in line with target reliability indices drawn from ISO 2394 and *fib* Model Code 2020, and the application of these safety factors to assess the safety level of St. Peter's Basilica under gravity load [6, 11, 12].

Although the framework is developed and tested on St. Peter's Basilica, the research scope is intentionally wide. The proposed combination of diagnostic campaigns, homogenization strategies, probabilistic material models, global 3D NLFEAs and reliability-based safety formats is designed to be transferable (with appropriate adaptations) to other complex monumental masonry buildings, particularly historic churches and cathedrals characterized by multi-leaf walls and complex vaulted systems.

I.2.2 Research methodology

This thesis presents the multidisciplinary approach used to evaluate the structural safety of monumental heritage structures, combining experimental investigation, computational modeling, and statistical analysis to develop an integrated framework.

The historical and construction knowledge are combined with diagnostic evidence to create realistic structural models, boundary conditions, and loading scenarios. Deterministic Finite Element (FE) simulations at material and wall scales are used to understand experimental results, and represents the base for the probabilistic phase,

where selected material parameters of the CDP model are treated as random variables. Bayesian inference is used to update these parameters using diagnostic, literature and prescriptions from standards.

Finally, the probabilistic material models and global 3D NLFEAs are embedded within a reliability-based safety assessment. Structural performance is evaluated through reliability indices and failure probabilities for specific limit states. PSFs for materials and actions are calibrated in accordance with target reliability levels. The proposed methodology combines experimental data, advanced numerical modeling, and reliability concepts, offering a rational basis for assessing safety and supporting decision-making in the preservation of historic masonry buildings.

I.3 Thesis layout

This thesis is organized into ten chapters, grouped into two main parts. The connectivity between the different chapters is visualized in Figure I.3.

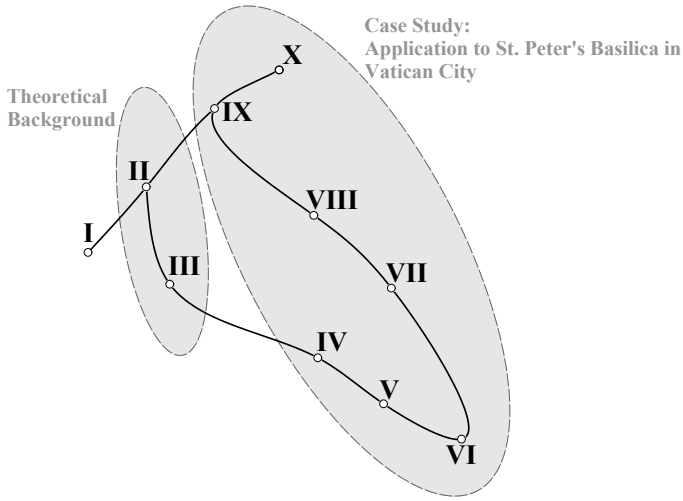

Figure I.3: Connectivity between the different chapters in this thesis. (Concept inspired by a graphical design from Caspeele's Ph.D. thesis, 2010 - Ghent University).

After the general introduction in the current Chapter I, the thesis is structured as follows:

(i) Theoretical background, which includes:

Chapter II, examines the principles of structural reliability theory and the safety formats used in current engineering practice;

Chapter III, introduces the material characterization framework and the modeling strategy adopted for global 3D NLFEAs.

(ii) Application to St. Peter's Basilica in Vatican City, which includes:

Chapter IV, describes the architectural and structural system of the Basilica, together with the historical and geometric knowledge used to define the numerical model;

Chapter V, summarizes the 2023 experimental diagnostic campaign conducted by SACERTIS INGEGNERIA S.R.L. and provides preliminary estimates of the mechanical properties;

Chapter VI, calibrates a deterministic elasto-plastic D–P model to represent the behavior of the multi-leaf masonry;

Chapter VII, extends the material modeling to a probabilistic Bayesian framework based on the CDP model;

Chapter VIII, presents the global 3D NLFE models of the Basilica, including modeling assumptions, boundary conditions, and load combinations;

Chapter IX, used the stochastic material models and numerical simulations to assess the structural reliability and the safety levels under gravity loads;

Finally, Chapter X summarizes the main outcomes of this research and outlines potential future developments.

I.4 References

[1] Bartoli, G., Betti, M., Marra, A. M., and Monchetti, S. (2019). A bayesian model updating framework for robust seismic fragility analysis of non-isolated historic masonry towers. *Philosophical Transactions of the Royal Society A*, 377(2155).

[2] Beconcini, M. L., Croce, P., Marsili, F., Muzzi, M., and Rosso, E. (2016). Probabilistic reliability assessment of a heritage structure under horizontal loads. *Probabilistic Engineering Mechanics*, 45:198–211.

[3] Canet, C., Sánchez-Aguirre, D., García-Sánchez, L., and Castañeda-Bastida, E. (2024). Geological heritage in unesco's world heritage list: A critical review. *International Journal of Geoheritage and Parks*, 12(4):531–543.

[4] Croce, P., Beconcini, M. L., Formichi, P., Landi, F., Puccini, B., and Zotti, V. (2021). Bayesian methodology for probabilistic description of mechanical parameters of masonry walls. *ASCE-ASME Journal of Risk and Uncertainty in Engineering Systems, Part A: Civil Engineering*, 7(2).

[5] EN.1990.Eurocode (2002). Basis of structural design.

[6] fib, 2020 – International Federation for Structural Concrete (2023). *fib Model Code 2020 for Concrete Structures*. fib, Lausanne, Switzerland.

[7] Funari, M. F., Auricchio, F., and Lourenço, P. B. (2023). Real-time structural stability of domes through limit analysis: Application to St. Peter's Dome in Rome. *Archives of Computational Methods in Engineering*, 30:997–1031.

[8] ICOMOS and ICCROM (2023). Guidance on post-disaster and post-conflict recovery and reconstruction for heritage places of cultural significance and world heritage cultural properties. https://www.iccrom.org/publication/guidance-post-disaster-and-post-conflict-recovery-and-reconstruction-heritage-places.

[9] ICOMOS/ISCARSAH Committee (2003). Recommendations for the analysis, conservation and structural restoration of architectural heritage. Technical report, ICOMOS International Scientific Committee for Analysis and Restoration of Structures of Architectural Heritage, Paris, France.

[10] ISO 13822:2010 (2010). Bases for design of structures — assessment of existing structures.

[11] ISO 2394:2015 (2015). General principles on reliability for structures.

[12] JCSS – Joint Committee on Structural Safety (2001). *Probabilistic Model Code*. JCSS, Zurich, Switzerland.

[13] Lagomarsino, S. and Cattari, S. (2015). Seismic vulnerability of masonry buildings: The PERPETUATE approach. *Bulletin of Earthquake Engineering*, 13(1):13–47.

[14] Roca, P. (2021). The ISCARSAH guidelines on the analysis, conservation and structural restoration of architectural heritage. *International Journal of Architectural Heritage*, 15(10):1480–1505.

[15] Roca, P., Cervera, M., Gariup, G., and Pelà, L. (2010). Structural analysis of masonry historical constructions: Classical and advanced approaches. *Archives of Computational Methods in Engineering*, 17(3):299–325.

[16] UNESCO World Heritage Centre (2024). World heritage list statistics. https://whc.unesco.org/en/list/stat/.

[17] UNESCO World Heritage Centre (2025). World heritage list. https://whc.unesco.org/en/list/.

[18] Venanzi, I., Kita, A., et al. (2020). Earthquake-induced damage localization in an historic masonry tower through long-term dynamic monitoring and FE model calibration. *Engineering Structures*, 209.

CHAPTER II

Fundamentals of structural reliability and safety formats

"Molti, Beatissimo Padre, misurando con picciol giudicio le cose grandi, le stimano più favole che vere."

("Many, Most Holy Father, measuring with small judgment great things, deem them rather fables than true.")

– Raffaello Sanzio

II.1 Introduction

Modern structural design and assessment are based on probabilistic concepts and codified safety formats that aim at assessing the probability of failure (P_f) over a specified reference period. International standards such as EN 1990 [11], ISO 2394 [22] and the *fib* Model Code 2020 [12] are explicitly based on limit state design and structural reliability framework, so that the safety assessment used in design practice can be interpreted as a simplified application of a probabilistic approach based on assigned target reliability indices.

The assessment of existing structures, and in particular of heritage masonry buildings, is becoming a central task in structural engineering. Rehabilitation, strengthening and maintenance account for a significant portion of the construction volume, although harmonized rules for existing structures are still incomplete in the current Eurocodes [10, 25]. Documents such as ISO 13822 [21], CEN/TS 17440 [5] and *fib* Bulletin 80 [13] therefore provide complementary guidance for the reliability-based assessment of existing structures, addressing remaining working life, inspection and testing, and differentiated target reliability levels [18, 32].

Structural reliability can be assessed at several levels of complexity. Starting from probabilistic models of actions and resistances, the failure probability of a given limit state can be evaluated by full-probabilistic methods (e.g., Monte Carlo simulation), or indirectly through semi-probabilistic formats calibrated to prescribed target reliability indices. Within this framework, different safety formats are organized in the *fib* Model Code 2020, and in the new generation of Eurocodes, in a hierarchy of Levels of Approximation (LoA), from simplified conservative checks to advanced non-linear and probabilistic models [4].

In the case of monumental masonry buildings such as cathedrals and basilicas, choosing a proper safety format is particularly delicate. These structures are characterized by complex 3D systems, multi-leaf walls and large-span vaults, often built with heterogeneous materials and exhibiting pronounced non-linear behavior. Advanced NLFEAs are frequently required to capture the actual load-carrying mechanisms and potential damage patterns, thereby supporting the use of global safety formats and probabilistic methods [20].

This chapter is divided into three main sections. It first recalls the fundamental concepts of structural reliability for new and existing structures, then reviews the main safety formats adopted in international standards and recent literature, and finally addresses specific issues related to the reliability assessment of existing and heritage masonry structures.

II.2 Principles of structural reliability analysis

Structural reliability analysis provides a quantitative framework to assess how much a structure satisfies the performance requirements with an acceptably low P_f during a given reference period. In this framework, the random variables that govern the structural behavior are treated as random variables, and failure is defined through a limit state function separating the safe and failure domains in the space of these variables [23, 27].

II.2.1 Random variables and sources of uncertainty

The structural behavior is influenced by several random variables, which are modeled as random quantities to take into account the uncertainties affecting their values. Typical categories of random variables include:

- Actions: (permanent, variable, accidental and environmental loads), including their time variability and spatial variability;
- Material properties: (e.g., strengths, stiffnesses), which exhibit variability due to manufacturing processes, aging and environmental influences;
- Geometrical properties: (dimensions, imperfections), including construction tolerances and measurement errors;
- Model uncertainties: accounting for the fact that analytical or numerical models only approximate the real structural behavior.

Moreover, these sources of uncertainty can be classified as aleatory or epistemic [4]. In particular, the aleatory uncertainties correspond to natural randomness that cannot be reduced by gathering more information (e.g., spatial variability of material strength, variability of traffic loads), whereas the epistemic uncertainties are due to limited knowledge and can in principle be reduced by improved modeling, testing, inspection or monitoring (e.g., uncertainty in mechanical models, limited number of test results).

Model uncertainty is often represented through a multiplicative random factor Θ applied to the response predicted by a physical or numerical model:

$$R(X,Y) \approx \Theta R_{\text{model}}(X) \tag{II.1}$$

where $R(X,Y)$ is the actual (unknown) resistance; $R_{\text{model}}(X)$ is the model prediction based on the random variables X explicitly taken into account in the model; and Y

represents other variables that influence the response but are not explicitly modeled. The mean and coefficient of variation of the model uncertainty parameter Θ are estimated by directly comparing the experimental data with the model predictions. In practice, the random variable Θ is typically assumed to follow a lognormal distribution.

For existing structures, the statistical models of random variables can be updated using inspection and test data through Bayesian methods, in order to reduce the epistemic uncertainties. This aspect becomes particularly important for heritage masonry buildings, where material properties and construction details often lack documentation and must be examined from in-situ investigations [10, 18].

Table II.1: Example of the classification of main sources of uncertainty in structural reliability analysis.

Category	Aleatory uncertainty	Epistemic uncertainty
Actions	Natural variability of loads	Limited information on load statistics, modeling simplifications
Material properties	Inherent variability of strength and stiffness	Limited test data, uncertain correlation between tests and in-situ properties
Geometry	Construction tolerances	Incomplete drawings, measurement errors, hidden details
Structural model	—	Simplifications in mechanical modeling, numerical discretization, boundary conditions

II.2.2 Limit state concept

In the limit state design philosophy, the performance requirements for a structure are expressed as limit states, which are conditions in which the structure fails to satisfy one or more of its design purposes. In structural applications, the most relevant types of limit states are:

- Ultimate Limit States (ULS): associated with structural collapse or other failure modes that could compromise human life or cause significant economic losses;
- Serviceability Limit States (SLS): associated with excessive deformations, damage, vibrations, or other events that could compromise functionality, durability, or comfort.

Additional limit states can be defined for existing and heritage structures to take into account preservation, aesthetics, or cultural value. These are often referred to as phenomenological limit states [2, 24, 29].

From a mathematical point of view, each limit state is expressed by a limit state function (or performance function) $g(X)$, defined in terms of a vector of random random variables $X = \{X_1, X_2, \ldots, X_N\}$. The sign of $g(X)$ identifies whether the structure is in a safe or failure condition:

$$g(X) = \begin{cases} > 0 & \text{safe domain} \\ = 0 & \text{limit state surface} \\ < 0 & \text{failure domain} \end{cases} \tag{II.2}$$

For many structural problems, a simple formulation at member or cross-section level is usually written in the following form:

$$g(X) = R(X) - E(X) \tag{II.3}$$

where $R(X)$ denotes the structural resistance and $E(X)$ the effect of actions.

Let $f_X(x)$ be the joint Probability Density Function (PDF) of the random variables, the P_f associated with the considered limit state is written as:

$$P_f \;=\; \mathbb{P}\big[g(X) \leq 0\big] \;=\; \int_{g(x)\leq 0} f_X(x)\,\mathrm{d}x \;=\; \int_{R_f} f_X(x)\,\mathrm{d}x \tag{II.4}$$

In this case, considering two random variables (X_1, X_2), the joint PDF $f_X(x)$ forms a surface over the $X_1 - X_2$ plane, and the limit state curve $g(X_1, X_2) = 0$ separates the safe domain ($R_s : g > 0$) from the failure domain ($R_f : g < 0$).

The P_f corresponds to the volume of the PDF surface above the failure domain, while $P_R = 1 - P_f$ represents the probability of survival, or equivalently, the probability of structural safety.

In higher dimensions, the limit state surface $g(X) = 0$ turns into a hypersurface embedded in the random variable space N_X.

Figure II.1 illustrates the visual representation of the Eq. (II.4).

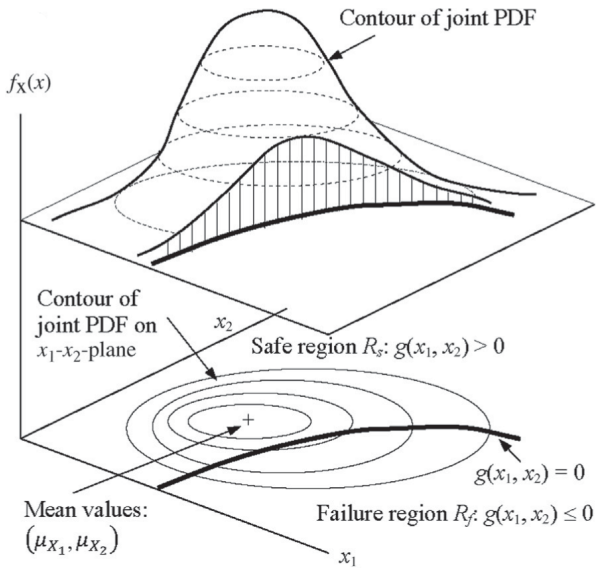

Figure II.1: Schematic 3D and projected 2D view of a limit state surface $g(X) = 0$ in the space of the random variables (X_1, X_2) (from [7]).

II.2.3 Reliability index

In most engineering applications, the direct evaluation of the integral in Eq. (II.4) is not feasible because (i) the number of random variables may be large, (ii) the joint PDF and the limit state function can be highly nonlinear, and (iii) each evaluation of $g(X)$ may require complex numerical models (e.g., NLFEAs). Monte Carlo simulations provide a simple and robust estimate of P_f, but they often requires many model evaluations and can become computationally prohibitive for complex structural models. For this reason, approximate reliability methods such as the First-Order Reliability Method (FORM) and the Second-Order Reliability Method (SORM) have been developed to estimate the structural reliability more efficiently [15].

First-order and second-order reliability methods

A key step in FORM and SORM is the transformation of the original random variables X into an equivalent set of statistically independent standard normal variables $U = \{U_1, \ldots, U_N\}$, through an iso-probabilistic transformation that preserves the Cumulative Distribution Function (CDF):

$$F_{X_i}(x_i) = \Phi(u_i) \quad \Rightarrow \quad u_i = \Phi^{-1}\big(F_{X_i}(x_i)\big) \tag{II.5}$$

where F_{X_i} is the CDF of X_i and Φ is the standard normal CDF. In this standard normal space, all U_i are independent standard normal variables, and the limit state function becomes:

$$G(U) = g\big(X(U)\big) \tag{II.6}$$

In the U-space, the probability of failure can be written as:

$$P_f = \mathbb{P}\big[G(U) \leq 0\big] = \int_{G(u)\leq 0} \varphi(u)\,\mathrm{d}u \tag{II.7}$$

where $\varphi(u)$ is the joint PDF of the standard normal variables (product of univariate standard normal PDFs). Based on the Hasofer–Lind formulation [16], the reliability index β is defined as the shortest distance from the origin to the limit state surface in the standard normal space:

$$\beta \;=\; \min_{u} \big\{ \|u\| \;:\; G(u) = 0 \big\} \tag{II.8}$$

and the corresponding point u^* on the surface $G(U) = 0$ is called the design point or most probable point of failure. Geometrically, u^* is the point where the limit state surface is tangent to the hypersphere of radius β centered at the origin (see Figure II.2).

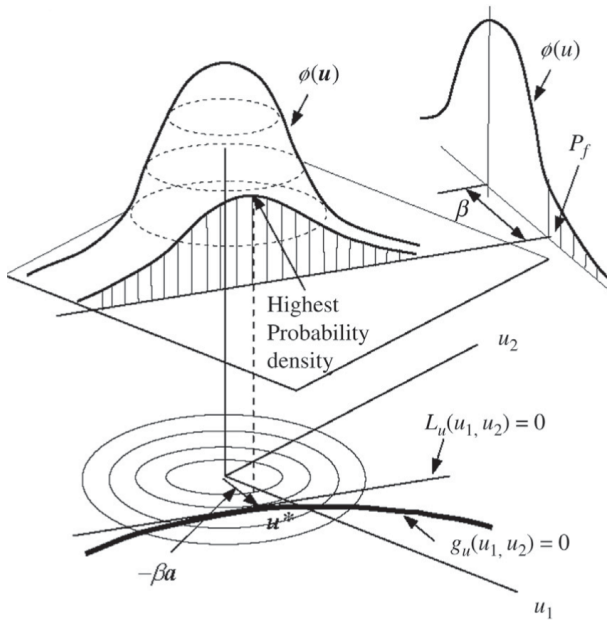

Figure II.2: Geometric interpretation of the reliability index β in the standard normal space (U_1, U_2) (from [7]).

Specifically, in FORM, the limit state surface is approximated by its tangent hyperplane at the design point u^*, obtained from a first-order Taylor expansion of $G(U)$ around u^*. Under this first-order approximation, the probability of failure can be expressed approximately in terms of the reliability index as:

$$P_f^{\text{FORM}} \approx \Phi(-\beta) \tag{II.9}$$

where $\Phi(\cdot)$ denotes the cumulative distribution function of the standard normal distribution. The reliability index β is found by solving the optimization problem in Eq. (II.8), typically through a constraint minimization algorithm. FORM provides a good compromise between accuracy and computational cost and is widely used in structural reliability analyses.

Further, when the limit state surface is markedly curved in the vicinity of the design point, the first-order (linear) approximation may not be sufficiently accurate. SORM introduces a second-order Taylor expansion of $G(U)$ around u^*, involving the Hessian matrix of second derivatives and the principal curvatures k_i of the limit state surface at the design point. In this framework, an asymptotic approximation of the probability of failure is given by the following formulation:

$$P_f^{\text{SORM}} \approx \Phi(-\beta) \prod_{i=1}^{N-1} \frac{1}{\sqrt{1+\beta\, k_i}} \tag{II.10}$$

which reduces to the FORM estimate when the principal curvatures vanish (i.e., when the limit state surface is locally flat at the design point).

Reliability index and its interpretation

Starting from the FORM approximation in Eq. (II.9), the reliability index β is introduced as a scalar measure of structural safety and is approximately related to the negative value of the inverse standard normal cumulative distribution function evaluated at the failure probability [12, 17]:

$$\beta = -\Phi^{-1}(P_f) \tag{II.11}$$

Higher values of β correspond to lower P_f. Figure II.3, shows graphically the relationship between P_f and β.

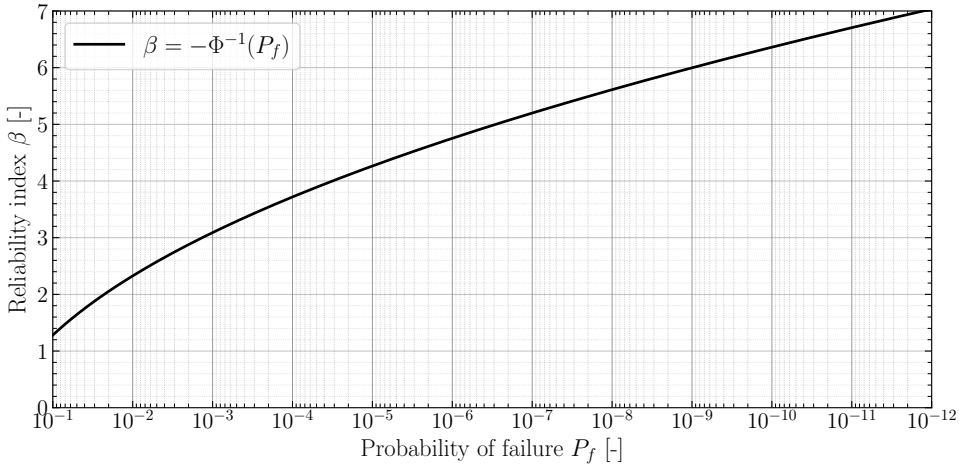

Figure II.3: Relationship between P_f and β on a logarithmic scale.

II.2.4 Reliability methods and levels of approximation

Various methods are available to assess the failure probability or reliability index. A common classification, also adopted in several standards and textbooks [12, 22, 23], is based on four reliability levels:

- Level III: Full-probabilistic methods, where the failure probability is evaluated (in principle) exactly, for example by direct numerical integration of Eq. (II.4) or by Monte Carlo simulations and related variance-reduction techniques;
- Level II: Approximate probabilistic methods, such as FORM and SORM, which transform the random variables into an equivalent standard normal space and provide a linear or quadratic approximation of the limit state surface around the design point;
- Level I: Semi-probabilistic methods, in which design values of actions and resistances are defined through partial safety factors calibrated for reaching target reliability indices;
- Level 0: Strictly deterministic checks, where no explicit probabilistic modeling is performed and safety is verified by simple inequality constraints (e.g., allowable stress design).

Level III methods provide the most complete description of uncertainty, but in general they are computationally expensive and need accurate probabilistic models of all random variables. They are frequently used for research, calibrating safety formats, or for exceptional structures with high consequences of failure.

Level II methods, especially FORM, provide a good balance of accuracy and computational effort and are often used for code calibration as well as for direct reliability-based design and assessment.

Level I methods are predominant in everyday engineering practice. Here, the complex probabilistic problem is reduced to semi-probabilistic design principles defined in terms of characteristic values and partial safety factors. These semi-probabilistic formats are calibrated, often using Level II or Level III analyses, so that agreement with the semi-probabilistic design implies that the target reliability indices are fulfilled for a wide range of structures and load conditions.

Level 0 methods are entirely deterministic, with no clear quantification of reliability obtained during the assessment or design. As a result, they may lead to an unconservative evaluation of structural safety and scattered reliability levels. With the development of probability-based design formats, these methodologies became obsolete and are no longer used in the current structural standards.

This hierarchy of reliability levels have a close relationship whit to the LoA used in the *fib* Model Code, where higher LoA involve more detailed models and more refined reliability tools. The connection between reliability levels and safety formats will be further discussed in Section II.3.

The *fib* Model Code introduces the concept of LoA to structure the choice of analysis methods and safety formats according to the complexity of the problem and the required accuracy [12], which can be summarized in the following levels:

- LoA I: Simple and conservative checks using empirical formulas or guidelines that are assumed to be satisfactory. Uncertainties are implicitly covered by large safety margins.
- LoA II: Standard member verifications (local) based on Partial Factor Method (PFM), as in current Eurocodes for conventional structures;
- LoA III: Advanced analyses (e.g., NLFEAs) combined with calibrated safety formats such as Global Resistance Factor method (GRM), Coefficient of Variation method (ECoV) or Global Safety Format (GSF);
- LoA IV: Full-Probabilistic Method (PM), if relevant, combined with advanced 3D NLFEAs and explicit evaluations of the failure probabilities, typically restricted to research or to exceptional structures.

A schematic representation of the LoA approach is shown in Figure II.4.

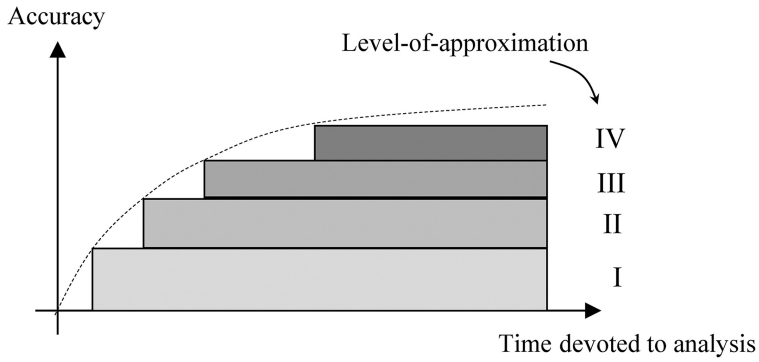

Figure II.4: Schematic representation of the LoA approach according to the *fib* Model Code 2020.

II.2.5 Target reliability for new and existing structures

Establishing target reliability levels is an essential step in structural reliability analysis, often expressed through a target reliability index β_t. International standards, such as EN 1990 [11], ISO 2394 [22], and the *fib* Model Code 2020 [12], recommend target values based on limit state type, reference period, and failure consequences.

For new structures, considering the ULS of ordinary buildings (Consequence Class 2, CC2) with a 50-year reference period, a commonly adopted target reliability index is $\beta_t = 3.8$, corresponding to $P_f \approx 7 \times 10^{-5}$ (see Table II.2). The CC reflects the severity of failure consequences (loss of life, economic damage, environmental effects), with higher classes indicating more severe consequences.

Lower β values are usually accepted for SLS, whereas higher reliability levels are required for structures with exceptional consequences of failure (e.g., major bridges and dams).

Table II.2: Target reliability indices β_t (and associated target failure probabilities $p_{f,t}$) for ULS (indicative values based on EN 1990, for new structures).

Consequence class	Reference period	β_t (ULS)
Low consequences (CC1)	50 years	3.3 ($p_{f,t} \approx 5 \times 10^{-4}$)
Normal consequences (CC2)	50 years	3.8 ($p_{f,t} \approx 7 \times 10^{-5}$)
High consequences (CC3)	50 years	4.3 ($p_{f,t} \approx 8 \times 10^{-6}$)

For existing structures, particularly heritage buildings, target reliability levels require a more detailed definition that accounts for the remaining working life, societal and cultural value, and the cost and feasibility of interventions.

Resistance decreases over time in degrading structures, so reliability is not stationary. A fixed 50-year reference period is therefore inappropriate; instead, an annual reference period is adopted, allowing updates to coincide with inspection and maintenance. An annual reference period is often preferable for the assessment (rather than the 50-year for the design) for the following reasons [10]:

- It reduces the dispersion of reliability levels across different load ratios;
- It avoids recalibrating targets for structures with different remaining service lives;
- It aligns better with life-safety acceptance criteria;
- It allows for the incorporation of deterioration and non-stationary effects (e.g., fatigue, corrosion, climate change), where long-term averaging is less meaningful;
- Annual maxima are typically better described for variable actions than long-term maxima.

Another possibility for specifying the target reliability index, is the economic optimization. In Table II.3, the annual target reliability indices and the corresponding failure probabilities for the ultimate limit states are shown, as recommended by the *fib* Model Code 2020 [12] and in accordance with the JCSS Probabilistic Model Code [23] and ISO 2394 [22].

Table II.3: Target reliability indices β_t (and associated target failure probabilities $p_{f,t}$) for a one-year reference period based on economic optimization and ULS, for existing structures.

	Consequence class		
Relative cost of safety measure	CC1	CC2	CC3
Large (A)	3.1 ($p_{f,t} \approx 10^{-3}$)	3.3 ($p_{f,t} \approx 5 \times 10^{-4}$)	3.7 ($p_{f,t} \approx 10^{-4}$)
Normal (B)	3.7 ($p_{f,t} \approx 10^{-4}$)	4.2 ($p_{f,t} \approx 10^{-5}$)	4.4 ($p_{f,t} \approx 5 \times 10^{-6}$)
Small (C)	4.2 ($p_{f,t} \approx 10^{-5}$)	4.4 ($p_{f,t} \approx 5 \times 10^{-6}$)	4.7 ($p_{f,t} \approx 10^{-6}$)

In general, ISO 2394 [22] and the *fib* Model Code 2020 [12] provide a reliability differentiation for existing structures. The assumption of statistical independence between consecutive years may be overly conservative for variable actions, as temporal correlation is generally present.

The target reliability level can be specified either as the maximum annual failure probability (one-year reference period) or as a maximum lifetime failure probability obtained by the following approximate formulation:

$$\Phi(\beta_{t,n}) = [\Phi(\beta_{t,1})]^{n/k} \tag{II.12}$$

where n indicates the number of years of the reference period $T_{\text{ref}}(n = T_{\text{n}})$, k represents the independence period of years $(k \leq n)$. The following guidance on the choice of k may be useful [31]:

- One year can be accepted in many cases, e.g. when climatic or traffic actions govern structural reliability.
- 5–10 years can be considered for structures dominated by a sustained component of the imposed load in office buildings.
- $k = n$ can be used for the cases in which the reliability is insignificantly affected by time-variant phenomena, e.g. for structures subjected to dominating permanent actions, masonry or geotechnical structures. In this case, the limit state function is independent of time. As a result, the reliability index remains constant over the entire reference period.

Based on Eq. II.12, Figure II.5 illustrates the transformation of a constant annual target reliability $\beta_{t,1} = 4.2$ (CC2, see Table II.3) into an equivalent target reliability over a reference period of n years, $\beta_{t,n}$. The effect of temporal correlation between consecutive years is accounted for through the parameter k.

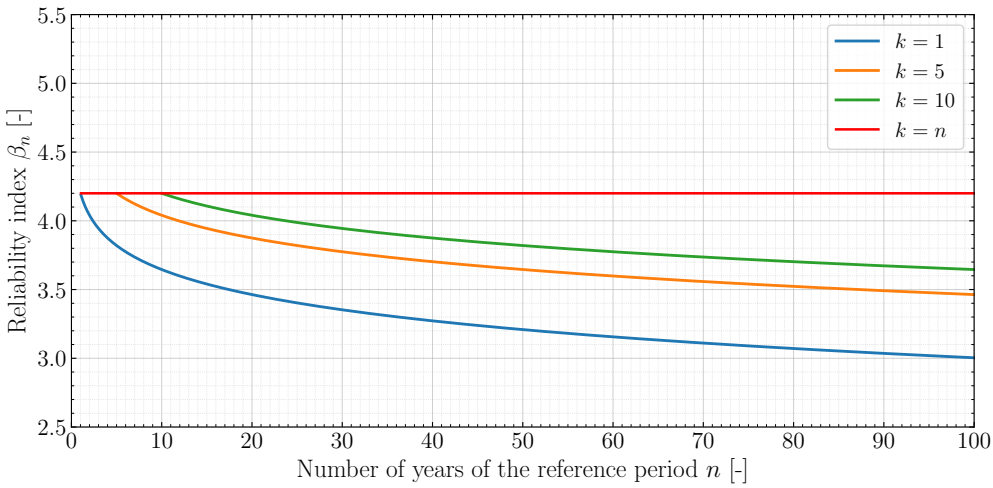

Figure II.5: Target reliability index $\beta_{t,n}$ as a function of the reference period n, assuming $\beta_{t,1} = 4.2$ and accounting for temporal correlation through the parameter k.

Furthermore, Table II.4 summarizes qualitatively some of the main differences between design of new structures and assessment of existing ones in terms of reliability concepts and partial factor treatment.

Table II.4: Qualitative comparison of reliability concepts for new and existing structures.

Aspect	New structures	Existing structures
Reference period	Typically 50–100 years	Preferable 1 year
Information level	Based on design assumptions and code models	Enhanced by inspection, tests, monitoring; unknown defects
Cost of safety measures	Incorporated in design optimization	Often high (strengthening, interruption of use)
Target reliability	Coded values for consequence classes	Possibly reduced β_t, case-dependent
PSFs	Fixed values calibrated for generic classes	Calibrated based on information quality and target reliability

As already outlined in Section II.1, the reliability assessment of existing structures differs from the design of new structures in several key aspects: the information level on the actual structural condition, the remaining working life, and the relative costs of safety measures. These differences have direct implications for the choice of target reliability levels and safety formats [17].

From an economic viewpoint, the optimum target reliability for a structure can be conceptualized by minimizing the sum of initial (costs of construction or upgrading) and expected failure costs over its working life.

For existing structures, the marginal cost of increasing safety by strengthening or retrofitting is typically higher than for optimizing a new design, and the remaining working life is shorter. Consequently, the cost-optimal target reliability for an existing structure is, in general, lower than that for a new structure with the same consequences of failure, provided that minimum requirements for human safety are still satisfied.

fib Bulletin 80 [13] and related studies propose differentiated target reliability indices for new and existing structures, together with procedures to adjust partial safety factors in assessment.

Moreover, standards such as ISO 13822 [21] and CEN/TS 17440 [5] highlighting that actual structural conditions, inspection results and past performance should be explicitly considered in the assessment of existing structures.

For heritage buildings, additional constraints related to conservation and minimal intervention further influence the acceptable reliability level and the choice of verification method [32], as discussed in Section II.4.

II.3 Safety formats for NLFEAs

In the last two decades, several safety formats have been developed for advanced numerical models and for the assessment of existing structures, providing practical rules for determining whether structural reliability is acceptable without carrying out an explicit probabilistic analysis for every single structure. These formats ensure that design actions do not exceed structural resistance, while maintaining an implicit relationship with the probabilistic concepts and target reliability levels discussed in Section II.2.

As illustrated in Section II.2.4, the *fib* Model Code 2020 extends the semi-probabilistic framework by introducing different safety formats, distinguished by a hierarchy of LoA.

Building on that discussion, this section examines in more detail the safety formats tailored to NLFEAs, starting from the fundamental distinction between local and global approaches, as illustrated in Figure II.6.

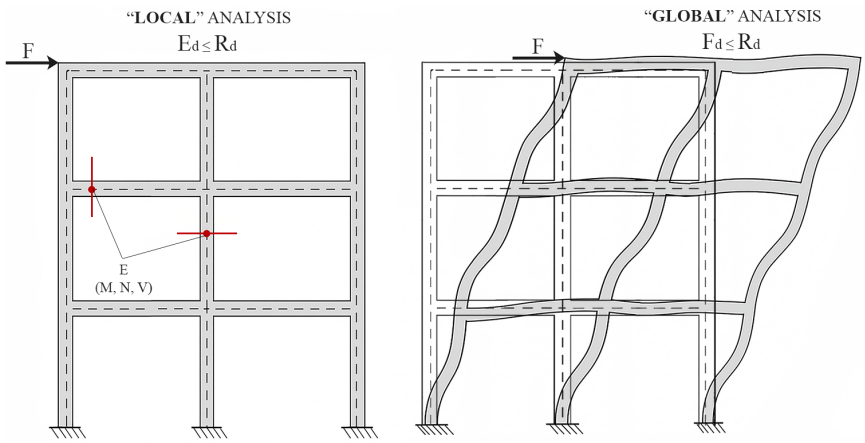

Figure II.6: Distinction between local and global approaches in structural reliability analysis (adapted from [4]).

In standard practice, LoA I assessment is based on local linear-elastic analyses at the component level, where only the most stressed cross-sections are checked by means of the design inequality $E_d \leq R_d$. In contrast, global approaches derive the structural capacity from NLFEAs at the system level, and the safety condition is verified by

comparing the design value of the external actions with the global design resistance through the inequality $F_d \leq R_d$.

In Figure II.6, F denotes the acting external actions, E_d the design value of the internal effects obtained from a linear-elastic analysis, and R_d the sectional design resistance in terms of internal forces (M,N,V). In the global format, F_d denotes the design value of the external actions and R_d the global design resistance of the structure to these actions as evaluated by NLFEAs.

II.3.1 Partial Factor Method (PFM)

The PFM is the most widely used safety format in structural engineering practice. In this format, design values of random variables X_d are obtained from their characteristic values X_k, which represent specified fractiles of the probability distribution (typically a lower fractile for material strengths and an upper fractile for actions), and are then divided or multiplied by appropriate PSFs γ_X, for example [11, 12, 22]:

$$X_d = \begin{cases} X_k/\gamma_X & \text{for resistances} \\ \gamma_X X_k & \text{for actions} \end{cases} \tag{II.13}$$

Considering ULS, the design inequality $E_d \leq R_d$ is typically written in the following form:

$$E\left(\gamma_G \sum G_k + \gamma_Q \sum \psi_0 Q_k\right) \leq \frac{R_k}{\gamma_M} \tag{II.14}$$

where G_k and Q_k are characteristic values of permanent and variable actions, ψ_0 is a combination factor, γ_G and γ_Q are action partial factors, and γ_M is the material partial factor. For structural materials, γ_M could be composed of different contributions, including a factor γ_m associated with the stochastic uncertainties of material properties and a factor γ_{Rd} accounting for model uncertainty in resistance models.

The statistical background of PSFs is rooted in Level II reliability methods. Given probabilistic models of actions, resistances and model uncertainties, and a target reliability index β_t, it is possible to derive design equations for the PSFs that ensure, for a wide class of structures, that $\beta \geq \beta_t$ [4, 12]. In practice, the detailed calibration is performed once for a representative set of structural typologies, and the resulting PSFs are then tabulated in standards.

For existing structures, the same PFM can in principle be retained, but the numerical values of the PSFs should be adapted to account for different target reliability levels, shorter reference periods and additional information from inspection and testing. For

instance, *fib* Bulletin 80 and later studies propose formulations for the PSFs as functions of the target reliability index, the coefficients of variation of the variables and the quality of information (e.g., presence of in-situ measurements) [3, 13, 25]. This approach is based on the Design Value Method (DVM) and the Adjusted Partial Factor Method (APFM), which have been applied to the assessment of existing concrete and masonry structures.

Table II.5: Illustrative PSFs for actions and materials for concrete structures (indicative values inspired by EN 1990 and *fib* Model Code 2020, for design purposes).

Quantity	Symbol	Fixed PSFs
Permanent action (unfavorable)	γ_G	1.20–1.35
Variable action (imposed load)	γ_Q	1.50
Concrete compressive strength	γ_c	1.50
Reinforcement yield strength	γ_s	1.15
Model uncertainty in resistance	γ_{Rd}	1.05–1.15

In the context of NLFEA, the standard PFM evaluates the design resistance from a single analysis performed with design values of the material strengths, in analogy with the partial safety factor format adopted in the Eurocodes [11]. Let f_k denote the characteristic strength and γ_M the corresponding material partial factors (e.g., γ_c and γ_s for concrete and reinforcement, respectively). The design strength is then given by:

$$f_d = \frac{f_k}{\gamma_M} \tag{II.15}$$

A NLFEA is then performed using f_d and nominal geometry a_{nom}, and the ultimate global resistance is interpreted as $R_{\text{NLFEA}}(f_d)$ divided by a model factor γ_{Rd}:

$$R_d = \frac{R_{\text{NLFEA}}(f_d)}{\gamma_{Rd}} \tag{II.16}$$

Several applications use a fixed value (usually $\gamma_{Rd} \approx 1.06$) to account for the uncertainty of the non-linear model [13], as this method is pretty simple and only requires a single NLFEA. However, some studies have been reported, including [4, 26] that: (i) using decreased strengths f_d could change the failure mode compared to the actual structure and (ii) reliability could vary significantly from the target level, particularly when modeling uncertainties are significant or the structure shows brittle or highly non-linear

behavior. The PFM is often utilized as a reference or benchmark, however more sophisticated global formats are recommended for advanced assessment using NLFEA.

Design Value Method (DVM)

The DVM derives PSFs directly from the probabilistic description of random variables, rather than fixing them [13]. The starting point is the conventional separation of the resistance partial factor into three contributions:

$$\gamma_M = \gamma_{Rd,1}\,\gamma_{Rd,2}\,\gamma_m \tag{II.17}$$

where γ_m accounts for the variability of the material properties, $\gamma_{Rd,1}$ for model uncertainty and $\gamma_{Rd,2}$ for geometrical deviations. For existing structures, the numerical values of these factors are derived such that the target reliability index β_t is achieved for the chosen reference period.

Consider a generic material property X (e.g., compressive strength) described as a lognormal random variable with mean μ_X and variance V_X. For a 5% lower fractile used as characteristic value, the DVM assumes:

$$X_k \approx \mu_X \exp(-k_n V_X), \qquad k_n \approx 1.645 \tag{II.18}$$

while the design value X_d associated with the target reliability β_{target} is written as:

$$X_d \approx \mu_X \exp(-\alpha_R \beta_t V_X) \tag{II.19}$$

where α_R is the sensitivity factor of the limit state with respect to the resistance variable (typically $\alpha_R \approx 0.8$ for a dominant resistance parameter, and $\alpha_R \approx 0.32$ for non-dominant parameters). The material-related partial factor then follows from the ratio between characteristic and design values:

$$\gamma_m = \frac{X_k}{X_d} \approx \exp\left[(\alpha_R \beta_t - k_n) V_X\right] \tag{II.20}$$

The model uncertainty is represented by a multiplicative random variable θ_R (e.g., accounting for simplifications in the resistance model) with mean μ_{θ_R} and coefficient of variation V_{θ_R}. Assuming again a lognormal model and a moderate coefficient of variation, the corresponding partial factor can be approximated as:

$$\gamma_{Rd,1} \approx \frac{\mu_{\theta_R}}{\theta_{R,d}} \approx \frac{1}{1 - \alpha_R \beta_t V_{\theta_R}} \tag{II.21}$$

where $\theta_{R,d}$ denotes the design value of the resistance model factor. In a similar way, geometrical uncertainties (e.g. effective depth of reinforcement, wall thickness) can be treated by introducing a random variable a and an associated partial factor $\gamma_{Rd,2}$. If detailed measurements show that the variability of geometrical properties is negligible, it is common to adopt $\gamma_{Rd,2} \approx 1.0$.

In a more general formulation, the resistance is written as a product of several random variables, for example as follows:

$$R = \theta_R \, \eta \, a \, f \tag{II.22}$$

where f is the random material strength, a a geometrical factor and η a conversion factor between test and in-situ conditions [3, 13]. Under the assumption that all four variables are lognormal and statistically independent, the coefficient of variation of R is obtained by combination of the component coefficients of variation:

$$V_R = \sqrt{V_{\theta_R}^2 + V_a^2 + V_\eta^2 + V_f^2} \tag{II.23}$$

and the DVM leads to a total resistance partial factor of the form:

$$\gamma_M \approx \frac{\exp(k_n V_f)}{\mu_{\theta_R} \, \mu_a \, \mu_\eta} \exp\big(\alpha_R \, \beta_t \, V_R\big) \tag{II.24}$$

where the first term essentially reflects the definition of the characteristic strength and the second term reflects the chosen target reliability index and the uncertainty on the resistance.

The same DVM philosophy can be applied to derive PSFs for actions G and Q, starting from the probabilistic models of the load effects and using appropriate sensitivity factors for the load-effect side of the limit state. This is the basis of the harmonized expressions proposed in *fib* Model Code 2020 for permanent and variable actions.

Adjusted Partial Factor Method (APFM)

The APFM provides an alternative, often more simple way to account for different target reliability levels and updated statistical information for existing structures. Instead of recomputing the full PSFs from the probabilistic model, the APFM starts from the partial factor $\gamma_{X,\text{new}}$ used for new structures and introduces an adjustment factor w_y:

$$\gamma_X = w_y \, \gamma_{X,\text{new}} \tag{II.25}$$

where γ_X is the partial factor adopted in the assessment of the existing structure and w_y reflects the difference in target reliability and in statistical properties between design and assessment.

The expression of w_y depends on how the representative value of the resistance variable is defined (characteristic or mean) and on the assumed distribution type. For a lognormal distribution for the material property X whose mean value is used as representative input in the resistance model, *fib* Bulletin 80 proposes the following expression for the adjustment factor [13]:

$$w_y = \frac{\gamma_{Rd}(\beta_{\text{ex}})}{\gamma_{Rd}(\beta_{\text{new}})} \exp\left[\alpha_R \beta_{\text{new}} V_{X,\text{new}} \left(\frac{\beta_{\text{ex}}}{\beta_{\text{new}}} \frac{V_{X,\text{ex}}}{V_{X,\text{new}}} - 1\right)\right] \tag{II.26}$$

where:

- β_{new} is the target reliability index adopted in the calibration of the PSFs for new structures;
- β_{ex} is the target reliability index chosen for the existing structure;
- $V_{X,\text{new}}$ and $V_{X,\text{ex}}$ are the coefficients of variation of X assumed in the design calibration and in the assessment, respectively;
- $\gamma_{Rd}(\beta)$ is the model/geometrical partial factor as a function of β (e.g., as in Eq. (II.21));
- α_R is the sensitivity factor of the limit state with respect to the resistance variable.

Equation (II.26) shows that w_y decreases when a lower target reliability is accepted for the existing structure ($\beta_{\text{ex}} < \beta_{\text{new}}$) or when the updated information reduces the uncertainty on X ($V_{X,\text{ex}} < V_{X,\text{new}}$), leading to partial factors smaller than those used in design. Conversely, if inspection or testing reveals larger variability than assumed for new structures, w_y becomes greater than one, and the partial factor is increased.

The APFM is particularly attractive for engineering practice, because it provides a transparent link between the familiar partial factor format of the Eurocodes and a more refined probabilistic treatment based on inspection and test data.

In the context of masonry and heritage structures, it has been applied, for instance, to the recalibration of PSFs for masonry shear strength based on in-situ tests, showing significant reductions in γ_M when the quality of information is high [25].

II.3.2 ECoV method

The basic idea of the ECoV method is to assess the variability of the global structural resistance R using only a very limited number of NLFEAs (typically two), and to translate this information into a global resistance factor γ_R associated with a given target reliability index [12].

First, two NLFEAs are carried out:

$$R_m = R_{\mathrm{NLFEA}}(f_m) \tag{II.27}$$

$$R_k = R_{\mathrm{NLFEA}}(f_k) \tag{II.28}$$

where f_m and f_k are the mean and characteristic material strengths, respectively. If the global resistance R is approximated as a lognormal distribution, its coefficient of variation V_R can be estimated from the two analysis results as [6]:

$$V_R \approx \frac{1}{1.65} \ln\left(\frac{R_m}{R_k}\right) \tag{II.29}$$

Once V_R is known, the global resistance factor is obtained as:

$$\gamma_R = \frac{\exp\left(\alpha_R \beta_t V_R\right)}{\delta_R} \geq 1.0 \tag{II.30}$$

where the symbols have the same meaning as previously defined, and δ_R is a bias factor defined as the ratio between the mean global resistance from a probabilistic analysis and the deterministic value R_m. If no explicit probabilistic analysis is available, δ_R is usually set to unity as a first approximation.

The design resistance is finally obtained as:

$$R_d = \frac{R_m}{\gamma_R \gamma_{Rd}} \tag{II.31}$$

To summarize, the ECoV method combines accuracy and computational effort: it requires only two NLFEAs, yet it provides a reliability-based assessment of γ_R under the lognormal assumption. Nevertheless, its accuracy depends on the representativeness of the mean and characteristic material models, and on the adequacy of the adopted values of α_R, β_t, δ_R and γ_{Rd} [4].

II.3.3 Global Resistance Factor (GRF)

The GRF method can be seen as a simplified version of the ECoV method, based on the same principles but with reduced computational and modeling efforts.

In this method the global resistance factor γ_R is taken as a fixed value, calibrated a priori from probabilistic studies on representative structural members [14].

A single NLFEA is performed with representative material strengths f_{rep} and nominal geometry, and the corresponding global resistance R_{rep} is obtained:

$$R_{\text{rep}} = R_{\text{NLFEA}}(f_{\text{rep}}) \tag{II.32}$$

For reinforced concrete structures, *fib* Model Code 2020 recommends using mean strengths as representative values, e.g., $f_{ym} = 1.1 f_{yk}$ for steel and an appropriate reduced mean value for concrete. The design resistance is then evaluated as:

$$R_d = \frac{R_{\text{rep}}}{\gamma_R \, \gamma_{Rd}} \tag{II.33}$$

where typical values proposed in [12] are $\gamma_R \approx 1.25$–1.30 and $\gamma_{Rd} \approx 1.06$ for non-linear analysis of reinforced concrete members.

The GRF method is thus formally equivalent to the ECoV and GSF formats in terms of Eq. (II.33), but the factor γ_R is not structure-specific: it is imported from previous reliability calibrations. This makes the method easy to apply in practice, but also less flexible in capturing the variability of complex structures or unusual failure mechanisms. Recent studies suggest that the fixed values of γ_R could not always provide the requested reliability level when applied to highly non-linear problems or to existing structures with significant epistemic uncertainties [4].

II.3.4 Global Safety Format (GSF)

The GSF method represents the most general implementation of the global resistance concept. In this format, the statistical properties of the global resistance are obtained explicitly from a probabilistic analysis of the NLFEA model, typically using Monte Carlo or Latin Hypercube Sampling (LHS) methods [1].

A large number of NLFEAs is carried out, each with sampled material and geometrical properties according to their probabilistic models (e.g., JCSS Probabilistic Model Code [23]). The resulting sample of global resistances $\{R^{(i)}\}$ is used to estimate the mean μ_R, standard deviation σ_R and coefficient of variation:

$$V_R = \frac{\sigma_R}{\mu_R} \tag{II.34}$$

Assuming a lognormal distribution for R, the global resistance factor is again expressed as:

$$\gamma_R = \frac{\exp(\alpha_R \beta_t V_R)}{\delta_R} \tag{II.35}$$

where $\delta_R = \mu_R / R_{\mathrm{NLFEA}}(f_m)$ is the mean-to-mean deviation between the probabilistic mean and the result of a deterministic NLFEA performed with mean strengths. The model uncertainty factor γ_{Rd} can be evaluated in an analogous way by treating the model uncertainty as a random variable and estimating its mean and coefficient of variation from comparisons between experiments and simulations [14].

Finally, the design resistance is obtained as in Eq. (II.31):

$$R_d = \frac{R_m}{\gamma_R \gamma_{Rd}}, \qquad R_m = R_{\mathrm{NLFEA}}(f_m) \tag{II.36}$$

The GSF provides the most consistent link between NLFEAs and structural reliability-based assessment, since the global factors γ_R and γ_{Rd} are derived directly from the simulated distribution of R and the model uncertainty. Its main drawback is the computational cost associated with running many NLFEAs, especially for large 3D models. For this reason, recent research has focused on simplified procedures to approximate V_R and δ_R without performing a full probabilistic analysis.

Table II.6: Qualitative comparison of safety formats for NLFEAs in a global approach.

Format	Key features	Required NLFEAs	Typical use
PFM	Design strengths f_d; single NLFEA with reduced material parameters; fixed γ_{Rd}	1	Code-oriented checks, reference solution
ECoV	Two NLFEAs with mean and characteristic strengths; V_R estimated via Eq. (II.29)	2	Practical reliability-based design
GRF	Single NLFEA with representative strengths; γ_R taken from prior calibration	1	Standard design of new RC structures
GSF	Probabilistic NLFEA; V_R and δ_R from sample of R; tailored γ_R, γ_{Rd}	$30-50$ (LHS)	Calibration studies, special/critical structures

II.3.5 Probabilistic Method (PM)

The PM represents the most rigorous method to combine NLFEAs with structural reliability concepts. Compared to simplified global formats that apply global factors to

a deterministic ultimate load to calculate design resistance R_d, the PM evaluates the failure probability (or reliability index) directly by means of numerous NLFEAs with random variable realizations [4, 14].

Let Z denote the vector of random random variables (material strengths, geometrical properties, model uncertainty parameters, etc.) with joint PDF $f_Z(z)$. For a given limit state, a performance function $g(Z)$ is defined in terms of the structural response obtained from NLFEA (e.g., difference between ultimate load factor and design load factor, or between ultimate displacement and allowed displacement). Failure is associated with the event $g(Z) < 0$, and the probability of failure is:

$$P_f = \mathbb{P}\big[g(Z) < 0\big] = \int_{g(z)<0} f_Z(z)\,\mathrm{d}z \tag{II.37}$$

In practice, the integral in Eq. (II.37) is approximated by simulation-based methods. In the simplest case, a direct Monte Carlo simulation is performed:

1. Generate N independent samples $z^{(i)}$ of the random variables from $f_Z(z)$;
2. For each sample, run a NLFEA up to the relevant limit state and compute the performance function $g^{(i)} = g(z^{(i)})$;
3. Count the number of simulations N_f for which $g^{(i)} < 0$ (failure);
4. Assess the P_f and the corresponding reliability index as:

$$\hat{P}_f = \frac{N_f}{N}, \qquad \hat{\beta} = -\Phi^{-1}(\hat{P}_f) \tag{II.38}$$

In order to reduce the computational effort, the LHS technique or FORM-based importance sampling can be used, so that an accurate estimate of P_f is obtained with a smaller number of NLFEAs [4].

In the PM, the safety check is expressed directly in probabilistic terms:

$$\hat{\beta} \geq \beta_t \qquad \text{or} \qquad \hat{P}_f \leq P_{f,t} \tag{II.39}$$

Specifically, no explicit global resistance factor γ_R is required; instead, the target reliability is ensured directly.

The PM provides the most transparent and accurate link between NLFEA and structural reliability, and it is therefore the preferred tool for:

- Calibration of global safety formats (PFM, ECoV, GRF, GSF) and of PSFs for new and existing structures;

- Verification of special or critical structures with very large consequences of failure;
- Research studies aiming at quantifying the influence of model uncertainty and parameter variability on structural performance.

Its main drawback is the high computational effort associated with repeated NLFEAs, especially for large 3D models.

For monumental masonry structures, where each NLFEA may already be computationally demanding, the PM is typically reserved for calibration studies on simplified models or on critical substructures.

II.4 Reliability of existing and heritage structures

The reliability assessment of existing structures differs in several fundamental aspects from the design of new structures. These differences are due to the presence of an existing physical object with an unique history, the availability of inspection and test data, the usually shorter remaining working life and the often considerable constraints on possible interventions [9, 18].

For heritage buildings, and in particular for monumental masonry structures, additional requirements related to preservation of authentic materials and cultural value further complicate the definition of acceptable safety levels and of appropriate safety formats [19, 30].

This section covers key ideas for the reliability-based assessment of existing and heritage structures and explains how the framework used in this thesis tries to apply these principles.

II.4.1 Specific issues in the assessment of existing structures

The existing structures, compared to the new structures, should be assessed based on their current condition, which could change significantly from the original design assumptions.

Furthermore, in addition to conventional structural analysis, the assessment framework includes several kinds of tasks associated to knowledge acquisition and diagnosis [10, 18], such as:

- Collection and critical review of historical documentation, original drawings and previous intervention;
- Survey of geometry, structural details and boundary conditions;

- Identification of materials, deterioration mechanisms, damage patterns and previous repairs;
- Evaluation of the history of actions and load combinations, including possible changes of use and environmental effects.

The outcome of these activities is a set of possible structural scenarios, each associated with a certain level of plausibility and uncertainty. These scenarios must be reflected in the probabilistic models of actions, resistances and model uncertainties introduced in Section II.2.

Standards such as ISO 13822 [21], CEN/TS 17440 [5] or Italian standard NTC2018 [8, 28] highlighting the concept of knowledge levels or information classes, which relate the amount and quality of information available (from documents, inspection, testing and monitoring) to the permissible simplifications in the analysis and to the numerical values of PSFs. Higher knowledge levels, supported by systematic investigations and calibrated material models, allow a reduction of epistemic uncertainty and may justify lower PSFs in assessment.

A further specific feature of existing structures is the influence of service history on reliability. The fact that a structure has survived for decades without apparent significant damage under past loads can be interpreted as an indication that the actual resistance is sufficient to resisting at least the experienced actions.

In a probabilistic context, this proven-strength effect could be used to update the distribution of resistance and justify different target reliabilities compared to new structures.

Figure II.7 illustrates, in a schematic and simple way, a typical reliability-based assessment process for existing structures as suggested in ISO 13822 and related guidelines.

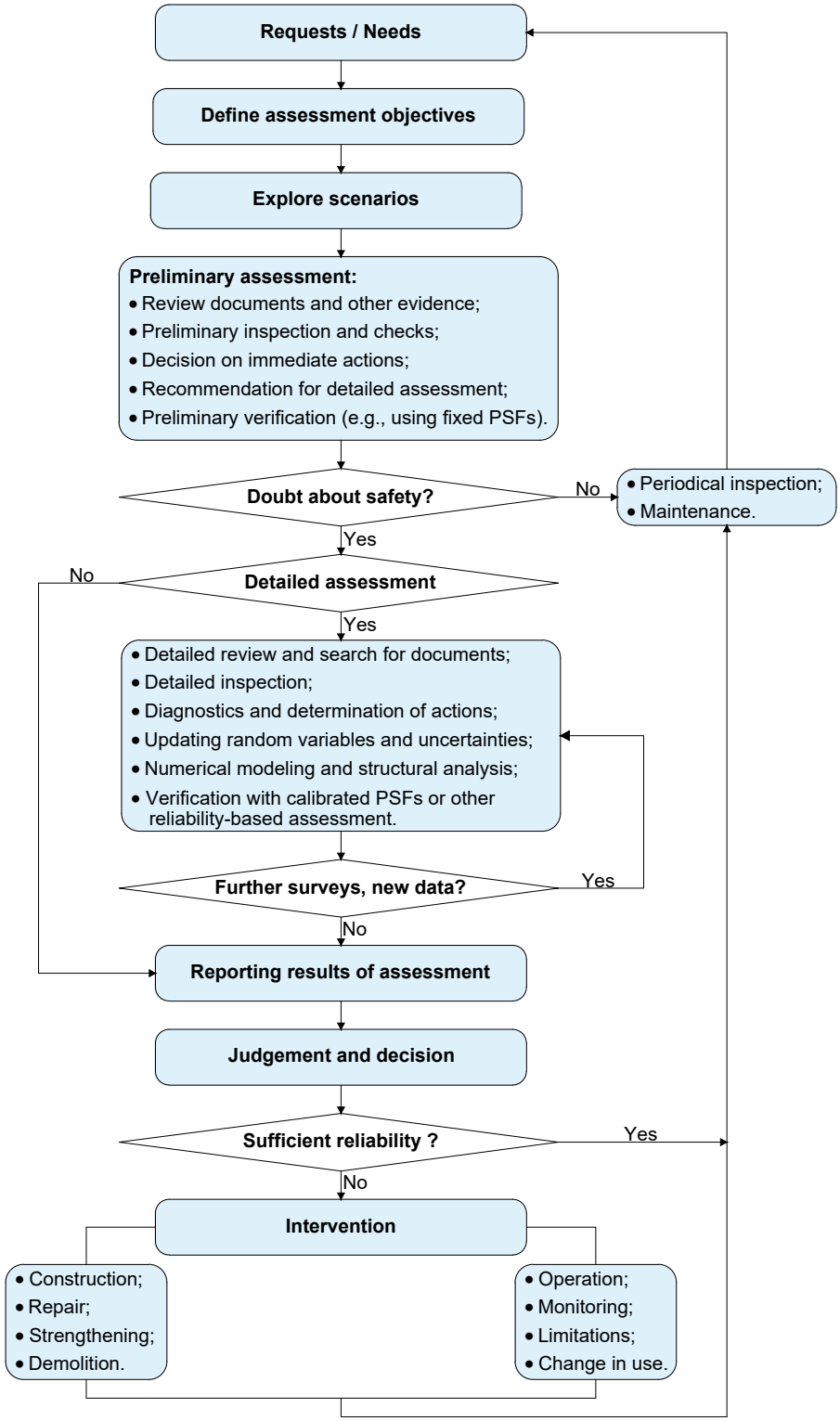

Figure II.7: Schematic flowchart for the reliability-based assessment of existing structures (adapted from ISO 13822, 2010).

II.4.2 Heritage buildings and monumental masonry

Heritage buildings, and particularly monumental masonry structures such as cathedrals and basilicas, pose additional challenges for reliability assessment. In addition to safety and serviceability, preservation of cultural value and authenticity becomes a primary objective [18–20, 30]. This has several implications:

- Limited intervention: Interventions should be compatible with the original materials, reversible where possible, and minimize loss of historic material. This limits the range of feasible strengthening measures and could preclude solutions that would be optimal from a purely structural viewpoint;
- Complex structural systems: Monumental masonry buildings often include massive multi-leaf walls, large-span vaults and domes, buttressing systems and heterogeneous substructures. Their behavior under gravity and lateral actions is strongly non-linear and often governed by geometric and material imperfections accumulated over centuries;
- Uncertain material properties: Masonry is a composite material with large spatial variability, and direct destructive tests are often limited by preservation requirements. Non-destructive and semi-destructive tests, combined with historical information, are therefore essential for probabilistic material modeling;
- Long service history: Heritage buildings have survived long periods under variable environmental and loading conditions, often including extreme events (earthquakes, strong winds, settlement episodes). Their survival provides valuable information on structural robustness, but also implies cumulative damage and past interventions that must be carefully documented and modeled.

From a reliability point of view, these features would require advanced modeling and verification strategies, such as:

- Detailed 3D NLFEA models, capable of capturing non-linear material behavior, cracking, crushing and interaction between macro-elements;
- Safety formats compatible with such models, preferably global formats (GRF/GRM) that operate at system level and can account for multiple failure mechanisms;
- Probabilistic material models calibrated from experimental campaigns using Bayesian or other statistical methods;

- explicit consideration of epistemic uncertainty and, where appropriate, updating of model parameters using monitoring data.

Several case studies in the literature demonstrate the feasibility and importance of reliability-based approaches for historic masonry towers, churches and bridges [17, 24, 25], although applications to very large and complex buildings such as St. Peter's Basilica are still scarce.

II.5 References

[1] Allaix, D. L., Carbone, V. I., and Mancini, G. (2013). Global safety format for non-linear analysis of reinforced concrete structures. *Structural concrete*, 14(1):29–42.

[2] Baldioli, A. (2012). Conservazione e priorità: criteri quantitativi e qualitativi per un processo valutativo ponderato. *Ananke*, (65):39–46. (in Italian).

[3] Caspeele, R. and Van Den Hende, K. (2023). Validation of the harmonized partial factor method for design and assessment of concrete structures as proposed for fib model code 2020. *Structural Concrete*, 24(4):4368–4376.

[4] Castaldo, P., Gino, D., and Mancini, G. (2019). Safety formats for non-linear finite element analysis of reinforced concrete structures: discussion, comparison and proposals. *Engineering Structures*, 193:136–153.

[5] CEN/TS 17440:2020. Assessment and retrofitting of existing structures (2020). Brussels, Belgium.

[6] Cervenka, V. (2013). Global safety formats in fib model code 2010 for design of concrete structures. In *Proceeding of the 11th International Probabilistic Workshop, Brno*, pages 27–31.

[7] Chang, K.-H. (2015). Chapter 10 – reliability analysis. In *e-Design: Computer-Aided Engineering Design*, pages 523–595. Academic Press, Boston.

[8] Circolare n. 7 del 21 gennaio 2019, Consiglio Superiore dei Lavori Pubblici (2019). *Istruzioni per l'applicazione dell'Aggiornamento delle Norme Tecniche per le Costruzioni di cui al Decreto Ministeriale 17 gennaio 2018*. Ministry of Infrastructures and Transportations. (In Italian).

[9] Diamantidis, D. (2001). *Report 32: probabilistic assessment of existing structures-a publication for the Joint Committee on Structural Safety (JCSS)*, volume 32. RILEM publications.

[10] Diamantidis, D., Tanner, P., Holicky, M., Madsen, H. O., and Sykora, M. (2025). On reliability assessment of existing structures. *Structural Safety*, 113.

[11] EN.1990.Eurocode (2002). Basis of structural design.

[12] fib, 2020 – International Federation for Structural Concrete (2023). *fib Model Code 2020 for Concrete Structures*. fib, Lausanne, Switzerland.

[13] fib. Bulletin No. 80 (2016). Partial safety factor methods for existing concrete structures.

[14] Gino, D., Miceli, E., Castaldo, P., Recupero, A., and Mancini, G. (2024). Strain-based method for assessment of global resistance safety factors for nlnas of reinforced concrete structures. *Engineering structures*, 304:117625.

[15] Haldar, A. and Mahadevan, S. (1995). First-order and second-order reliability methods. In *Probabilistic Structural Mechanics Handbook: theory and industrial applications*, pages 27–52. Springer.

[16] Hasofer, A. M. and Lind, N. C. (1974). Exact and invariant second-moment code format. *Journal of the Engineering Mechanics Division, ASCE*, 100(1):111–121.

[17] Holický, M. (2009). *Reliability Analysis for Structural Design*. SUN Press, Stellenbosch, South Africa.

[18] Holicky, M. and Sykora, M. (2012). Structural assessment of heritage buildings. *WIT Trans. Built. Environ*, 123:69–80.

[19] ICOMOS/ISCARSAH Committee (2003). Recommendations for the analysis, conservation and structural restoration of architectural heritage. Technical report, ICOMOS International Scientific Committee for Analysis and Restoration of Structures of Architectural Heritage, Paris, France.

[20] Isfeld, A. C., Stewart, M. G., and Masia, M. J. (2023). Structural reliability and partial safety factor assessment of unreinforced masonry in vertical bending. *Australian Journal of Structural Engineering*, 24(3):191–205.

[21] ISO 13822:2010 (2010). Bases for design of structures — assessment of existing structures.

[22] ISO 2394:2015 (2015). General principles on reliability for structures.

[23] JCSS – Joint Committee on Structural Safety (2001). *Probabilistic Model Code*. JCSS, Zurich, Switzerland.

[24] Konsta, A. and Della Torre, S. (2023). The concept of risk and its measurement in the field of built heritage conservation: critical aspects and potential improvements. *Technical Annals*, 1(3).

[25] Lulić, L., Lukačević, I., Skejić, D., and Stepinac, M. (2023). Assessment of existing masonry resistance using partial factors approaches and field measurements. *Buildings*, 13(11):2790.

[26] Mancini, G. (2019). Partial factor methods for existing structures according to fib bulletin 80: Assessment of an existing prestressed concrete bridge. *Structural Concrete*.

[27] Melchers, R. E. and Beck, A. T. (2018). *Structural Reliability Analysis and Prediction*. John Wiley & Sons Ltd, Hoboken, New Jersey, 3 edition.

[28] NTC 2018: Norme Tecniche per le Costruzioni, Decreto Ministeriale 17/01/2018 (2018). Ministry of Infrastructures and Transportations. (in Italian).

[29] Oppio, A., Bottero, M., Ferretti, V., Fratesi, U., Ponzini, D., and Pracchi, V. (2015). Giving space to multicriteria analysis for complex cultural heritage systems: The case of the castles in valle d'aosta region, italy. *Journal of Cultural Heritage*, 16(6):779–789.

[30] Roca, P. (2021). The ISCARSAH guidelines on the analysis, conservation and structural restoration of architectural heritage. *International Journal of Architectural Heritage*, 15(10):1480–1505.

[31] Sykora, M., Diamantidis, D., Holicky, M., and Jung, K. (2018). Target reliability for existing structures considering economic and societal aspects. In *Life-Cycle of Structural Systems*, pages 181–194. Routledge.

[32] Van Den Hende, K., Caspeele, R., Sykora, M., and Way, A. (2024). Target reliabilities for heritage structures derived from cost optimization. *Structural Concrete*.

This page intentionally left blank.

CHAPTER III

Cultural heritage diagnostics and modeling strategy for 3D NLFEA

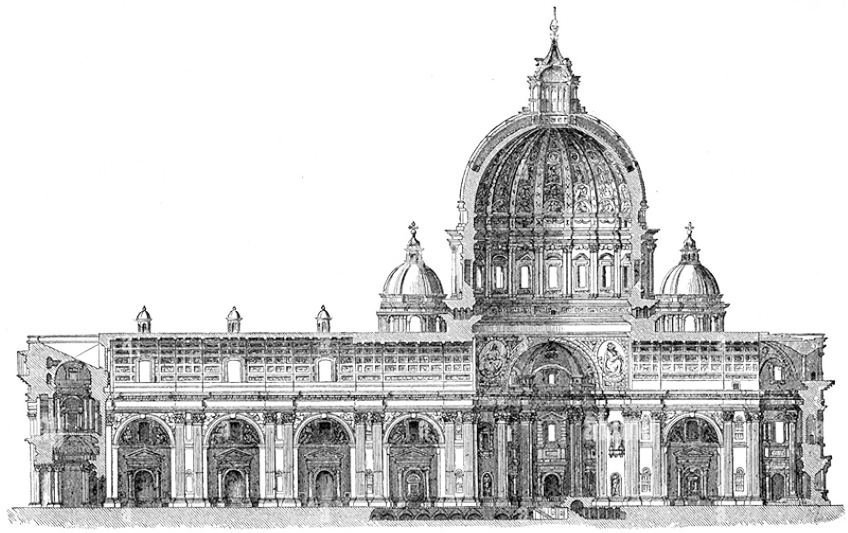

"Antiquam Vaticani templi partem cum porticu delineasset."

("He had designed the ancient part of the Vatican temple together with the portico.")

– Carlo Maderno

III.1 Introduction

This chapter provides the theoretical background needed for the global 3D NLFEA of monumental masonry buildings.

Assessing monumental masonry structures requires combining different fields of knowledge, from the historical evolution of the construction to the mechanical characterization of materials supported by diagnostic investigations and advanced numerical modeling. Large churches and cathedrals have complex structural systems with very thick multi-leaf walls, massive piers, large-span vaults and domes, and heterogeneous materials. This complexity often makes 3D NLFEAs necessary to investigate the global behavior under gravity and seismic actions [34, 49].

Within modern conservation practice, diagnostics is recognized as a fundamental prerequisite for any intervention on cultural heritage. Non-Destructive Tests (NDT) and Minor-Destructive Tests (MDT) provide the information needed to identify masonry typologies, detect internal defects and estimate stiffness and strength parameters in a way that is compatible with the requirement of minimal invasiveness [29].

Furthermore, Destructive Tests (DT) on laboratory specimens continues to play a significant part in the material mechanical characterization. For instance, compression and splitting tensile tests on cubes or cylinders, allow for direct measurements of strength, stiffness, and post-peak behavior under controlled boundary conditions. Although their use in historic structures is limited by conservation constraints and the representativeness of the extracted samples [16, 38].

From a numerical viewpoint, a wide spectrum of modeling strategies is available for masonry, from 1D equivalent-frame models to 2D shell or plane-stress formulations and fully 3D continuum FE models. Each modeling level involves specific assumptions on kinematics, material behavior and computational cost, and is tailored to different research objectives and scales. For complex monumental buildings, 3D macro-modeling with homogenized constitutive laws offers a practical compromise: it is capable of representing the global geometry and load paths, while still providing access to local stress and damage patterns in key regions [25, 50].

Choosing an appropriate non-linear constitutive model for describing historical structural materials is a crucial task. Among the numerous models proposed in the literature, pressure-sensitive plasticity models based on the D–P failure criterion and combined plastic–damage formulations such as the CDP model have become standard tools for concrete and masonry and are commonly implemented in commercial FE codes. Their effective use, however, requires a good understanding, and appropriate parameter calibration [36, 42].

III.2 Cultural heritage diagnostics

Diagnostics has a central role in the assessment of historic and monumental masonry structures. Its main objective is to develop a reliable knowledge of geometry, construction techniques, material properties, internal configuration and current damage patterns of the building. This information is indispensable for defining appropriate structural models and for calibrating their material parameters [49].

The process of diagnosis in monumental churches and basilicas must deal with many different materials, such as brickwork masonry, natural stone, lime mortars, as well as complex structural components like multi-leaf walls, infilled cores, massive piers, and large vaulted systems.

Figure III.1 shows the diagnostic framework integrating four complementary phases.

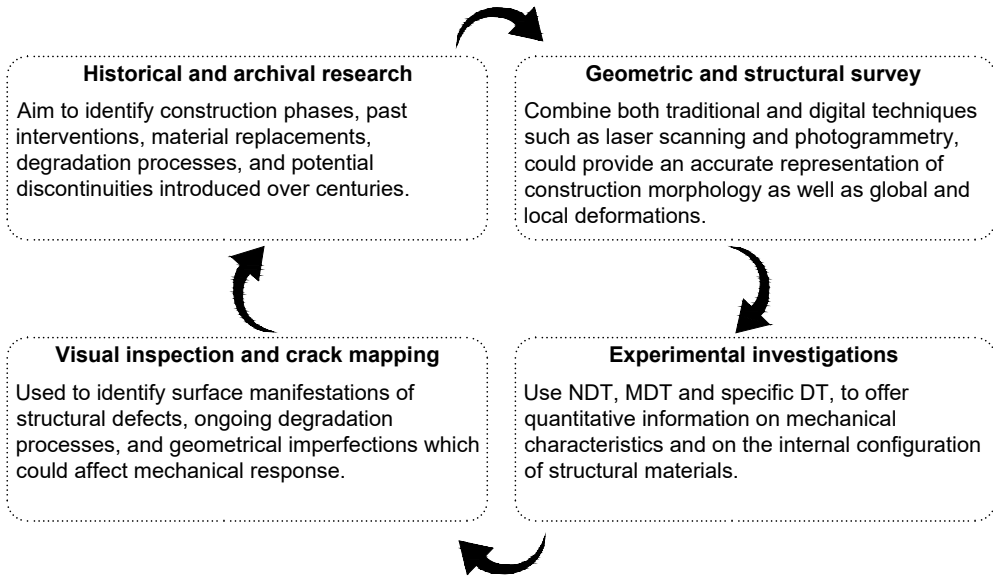

Figure III.1: Integration of the diagnostic framework.

These phases should be viewed as an iterative, mutually supportive process. Archival analysis clarifies construction stages observed in NDT scans; crack patterns guide the localization of MDT or DT; geometric surveys help interpret test results by highlighting deformation patterns; and experimental results validate or refine modeling assumptions. Recent contributions by RILEM [47] and modern integrated approaches based on diagnostics supported by numerical modeling [23] highlight that diagnostics should not be seen as a stand-alone activity, but as a knowledge-building process closely connected with advanced modeling and structural analysis.

III.2.1 Experimental investigations

The experimental investigations are at the core of structural diagnostics, allowing characterize the material properties, detect hidden defects, and also validate modeling assumptions. Basically, their choice is based on the construction materials, structural system, accessibility, and acceptable level of invasiveness. They could be divided into three main categories: NDT, MDT and DT.

Non-Destructive Tests (NDT)

NDT techniques allow materials and structural components to be investigated in situ without removal, making them appropriate for both existing and new structures [29, 41, 54].

The most common methods include (i) ultrasonic/sonic testing, (ii) Ground-Penetrating Radar (GPR), (iii) infrared thermography, (iv) rebound hammer tests and (v) dynamic identification based on ambient vibration measurements. Each is described in detail below.

(i) Ultrasonic and sonic testing

These techniques are based on the propagation of mechanical waves through the material [9, 57]. Specifically, sonic tests adopt low-frequency pulses below about 20 kHz (typically $\approx$ 1–20 kHz), whereas Ultrasonic Pulse-Velocity (UPV) tests use piezoelectric transducers above 20 kHz (typically $\approx$ 40–150 kHz). Lower frequencies provide greater penetration and averaging in heterogeneous masonry, while higher frequencies improve resolution but require better coupling and suffer higher attenuation. In practice, transmitter and receiver can be arranged in direct (opposite faces), semi-direct (adjacent faces), or indirect (same face) configurations (see Figure III.2).

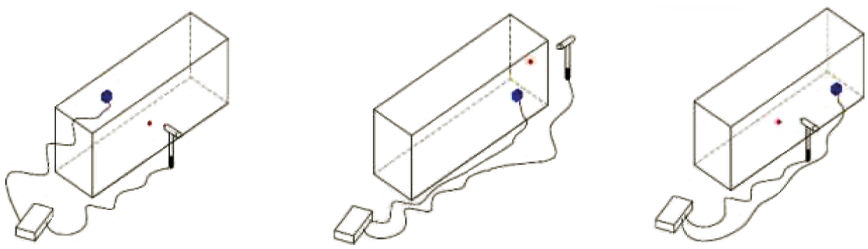

(a) (b) (c)

Figure III.2: Schematic in-situ configurations of ultrasonic/sonic testing (adapted from [35]): (a) direct; (b) semi-direct; (c) indirect.

A short mechanical or piezoelectric pulse is generated and the pulse travel time is measured; the apparent wave velocity is then computed as $v_p = L/t$, with known path length L and measured time t.

For masonry and concrete, velocities are typically in the range of $1,000$–$4,500$ m/s, depending on density, stiffness, cracking, and moisture content. By acquiring multiple paths and inverting the data, one can derive 1D/2D velocity profiles (sonic/ultrasonic tomography) that highlight zones of reduced stiffness and internal defects. Different coupling agents (e.g., gel, grease, clay) are commonly used to ensure good contact, and measurement geometries are chosen to balance accessibility and sensitivity to internal anomalies. For further details, see Section V.3.1.

(ii) Ground-Penetrating Radar (GPR)

GPR uses short electromagnetic pulses generated by an antenna and transmitted into the material; reflections arise at interfaces where dielectric characteristics change (e.g., between distinct layers, at voids, reinforcing bars, or delaminations) [4, 27].

In a survey, the antenna traverses defined scan lines, while the system records the reflected signal amplitude relative to time and place. The outcome is a series of radargrams (time–distance plots), in which hyperbolic reflections typically represent the presence of distinct objects such as rebars or metallic connections (see Figure III.3).

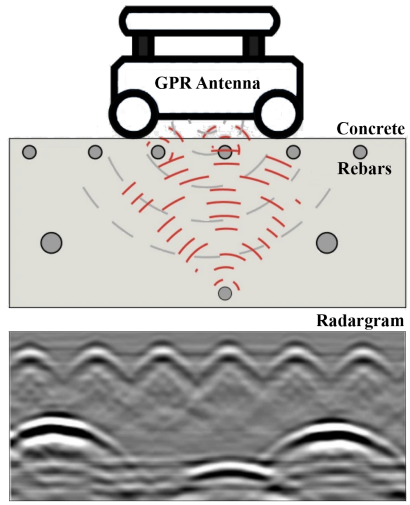

Figure III.3: Schematic of a handheld GPR unit with antenna and a representative output (radargram).

Data interpretation involves converting travel times to depth using an estimate of electromagnetic wave velocity (related to the material's relative permittivity) and identifying

reflection patterns associated with interfaces, voids, delaminations, or reinforcement. In building diagnostics, GPR is commonly used to assess cover thickness, discover hidden layers, find voids under cladding, and map reinforcement positions.

(iii) Infrared thermography

Infrared thermography estimates the infrared radiation emitted by a surface and converts it into a visible temperature distribution. Commercial thermal cameras used in building diagnostics typically operate in the Long-Wave Infrared (LWIR) band, between approximately 8 and 14 μm, where most building materials exhibit high and relatively constant emissivity and where atmospheric absorption is minimal. Some specialized systems operate inside the Mid-Wave Infrared (MWIR) spectrum, between 3 and 5 μm; nevertheless, their use in civil engineering applications is limited due to financial and operational limitations [11, 56]. The sensitivity of diagnostic thermography is usually on the order of 0.02–0.1°C, allowing the detection of small thermal contrasts associated with subsurface anomalies.

In building diagnostics, thermography is used in either passive mode (under natural thermal gradients, such as solar heating and night cooling) or active mode uses artificial heat sources (such as radiators, warm air, or lamps) to detect detachments, voids, moisture accumulation, thermal bridges and shallow defects (see Figure III.4).

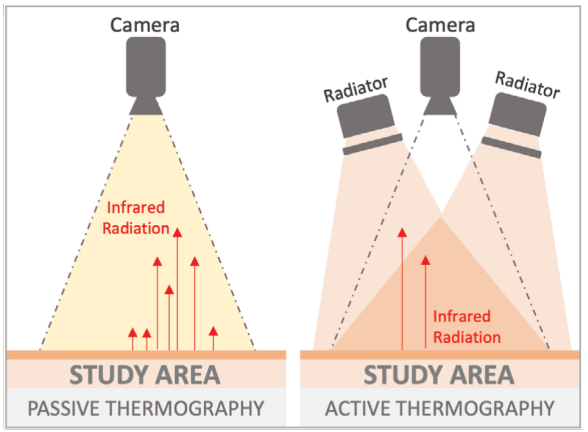

Figure III.4: Schematic of passive and active infrared thermography with camera (adapted from [26], licensed under CC BY 4.0).

Operationally, the technique is based on capturing thermal images with an infrared camera while maintaining appropriate emissivity settings, ambient conditions, and acceptable viewing geometry. Areas that have different subsurface characteristics, such as voids, delaminated plaster layers, moisture pockets, or zones with changed thermal

conductivity, induce visible temperature anomalies due to changing heat transfer paths. These anomalies can be highlighted by means of time-lapse images or thermal contrast processing, which uses temperature variations by means the following formulation:

$$\Delta T(x,y,t) = T(x,y,t) - T_{\text{ref}}(x,y,t) \tag{III.1}$$

where $\Delta T(x,y,t)$ is the thermal contrast at the image point (x,y) and time t, $T(x,y,t)$ is the measured surface temperature field, and $T_{\text{ref}}(x,y,t)$ is the corresponding reference temperature (e.g., background or initial condition).

Thermography is applicable to a wide range of construction materials and systems, including masonry, concrete, infill panels, claddings, renders, insulation layers and composite materials.

(iv) Rebound hammer test

The rebound hammer test (also known as the Schmidt hammer) measures surface hardness by hitting it with a controlled quantity of energy and measuring the rebound [14, 22]. The rebound index can be empirically correlated with compressive strength in concrete and, with greater variability, in some types of masonry units. The test is performed by pressing the instrument onto the surface at the desired point, triggering the spring-loaded hammer and reading the rebound value on a scale or electronic display. Multiple measurements are taken and statistically treated to obtain representative indices (see Figure III.5).

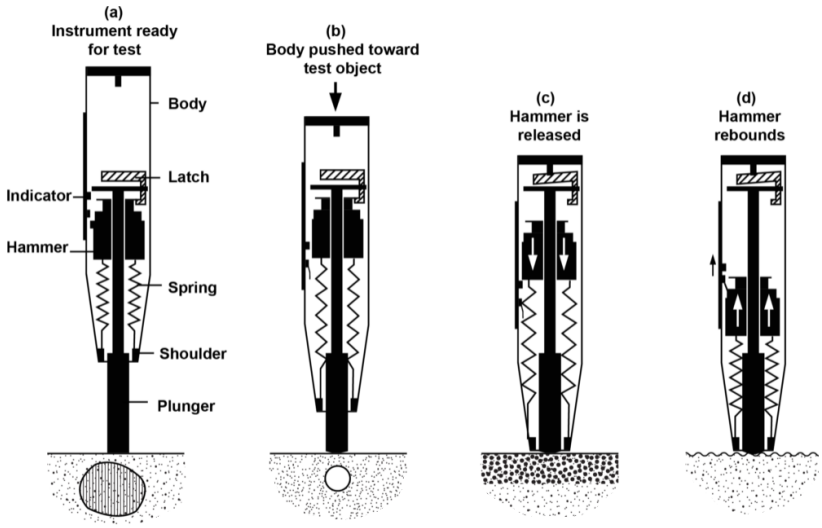

Figure III.5: Schematic representation of the phases of the rebound hammer test.

(v) Dynamic identification

Dynamic identification techniques are based on measuring the structural response to ambient, operational or controlled excitations. For buildings, bridges and towers, Ambient Vibration Tests (AVT) analyzed through output-only methods are widely used to determine natural frequencies, mode shapes and damping ratios without the need for artificial excitation [51, 54]. This output-only framework is generally referred to as Operational Modal Analysis (OMA). Alternatively, forced-vibration tests use artificial excitation sources (e.g., impact hammers, eccentric-mass or electro-dynamic shakers) to inject a controlled input, improving the signal-to-noise ratio and allowing a more detailed investigation of specific modes.

In a typical OMA campaign, a series of accelerometers or velocimeters are placed at strategic locations throughout the structure. Time histories of accelerations (or velocities) are recorded under ambient or operational loads (wind, traffic, microtremors), and the modal parameters are extracted by OMA algorithms such as Frequency Domain Decomposition or Stochastic Subspace Identification. These parameters are highly sensitive to the global stiffness and boundary conditions and are therefore crucial for calibrating FE models, detecting damage and implementing continuous structural health monitoring (see Figure III.6).

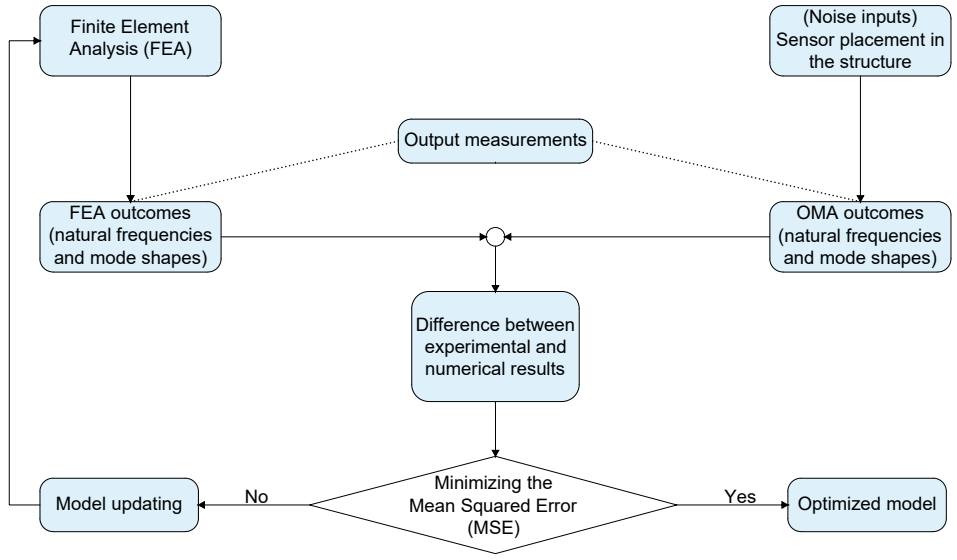

Figure III.6: Schematic framework of the phases of ambient vibration testing (inspired by [28]).

Minor-Destructive Tests (MDT)

MDT include all investigation techniques that require limited, repairable interventions on the structural element. MDT methods provide quantitative information on mechanical properties: elastic modulus, compressive/tensile strength, stress state, mortar quality, while maintaining an acceptable level of invasiveness for both historic and modern constructions [38, 54]. Compared to NDT, MDT allows direct stress–strain measurements and more reliable strength estimates, making these tests fundamental for calibrating material models used in structural analyses.

The MDT methods most commonly adopted in structural diagnostics include (i) endoscopic inspections, (ii) flat-jack tests, (iii) mortar testing and (iv) micro-drilling. Each is described in detail below.

(i) Endoscopic inspections

Endoscopic inspections are semi-invasive investigations that allow direct visualization of the internal structure of walls, slabs, columns or joints through small drill holes (typically 10–30 mm). Despite the minimal and easily repairable intrusion, they provide unique qualitative and quantitative information on internal composition, thickness of construction layers, presence of voids or cracks, condition of mortar joints, reinforcement layout and local degradation patterns [21].

A small-diameter borehole is drilled to the required depth and a rigid or flexible endoscope with LED lighting and a miniature camera is inserted, along a horizontal, vertical or inclined axis depending on the objective (see Figure III.7).

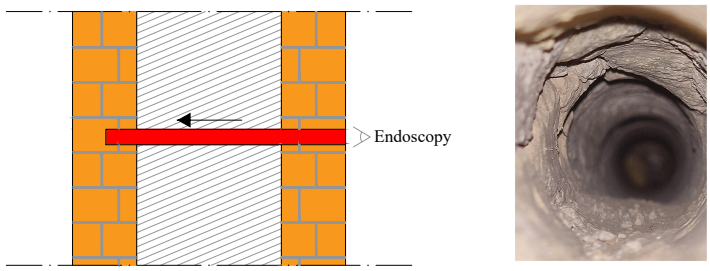

Figure III.7: Schematic in-situ endoscopic inspection: (a) schematic view of the inspection; (b) image of the inner wall.

The device transmits real-time video to a recording unit, from which it is possible to evaluate: (i) geometry and arrangement of internal leaves or layers; (ii) thickness

and condition of mortar joints; (iii) presence of cavities, cracks or delaminations; (iv) material discontinuities (change of brick/stone/block type); (v) presence and condition of internal reinforcement or inserts; and (vi) moisture patterns or efflorescence on internal surfaces.

Nevertheless, endoscopic inspections require local drilling, limited line-of-sight in highly irregular materials, and may not detect features outside the borehole's illumination cone. Moisture, dust and coarse aggregates can reduce image quality. For these reasons, endoscopy is often paired with NDT techniques to improve representativeness and reduce the number of boreholes needed.

(ii) Flat-jack tests

Flat-jack tests are widely used in masonry diagnostics to estimate the in-situ stress state (single flat-jack) and the compressive stress–strain behavior (double flat-jack). These tests are particularly valuable for existing structures where direct extraction of specimens is limited [8, 44].

In a single flat-jack test, a single horizontal slot is cut along a mortar bed joint using a thin diamond blade. A deformable steel diaphragm (flat-jack) is inserted into the slot and pressurized with hydraulic oil. Two or more displacement transducers measure deformation across the slot before cutting and during re-pressurization.

The principle is based on restoring the pre-cut strain state:

$$\sigma_{\text{in-situ}} \approx p_{\text{jack}} \quad \text{(after calibration)}$$

where p_{jack} is the hydraulic pressure required to return the wall to its original deformation profile.

In a double flat-jack test, two parallel horizontal slots are cut and two flat-jacks are installed, creating a masonry specimen between them. The jacks apply increasing pressure, while displacement transducers or strain gauges measure vertical deformation (see Figure III.8).

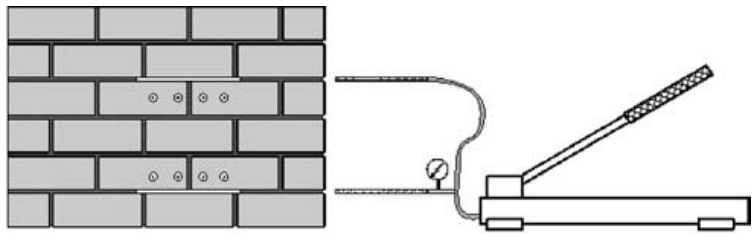

Figure III.8: In-situ schematic of the double flat-jack test on masonry (from [44]).

Flat-jack tests require correction factors for jack geometry, slot width, local stiffness and boundary-effect calibration, usually determined through laboratory testing or numerical analysis. For further details, see Section V.4.2.

(iii) Minor-destructive testing of mortars

Mortar properties strongly influence shear capacity, deformability and crack formation. Because extracting standard mortar specimens is generally impractical, MDT methods such as the Double Punch Test (DPT), Helix Pull-out Test (HPT) and Pin Penetration Test (PPT) are widely adopted [13, 24, 46].

In the DPT a cylindrical mortar specimen (typically 50–75 mm diameter) is locked between two steel punches and compressed until failure. The test simulates local bearing conditions and provides a compressive strength estimate by the following formulation:

$$f_{\mathrm{DPT}} = \frac{P_{\max}}{A_{\mathrm{eff}}} \tag{III.2}$$

where $P_{\max}$ is the peak load and A_{eff} is the effective bearing area corrected for confinement effects.

In the HPT, a helical steel insert is screwed into the mortar joint to a specified depth and then pulled out. During extraction, the applied force and corresponding displacement are recorded, producing a load–displacement curve. The maximum pull-out force is empirically correlated with the mortar's shear or bond strength.

In PPT a steel pin is driven into the mortar at a controlled rate. The penetration depth is correlated with mortar compressive strength through empirical calibration.

These tests produce repeatable results with minimal visual intrusion and are particularly effective when combined with NDT mapping to select representative testing areas (see Figure III.9).

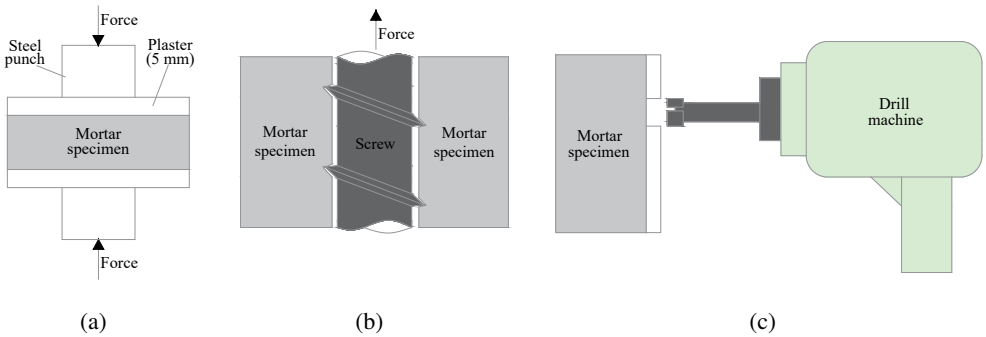

Figure III.9: Schematic MDT for mortar characterization: (a) DPT; (b) HPT; (c) PPT.

(iv) Micro-drilling resistance test

Micro-drilling assesses material quality by measuring the resistance opposed to a small rotating drill bit advancing at a constant feed rate [45]. The instrument measures drilling torque or penetration resistance vs depth. The basic relation is:

$$R(z) = T(z) \cdot \omega \tag{III.3}$$

where $R(z)$ is the drilling resistance, $T(z)$ the measured torque and ω the angular velocity.

It is highly sensitive to: (i) voids, cracks or weak mortar; (ii) surface deterioration; (iii) layer boundaries in composite sections and (iv) carbonation depth (in concrete).

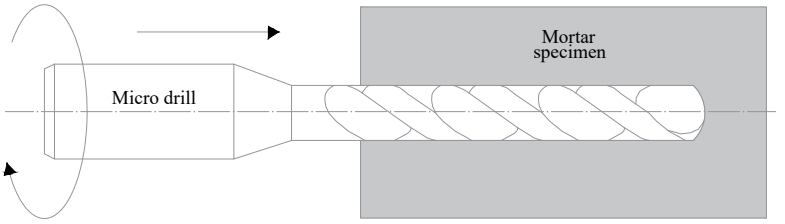

Figure III.10: In-situ schematic of micro-drilling resistance test on mortar specimen.

Micro-drilling is widely used in conservation engineering because it provides detailed information on stratigraphy and local mechanical integrity with negligible structural impact.

Destructive Tests (DT)

DT are the most direct and reliable way to determine the mechanical properties of structural materials. They consist of extracting specimens from the structure or creating representative samples that are tested to failure in a laboratory with controlled conditions. Although its application is limited by economic, logistical, and conservation constraints, DT are still required for the calibration of constitutive models, the validation of NDT/MDT correlations, and the development of benchmark values for strength and deformability.

At the same time, DT result must be interpreted carefully in the context of structural assessment: the representativeness of the extracted samples is often limited in relation to large-scale heterogeneity; specimen geometry, preparation, and boundary conditions can cause non-negligible corrections; size effects can lead to strength values higher than those effectively applied in situ; and differences in moisture and environmental

conditions between laboratory and field may significantly affect measured properties. For these reasons, DT result are typically used in conjunction with NDT and MDT to calibrate empirical or semi-empirical relationships (e.g., between ultrasonic velocity, rebound index, or flat-jack elastic modulus) rather than being applied directly to the structural scale.

Despite their invasiveness, DT remain the benchmark for material characterization and are indispensable for validating the constitutive models and input parameters used in non-linear FE analysis; their combination with NDT and MDT form the core of reliable diagnostic strategies for existing structures [32, 39].

DT methods can be grouped into three principal categories: (i) destructive sampling and laboratory material testing, (ii) component-level destructive testing, and (iii) microstructural, chemical and petrographic analyses. Each is discussed in detail below.

(i) Material sampling and laboratory testing

Material extraction produces specimens (cores, blocks, prisms, or tiny elements) that could be tested using standard laboratory procedures. These tests allow very accurate measurements of stress-strain relationships, pre- and post-peak behavior, fracture energy, modulus of elasticity, and Poisson's ratio. Table III.1 shows the most common DT laboratory testing:

Table III.1: Overview of destructive core and coupon tests at material level.

Test type	Main purpose / parameters investigated	Reference
Core compression tests	Compressive strength f_c, full stress–strain response, effects of aspect ratio, end friction and surface preparation	[1]
Splitting tensile tests (Brazilian test)	Indirect tensile strength f_t from diametral loading of cores or disks	[12]
Direct tensile tests on specimens	Tensile stress–strain curve and fracture energy for model calibration	[6]
Shear or triplet tests on masonry joints	Cohesion, friction angle and dilatancy parameters for interfaces and shear-critical elements	[19]

(ii) Component-level destructive tests

Component-level DT focus on the mechanical behavior of small structural elements, blocks, joints, brickwork prisms, concrete cylinders, timber sections or steel elements. The purpose is to investigate mechanisms that cannot be captured by isolated material

samples, such as composite behavior, anisotropy, interface failure and size effects. Table III.2 shows the most common DT at component level.

Table III.2: Overview of the most common DT at component level.

Test type	Main purpose / parameters investigated	Reference
Masonry walls under uniaxial compression	Compressive strength, global stiffness, cracking patterns and confinement effects	[20]
Diagonal compression tests on masonry panels	Shear stress–strain response and failure mode, for structures where in-plane shear governs behavior	[3]
Shear–compression tests on rectangular specimens	Interaction between axial load, shear strength and joint behavior	[18]
Flexural tests on beams, arches or concrete/timber elements	Bending stiffness, tensile strength and post-cracking behavior	[10]
Bond and anchorage tests (pull-out / embedment)	Bond–slip law and anchorage capacity of reinforcement	[2]

Compared to small specimen tests, component-level tests better represent real structural behavior because they capture material heterogeneity, construction technique, joint morphology and composite action. Their results are frequently used to benchmark numerical simulations in NLFEA, particularly when validating crack patterns or collapse mechanisms.

(iii) Microstructural, chemical and petrographic analyses

DT also include material characterization procedures aimed to better understand the composition, microstructure, and deterioration mechanisms of construction materials. These analyses do not directly produce mechanical characteristics, but they are important for understanding mechanical behavior and deterioration. Table III.3 shows the most common laboratory analyses.

Table III.3: Overview of the most common DT laboratory material characterization techniques.

Test type	Main purpose / parameters investigated	Reference
Petrographic thin-section analysis	Aggregate type, matrix composition, porosity, bonding quality and microcrack patterns	[7]
Scanning electron microscopy (SEM) with EDS	Microstructural morphology and elemental / chemical composition at the microscale	[5]
X-ray diffraction (XRD) and X-ray fluorescence (XRF)	Identification of mineralogical phases and bulk chemical/oxide composition	[30, 31]
Mercury intrusion porosimetry (MIP)	Pore size distribution and total porosity, affecting strength, stiffness and moisture transport	[55]

III.3 Modeling strategy for global FE analysis

The numerical analysis of existing structures can be formulated at different levels of idealization, depending on the structural system, the objectives of the assessment and the amount and quality of available information on geometry and materials.

Global FE analysis often are divided into three different modeling scales: 1D frame-type models, 2D models based on shell or plane-stress/plane-strain elements, and full 3D continuum models. Each modeling level reflects a different balance between physical realism, numerical stability and computational cost, and none of them can be regarded as universally preferable.

III.3.1 1D modeling: equivalent-frame strategies

In 1D models, the structure is idealized as an assembly of line elements whose kinematics are given by generalized displacements and rotations at their ends. For reinforced concrete and steel structures, this is equivalent to standard space-frame modeling, in which beams, columns, and braces are represented by beam-type finite elements with appropriate cross-section and stiffness parameters. Nonlinearity is usually localized at plastic hinges or distributed throughout the element using fiber-section formulations.

For unreinforced masonry (URM) buildings, the most widely adopted 1D strategy is the Equivalent-Frame (EF) approach, originally developed in Italy and subsequently implemented in software such as 3MURI [33, 40].

In this approach, each wall is divided into vertical macro-elements (piers) and horizontal macro-elements (spandrels). Piers represent the portions of wall between

openings and adjacent vertical discontinuities, while spandrels represent the masonry strips above and below openings, connected through rigid joints at the intersection with floor diaphragms and orthogonal walls. The in-plane response of each macro-element is then modeled by a non-linear beam-type element whose force–deformation law is calibrated on experimental results or on detailed continuum numerical analyses [43, 58].

A schematic representation of the EF idealization is shown in Figure III.11. The global building model is obtained by assembling the EF of all walls and connecting them at the floor levels, which are usually assumed to behave as rigid or semi-rigid diaphragms.

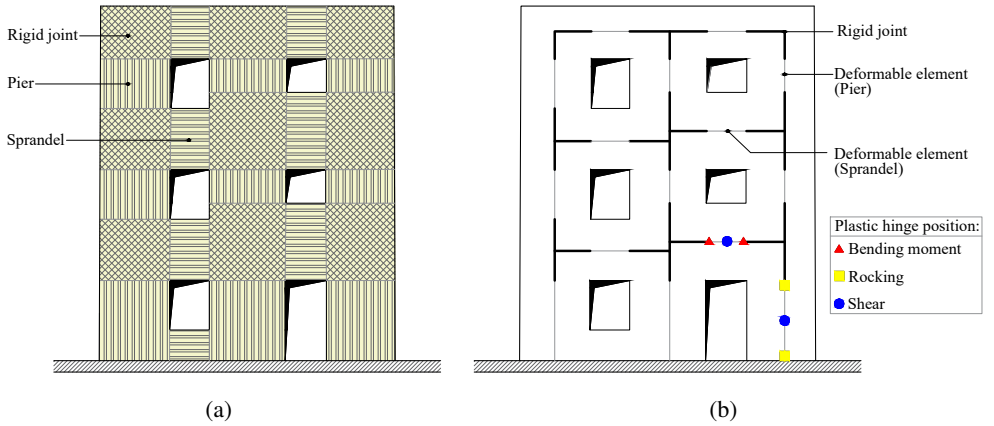

Figure III.11: Equivalent-frame idealization of a masonry wall: (a) identification of the macro-elements in the actual geometry; (b) scheme of the EF model and position of plastic hinges.

In its most common implementation, the EF approach assigns to each macro-element distinct non-linear laws for combined flexural and rocking behavior, shear and axial behavior, often based on simplified cross-section models or on macro-element formulations that couple shear and flexure in a single element [33, 40]. Degradation of stiffness and strength is represented through backbone curves and hysteretic rules, allowing for cyclic and post-peak analyses.

The global response of the structure is then obtained by assembling the contributions of all macro-elements and performing non-linear static (pushover) or dynamic analyses under seismic actions. This modeling methodology has progressively developed into an accepted standard for 1D analysis of URM buildings, and it is explicitly acknowledged by several national guidelines and standards, particularly in the context of seismic assessment and retrofit of existing masonry structures.

The main advantage of 1D EF models is its computational efficiency and robustness. The number of degrees of freedom is relatively small compared with 2D and 3D discretizations; the models are straightforward to build starting from architectural drawings or simplified surveys; and NLFEAs can be repeated many times within parametric or reliability studies at an affordable computational cost. This explains why such models are widely employed in large-scale seismic vulnerability assessments, in the calibration of simplified code-based procedures and in preliminary design of strengthening interventions [17, 52, 58].

These advantages, however, come at a cost of significant simplifications. The kinematic description is essentially planar, and out-of-plane mechanisms are either neglected or represented through separate checks and empirical criteria.

The 3D interaction among orthogonal walls and diaphragms, local stress concentrations around irregular openings or geometric discontinuities, and complex collapse mechanisms involving combinations of in-plane and out-of-plane response can only be captured in an approximate way, if at all. Moreover, the macro-element laws themselves are often calibrated under idealized conditions and may not fully account for the effects of irregular masonry textures, multi-leaf wall configurations or localized damage patterns.

In summary, 1D EF models are particularly useful when the main objective is to define the global response of the structure, generate capacity curves and performance points, or conduct comparison studies over a wide range of structural configurations. Detailed descriptions of local damage and 3D collapse mechanisms need more sophisticated 2D or 3D continuum models, making their usage less appropriate [17, 53].

III.3.2 2D modeling: plane-stress, plane-strain and shell formulations

2D FE models are an intermediate level of refinement between EF techniques and full 3D continuum discretizations. In 2D models, structural components are idealized as shell elements whose kinematics is defined over a surface, thus allowing the representation of in-plane stresses, bending actions (in the case of shells) and localized cracking patterns with significantly greater detail than in 1D formulations [17, 48].

These models are ideal to describing those portions of a structure whose behavior is predominantly 2D, such as masonry walls, shear walls in reinforced concrete buildings, slabs, diaphragms or slices extracted from a more complex geometry.

Figure III.12 illustrates a typical application of 2D modeling to a masonry wall with openings. The actual geometry is discretized using quadrilateral plane-stress elements.

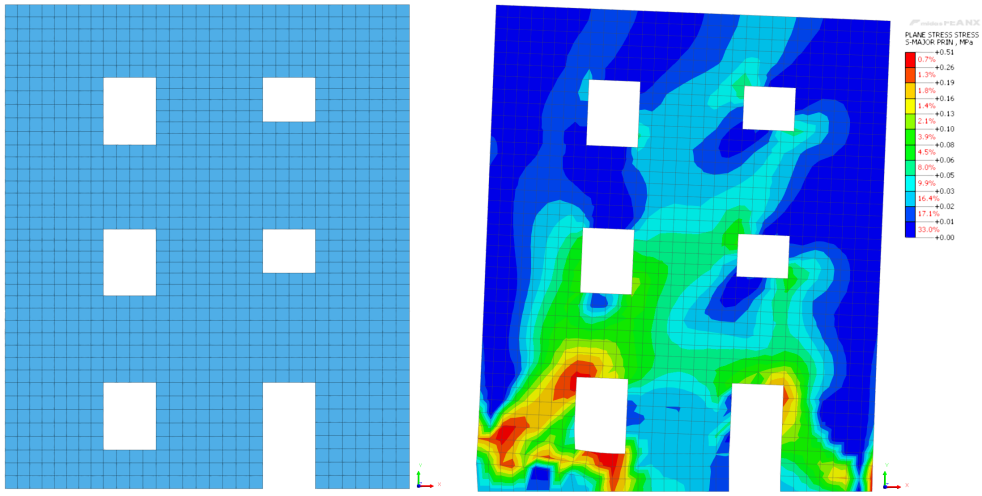

(a) (b)

Figure III.12: Example of 2D modeling of a wall with openings: (a) mesh discretization with plane-stress elements; (b) example of principal stress distribution from a NLFEA with lateral displacement applied at the top node, performed in MIDAS FEA NX.

In 2D models, the governing equations are obtained by assuming either plane-stress or plane-strain conditions. Plane-stress is typically adopted for slender masonry panels or reinforced concrete walls with thickness small compared to the in-plane dimensions, whereas plane-strain is more appropriate for massive walls or slices of thick structural components.

For vaulted or plate-like elements, shell formulations based on Kirchhoff–Love or Reissner–Mindlin kinematics provide an efficient way of incorporating both membrane and bending actions while retaining a reduced number of degrees of freedom.

Compared with 1D models, 2D formulations enable a more realistic description of the stress redistribution induced by openings, local discontinuities or material heterogeneity. They also allow the direct implementation of non-linear constitutive laws at the continuum level, such as damage–plasticity models, smeared-crack formulations or orthotropic material models calibrated on experimental tests [15, 53]. This makes it possible to simulate the onset and propagation of cracks, the formation of shear bands, the activation of sliding interfaces, and the progressive degradation of stiffness, which are essential features for an accurate representation of masonry in-plane response. As a consequence, 2D modeling is widely used to investigate local mechanisms, to study the interaction between openings and load-bearing wall segments, and to evaluate shear and flexural failure modes under lateral loading.

Despite these strengths, the 2D idealization introduces intrinsic limitations. Since the kinematic field is defined on a plane, torsional effects and the 3D interaction between orthogonal walls or coupled structural components cannot be naturally captured. The out-of-plane behavior must either be modeled with shell elements, implying assumptions about through-thickness properties and stiffness, or neglected altogether.

In structures where the global response stems from complex spatial interactions (for example, at the intersection between walls and diaphragms, or in buildings with irregular geometry), a purely 2D model may fail to reproduce important aspects of the structural behavior [17, 34].

Nevertheless, 2D models remain a powerful tool within a hierarchical modeling framework. They represent an acceptable balance between descriptive capacity and computational cost, making them especially useful for:

- Calibrating material parameters prior to 3D macro-modeling;
- Performing sensitivity analyses and exploring the influence of local geometric or mechanical variations;
- Analyzing isolated structural portions (e.g., shear walls, vaulted segments) before embedding them into a more detailed 3D framework.

Their computational efficiency permits refined NLFEAs, including cyclic loading and progressive collapse studies, that would be prohibitively expensive in 3D. Moreover, they serve as an essential validation layer: when 1D, 2D and 3D models are used in parallel, inconsistencies between modeling levels can be identified early and corrected before proceeding to full-scale analyses.

For these reasons, 2D FE modeling represents a cornerstone of advanced structural assessment strategies for both historic masonry and modern reinforced concrete buildings.

III.3.3 3D modeling: continuum approaches, micro and macro-modeling

3D FE models represent the highest level of refinement in the numerical analysis of existing structures. In these models, the building is described as a spatial continuum whose geometry is discretized using solid or shell elements, and the full 3D stress and strain state is computed directly from the governing equations of non-linear continuum mechanics.

Compared with 1D and 2D formulations, 3D models provide a substantially richer kinematic description, allowing the representation of spatial load paths, multi-axial stress interactions, and highly complex collapse mechanisms [34, 53].

Macro-modeling: homogenized continuum approaches

The most widely used 3D strategy for global analysis of existing structures is the macro-modeling approach, in which masonry, concrete or composite materials are idealized as a continuum characterized by appropriate non-linear constitutive laws. The material is typically described by non-linear isotropic or orthotropic CDP models, D–P failure criterion, or smeared crack formulations, whose parameters are calibrated through diagnostic testing and inverse analyses [15, 37].

This idealization enables the representation of large portions of the structure, walls, vaults, piers, slabs, diaphragms, while maintaining computational feasibility even for large buildings. The main advantages of the 3D macro-model approach is its ability to represent spatial interaction effects. The transmission of stresses between crossing walls, the torsional response caused by different floor plans, and the effect of diaphragms on lateral stability could be reproduced realistically.

Furthermore, the constitutive laws and mesh discretization provide non-linear damage patterns such as multi-axial cracking, crushing, shear sliding, and stiffness degradation, allowing for a realistic modeling of collapse mechanisms.

For historic masonry, where the geometry is often highly irregular, 3D macro-modeling also enables the incorporation of detailed laser-scan surveys, resulting in a close correspondence between numerical and physical geometry.

Despite these advantages, macro-models remain highly sensitive to mesh density, element type and the calibration of constitutive parameters. Localization effects, snap-back behavior and softening can lead to mesh dependence or convergence difficulties if not properly regularized.

Furthermore, the homogenization inherent in macro-modeling implies that microscopic features, such as joints, weak interfaces or infill heterogeneity, are represented only in an averaged sense.

Nevertheless, when the objective is to capture the global non-linear response of a complex structure, macro-modeling provides the most effective compromise between realism and computational efficiency [34, 53].

Micro-modeling: detailed and simplified strategies

On the other hand, micro-modeling specifically describes the internal components of the material, such as units, mortar joints, and interfaces. There are two main variants:

- Detailed micro-modeling: where units and mortar joints are discretized with continuum elements, and contact or interface elements govern the interaction between them;
- Simplified micro-modeling: where units are modeled with continuum elements while mortar joints are represented by non-linear interface elements alone.

Micro-models offer a very high descriptive capability: cracking can initiate and propagate along mortar joints or through units, sliding and opening at interfaces are captured explicitly, and local collapse mechanisms can be reproduced with high fidelity. For modern reinforced masonry or hybrid structures, they allow an accurate representation of reinforcement, bond–slip behavior and local anchorage failure.

In addition, they are often used to derive macro-scale material parameters through homogenization, for example by analyzing the response of representative volume elements (RVEs) under controlled boundary conditions [15].

Figure III.13 illustrates two representative approaches within the 3D modeling framework.

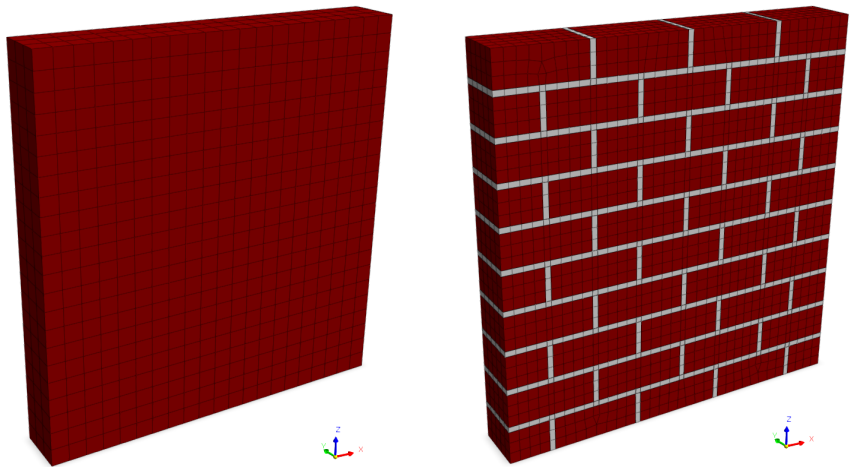

(a) (b)

Figure III.13: Example of 3D masonry wall: (a) homogenized 3D macro-model; (b) detailed micro-model.

In particular, Figure III.13(a) shows a homogenized 3D continuum model, in which a masonry wall is treated as an equivalent anisotropic or isotropic material; whereas Figure III.13(b) shows a detailed micro-model, in which each brick and each mortar joint is discretized explicitly.

However, the computational cost of micro-modeling grows rapidly with model size. Even small wall panels may require hundreds of thousands of degrees of freedom, and convergence of NLFEAs can be challenging, especially in the post-peak branch. For this reason, detailed micro-modeling is generally restricted to local analyses, such as testing the behavior of a single pier, validating a macro-element law, or simulating the collapse of a small portion of masonry under controlled conditions. Its use for global building analysis remains limited to research applications or to small structures.

Meso-modeling: block-based or discontinuum strategies

Between macro- and micro-modeling approaches, a meso-modeling strategy can be adopted, in which masonry is idealized as an assemblage of rigid or deformable blocks connected by interfaces.

This approach, implemented for example in the Distinct Element Method (DEM) or in block-based FE formulations, is particularly well suited to structures where collapse involves large displacements or block rocking, such as slender towers, parapets, arches or structures affected by significant discontinuities.

Meso-models naturally capture opening and closure of joints, sliding motions and fragmented collapse patterns, but their adoption for global assessments of entire buildings is constrained by computational cost and the difficulty of calibrating interface laws at scale [53].

III.3.4 Comparison of modeling strategies for global analysis

The three levels of idealization discussed above should not be viewed as mutually exclusive alternatives, but rather as complementary tools within a hierarchical modeling strategy.

In practice, many recent applications adopt a multi-level approach in which simpler 1D or 2D models are first used to explore the parameter space and identify critical regions, while refined 3D models are reserved for the final assessment of selected parts of the structure or of the building as a whole [15, 17, 43].

From a geometrical viewpoint, the choice between 2D and 3D FE models is strongly influenced by the wall thickness t relative to its in-plane dimensions (length L, height H) and by the expected stress state. For walls that are relatively slender in the out-

of-plane direction, a 2D idealization (plane-stress, plane-strain or shell) is generally acceptable. Several authors suggest that 2D models are appropriate when the thickness is significantly smaller than the in-plane dimensions, typically in the range

$$\frac{t}{L} < 0.10\text{–}0.15, \qquad \frac{t}{H} < 0.10\text{–}0.20 \tag{III.4}$$

provided that the behavior of interest is predominantly in-plane and that the out-of-plane response can be treated separately or represented through simplified assumptions [34].

In such conditions, plane-stress or plane-strain elements (for panels and slices) and shell elements (for slabs or vaults) offer a favorable compromise between physical realism and computational cost.

When these slenderness conditions are not met, or when significant variations of material properties and geometry occur along the thickness, the assumptions underlying 2D formulations become questionable and a 3D description is generally required. This is often the case for historic masonry buildings with massive walls (e.g., $t > 0.60$–0.80 m) or for multi-leaf walls where the core and outer leaves exhibit markedly different stiffness and strength.

Furthermore, in such situations the wall thickness may represent a non-negligible fraction of the in-plane dimensions, with

$$\frac{t}{L} > 0.20 \tag{III.5}$$

and the stress and damage fields become intrinsically 3D [37, 53].

Furthermore, 3D continuum models are also recommended when the global structural behavior is governed by complex spatial interactions, such as the coupling between orthogonal walls, the joint response of walls and vaults, or the influence of non-planar diaphragms and irregular foundations.

Table III.4 summarizes, in a compact form, the main characteristics of 1D, 2D and 3D global models as they are typically used in the assessment of existing structures.

Table III.4: Qualitative comparison between 1D, 2D and 3D FE models.

	1D EF	2D plane / shell	3D continuum
Kinematic description	Line elements with generalized displacements and rotations; macro-elements for walls	Surface elements (plane-stress, plane-strain, shells) with planar kinematics	Full 3D continuum with three displacement components per node
Typical use	Global capacity curves, large-scale vulnerability studies, rapid parametric analyses	Detailed in-plane analysis of walls, slabs, local mechanisms	Detailed global analysis of complex structures, interaction between components
Representation of local damage	Implicit, through plastic hinges or macro-element laws	Explicit in plane (cracks, shear bands, sliding)	Explicit in 3D (multi-axial cracking, crushing, sliding, delamination)
Computational cost	Low	Moderate	High to very high
Data requirements	Limited; global geometry and equivalent properties	Detailed geometry of individual panels/slabs; calibrated 2D constitutive laws	Full 3D geometry, boundary conditions, spatially varying material parameters
Main strengths	Robustness, efficiency, code-oriented assessment	Good balance between realism and cost; appropriate for local studies	Highest descriptive power; captures full 3D interaction and complex mechanisms

III.4 References

[1] ASTM (2010). C39, standard test method for compressive strength of cylindrical concrete specimens. *ASTM C39*.

[2] ASTM (2015a). A944-15 – standard test method for comparing bond strength of steel reinforcing bars to concrete using beam-end specimens. ASTM International, West Conshohocken, PA.

[3] ASTM (2015b). E519/E519M-15 – standard test method for diagonal tension (shear) in masonry assemblages. ASTM International, West Conshohocken, PA.

[4] ASTM (2019a). D6432-19 – standard guide for using the surface ground penetrating radar (gpr) method for subsurface investigation. ASTM International, West Conshohocken, PA.

[5] ASTM (2019b). E1508-12a(2019) – standard guide for quantitative analysis by energy-dispersive spectroscopy. ASTM International, West Conshohocken, PA.

[6] ASTM (2020a). C1583/C1583M-20 – standard test method for tensile strength of concrete surfaces and the bond strength or tensile strength of concrete repair and overlay materials by direct tension (pull-off method). ASTM International, West Conshohocken, PA.

[7] ASTM (2020b). C856/C856M-20 – standard practice for petrographic examination of hardened concrete. ASTM International, West Conshohocken, PA.

[8] ASTM (2022a). C1197, standard test method for in situ measurement of masonry deformability properties using the flatjack method.

[9] ASTM (2022b). C597, standard test method for pulse velocity through concrete.

[10] ASTM (2022). C78/C78M-22 – standard test method for flexural strength of concrete (using simple beam with third-point loading). ASTM International, West Conshohocken, PA.

[11] ASTM (2023a). C1060-23 – standard practice for thermographic inspection of insulation installations in envelope cavities of frame buildings. ASTM International, West Conshohocken, PA.

[12] ASTM (2023b). C496/C496M-23 – standard test method for splitting tensile strength of cylindrical concrete specimens. ASTM International, West Conshohocken, PA.

[13] ASTM (2023c). C803-2023 standard test method for penetration resistance of hardened concrete. ASTM International.

[14] ASTM (2025). C805/C805M – standard test method for rebound number of hardened concrete. ASTM International, West Conshohocken, PA.

[15] Bomben, M., Milani, G., and Aprile, A. (2025). A mesoscale modelling strategy for the nonlinear seismic analysis of masonry structures: Validation and comparison with macro-modelling approaches. *Engineering Structures*, 297:116985.

[16] Brune, P. and Perucchio, R. (2012). Roman concrete vaulting in the great hall of trajan's markets: Structural evaluation. *Journal of Architectural Engineering*, 18(4):332–340.

[17] Cattari, S. and Lagomarsino, S. (2020). Modelling strategies for masonry structures. In Milani, G., Lourenço, P. B., and Tralli, A., editors, *Computational Modeling of Masonry Structures Using the Finite Element Method*, chapter 2, pages 29–68. Elsevier, Amsterdam.

[18] CEN (1999). EN 1052-4:1999 – methods of test for masonry – part 4: Determination of shear strength between masonry units. European Committee for Standardization, Brussels.

[19] CEN (2002). EN 1052-3:2002 – methods of test for masonry – part 3: Determination of initial shear strength. European Committee for Standardization, Brussels.

[20] CEN (2016a). EN 1052-1:2016 – methods of test for masonry – part 1: Determination of compressive strength. European Committee for Standardization, Brussels.

[21] CEN (2016b). EN 13018:2016 – non-destructive testing – visual testing – general principles. European Committee for Standardization, Brussels.

[22] CEN (2021). EN 12504-2:2021 – testing concrete in structures – part 2: Non-destructive testing – determination of rebound number. European Committee for Standardization, Brussels.

[23] D'Altri, A. M., de Miranda, S., Castellazzi, G., and Glisic, B. (2023). Numerical modelling-based damage diagnostics in cultural heritage structures. *Journal of Cultural Heritage*, 61:1–12.

[24] DIN (2019). 18555-9 testing of mortars containing minreal binder - part 9: Determination of the compressive strength of hardened mortars in the bed joint. Deutsches Institut für Normung. (In German).

[25] D'Altri, A. M., Sarhosis, V., Milani, G., Rots, J., Cattari, S., Lagomarsino, S., Sacco, E., Tralli, A., Castellazzi, G., and de Miranda, S. (2020). Modeling strategies

for the computational analysis of unreinforced masonry structures: review and classification. *Archives of computational methods in engineering*, 27:1153–1185.

[26] Esel, Y., Erkul, E., Hintz, S., Schulte-Kortnack, D., Leonhardt, C., Heller, J., Meier, T., et al. (2023). St. petri cathedral schleswig: non-destructive geophysical damage analysis of medieval plaster. In *Proceedings of the 15th International Conference on Archaeological Prospection*, pages 345–348.

[27] ETSI (2022). EN 302 066 V2.2.1 – short range devices (srd); ground- and wall-probing radio determination (gpr/wpr) devices; harmonised standard for access to radio spectrum. European Telecommunications Standards Institute, Sophia Antipolis.

[28] Gentile, C. and Saisi, A. (2007). Ambient vibration testing of historic masonry towers for structural identification and damage assessment. *Construction and building materials*, 21(6):1311–1321.

[29] Hoła, J. and Schabowicz, K. (2010). State-of-the-art non-destructive methods for diagnostic testing of building structures–anticipated development trends. *Archives of Civil and Mechanical Engineering*, 10(3):5–18.

[30] ISO (2010a). 29501:2010 – microbeam analysis – analytical electron microscopy – methods for calibrating the magnification. International Organization for Standardization, Geneva.

[31] ISO (2010b). 29581-2:2010 – cement – test methods – part 2: Chemical analysis by x-ray fluorescence spectrometry. International Organization for Standardization, Geneva.

[32] Keshmiry, A. et al. (2024). Assessment, repair, and retrofitting of masonry structures: A state-of-the-art review. *Construction and Building Materials*, 410:134107.

[33] Lagomarsino, S., Penna, A., Galasco, A., and Cattari, S. (2013). Tremuri program: An equivalent frame model for the nonlinear seismic analysis of masonry buildings. *Engineering Structures*, 56:1787–1799.

[34] Lourenço, P. B. and Gaetani, A. (2022). *Finite Element Analysis for Building Assessment: Advanced Use and Examples*. CRC Press, Boca Raton.

[35] Martini, R., Mariscal, J. D. R., Carvalho, J., Solís, M., and VARUM, H. (2020). Towards a methodology for use of sonic and ultrasonic tests in earthen materials. *12th International Conference on Structural Analysis of Historical Constructions SAHC 2020*.

[36] Nastri, E. and Todisco, L. (2022). Macromechanical failure criteria for masonry: Elasticity, plasticity and numerical modelling. *International Journal of Architectural Heritage*, 16(11):1703–1730.

[37] Olsson, L., Lourenço, P. B., and Milani, G. (2023). Macro-model finite element strategies for the nonlinear analysis of masonry structures: State of the art and recent developments. *Engineering Structures*, 284:115814.

[38] Pelà, L., Cervera, M., and et al. (2018). Combined in-situ and laboratory minor destructive testing of historic mortars. *International Journal of Architectural Heritage*, 12(7–8):1157–1174.

[39] Pelà, L. et al. (2015). Mechanical characterization of historical masonry by core drilling and testing of cylindrical samples. *Construction and Building Materials*, 101:959–967.

[40] Penna, A., Lagomarsino, S., and Galasco, A. (2014). A nonlinear macro-element model for the seismic analysis of masonry buildings. *Earthquake Engineering & Structural Dynamics*, 43(2):159–179.

[41] Pirchio, D. et al. (2022). An aggregated non-destructive testing framework for the assessment of historic masonry structures. *Structures*, 36:1474–1490.

[42] Rainone, F., D'Altri, A. M., and et al. (2023). About the use of concrete damage plasticity for modeling masonry. *Engineering Structures*, 275:115–145.

[43] Requena-García, C., Cattari, S., and Lagomarsino, S. (2023). On the influence of equivalent frame modelling assumptions in the seismic assessment of masonry buildings. *Engineering Structures*, 280:115631.

[44] RILEM (2004). Mdt-d5, in-situ stress-strain behaviour tests based on the flat jack.

[45] RILEM (2004). TC 177 D1 mdt recommendation - indirect determination of the surface strength of unweathered hydraulic cement mortar by the drill energy method.

[46] RILEM TC 127-MS (1997). Recommendation ms-d.9: Determination of mortar strength by the screw (helix) pull-out method. *Materials and Structures*, 30:325–327.

[47] RILEM TC 216-SAM (2005). Strategies for the assessment of historic masonry structures with ndt.

[48] Roca, P., Cervera, M., Gariup, G., and Pelà, L. (2010). Structural analysis of masonry historical constructions: Classical and advanced approaches. *Archives of Computational Methods in Engineering*, 17(3):299–325.

[49] Roca, P., Lourenço, P. B., and Gaetani, A. (2020). *Historic Construction and Conservation: Materials, Systems and Damage*. CRC Press, Boca Raton.

[50] Rots, J. G. and Blaauwendraad, J. (1995). Two approaches for the analysis of masonry structures: micro and macro-modeling. *Heron*.

[51] Saisi, A. et al. (2024). Non-destructive testing and synergistic investigation of a heritage masonry structure with ambient vibration tests and monitoring. *Buildings*, 14(4):1101.

[52] Salvatori, L., Pelà, L., and Aprile, A. (2023). Global seismic assessment of existing masonry buildings using equivalent-frame and continuum finite-element approaches. *Engineering Structures*, 288:115401.

[53] Schiavoni, M., Milani, G., and Tralli, A. (2023). A numerical review of 3d modelling strategies for masonry structures: From micro-modelling to advanced macro-modelling. *Engineering Structures*, 275:115232.

[54] Tejedor, B. et al. (2022). Non-destructive techniques (ndt) for the diagnosis of historic masonry structures: A critical review. *Energy and Buildings*, 262:111977.

[55] Thommes, M., Kaneko, K., Neimark, A. V., Olivier, J. P., Rodriguez-Reinoso, F., Rouquerol, J., and Sing, K. S. W. (2015). Physisorption of gases, with special reference to the evaluation of surface area and pore size distribution (iupac technical report). *Pure and Applied Chemistry*, 87(9–10):1051–1069.

[56] UNI (2000 (in Italian)). EN 13187:2000 – prestazione termica degli edifici – rivelazione qualitativa delle irregolarità termiche negli involucri edilizi – metodo all'infrarosso. Ente Nazionale Italiano di Unificazione, Milano.

[57] UNI (2021). EN 12504-4:2021 – testing concrete in structures – part 4: Determination of ultrasonic pulse velocity. Ente Nazionale Italiano di Unificazione, Milano.

[58] Vanin, F., Penna, A., and Beyer, K. (2020). Seismic behaviour of masonry buildings: Comparison between equivalent frame and finite element modelling. *Engineering Structures*, 206:110147.

This page intentionally left blank.

CHAPTER IV

Case study of St. Peter's Basilica: historical–structural overview

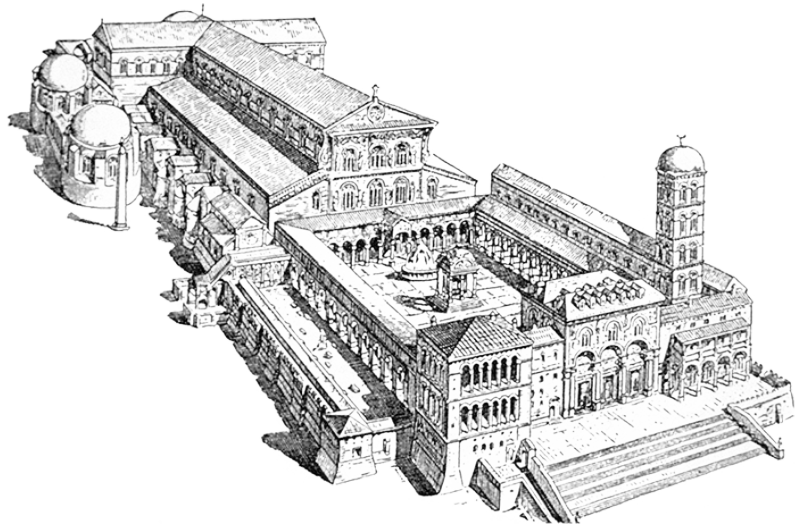

"Come muta il tempo in un momento, così muta il pensiero che lo segue."

("As time changes in a moment, so changes my thought that follows it.")

– Donato Bramante

IV.1 Introduction

This chapter provides a synthetic comprehensive historical and structural overview of St. Peter's Basilica, which forms the background for the probabilistic and numerical analyses developed in the following chapters.

First, it retraces the main building process from the Constantinian Basilica to the 16th–17th-century reconstruction and later alterations, outlining the role of the principal architects and the associated changes in spatial and structural conception.

The architectural and structural layout are then described, with particular attention to the system of piers, arches, vaults, drum and dome, the 17th-century Façade and nave extension, and the large colonnades. The discussion highlighting the main load paths and the buttressing mechanisms that govern the global stability of the monument.

Further, the chapter reviews the materials and construction techniques adopted in the Basilica. The typology and geometry of the foundations and substructures are summarized together with the available information on the mechanical and stratigraphic characteristics of the ground. The chapter then provides evidence on some existing damage patterns, past strengthening and maintenance interventions, and the most significant monitoring activities carried out on the Basilica [12].

Finally, it examines how the idealized geometry of the global 3D NLFE models is defined using the geometric and documentary sources used in this work, including historical surveys, archival drawings, and the Heritage Building Information Model (H-BIM) based on the digital twin derived from the 2022–2023 laser-scanner, drone, and photogrammetric survey campaign [2, 14, 17].

IV.2 Historical construction timeline

Many people consider the Papal Basilica of St. Peter the most important structure and the most important cathedral in Western Christendom. Constructed on the site of a church that had existed for nearly twelve centuries, the church that is visible currently is a relatively recent building, only four centuries old. Only a very small portion of the earlier building is still in place, and it is entirely covered by the new basilica, yet enough remains to allow a reliable reconstruction of the first St. Peter's Church [13].

The heritage building stands on the southern slope of Vatican Hill, above a Roman necropolis (2nd–4th century). Alongside the area ran the Circus of Caligula and Nero. The topography and the long cult of the Apostle's tomb made the place a sacred and symbolic anchor well before the present church.

In the 4th century, Emperor Constantine and Pope Sylvester erected a five-aisled basilica divided by 88 columns, complete with an atrium and a transept. To place the floor directly above Peter's tomb, more than 40,000 m^3 of soil was deposited on the necropolis. For more than a millennium, this "Old St. Peter's Basilica" served as the liturgical and civic heart of Christian Rome (see Figure IV.1).

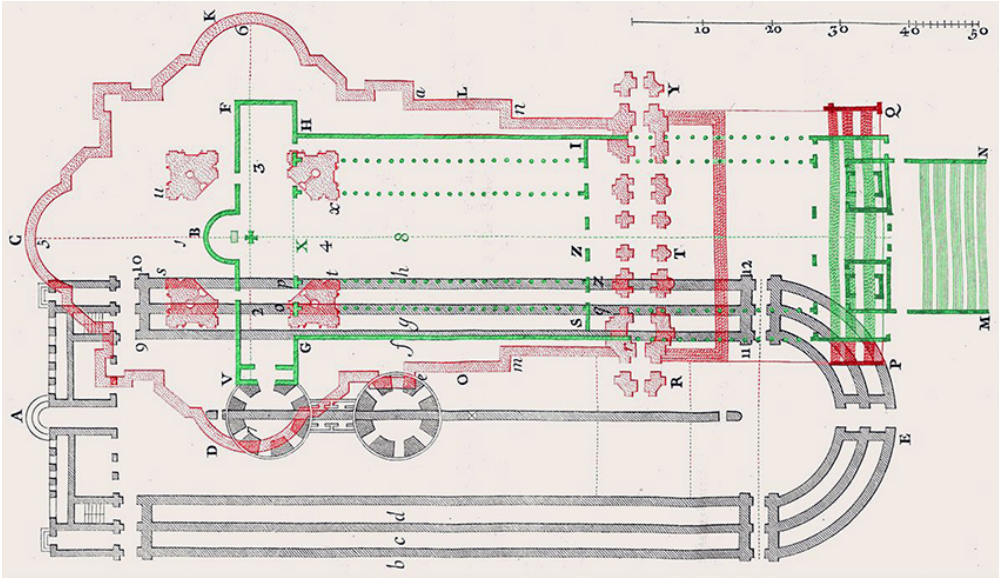

Figure IV.1: Overlaid overview of the main heritage structures: the Renaissance St. Peter's Basilica (red), the Constantinian Basilica (green), and the Circus of Caligula and Nero (black). Source: https://www.barbarabattilana.it.

The Constantinian Basilica had significant structural deterioration by the 15th century, as seen by collapsed walls, damaged wood, and general degradation, according to papal surveys. Pope Nicholas V initiated plans for major rebuilding in the 1450s, and the decisive turn came with Pope Julius II, who opted for complete replacement and placed the foundation stone of the new Basilica on 18 April 1506 based on the work of Donato Bramante. The Constantinian Basilica had to be gradually demolished in order to implement the centrally planned Greek-cross project developed by Donato Bramante, which was organized around four massive piers and a large dome above the Confessio. After Bramante died in 1514, the project was taken over by Raphael, Fra' Giocondo, and Giuliano da Sangallo. Under Leo X the design alternated between central and longitudinal solutions, with Raphael exploring a Latin-cross tendency while retaining a dominant dome at the crossing [1].

In the 1520s and 1530s Baldassarre Peruzzi and, above all, Antonio da Sangallo the Younger re-examined the design. Peruzzi proposed variants that re-centered the plan,

whereas Sangallo the Younger developed a powerful and highly engineered project, documented by his large timber model and robust external buttressing conceived to control the thrusts of the future dome. Following the Sack of Rome in 1527, economic and political instability impeded development and kept the debate open [9].

A decisive turn occurred in 1546, when Michelangelo Buonarroti was chosen *capomastro*. He simplified and strengthened the entire building, reasserted the central plan with a compact Greek-cross core, thickened and rationalized the huge piers, redesigned the drum and the exterior order, and erected the structure to the start of the dome before his death in 1564. The dome itself was erected rapidly between 1588 and 1590 by Giacomo della Porta, working with Domenico Fontana; its profile is slightly more pointed than the model of Michelangelo, and the sphere and cross were set in 1593.

In the same Sixtine program, Fontana executed the celebrated relocation of the ancient Vatican obelisk to the center of the new forecourt in 1586, an operation that employed hundreds of men, scores of horses, and large cranes [3, 18].

Under Pope Paul V, Carlo Maderno resolved the long central versus longitudinal debate by extending the nucleus of Michelangelo with a deep nave and by constructing the monumental Façade, thus fixing the Basilica in the form of a Latin cross. The church was consecrated by Urban VIII on 18 November 1626. In the Baroque phase, Gian Lorenzo Bernini gave spatial and ceremonial unity to the interior with the great bronze Baldacchino over the papal altar (1624–1633) and the *Cathedra Petri* in the apse, and he organized the urban setting with the embracing colonnades of Saint Peter's Square, completed in 1667 at the request of Pope Alexander VII [11].

The complex structure that exists today was created in a sequential phases, which included the radical central design by Bramante, the structural synthesis by Michelangelo, the longitudinal completion by Maderno, and the liturgical and urban design by Bernini.

In summary, the construction of St. Peter's Basilica proceeded through the sequential phases illustrated in Figure IV.2).

This historical synthesis frames the geometric and structural choices that shaped the present building. The following pages describe the architectural layout and the macro-elements that will be used as reference in the global FE modeling.

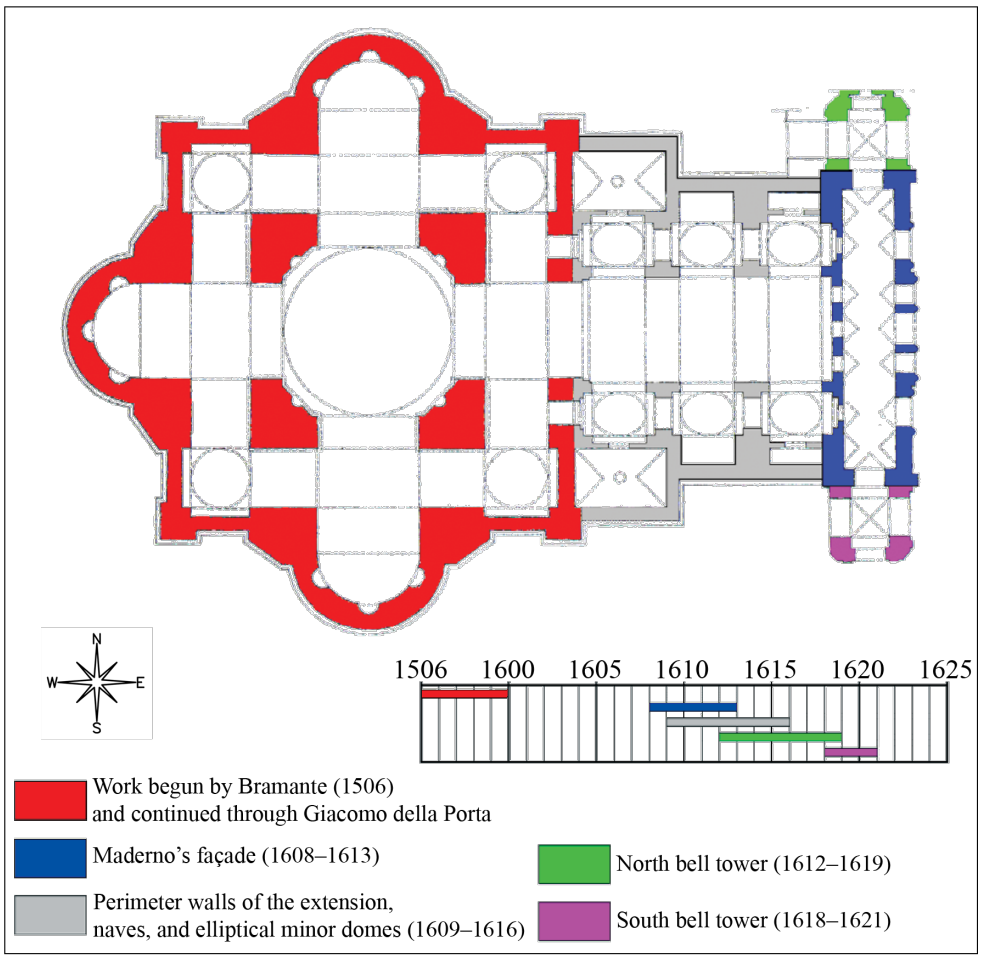

Figure IV.2: Construction phases of St. Peter's Basilica [16].

IV.3 Architectural–structural system

The current Basilica measures approximately 211 m in length from the main Façade to the end of the apse, and 154 m at its widest point across the transept. The structure rises to approximately 137 m at the top of the exterior dome, covers around 22,000 m^2, and host up to 60,000 people. In its 16th-century configuration, before to the longitudinal extension of the nave and the construction of the current Façade, the main structure was around 187 m in length; the 17th-century renovations finalized the church's present longitudinal dimensions.

The present church can be read structurally as two principal construction bodies (see Figure IV.3).

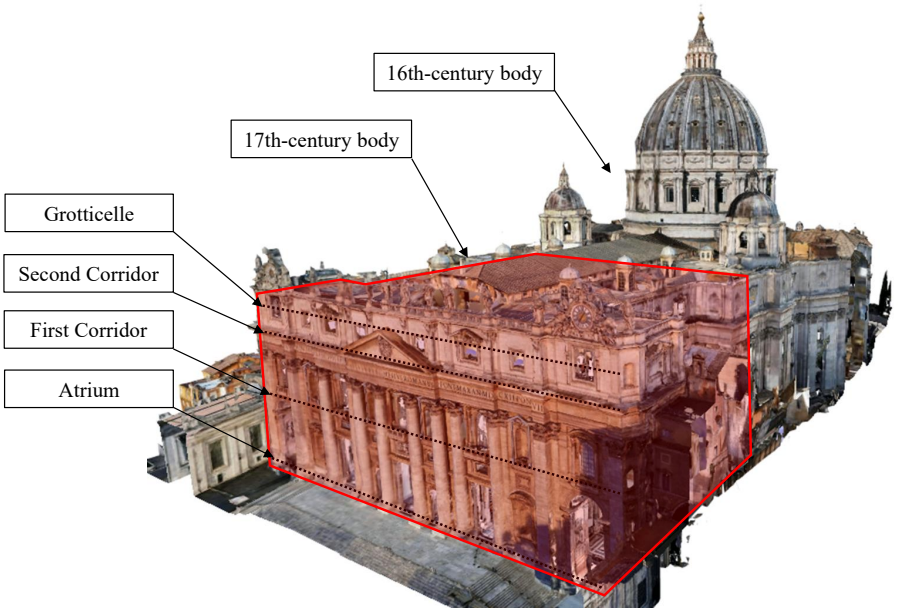

Figure IV.3: A 3D view of the 16th–17th-century structures in the digital twin of St. Peter's Basilica [6].

The first structure, constructed in the 16th century, features a central Greek-cross core supported by four large piers at the intersection, which support the drum and main dome, surrounded by large barrel and groin vaults, as well as massive surrounding walls providing structural support. The second structure, finalized in the 17th century, features the Façade body, the surrounding walls which divide the original core into a longitudinal nave, the nave complemented by side chapels and minor elliptical domes, as well as the adjacent towers. From a structural point of view, this latter body distributes horizontal thrusts from the vaults and the dome toward the ground by acting as a longitudinal stiffening and support system.

A system of service corridors used for maintenance and for access to the higher levels of the Basilica is integrated into the perimeter walls. The third corridor, also called the *Grotticelle*, is located between the extrados of the Hall of Blessings vault and the roof behind the Façade. The first corridor runs at the level of the Hall of Blessings but does not directly cross it. The second corridor is located above along the main cornice and follows the entire perimeter of the basilica. These circulation passageways, which are frequently included in the thickness of the multi-leaf walls, alter the masonry's effective cross-section locally and have an impact on the distribution of loads as well as the global stiffness.

The high-resolution digital twin of St. Peter's Basilica, which was recently created by Italferr S.p.A. on behalf of the Fabbrica di San Pietro, is the source of the 3D architectural-structural configuration used in this work from a geometric and documentation viewpoint [4]. The main objective of the project is to use cutting-edge digital technologies to map and analyze the basilica as a foundation for ongoing management and monitoring in the future. The study started with an extensive survey effort that gathered about 3.1 TB of raw data during public closure hours in July and August of 2022.

Using a combination of terrestrial laser scanners, drones, and a tethered aerostatic balloon to reach the higher vaults and domes, the two-month acquisition phase covered the exterior of the Basilica and interior. A total of nearly 15,000 high-resolution photos, or approximately 630 gigapixels, were obtained. After processing the point clouds, an architectural H-BIM was created (see https://www.italferr.it/).

In the present thesis, the H-BIM is used as the primary geometric source for the generation and idealization of the 3D FE models within MIDAS FEA NX, which are presented in Chapter VIII. In this way, the numerical models are fully consistent with the surveyed geometry of St. Peter's Basilica.

IV.3.1 The Façade

The main Façade of the Basilica (excluding the two lateral towers) is a parallelepiped volume measuring approximately 80 m in length (115 m including the two lateral towers), 45 m in height, and 23 m in depth.

The Atrium at ground level and the Hall of Blessings above are two superimposed volumes arranged longitudinally. Five main portals toward St. Peter's Square and five entrances leading into the Basilica divide it transversely. Vertically, the Façade is articulated, from bottom to top, into three principal sections, as shown in Figure IV.4:

- a giant order of Corinthian columns and pillars, framing the entrances to the Atrium and the large arched windows of the Hall of Blessings;
- an entablature, continuous classical structure running across the full width of the elevation;
- an attic level with a balustrade and surmounted by thirteen colossal statues (5-6 m in height) representing Christ the Redeemer (in the center) and twelve Apostles.

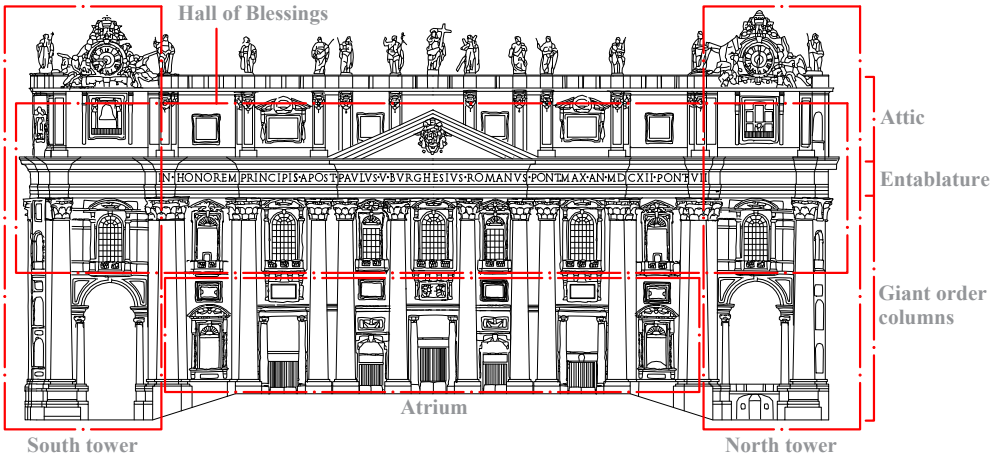

Figure IV.4: Façade of St. Peter's Basilica with indication of the three principal registers.

The monumental giant order includes four columns and four pillars, symmetrically arranged along the Façade (see Figure IV.4). The columns have a diameter of approximately 2.8 m and rise, together with the pillars, to a height of approximately 28 m from the base to the entrance. The pillars are approximately 2.7 m wide and 1.30 m deep.

Pillars and columns are both made of composite masonry. They consist of a travertine surround of varying thickness, usually between 0.40–1.00 m, around an internal core of masonry (mixed brick and stone with Opus Caementicium and lime-based mortars). The inner core guarantees mass and structural continuity with the nearby wall piers, while the travertine face is assembled in large ashlars that are locally connected by iron cramps.

While the interior core of the Façade is primarily composed of brick masonry, the wall planes facing the square are primarily covered in travertine blocks. The major vertical resistance is supplied by the large masonry piers merged with the four giant pillars and by the wall segments between the openings; decorative moldings, frames, and lesser pillars mainly contribute to architectural articulation.

Structurally, the Façade is connected to the main body of the Basilica through the arches and vaults of the nave, the supporting arches of the elliptical dome, and the perimeter walls rising up to the attic level. It forms a continuous 3D masonry system on the north side, where it is further integrated into the Vatican building complex, which includes the Pauline Chapel, the *Scala Regia*, and adjacent buildings [12].

IV.3.2 The Towers

Two C-shaped towers that were intended to support bell towers but were never finished stand on either side of the front. Each tower is about 18 m high. Due to foundation asymmetries revealed during construction, the southern tower is about 1.5 m wider than the northern tower. At the level of the south tower, a structural expansion joint separates the Basilica from Bernini's outer colonnade (see Figure IV.5(a)), whereas the north tower, as previously mentioned, is structurally connected to adjacent buildings (see Figure IV.5(b)).

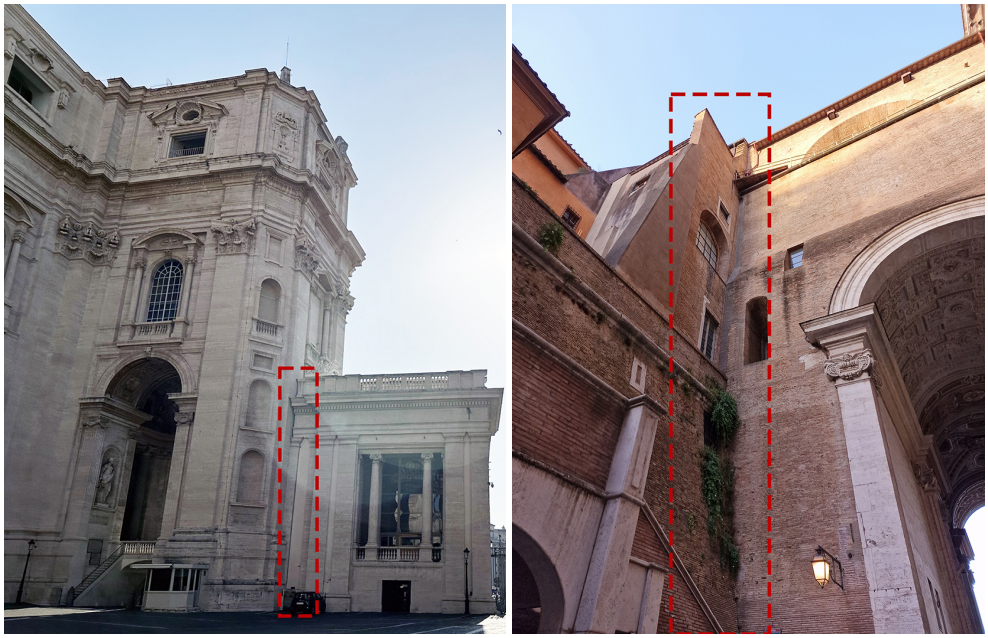

(a) (b)

Figure IV.5: South and north towers of St. Peter's Basilica: (a) detail of south tower-Bernini's outer colonnade connection; (b) detail north tower-adjacent buildings connection.

Each tower follows the vertical articulation of the main Façade and features a large arched opening at the Atrium level. Internally, the towers are crossed by vaults at the Atrium, Hall of Blessings, and roof levels. At the attic level, they incorporate two large transverse arches originally intended to carry the weight of the proposed bell towers. Furthermore, the towers are surmounted by large clocks added in later periods.

IV.3.3 The Atrium

The Atrium is a rectangular hall about 70 m long, 12.75 m wide and 18.50 m high at the crown of the vault (see Figure IV.6). It has five openings facing the square (two arched and three with architraves and monolithic columns), five internal doorways leading into the Basilica, and one lateral opening into each of the two towers.

Figure IV.6: Interior view of the Atrium of St. Peter's Basilica.

A barrel vault with lunettes over the doors surrounds the Atrium. The vault is 12.75 m wide and rises to a height of 18.50 m at the top. The elements of the inner wall (pillars and cornices) are decorative only; structural piers are made entirely of brick masonry. The building is covered in travertine masonry on the outside.

IV.3.4 The Hall of Blessings

The Hall of Blessings replicates its plan dimensions (70 m × 12.75 m × 21.00 m) and is located above the Atrium. It has five arched windows facing the square and five apertures inside, two of which face the lateral chapels and three of which face the nave. A barrel vault that reaches a crown height of 21.00 m covers it (see Figure IV.7).

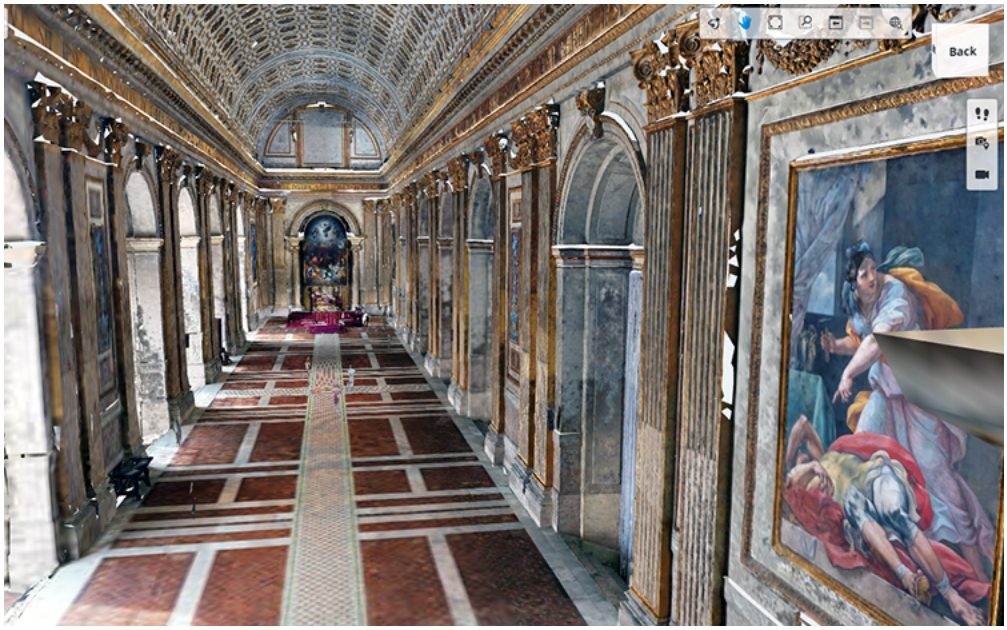

Figure IV.7: Interior view of the Hall of Blessings of St. Peter's Basilica (image from the digital twin).

Above the vault is the so-called Second Corridor, a passage within the Façade thickness aligned with the Hall of Blessings' cornice. This corridor continues along the entire length of the Basilica beneath the attic windows.

Above this level the third corridor (Grotticelle) is positioned, located between the extrados of the Hall of Blessings vault and the main roof. It is divided by irregularly spaced transverse walls that terminate in the central area to accommodate the three large nave windows.

IV.3.5 The Central Nave

The longitudinal addition by Carlo Maderno converts the plan of the Basilica from a Greek to a Latin cross, adding about 120 m in length. This extension includes the central nave, surrounded by side corridors and chapels.

The nave measures approximately 25 m in width and 46 m in internal height. Including the corridors, the total width is approximately 58 m (see Figure IV.8).

Figure IV.8: Interior view of the central Nave of St. Peter's Basilica.

The central nave includes six elliptical domed chapels above the side windows, three on each side of the central nave, and a barrel vault roof supported by masonry piers. Each of the six structural windows that make up the nave is articulated with ornamental cornices and transverse arches.

IV.3.6 The Dome

The main dome, designed by Michelangelo and completed by Giacomo della Porta and Domenico Fontana in 1590, is supported by four huge piers and a circular drum with sixteen large windows (see Figure IV.9(a)).

Furthermore, there is a small service tunnel between the inner and outer shells of the dome. The outer shell, which is about 1 m thick and covered with copper layers, protects the inner shell and defines the outward profile, while the inner shell, which is about 2 m thick, serves as the main load-bearing surface (see Figure IV.9(b)) [7].

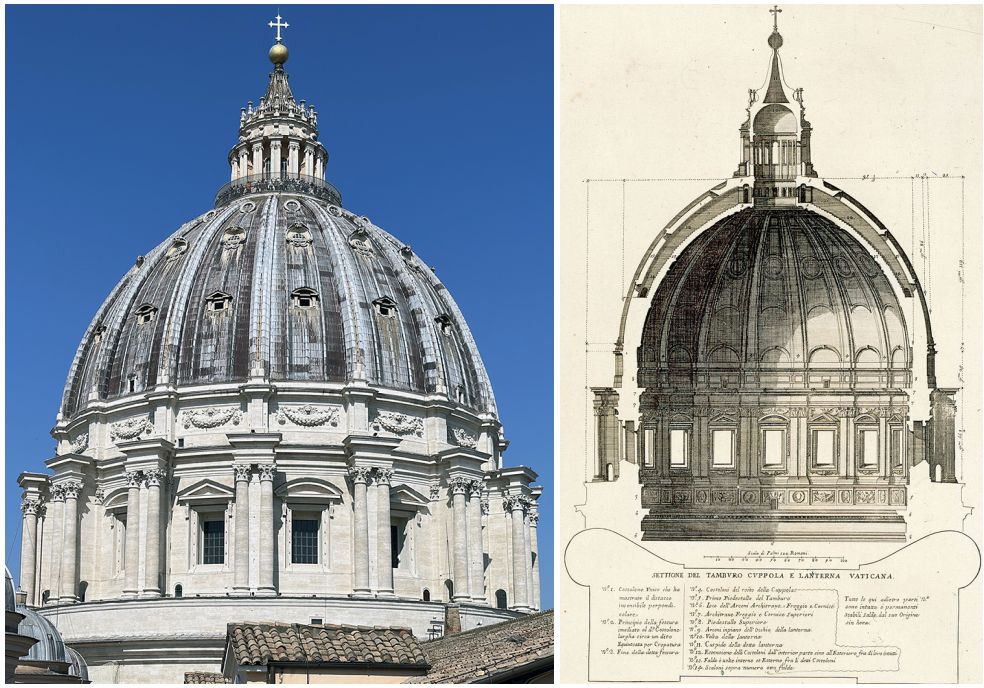

(a) (b)

Figure IV.9: Dome of St. Peter's Basilica: (a) External current view; (b) cross-sectional view according to Giacomo della Porta's 1564 design (after C. Fontana, 1694).

It is one of the tallest masonry domes ever constructed, with an internal diameter of approximately 41.5 m, an external diameter of approximately 59 m, and a total height of 136.6 m from the Basilica floor to the top of the external cross. The drum, buttresses, and metal ties must balance the high meridional compressive stresses and circumferential thrusts caused by the dome, lantern, and support the structure combined weight of about $14,000$ t (source: https://www.vatican.va/content/vatican/it/ra/cupolone-lanterna.html).

Since the 17th century, the dome has shown meridional cracking, especially above the drum windows and along some ribs. These damage patterns motivated Giovanni Poleni's well-known work in the 18th century, when he analyzed the stability of the fractured dome and designed an iron chain system to limit the damage. During the 1740s, circumferential rings were placed at various elevations between the drum and

the lower section of the dome to support the iron ties and clamps and provide efficient confinement against further opening of the meridional cracks [15].

In recent years, the dome has been the object of several detailed structural investigations, including FEAs of the double-shell system, simplified 3D models of the dome–drum–buttress assembly, limit-analysis–based assessments of the thrust forces and evaluations of the dome's structural safety [5, 10].

However, the FE modeling of the main dome is beyond the scope of the present work, which focuses on the 17th-century body and the main Façade of the Basilica.

IV.3.7 The Foundations

From a foundation point of view, St. Peter's Basilica rests on a highly complex archaeological substratum. Immediately beneath the present Basilica floor the level of the so-called Vatican Grottoes is located, which extend beneath much of the central nave and the area of the crossing. Below this intermediate level are the archaeological remains of Nero's Circus and an extensive Necropolis (see Figure IV.10).

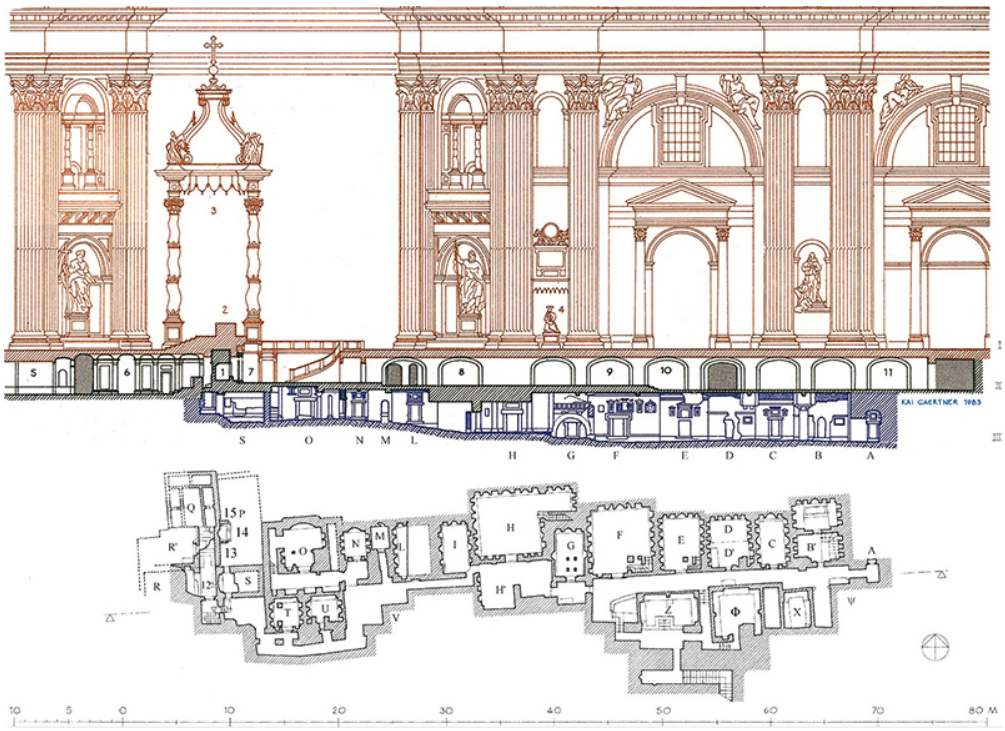

Figure IV.10: Archaeological substratum of St. Peter's Basilica: Vatican Grottoes and pre-Constantinian Necropolis (image © Fabbrica di San Pietro in Vaticano).

In particular, the pre-Constantinian Necropolis is located at depths of approximately 4–11 m below the current floor level [19]. This multi-layered structure, which includes ancient multi-leaf masonry, tomb chambers, backfills, and substructures at different elevations, resulting in a various interaction between the Basilica and the underlying earth. Foundation levels, soil stiffness, and the nature of the supporting stratigraphy can thus change significantly, particularly beneath the nave's longitudinal axis and in the transition zones between the transept and the crossing.

In addition, the foundations beneath the 17th-century body have not yet been investigated in a complete and homogeneous manner over the entire footprint of the Basilica. Geognostic campaigns are still ongoing at the time of writing, and the available data are locally detailed but spatially discontinuous. To compensate for this lack of information, a simplified foundation modeling strategy was adopted in the global 3D FE model, as discussed in Chapter VIII, in which the interaction with the ground and with the underlying archaeological structures is represented in an simplified manner.

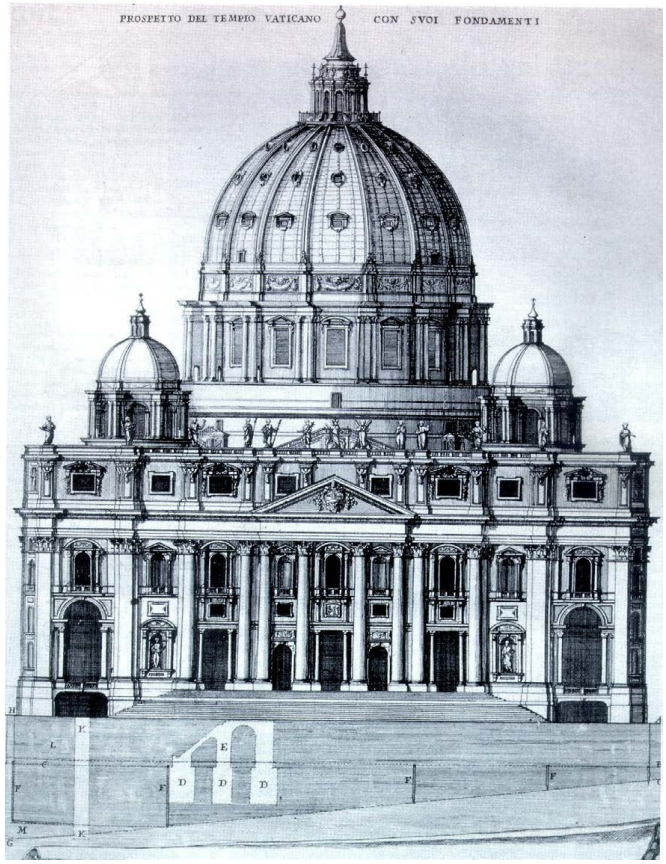

Figure IV.11: Archaeological substratum of St. Peter's Basilica: foundation block beneath the Façade body (after C. Fontana, 1694).

The only foundation element modeled on the basis of detailed in-situ information is the area beneath the main Façade. In this region, the geometry of the massive masonry substructures was first reconstructed from the historical drawings by Carlo Fontana (see Figure IV.11), which document the configuration of the foundations and their relationship with the ruins of Nero's Circus. This historical reconstruction was then refined and constrained using the results of the geognostic investigations carried out by EniTecnologie S.p.A. during the 1998–1999 experimental campaign. The Façade foundations are thus the best-characterized part of the substructure and are explicitly represented in the 3D FE model. This modeling choice reflects the current state of knowledge and underlines the need to progressively integrate archaeological evidence (Nero's Circus, Vatican Grottoes, and Necropolis), with new investigation results within a coherent reliability-based assessment framework.

IV.4 Known interventions and monitoring

This section presents key information from historical interventions and monitoring activities on the main Façade and the 17th-century body of St. Peter's Basilica.

In 1998-1999, EniTecnologie S.p.A. carried out an intensive non-destructive investigative campaign using Ground-Penetrating Radar (GPR) [8]. This GPR survey had two objectives: (i) to acquire information on the geometry and features of the foundations down to a depth of around 10 m, and (ii) to detect the presence of transverse metallic elements inside the masonry. Importantly, the studies revealed that no steel ties had previously been found within the masonry in the direction orthogonal to the Façade, taking away the hypothesis of hidden transverse tie systems.

The GPR investigation on the Façade included the large columns of the colonnade and the zones associated with the four major *Cretti*, which are significant through-thickness fractures that cross the Façade almost orthogonally. These Cretti, which date back at least to the 18th century, have long been monitored using marble tell-tales (simple crack-monitoring devices, as shown in Figure IV.12(a)) installed across the fractures to assess their temporal evolution. The colonnade survey provided information on both the structural configuration and the materials used. The large columns were recognized as composite pieces consisting of an inner masonry core surrounded by travertine blocks of 40-90 cm thickness. The survey not only confirmed the thickness of the travertine blocks, but also highlighted local separations between the stone facing and the masonry core, and revealed the presence of metallic clamps used to connect

adjacent blocks. This information is particularly valuable for understanding the local vulnerability of the colonnade and its interaction with the Façade.

Historical evidence indicates that the main cracks had already developed during the early construction phases, particularly in the Façade, and have been the object of periodic observation since at least 1793. From a spatial point of view, the largest cracks are observed at the level of the Grotticelle, where wide fractures run longitudinally across the entire Façade body. They are located both at mid-span of the intrados of the upper vaults and along the inner side of the corridor (see Figure IV.12(a)). In addition, a crack monitoring system was installed in 1999 to monitor the fractures at mid-span of the upper vaults, consisting of instrumented crack gauges that measure the crack opening displacements (see Figure IV.12(b)).

(a) (b)

Figure IV.12: Crack pattern at the level of the Grotticelle: (a) longitudinal fractures across the Façade body; (b) instrumented crack gauges.

Additional cracks, monitored since 1793 by means of marble tell-tales, have been detected within the second corridor (see Figure IV.13(a)). Significant damage is also present at the so-called *Catafalchi–Burbera* level (see Appendix A - Sheet 03, for the location), where all the vaults of the three rooms exhibit cracking patterns of varying extent and orientation (see Figures IV.13(b)). In general, the pattern and orientation of these cracks support the interpretation that the damage is strongly influenced by

the subsoil conditions beneath the Façade and by the heterogeneity of the foundations, which are known to be affected by the presence of the remains of Nero's Circus.

(a) (b)

Figure IV.13: Crack pattern at the level of the second corridor: (a) ancient marble tell-tales inside the corridor; (b) diagonal fractures across the vaults at the Catafalchi-Burbera level.

Following the structural analyses performed in the late 1990s by Prof. G. Macchi et al., a first series of corrective measures was designed and implemented with the specific aim of improving the stability of the Façade (see Figure IV.14).

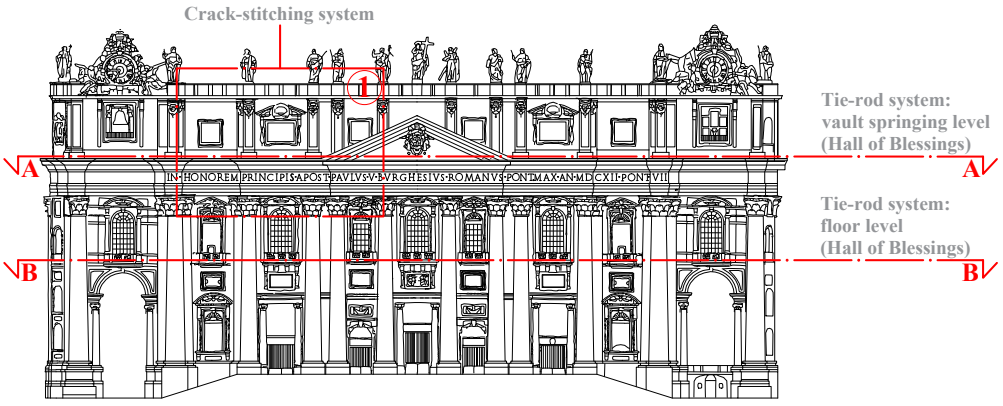

Figure IV.14: Façade of St. Peter's Basilica with indication of the locations of the structural tie-rods and crack-stitching systems.

In particular, in view of the Jubilee of 2000, a system of steel tie-rods was placed starting in 1999. Tie-rods with strain gauges were placed at the vault springing level and the floor level of the Hall of Blessings (see Figures IV.15 and IV.16), providing both a strengthening intervention and an early structural health monitoring system capable of tracking long-term deformations in the Façade body.

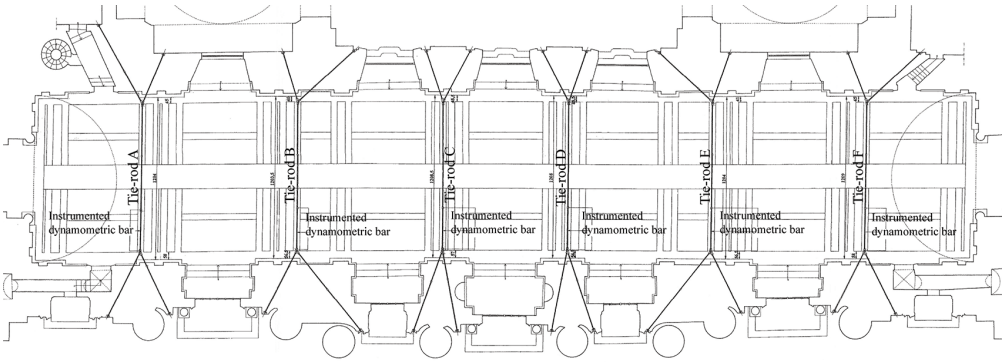

Figure IV.15: Cross-section A-A: vault springing level of the Hall of Blessings showing the system of structural tie-rods (location indicated in Figure IV.14).

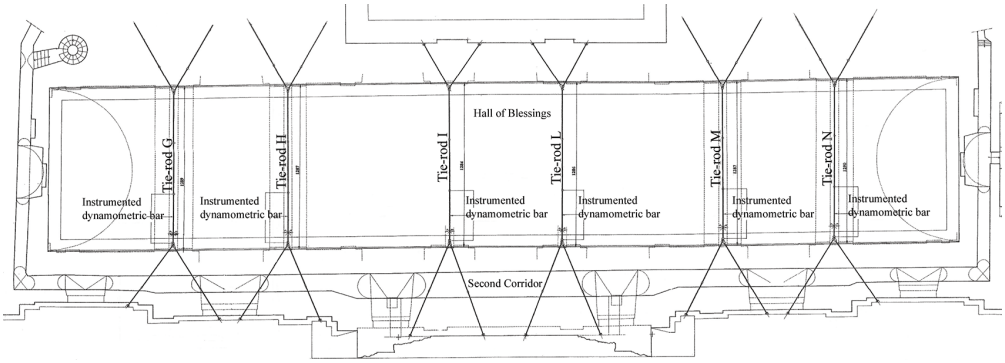

Figure IV.16: Cross-section B-B: floor level of the Hall of Blessings showing the system of structural tie-rods (location indicated in Figure IV.14).

The reinforcing system is composed of stainless steel bars (type AISI 313). More specifically, the twelve tie-rods (six for each level) introduced during these restoration works have a peculiar geometry: each tie-rod has a central segment with a diameter of 50 mm that splits near the extremities into branches with a decreased diameter of 40 mm. These terminal branches are put into drilled holes with a diameter of 75 mm, which run through the masonry thickness, and then grouted to provide proper bonding (type Emaco S38), weight transfer, and corrosion protection. Tie-rods are placed with a downward slope of approximately 10% and anchored by plate-type anchor heads

bearing against outer travertine masonry surfaces. In addition, ancient tie-rod systems have been discovered inside the two lateral towers of the Façade body. Each tower consists of two pairs of steel tie-rods with square cross-sections (see Figure IV.17).

(a) (b)

Figure IV.17: Structural tie-rod systems in St. Peter's Basilica: (a) a tie-rod system at the vault springing level of the Hall of Blessings (placed in 1999), and (b) ancient tie-rods inside the north tower.

Furthermore, a crack-stitching system was implemented at the level of the second corridor, with the specific aim of closing the major cracks (Cretti) (see Figure IV.18).

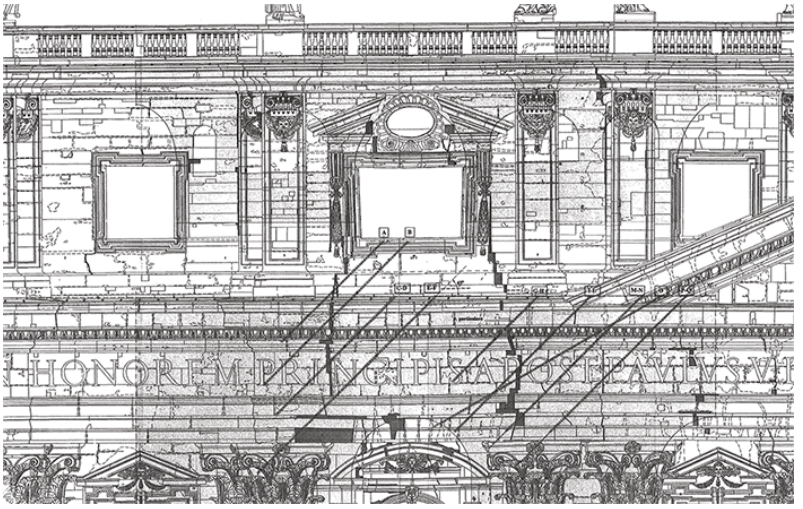

Figure IV.18: Detail 1: crack-stitching system applied to the Façade crack pattern (Cretti) of St. Peter's Basilica (location indicated in Figure IV.14).

This system consists of stainless steel bars (type AISI 313) with a diameter of 35 mm, inserted across the crack planes into drilled holes with a diameter of 81 mm. The circular gap between the bars and the surrounding masonry is filled with high-strength repair grout (type Emaco S88), which provides mechanical continuity across the damaged portions as well as increased intervention durability.

IV.5 References

[1] Allen, J. (2013). Nicholas v's tribuna for old st. peter's in rome as a model for the new apsidal choir at padua cathedral. *Journal of the Society of Architectural Historians*, 72(2):166–188.

[2] Angjeliu, G., Coronelli, D., and Cardani, G. (2020). Development of the simulation model for digital twin applications in historical masonry buildings: The integration between numerical and experimental reality. *Computers and Structures*, 238:106282.

[3] Bianchini, C. (2020). A methodological approach for the study of domes. *Nexus Network Journal*, 22(3):671–699.

[4] Camus, A. (2024). Preserving historic st. peter's basilica with a digital twin. *GIM International*.

[5] Como, M. (2019). Thrust evaluations of masonry domes. an application to the st. peter's dome. *International Journal of Masonry Research and Innovation*, 4(1-2):32–49.

[6] Darò, P., Iacussi, L., Turrisi, S., Rusticano, G., Chiariotti, P., Zappa, E., Cigada, A., and Mancini, G. (2025). Dynamic characterization of monumental building for shm purpose: The case of the papal basilica of st peter. In *International Conference on Experimental Vibration Analysis for Civil Engineering Structures*, pages 84–93. Springer.

[7] Funari, M. F., Silva, L. C., Mousavian, E., and Lourenço, P. B. (2023). Real-time structural stability of domes through limit analysis: application to st. peter's dome. *International Journal of Architectural Heritage*, 17(6):915–937.

[8] Giunta, G. and Calloni, G. (2000). Ground penetrating radar applications on the facade of st. peter's basilica in vatican. In *Proc. 15 World Conference on Non Destructive Testing, Rome*, pages 172–176.

[9] Huppert, A. C. (2009). Envisioning new st. peter's: Perspectival drawings and the process of design. *Journal of the Society of Architectural Historians*, 68(2):158–183.

[10] Jasieńko, J., Raszczuk, K., Kleszcz, K., and Frąckiewicz, P. (2021). Numerical analysis of historical masonry domes: A study of st. peter's basilica dome. *Structures*, 31:80–86.

[11] Kuntz, M. A. (2005). Maderno's building procedures at new st. peter's: Why the façade first? *Zeitschrift für Kunstgeschichte*, 68(1):41–60.

[12] Macchi, G. (2001). Diagnosis of the facade of st. peter's basilica in rome. In Lourenço, P. B. and Roca, P., editors, *Historical Constructions*, pages 309–318, Guimarães, Portugal.

[13] McKitterick, R., Osborne, J., Richardson, C. M., and Story, J. (2013). *Old Saint Peter's, Rome*. Cambridge University Press.

[14] Pocobelli, D. P., Boehm, J., Bryan, P., Still, J., and Grau-Bové, J. (2018). Bim for heritage science: a review. *Heritage Science*, 6(1):1–15.

[15] Poleni, G. (1748). *Memorie istoriche della gran cupola del tempio vaticano, e de' danni di essa, e de' ristoramenti loro, divise in libri cinque*. Giovanni Manfrè, Padova, Italy. (in Italian).

[16] Spagnesi, P. C. (1997). Carlo maderno in s. pietro: note sul prolungamento della basilica vaticana. In Spagnesi, G., editor, *L'architettura della Basilica di San Pietro: storia e costruzione. Atti del Convegno internazionale di studi (Roma, Castel S. Angelo, 7–10 novembre 1995)*, number 25–30 in Quaderni dell'Istituto di Storia dell'Architettura, nuova serie, pages 261–268. Bonsignori, Roma. (in Italian).

[17] Vuoto, L., Funari, M. F., and Lourenço, P. B. (2023). On the use of the digital twin concept for the structural performance assessment of existing structures. *Infrastructures*, 8(5):86.

[18] Wallace, W. E. (2023). *Michelangelo architetto di Dio*. Donzelli, Roma. (in Italian).

[19] Zander, P. (2007). *La necropoli sotto la basilica di San Pietro in Vaticano*. Fabbrica di San Pietro. (in Italian).

CHAPTER V

Experimental diagnostic campaign

"L'atto pratico del costruire è il vero fine dell'Architettura."

("The practical act of building is the true end of Architecture.")

– Giacomo dalla Porta

Partly redrafted after *"Material Characterization of Multi-leaf Masonry Walls in Historical Buildings: Non-linear FEM Approach."* G. Rusticano, P. Daró & L. La Mendola. In International Brick and Block Masonry Conference (2024, July) [17] and *"Dynamic Characterization of Monumental Building for SHM Purpose: The Case of the Papal Basilica of St Peter."* P. Daró, L. Iacussi, S. Turrisi, G. Rusticano, P. Chiarotti, E. Zappa, A. Cigada & G. Mancini. In International Conference on Experimental Vibration Analysis for Civil Engineering Structures (2025, July) [9].

V.1 Introduction

This chapter presents and interprets the results of the experimental diagnostic campaign carried out by SACERTIS INGEGNERIA S.R.L. in 2023 on St. Peter's Basilica, with particular attention to the portions of the 17th-century body and the main Façade that are relevant for the numerical modeling and reliability-based assessment developed in the following chapters.

The investigations were designed to obtain consistent and cross-validated information on: (i) the internal arrangement and thickness of the multi-leaf masonry walls; (ii) the in-situ mechanical properties of the brickwork leaves and of the ARC core; and (iii) the global dynamic behavior and structural continuity between different construction phases.

The chapter outlines some experimental technique that combines NDT, MDT, and DT to define the masonry material and structural behavior. In particular, in-situ NDT, including ultrasonic pulse velocity measurements and ambient vibration monitoring, are utilized to evaluate masonry quality, detect anomalies, and determine the main dynamics characteristics of the Basilica. In-situ MDT, such as endoscopic surveys and single/double flat-jack tests, provide insight into the wall stratigraphy, in-situ stress state, and deformability of the brickwork masonry leaves.

The chapter also describes DT, such as core extractions and laboratory tests on ARC, to assess the strength and stiffness of the inner concrete-like core and validate assumptions based on in situ measurements.

Finally, the experimental results are summarized into a set of deterministic mechanical parameters for both the external brickwork and the ARC core. These parameters are adopted in the elasto-plastic D–P constitutive model and in the homogenization of the multi-leaf masonry wall into an equivalent single material, as further developed in Chapter VI. The resulting mechanical parameters, together with the identified sources of uncertainty, provides the basis for the probabilistic material characterization and for the formulation of the CDP model presented in Chapter VII.

V.2 Overview of the experimental diagnostic campaign

The 2023 experimental diagnostic campaign on St. Peter's Basilica (see the flowchart in Figure V.1) was designed as a minimally invasive, multi-scale program combining NDT, MDT, and DT.

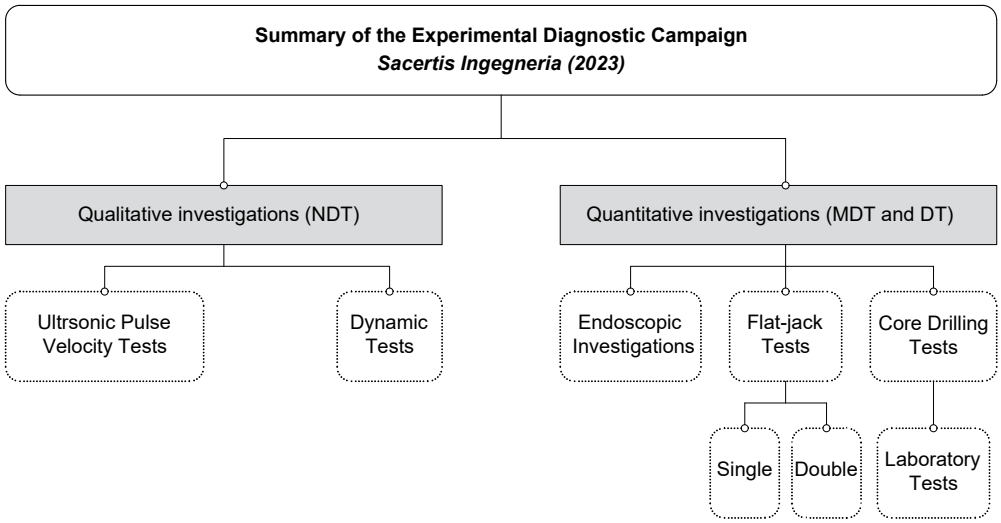

Figure V.1: Flowchart of the NDT, MDT and DT conducted within the 2023 experimental diagnostic campaign on St. Peter's Basilica.

The objective was to reconstruct geometry and construction details, and to quantify the mechanical properties of the historic multi-leaf masonry in a coherent and cross-consistent manner.

Multi-leaf masonry is widespread in monumental heritage across historic city centers. These walls typically comprise two or three leaves made of stone, brick, or rubble, enclosing an inner core [5, 8, 10, 12].

In the Roman tradition, the core was a high-performance conglomerate known as Opus Caementicium, while the inner and outer leaves often consisted of thin brick walls (*Opus Latericium*) acting as permanent formwork and finishing (see Figure V.2). The global load-bearing capacity thus depends on the relative thickness of the leaves and core, as well as on the constituent materials' mechanical properties [18–20].

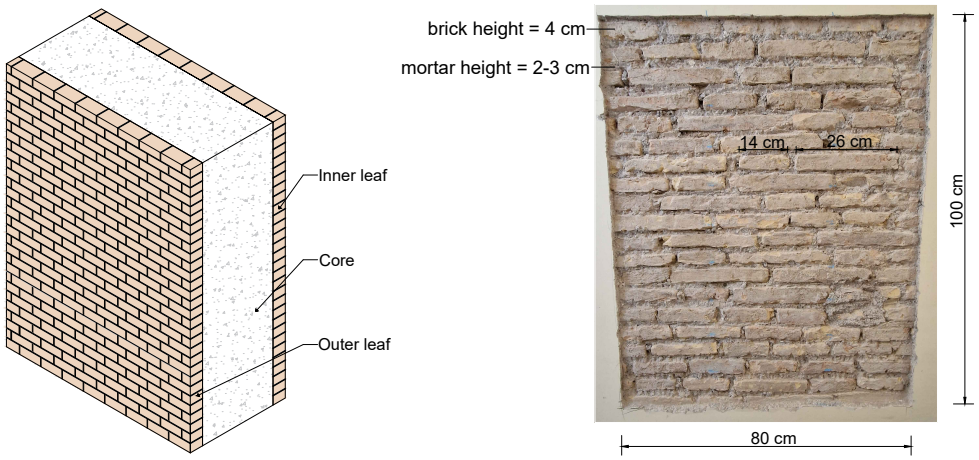

(a) (b)

Figure V.2: (a) Schematic layout of Ancient Roman multi-leaf walls (ARC core with Opus Latericium faces); (b) Front view of a brickwork wall panel inside St. Peter's Basilica.

The use of thick mortar joints, documented from the late Roman Empire and frequent in Byzantine masonry, has been associated with increased deformability and a lower wall elastic modulus [7, 13]. Economic motives (reduced brick consumption) are often cited; however, when aggregate grading is scaled to joint thickness, this construction practice has proved mechanically reliable over time. In the Basilica, the external leaves are built with lime–pozzolan mortar and yellow–pink bricks in a regular bond; brick lengths range from about 14 cm to 26 cm with an average thickness of about 4 cm, while mortar joints are typically 2–3 cm thick. Very thick joints (comparable to brick thickness) are attested in sixteenth-century Byzantine contexts and have been mechanically investigated, although the specific literature remains limited [6, 10].

The diagnostic program combined NDT, MDT and DT. In particular, NDT (ultrasonic pulse velocity and ambient vibration) provided continuous or quasi-continuous information on internal morphology, stiffness distribution and global dynamic behavior with minimal interference; MDT (endoscopy and single/double flat-jack tests) yielded direct evidence of masonry stratigraphy, in-situ stress and the stress–strain curves of the brickwork leaves; DT (compression tests on drilled ARC core) supplied the compressive strength and elastic modulus of the concrete-like core, clarifying its structural role within the multi-leaf system.

By jointly interpreting these results, the campaign allowed: (i) identification of the actual build-up and thicknesses of the multi-leaf walls; (ii) calibration of realistic elastic

and strength parameters for both brickwork faces and ARC core; and (iii) verification of structural continuity across different construction phases.

A detailed mapping of investigation areas and exact test locations (NDT, MDT, DT) is reported in Appendix B. The following sections summarize the main outcomes of the 2023 diagnostic campaign.

V.3 Non-Destructive Tests (NDT)

V.3.1 Ultrasonic pulse velocity tests

An UPV testing campaign was carried out on selected masonry portions of St. Peter's Basilica in order to assess the internal quality of the material and to derive indicative values of the dynamic elastic modulus, in accordance with [11, 16].

The investigations focused on areas where sonic tests were combined with double flat-jack tests (see Section V.4.2), namely in the Atrium, along the First and Second Corridors, and within the Third Corridor (Grotticelle), so as to enable a direct comparison between dynamic and static elastic modulus [15].

Ultrasonic measurements were performed in direct transmission using a digital ultrasonic device equipped with 55 kHz piezoelectric transducers, positioned on both faces of the wall within the same regions investigated by MDT. For each chosen area, after removal of the plaster layer (typically 80×100 cm), a regular grid of measuring points at 10 cm spacing was traced. Multiple transmitter–receiver paths were acquired along vertical alignments to reconstruct P-wave travel times across the thickness (see Figure V.3).

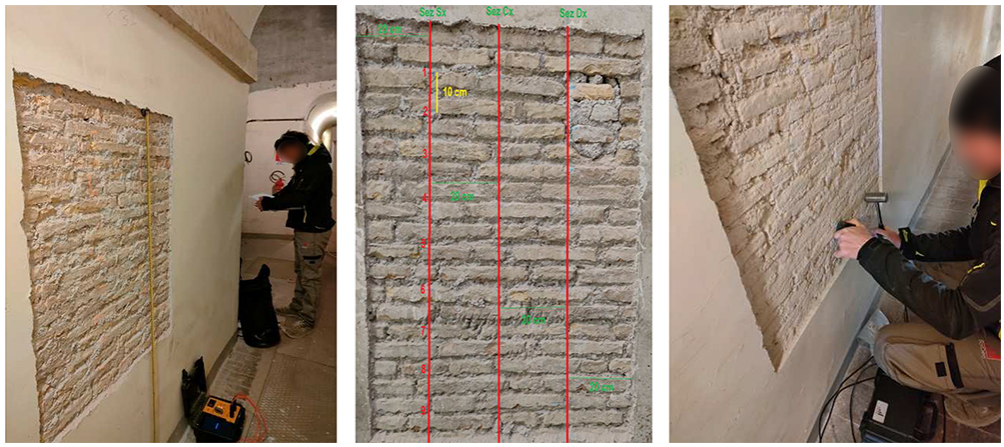

Figure V.3: Example of UPV investigation area and acquisition phase inside St. Peter's Basilica.

First-arrival times were processed to obtain apparent P-wave velocities V_p, and velocity maps were constructed to visualize the ultrasonic velocity distribution along each section. In the adopted configuration, the test is mainly sensitive to the outer leaf and explores an effective investigation depth of about 25 cm in the multi-leaf wall (see Figure V.4).

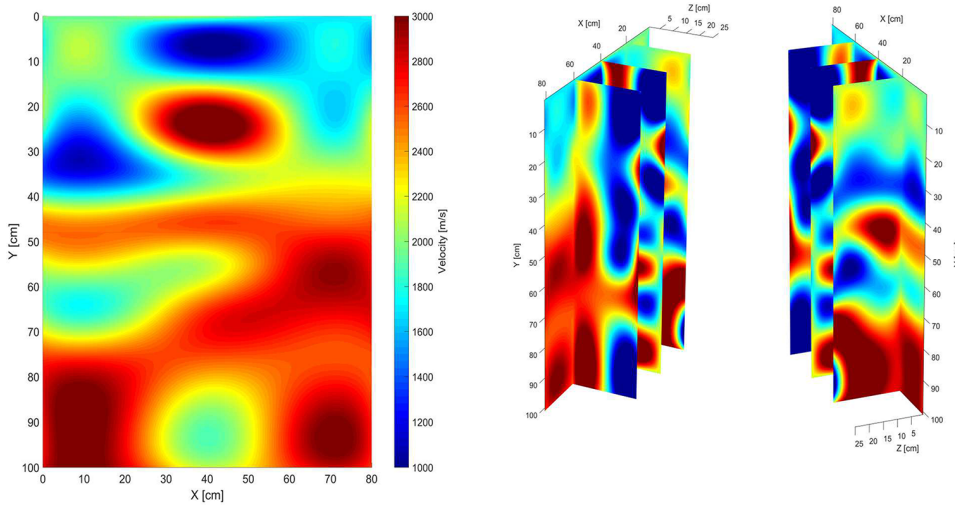

Figure V.4: Example of ultrasonic velocity distribution along investigated paths inside St. Peter's Basilica.

The measured velocities exhibit a heterogeneous but coherent pattern, with most values in the range of approximately 1,000–3,000 m/s, depending on the location. This variability reflects the complex multi-leaf nature of the masonry (brick units, thick mortar joints, rubble infill, local voids) and the presence of interfaces or slightly altered surface layers. Higher velocities correspond to more compact and continuous paths, whereas local reductions in V_p suggest increased porosity, weaker mortar or internal discontinuities.

The polar diagram in Figure V.5 synthesizes the mean ultrasonic velocities at sections P4–P39 (coinciding with flat-jack locations), highlighting the spatial variability of the material and confirming the absence of extensive through-thickness degradation in the investigated areas.

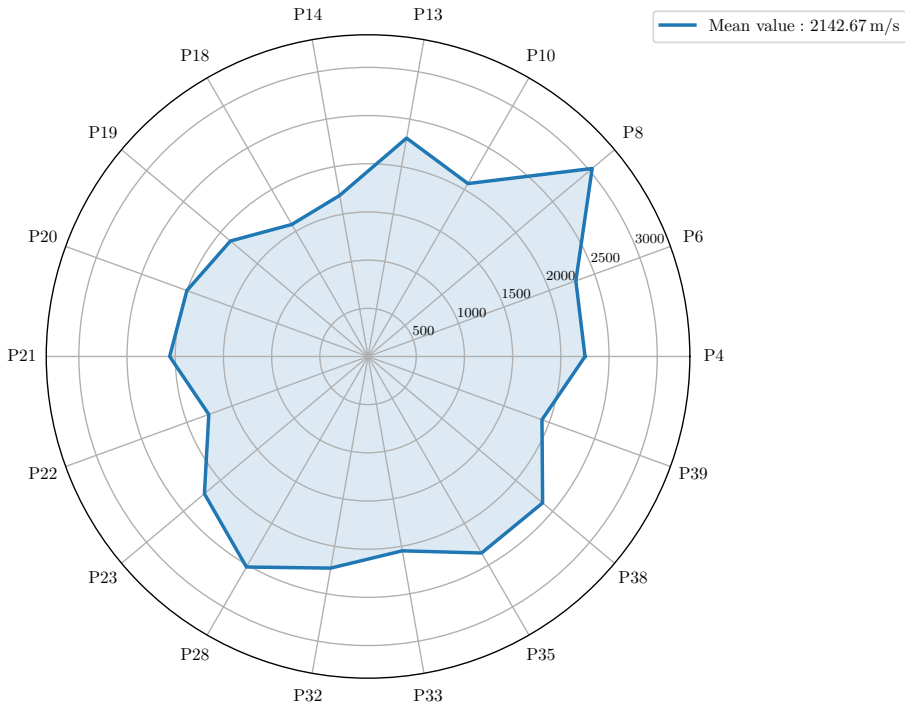

Figure V.5: Polar distribution of UPV (m/s) measured at the same locations as the double flat-jack tests in St. Peter's Basilica.

Following the standard elastic-wave formulation for homogeneous materials [3], the dynamic Young's modulus can be estimated from the measured P-wave velocities as

$$E_{\text{dyn}} = \rho V_p^2 \frac{(1+\nu)(1-2\nu)}{1-\nu} \tag{V.1}$$

where ρ is the masonry unit weight (assumed equal to 18 kN/m^3), V_p is the mean ultrasonic velocity along the investigated paths (2,142.67 m/s), and ν is an effective Poisson's ratio (0.20). Substituting the experimentally obtained values into Eq. (V.1) provides an estimated average dynamic modulus of elasticity $E_{\text{dyn}} \approx 7,600$ MPa.

Comparison with the mean static elastic modulus $E_{\text{stat}} = 801$ MPa obtained from double flat-jack tests (see Section V.4.2) highlights a systematic discrepancy:

$$\frac{E_{\text{dyn}}}{E_{\text{stat}}} \approx 9.5$$

This behavior is consistent with observations reported in [4] for *Opus Incertum* masonry, where Eq. (V.1) led to dynamic moduli up to one order of magnitude larger than static values from compression tests. Relationships calibrated for homogeneous materials

are therefore not directly applicable for deriving the Elastic modulus of heterogeneous rubble or multi-leaf masonry.

In the present study, ultrasonic tests are used primarily to detect relative variations in stiffness and to identify anomalous or degraded zones. The elastic parameters adopted in the global 3D FE model are based mainly on MDT, while ultrasonic data support the mapping of material quality and the interpretation of masonry heterogeneity.

V.3.2 Dynamic tests and identification of the global dynamic behavior

An ambient vibration monitoring campaign was carried out in July 2023 on St. Peter's Basilica to characterize the dynamic behavior of the 17th-century body and Façade and to detect possible discontinuities between the 16th- and 17th-century portions [9]. The monitoring system consisted of a temporary network of high-sensitivity piezoelectric accelerometers installed along the First, Second and Third Corridors (Grotticelle) and on the Façade body (see Figure V.6), providing synchronous measurements in selected horizontal and vertical directions under architectural and operational constraints. Table V.1 summarizes the measurement nodes and monitored directions.

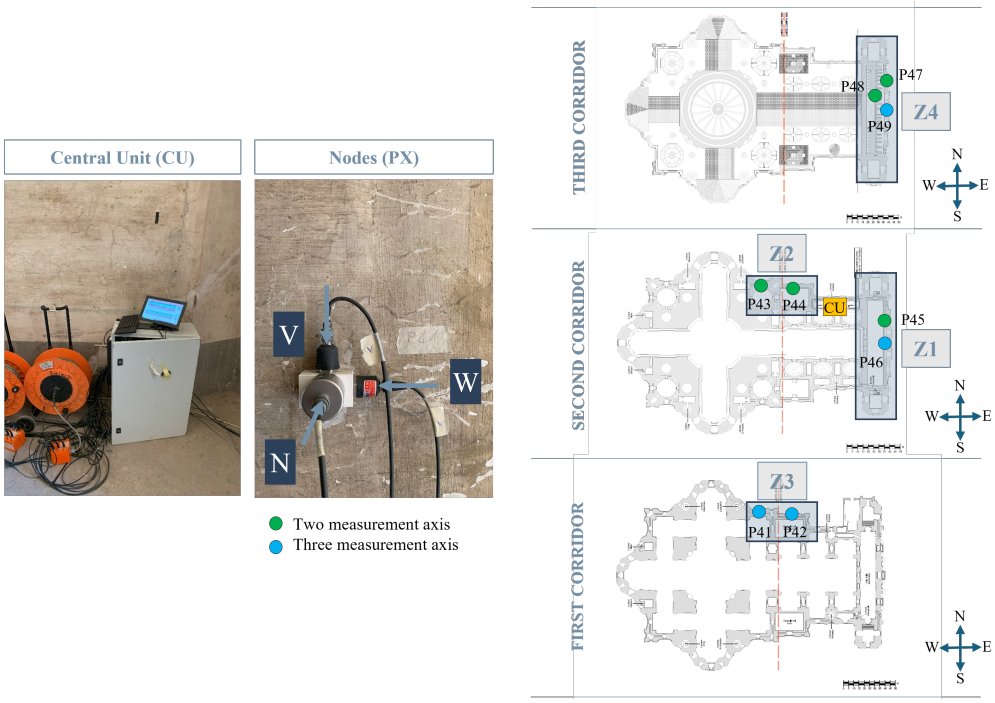

Figure V.6: Investigated areas and temporary accelerometer layout adopted for the ambient vibration tests on St. Peter's Basilica (July 2023).

Table V.1: Measurement nodes, installation positions and monitoring directions in the dynamic tests.

Measurement node	Installation level – Position	Monitoring directions
P41	First Corridor / 16th-century body	North, West, Vertical
P42	First Corridor / 17th-century body	North, West, Vertical
P43	Second Corridor / 16th-century body	North, West
P44	Second Corridor / 17th-century body	North, West, Vertical
P45	Second Corridor / Façade	North, East
P46	Second Corridor / Façade	North, East, Vertical
P47	Third Corridor / Grotticelle	North, West
P48	Third Corridor / Grotticelle	North, East
P49	Third Corridor / Grotticelle	North, East, Vertical

Ambient vibrations from environmental and operational sources were recorded over several days; the running Root Mean Square (RMS) acceleration, computed with a 10-minute window for in- and out-of-plane components, is shown in Figure V.7. Measured levels (typically 50–300 μg) confirm the very low vibration state of the monument and indicate no serviceability-related vibration issues in the monitored areas. Cross Spectral Density (CSD) analyses in the 0–12 Hz range identified dominant frequencies and inter-node phase relationships: along the North Wall, across the 16th- and 17th-century sections and corridor levels, responses were nearly in phase in- and out-of-plane, with no appreciable differential motion (see Figure V.8).

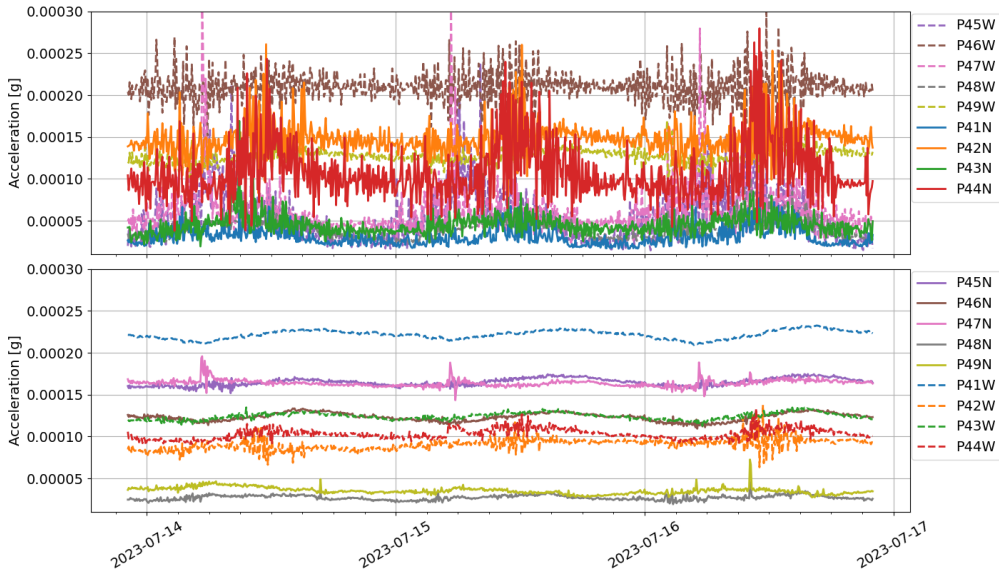

Figure V.7: Running RMS acceleration trends for out-of-plane (top) and in-plane (bottom) components at the North Wall and Façade body.

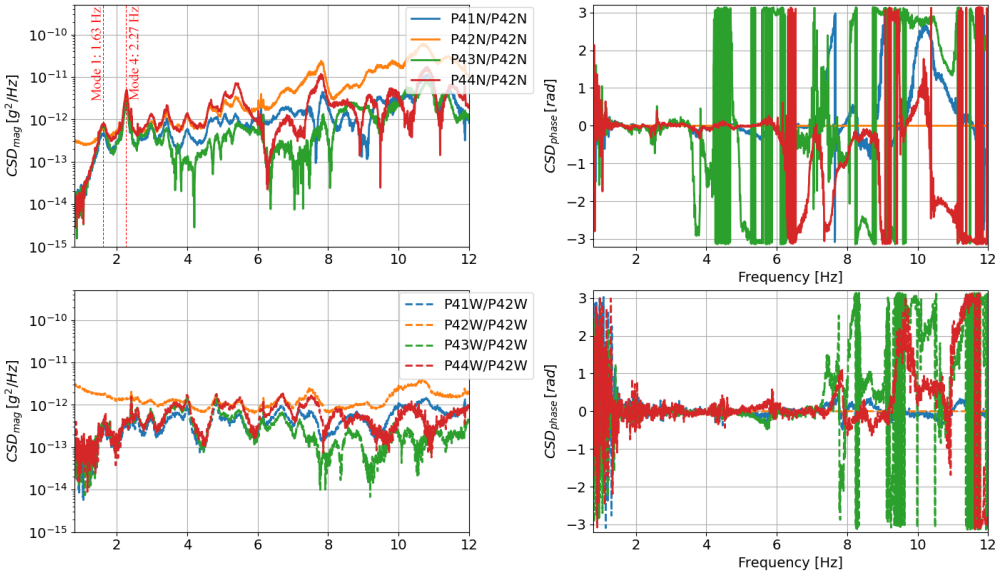

Figure V.8: North Wall: CSD between nodes P41–P44 (ref. P42); out-of-plane (left) and in-plane (right).

A similarly coherent pattern was observed on the Façade: monitored points vibrated almost in phase out of plane, indicating monolithic dynamic behavior of the 17th-century front (see Figure V.9).

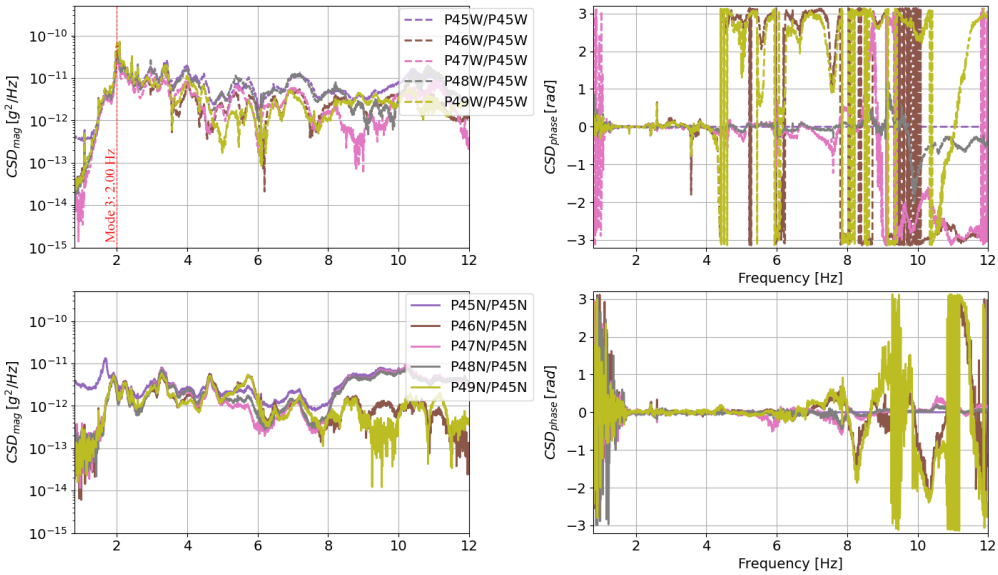

Figure V.9: Façade: CSD between nodes P45–P49 (ref. P45); out-of-plane (left) and in-plane (right).

These results provide experimental evidence of the Basilica's globally coherent dynamic behavior and serve as a reliable reference for future model calibration and the development of long-term monitoring measurements.

V.4 Minor-Destructive Tests (MDT)

V.4.1 Endoscopic investigations

A dedicated endoscopic investigation campaign was carried out to verify the internal stratigraphy of the multi-leaf masonry walls at different levels of St. Peter's Basilica. A total of 42 inspections were performed through pre-drilled boreholes, distributed as:

- 8 investigations along the Atrium;
- 16 investigations along the First Corridor;
- 10 investigations along the Second Corridor;
- 8 investigations along the Third Corridor (Grotticelle).

The endoscopic surveys enabled direct visual inspection of the internal masonry structure, providing qualitative information on the state of conservation, the presence of cavities or discontinuities, and the actual arrangement of the leaves forming the wall thickness. The equipment consisted of a video-endoscopic system with integrated LED illumination connected to a portable computer. The flexible tool was housed in a rigid aluminum tube anchored at the borehole mouth, allowing for secure positioning, regulated research depth, and protection of adjacent surfaces.

For conservation reasons, no water cleaning was allowed inside the boreholes in order to avoid uncontrolled moisture ingress. Despite careful mechanical cleaning with compressed air and brushes, drilling dust locally reduced visibility and, in some cases, limited the precise identification of the binder and fine aggregates.

Basically, the endoscopic campaign confirmed a recurrent multi-leaf configuration: external brickwork leaves, with thickness generally between 120 mm and 500 mm, enclosing an inner core composed of heterogeneous stone and brick fragments embedded in a hydraulic lime-based matrix compatible with ARC, with variable thickness. Table V.2, summarizes the thickness of the stratigraphy investigated.

Table V.2: Summary of endoscopic investigations: borehole geometry and multi-leaf wall thicknesses.

Level	Position id	Hole diameter [mm]	Hole depth [mm]	Inner brickwork masonry [mm]	ARC core [mm]	Outer brickwork masonry [mm]
Atrium	1	100	1,000	300	700	N/A
	1bis	80	3,950	320	3,630	N/A
	2	100	2,500	480	1,720	300
	2a	80	82	480	340	N/A
	2b	80	82	480	340	N/A
	3	100	3,000	400	2,300	300
	3bis	100	2,700	150	2,550	N/A
	4	32	460	460	N/A	N/A
First Corridor	5	32	750	350	400	N/A
	6	32	600	150	450	N/A
	7	32	700	150	550	N/A
	8	32	950	250	700	N/A
	9	32	800	270	530	N/A
	10	32	1,000	130	870	N/A
	11	32	1,000	240	760	N/A
	12	32	850	150	700	N/A
	13	32	1,100	270	830	N/A
	14	32	600	270	330	N/A
	15	32	600	150	450	N/A
	16	32	750	200	550	N/A
	17	32	1,200	300	900	N/A
	18	32	1,100	150	950	N/A
	19	32	1,200	200	950	N/A
	20	32	1,200	250	950	N/A
Second Corridor	21	32	500	150	350	N/A
	22	32	1,200	150	1,050	N/A
	23	32	1,200	250	950	N/A
	25	32	1,200	250	950	N/A
	26	32	1,200	200	1,000	N/A
	28	32	1,150	250	900	N/A
	29	32	1,200	300	900	N/A
	30	32	1,200	500	700	N/A
	31	32	850	180	670	N/A
	32	32	1,200	500	700	N/A
Third Corridor (Grotticelle)	33	32	750	380	370	N/A
	34	32	400	120	280	N/A
	35	32	500	120	380	N/A
	36	32	500	150	350	N/A
	37	32	500	150	350	N/A
	38	32	750	180	570	N/A
	39	32	600	270	330	N/A
	40	32	600	250	350	N/A

N/A = not available (borehole did not reach the corresponding layer).

V.4.2 Flat-jack tests on brickwork masonry

The in-situ deformability and stress–strain response of the historic brickwork masonry were investigated by means of the single and double flat-jack technique, applied to selected wall panels in the Atrium, First and Second Corridors and Grotticelle.

Semi-circular flat-jacks (350 mm × 260 mm × 4 mm) made of 0.8 mm thick steel foils were employed. Figure V.10 illustrates the type of jack used and an example of double flat-jack test execution inside St. Peter's Basilica.

(a) (b)

Figure V.10: (a) Flat-jack used in the in-situ tests; (b) execution of a double flat-jack test in St. Peter's Basilica.

The single flat-jack test is used to estimate the average in-situ compressive stress $\sigma_{\text{in-situ}}$ in the masonry according to the following formulation:

$$\sigma_{\text{in-situ}} = K_m \, K_a \, p_{jack} \tag{V.2}$$

where K_m is the calibration factor (depending on jack stiffness and geometry), K_a is the ratio between the nominal jack area $A_J = 77{,}506$ mm^2 and the cutting area $A_C = 88{,}200$ mm^2, and p_{jack} is the applied jack pressure. The calibration factor provided by the manufacturer was $K_m = 0.925$, in agreement with the independent calibration tests reported in [14].

To evaluate the deformability characteristics, a second parallel cut is made and a second jack is inserted (double flat-jack test). The masonry portion between the cuts acts as a specimen subjected to an almost uniaxial compressive state, while the surrounding masonry behaves as a loading frame. Multiple loading–unloading cycles are applied.

Longitudinal and transverse deformations are measured by a removable mechanical extensometer using three longitudinal bases (1, 2 and 3) of 200 mm and one transverse base (4) of 350 mm. The vertical stress–strain curves reported herein refer to the central longitudinal base (2), which is considered representative (see Figure V.11).

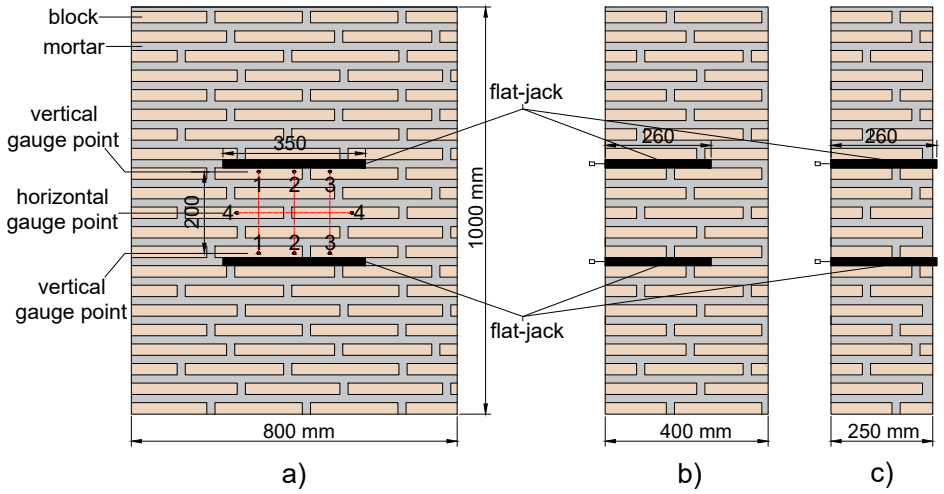

Figure V.11: (a) Geometry of the double flat-jack test and measurement bases; (b)–(c) cross-sections of the main investigated thickness configurations of brickwork masonry panels in St. Peter's Basilica.

The tangent stiffness modulus E_t in a given stress interval is obtained as

$$E_t = \frac{\Delta\sigma_m}{\Delta\varepsilon_m} \tag{V.3}$$

where $\Delta\sigma_m$ is the stress increment and $\Delta\varepsilon_m$ is the corresponding strain increment.

Eighteen double flat-jack tests were performed on brickwork panels at different levels inside St. Peter's Basilica. Table V.3 summarizes the results of the single and double flat-jack tests, where ν is Poisson's ratio, E the elastic modulus and $\sigma_{\text{in situ}}$ the measured normal stress in the panel.

The experimental curves obtained from the double flat-jack tests are shown in Figure V.12. The stress–strain response of the tested panels exhibited peak compressive stress in the range of 2.00–6.50 MPa (during the tests), an average Poisson's ratio of 0.20, and an elastic modulus E ranging from 375 to 1,470 MPa, with an average value of 801 MPa, in line with values reported in the literature for historical brick masonry with thick joints [6].

The primary aim of the tests was the evaluation of the elastic modulus, for which the double flat-jack method is considered reliable within the pre-peak linear range.

Because the process is fundamentally force/pressure-controlled rather than deformation-controlled, it is not possible to reliably capture the post-peak (softening) behavior. Accordingly, the loading was progressively increased beyond the onset of first cracking, up to the development of clearly observable material damage.

Table V.3: Experimental results obtained from single and double flat-jack tests.

Position id	Sample id	ν [–]	E [MPa]	$\sigma_{\text{in situ}}$ [MPa]
P4	0_MPD_02	0.25	850	0.85
P6	1_MPD_03	0.34	380	0.63
P8	1_MPD_04	0.32	720	0.18
P10	1_MPD_05	0.14	895	0.46
P13	1_MPD_07	0.19	1164	1.34
P14	1_MPD_08	0.08	887	0.65
P18	1_MPD_10	0.26	500	0.20
P19	1_MPD_11	0.17	1165	0.68
P20	1_MPD_12	0.11	775	0.00
P21	2_MPD_13	0.18	780	0.77
P22	2_MPD_14	0.30	410	0.04
P23	2_MPD_15	0.17	561	0.41
P28	2_MPD_16	0.09	630	0.45
P32	2_MPD_17	0.11	1470	0.85
P33	3_MPD_18	0.17	690	0.55
P35	3_MPD_19	0.19	1046	0.54
P38	3_MPD_20	0.38	735	0.54
P39	3_MPD_21	0.09	764	0.70
Average value	–	0.20	801	–

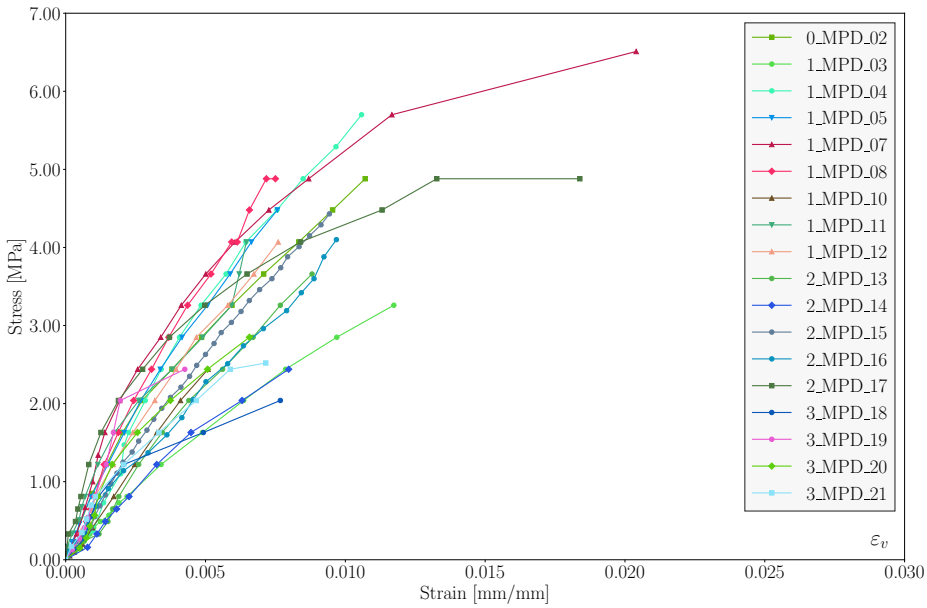

Figure V.12: Double flat-jack tests on brickwork masonry panels: stress–strain curves.

V.5 Destructive Tests (DT) and laboratory testing

V.5.1 Core extractions and laboratory tests on ARC

The mechanical properties of the ARC core were characterized by means of laboratory compression tests on the extracted cores. Core testing provides a direct and reliable estimate of in-situ concrete strength and stiffness and is therefore particularly appropriate to quantify the contribution of the ARC core within the multi-leaf wall system.

During the 2023 campaign, four continuous stratigraphic cores were extracted in the Atrium by diamond core drilling (see Figure V.13). The procedure followed the ASTM recommendations for core sampling [2], with particular attention to the conservation requirements of the monument.

Figure V.13: Stratigraphic core samples extracted in the Atrium of St. Peter's Basilica.

Critical examination of thicknesses in stratigraphic sections, illustrated schematically in Figure V.14, showed that the material inside the outer layers, consisting of the core built with the Roman technique Opus Caementicium, plays a predominant structural role. The concrete nucleus is composed of pozzolanic lime and brick fragments, which significantly increases the wall's compressive strength. Its thickness is greater than that of the adjacent layers, highlighting the important role this material plays in the durability of the walls. Specifically, it is a type of wall panel characterized by the following stratigraphy, typically goes from the interior to the exterior of the wall panel: **(1)** Inner brickwork masonry panel built of brick and mortar elements,

(2a) Internal core built of incoherent ARC, **(2b)** Internal core built of compact ARC, and **(3)** Outer brickwork masonry panel built of brick-and-mortar elements.

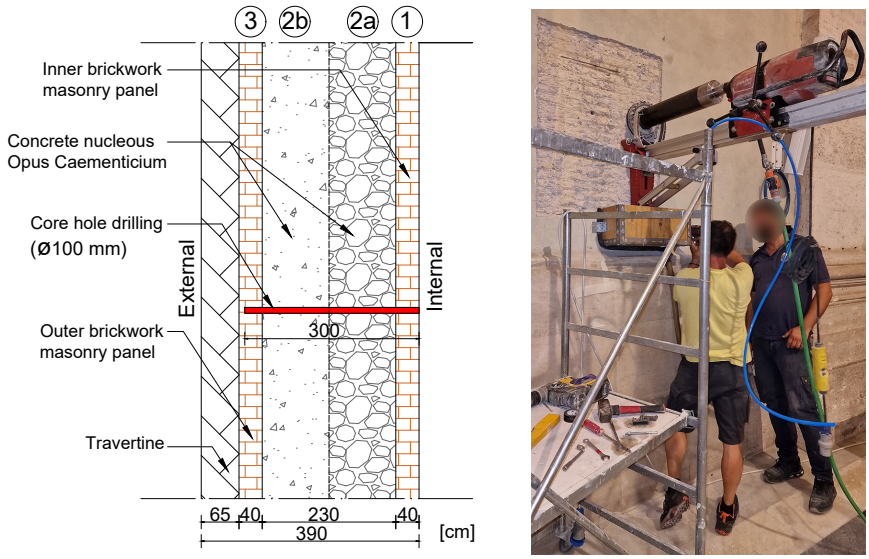

(a) (b)

Figure V.14: (a) Schematic stratigraphy of a multi-leaf wall panel in the Atrium of St. Peter's Basilica; (b) execution of a core drilling test.

Seven cylindrical core specimens were tested in uniaxial compression for strength and three for elastic modulus; the latter had a diameter-to-height ratio of about 1:2 (see Figure V.15).

Figure V.15: Test configuration for determining the elastic modulus of ARC cylindrical specimens with diameter-to-height ratio close to 1:1 (specimen P3-1 ME).

The compressive strength tests were performed on cylindrical specimens with diameter-to-height ratio close to 1:1 (see Figure V.16). The testing procedures were carried out in accordance with the ASTM standards [1].

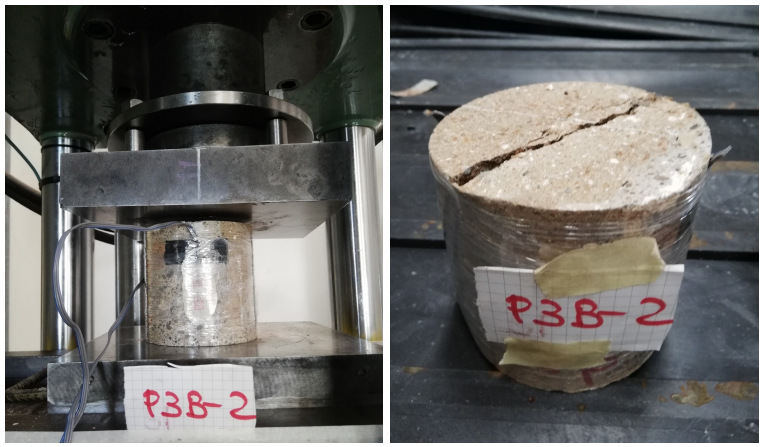

Figure V.16: Test configuration for uniaxial compression on ARC cylindrical specimens with diameter-to-height ratio close to 1:1 (specimen P3B-2 CP).

The experimental results from compression tests are summarized in Tables V.4 and V.5, where D and h are the cylindrical specimen diameter and height, γ is the unit weight, R_c is the cubic compressive strength, f_c is the cylindrical compressive strength.

Table V.4: Compression test results for determining the compressive strength of ARC.

Sample id	D [mm]	h [mm]	γ [kN/m^3]	R_c [MPa]	f_c [MPa]
P2-2 CP	96.00	96.00	15.40	8.00	6.64
P3-3 CP	96.00	96.00	15.60	8.50	7.06
P3-4 CP	96.00	96.00	16.10	7.90	6.56
P3B-1 CP	97.00	98.00	16.20	9.80	8.13
P3B-2 CP	96.00	96.00	17.55	8.20	6.80
P3B-3 CP	96.00	96.00	15.10	7.90	6.56
P3B-4 CP	97.00	96.00	15.40	10.20	8.47
Average value	96.14	96.43	15.95	8.64	7.17

Table V.5: Compression test results for determining the elastic modulus of ARC.

Sample id	D [mm]	h [mm]	γ [kN/m^3]	f_c [MPa]	E [MPa]
P2-1 ME	96.00	200.00	15.80	8.50	6,900
P3-1 ME	96.00	202.00	15.30	6.00	5,800
P3-2 ME	96.00	194.00	16.40	12.20	5,000
Average value	96.00	198.67	15.87	8.90	5,900

On average, the ARC exhibits a cylinder compressive strength of about 8.00 MPa and an elastic modulus of about 5,900 MPa. The corresponding stress–strain curves obtained up to failure are reported in Figure V.17.

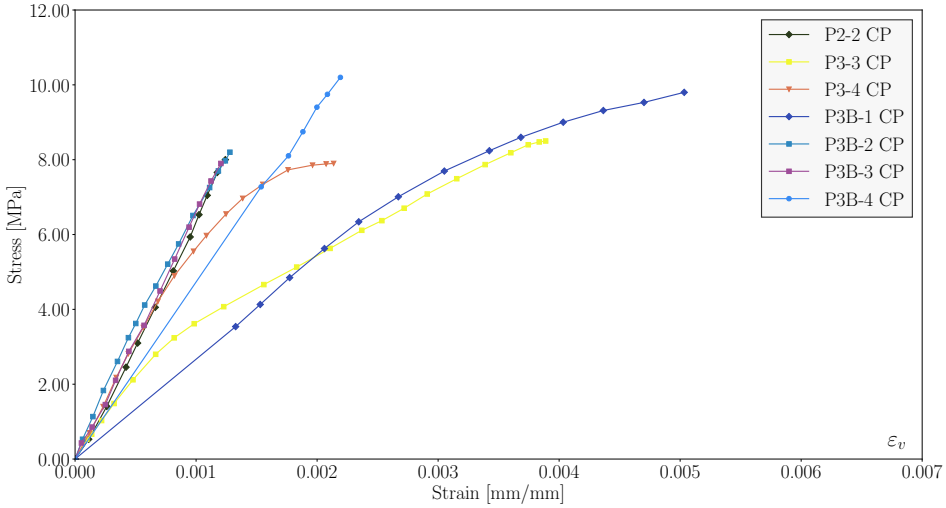

Figure V.17: ARC core compression tests on cylindrical specimens with diameter-to-height ratio close to 1:1: stress–strain curves.

V.6 Discussion of the results and limitations

The NDT, MDT, and DT provide a coherent picture of the masonry system of St. Peter's Basilica and support the definition of material parameters for next constitutive models. However, each test method has limitations and sources of uncertainty that must be considered when transferring the results to the element or global structure scale.

Endoscopic surveys and core stratigraphies confirm that the investigated walls can be idealized as multi-leaf systems, consisting of: (i) external brickwork masonry leaves with an average elastic modulus of about 800 MPa and a Poisson's ratio of 0.20, as derived from double flat-jack tests; and (ii) an inner ARC core with average compressive strength of about 8.0 MPa and an elastic modulus of about 5,900 MPa, as obtained from laboratory tests on cylindrical specimens.

Double flat-jack tests properly evaluate the deformability of brickwork leaves, but do not directly estimate compressive strength. Empirical correlations between elastic modulus and compressive strength can be utilized to estimate the latter for external brickwork masonry. However, the associated variability must be considered. The mechanical characteristics obtained through ARC core testing always reflect sampling

effects, local heterogeneity, and drilling-induced perturbation. Therefore, they should be considered typical of the tested areas rather than the entire Basilica.

Sonic pulse velocity measurements can detect potential local anomalies but do not reveal significant through-thickness degradation in the investigated areas. They are mainly sensitive to the elastic response and to the quality of the transmission path and therefore cannot provide a direct estimate of strength and deformability properties.

Ambient vibration measurements indicate a globally coherent dynamic behavior of the 17th-century body and the main Façade, supporting the calibration of the global 3D FE model. Their interpretation, however, is constrained by the limited number of instrumented points.

The experimental campaign characterizes the multi-leaf masonry and its components accurately but within local limitations. The mechanical parameters, their uncertainties, and spatial variability highlighted the need for homogenization procedures and probabilistic material characterization when assessing St. Peter's Basilica beyond material tests. These issues are discussed in the next chapters.

V.7 References

[1] ASTM (2010). C39, standard test method for compressive strength of cylindrical concrete specimens. *ASTM C39*.

[2] ASTM (2020). C42, standard test method for obtaining and testing drilled cores and sawed beams of concrete.

[3] ASTM (2022). C597, standard test method for pulse velocity through concrete.

[4] Autiero, F., De Martino, G., Di Ludovico, M., Prota, A., et al. (2021). Non-destructive and destructive tests on opus incertum masonry panels. In *Eccomas Proceedia COMPDYN 2021*, volume 2021, pages 231–243.

[5] Binda, L., Pina-Henriques, J., Anzani, A., Fontana, A., and Lourenço, P. B. (2006). A contribution for the understanding of load-transfer mechanisms in multi-leaf masonry walls: Testing and modelling. *Engineering Structures*, 28(8):1132–1148.

[6] Binda, L., Tedeschi, C., and Baronio, G. (1970). Influence of thick mortar joints on the early and late mechanical behaviour of byzantine constructions. *WIT Transactions on The Built Environment*, 42.

[7] Binda, L., Tedeschi, C., and Baronio, G. (1999). Mechanical behaviour at different ages, of masonry prisms with thick mortar joints reproducing a byzantine

masonry. In *Proceedings of international conference 8NAMC-North American Masonry Conference, Austin, USA*, pages 382–392.

[8] Brune, P. and Perucchio, R. (2012). Roman concrete vaulting in the great hall of trajan's markets: Structural evaluation. *Journal of Architectural Engineering*, 18(4):332–340.

[9] Darò, P., Iacussi, L., Turrisi, S., Rusticano, G., Chiariotti, P., Zappa, E., Cigada, A., and Mancini, G. (2025). Dynamic characterization of monumental building for shm purpose: The case of the papal basilica of st peter. In *International Conference on Experimental Vibration Analysis for Civil Engineering Structures*, pages 84–93. Springer.

[10] Demir, C. and Ilki, A. (2014). Characterization of the materials used in the multi-leaf masonry walls of monumental structures in istanbul, turkey. *Construction and building materials*, 64:398–413.

[11] EN 12504-4:2004 (2004). Testing concrete in structures – part 4: Determination of ultrasonic pulse velocity. *European Committee for Standardization*.

[12] Giavarini, C., Ferretti, A. S., and Santarelli, M. L. (2006). Mechanical behaviour and properties: Mechanical characteristics of roman "opus caementicium". In *Fracture and Failure of Natural Building Stones: Applications in the Restoration of Ancient Monuments*, pages 107–120. Springer.

[13] Ignatakis, C. and Zygomalas, M. (1998). Mechanical behaviour of thick mortar joints under compression: Experimental and analytical evaluation. In *Computer Methods in Structural Masonry-4: Fourth International Symposium*, volume 4, page 261. CRC Press.

[14] La Mendola, L., Lo Giudice, E., and Minafò, G. (2019). Experimental calibration of flat jacks for in-situ testing of masonry. *International Journal of Architectural Heritage*, 13(5):619–629.

[15] Makoond, N., Cabané, A., Pelà, L., and Molins, C. (2020). Relationship between the static and dynamic elastic modulus of brick masonry constituents. *Construction and Building Materials*, 259:120386.

[16] RILEM TC 127-MS (2001). MS.D1: Measurement of mechanical pulse velocity for masonry. *Materials and Structures*, 34(238):134–143.

[17] Rusticano, G., Daró, P., and La Mendola, L. (2024). Material characterization of multi-leaf masonry walls in historical buildings: Non-linear fem approach. In *International Brick and Block Masonry Conference*, pages 137–154. Springer.

[18] Seymour, L. M., Maragh, J., Sabatini, P., Di Tommaso, M., Weaver, J. C., and Masic, A. (2023). Hot mixing: Mechanistic insights into the durability of ancient roman concrete. *Science Advances*, 9(1):eadd1602.

[19] Stefanidou, M., Papayianni, I., and Pachta, V. (2015). Analysis and characterization of roman and byzantine fired bricks from greece. *Materials and Structures*, 48:2251–2260.

[20] Vola, G., Gotti, E., Brandon, C., Oleson, J. P., and Holfelder, R. L. (2011). Chemical, mineralogical and petrographic characterization of roman ancient hydraulic concretes cores from santa liberata, italy, and caesareapalestinae, israel. *Periodico di mineralogia*, 80(2).

CHAPTER VI

Deterministic material characterization: Drucker–Prager model

---

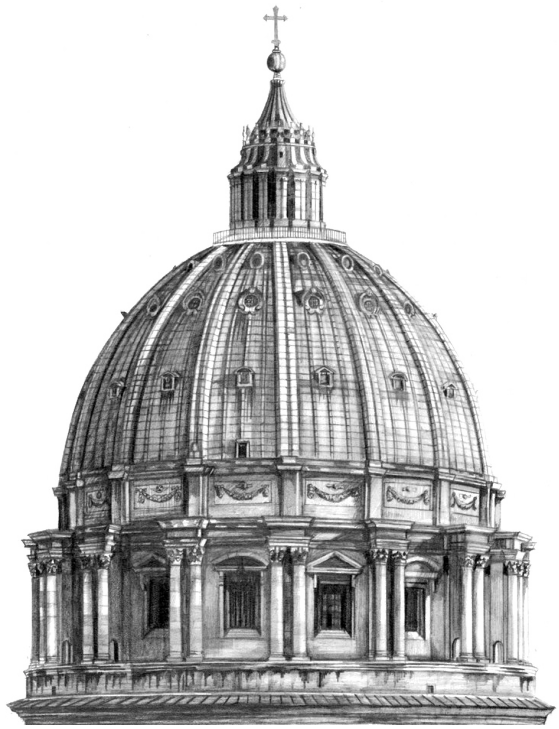

"Il miglior artista non ha alcun concetto che un singolo blocco di marmo non contenga già in sé."

("The best artist has no concept which a single block of marble does not contain.")

– Michelangelo Buonarroti

Partly redrafted after *"Homogenization Techniques for Multi-leaf Masonry Wall Analysis: FEM Strategies for Historical Structures."* G. Rusticano, P. Daró, & L. La Mendola. In International Brick and Block Masonry Conference (2024, July) [16].

VI.1 Introduction

This chapter aims to derive deterministic mechanical characteristics for the multi-leaf masonry walls of St. Peter's Basilica and homogenize them into an equivalent single-layer material for global NLFEAs [5, 20, 21].

The D-P failure criterion model is used to simulate the behavior of materials under multi-axial stress states and provide a description that is compatible with frictional, quasi-cohesive geomaterials like brick masonry and ARC. The D-P failure criterion, first introduced in 1952 as a smooth approximation of the Mohr-Coulomb envelope, has evolved for concrete and masonry [3, 14]. In this work, a non-associated D-P model is used, in which the dilation angle ψ is introduced in addition to cohesion c, friction angle ϕ and Young's modulus E [10].

The calibration of this model is based on two experimental configurations: (i) double flat-jack testing on brickwork masonry wall and (ii) compression tests on cylindrical ARC specimens. Specific FE models are developed for each configuration, and Non-Linear Static Analyses (NLSAs) are performed in MIDAS FEA NX using a macro-modeling approach to reproduce the structural behavior of the Basilica's historical materials [11, 25]. The masonry is modeled as a homogeneous, isotropic continuum with non-linear behavior, sacrificing local detail for robustness and computational efficiency. This approach aligns with previous literature research on historic masonry structures [6, 9, 12].

First, a possible set of D-P parameters of the external brickwork leaves are calibrated by reproducing the in-situ double flat-jack tests and iteratively matching the numerical stress–strain curve of a 3D FE masonry wall to a representative experimental curve. Then, an analogous calibration procedure is applied to the ARC core by means of 3D FE simulations of compression tests on cylindrical specimens, resulting in similar D-P parameters for the core material.

Finally, the calibrated material models are used in 3D FE simulations of multi-leaf wall panels under uniaxial compression and combined shear–axial load condition [4, 23]. These studies reduce the computational effort by homogenizing multi-layer walls into an equivalent single-layer material, minimizing the FE in the global 3D model [1, 19].

VI.2 3D FE simulation of double flat-jack tests on brickwork masonry walls

The MDT that used double flat-jacks were performed to assess the local stress-strain response of the brick-and-mortar leaves on the two external leaves of St. Peter's Basilica. On the basis of a representative masonry wall, the monotonic uniaxial loading branch of the stress-strain curve was reconstructed, allowing an estimate of the local modulus of elasticity and Poisson's ratio. Figure VI.1(a)–(b) shows a schematic representation of the 3D FE model used to simulate the in-situ test.

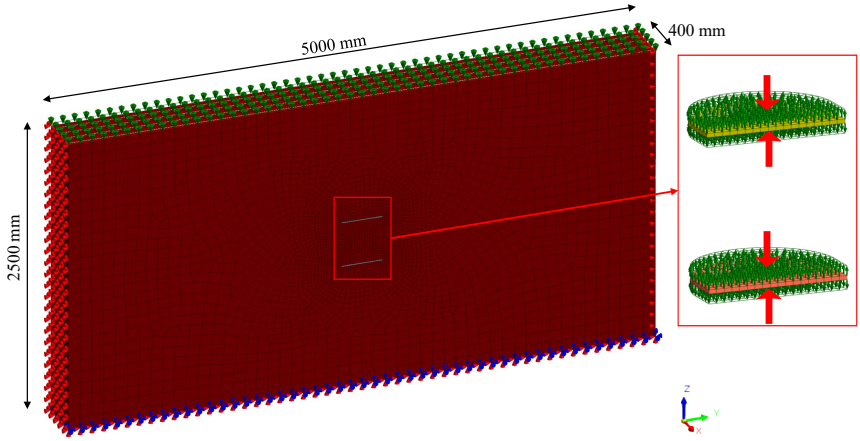

(a)

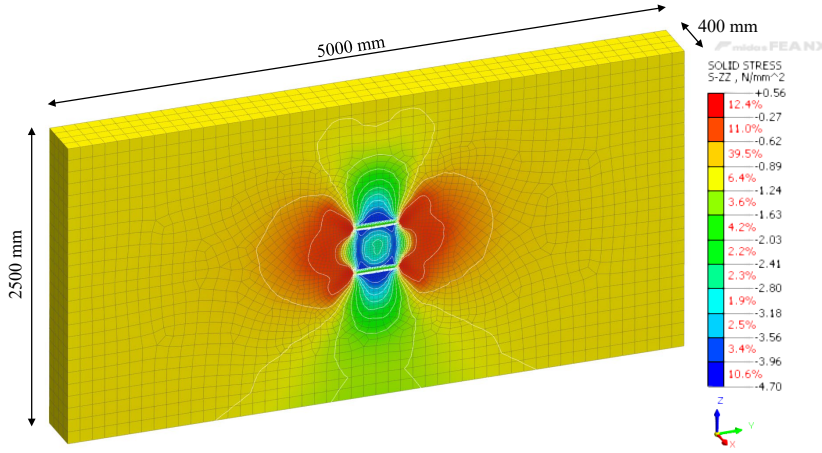

(b)

Figure VI.1: Schematic 3D FE model of brickwork masonry panel: (a) Application load and boundary constraints; (b) Stress distribution σ_{zz} during the final step when vertical incremental pressure is applied.

The experimental curves in Figure VI.2 and reported in Section V.4.2 of the previous chapter show the variability of the in-situ double flat-jack tests within the investigated range. From this set of data, a representative curve (0_MPD_02) was chosen and highlighted in the figure; It shows a global picture of the average behavior of the brickwork leaf under vertical compressive stress.

To determine the mean parameters associated with the adopted failure criterion (D-P elasto-plastic model) and describing the non-linear response of the brickwork, numerical simulations were performed on a portion of masonry extracted from the global FE model of the Basilica. These simulations were set up to replicate, in a numerical environment, the stress path induced by the double flat-jack tests [2, 22].

The 3D NLFE model of the wall panel, with dimensions of 5.0 m in height, 2.5 m in length, and 0.40 m in thickness, was developed in FE software and discretized using 20,172 four-node hexahedral FE with an average structured mesh size of 100 mm. The base of the wall was fixed, whereas the lateral faces orthogonal to the Y-axis were constrained in the horizontal direction in order to reproduce the in-situ boundary conditions.

In the NLSAs, an imposed compression of 0.85 MPa was applied to the top face of the wall to reproduce the in-situ vertical stress measured with single flat-jack tests (see ID 0_MPD_02 in Table V.3) in the examined area. Subsequently, gradually increasing pressures were applied to the faces representing the double flat-jacks, modeled as highly deformable thin steel plates, in order to reproduce the loading sequence of the field tests.

The results of the double flat-jack tests allowed us to determine the local deformability features of the tested brickwork panels, as well as their stress-strain response to be estimated. By analyzing the mechanical properties reported in Table V.3, an average value of $\nu = 0.20$ was obtained, while E ranges from 380 to 1,470 MPa, in agreement with values reported in the literature for historic brick masonry with thick mortar joints [2, 7]. In Figure VI.2, the experimental curves obtained from the in-situ double flat-jack tests on the examined walls, whose values are summarized in Table V.3, represent the stress–strain response of the brickwork. Each test, organized according to its location inside the Basilica, is characterized by a curve with peak stresses between 2.00 and 6.50 MPa, with an average peak stress of around 4.00 MPa and vertical strains ε_v ranging from 8‰ to roughly 2%. These results are equivalent to those obtained for masonry with similar geometric properties (e.g., masonry with very thick mortar joints).

It is important to highlight that double flat-jack tests are primarily reliable for determining the in-situ deformability properties of the brickwork leaves (elastic modulus and Poisson's ratio), whereas their use for estimating compressive strength is more

indirect and affected by larger uncertainty [15, 18]. For this reason, in the present work the flat-jack results are mainly used to calibrate the stiffness parameters, while an estimate of the masonry compressive strength is obtained in Chapter VII through an empirical linear correlation between elastic modulus and compressive strength, following approaches proposed in recent studies on brick and block masonry [13].

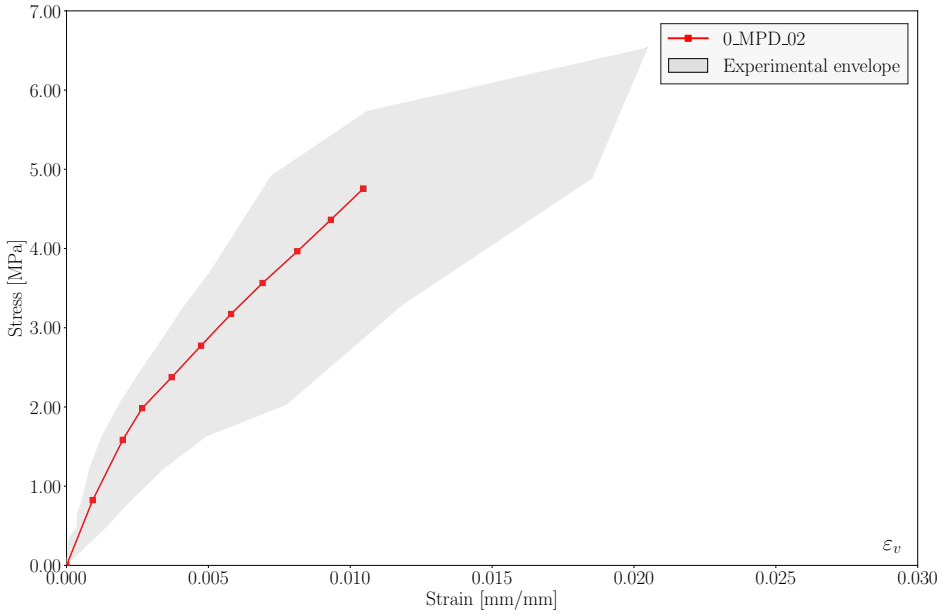

Figure VI.2: Double flat-jack tests on brickwork masonry panels: envelope of the experimental stress–strain curves and the corresponding representative curve.

Figure VI.3 shows the outcome of the calibration process of the D–P parameters for the brickwork material. For each trial set of c, ϕ and ψ, combined with a trial value of the elastic modulus E, a NLFE simulation of the flat-jack test was performed, and the resulting numerical stress–strain curve was compared with the representative experimental curve (0_MPD_02). Specifically, the sensitivity of the numerical response to each parameter is illustrated in Figures VI.3(a)–(c), while Figure VI.3(d) reports the best-fit numerical curve.

It is worth noting that this calibration procedure does not lead to a unique identification of the three constitutive parameters. Different combinations of these parameters, together with appropriate values of E, may result in a comparable reproduction of the experimental stress–strain response. Therefore, the parameter set reported herein should be regarded as one of several possible solutions capable of reproducing the observed experimental behavior, rather than as a uniquely determined material characterization.

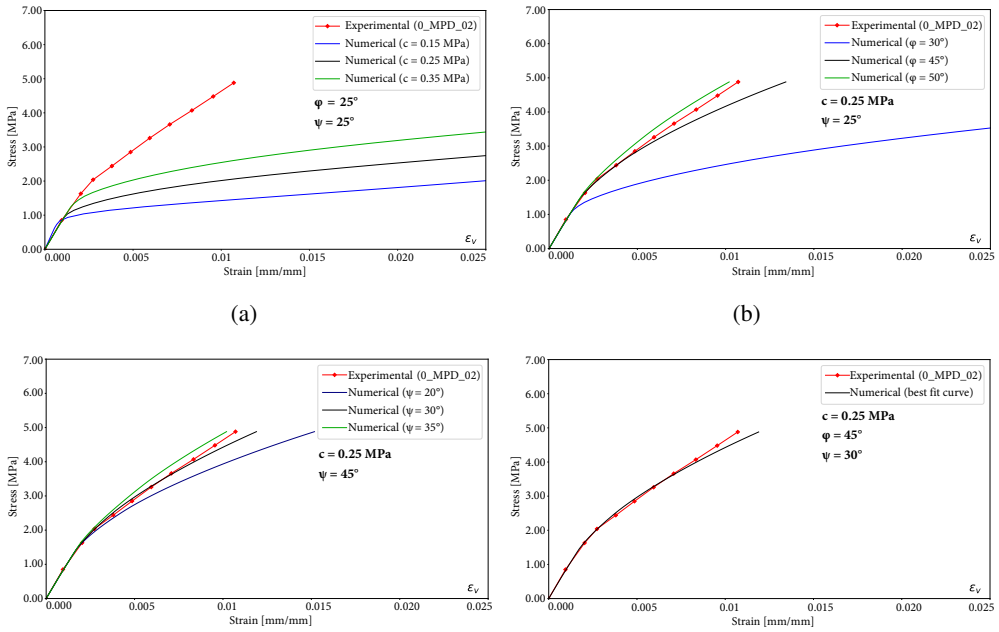

Figure VI.3: Sensitivity analyses for calibrating D-P parameters on double flat-jack numerical simulations of brickwork masonry panel: (a) Variation in c; (b) Variation in ϕ; (c) Variation in ψ; (d) Best-fit curve.

Accordingly, the agreement between experimental and numerical stress–strain curves was quantified by means of an iterative fitting procedure, in which the vector of model parameters θ was obtained by minimizing the Mean Squared Error (MSE), which represents the objective function, between the experimental and numerical stress values evaluated at chosen strain levels [8].

The optimization problem is defined as:

$$\min_{\theta} \mathrm{MSE}(\theta) = \min_{\theta} \left(\frac{1}{N} \sum_{i=1}^{N} \left[\sigma_i^{\mathrm{exp}}(\varepsilon_i) - \sigma_i^{\mathrm{num}}(\varepsilon_i;\theta) \right]^2 \right) \tag{VI.1}$$

where $\sigma_i^{\mathrm{exp}}(\varepsilon_i)$ and $\sigma_i^{\mathrm{num}}(\varepsilon_i;\theta)$ are, respectively, the experimental and numerical stresses at the i-th strain level ε_i, and N is the total number of sampling points considered along the loading branch. The optimal parameter corresponds to the minimum value of $\mathrm{MSE}(\theta)$ in the space of trial parameters.

Using this procedure, the curve that best reproduces the representative experimental curve 0_MPD_02 was obtained by adopting a compressive elastic modulus of the masonry material equal to 850 MPa, a cohesion c equal to 0.25 MPa, a friction angle ϕ

of 45° and a dilation angle ψ of 30°. The stress–strain curve analytically obtained on the basis of these parameters shows a good approximation of the experimental results over the range of interest.

VI.3 3D FE simulation of laboratory compression tests on ARC cylinder specimens

To identify the parameters required to describe the structural behavior of the ARC material observed in the laboratory tests, a dedicated calibration 3D NLFE model was developed. The objective of this model was to reproduce the uniaxial compression tests on cylindrical specimens and to obtain a good fit to the experimental stress–strain curves [17].

Figure VI.4(a)–(b) shows the 3D FE model of the ARC cylindrical specimen, developed in FE software. The model consists of 54,560 four-node hexahedral FE, with an average structured mesh size of 4 mm. The cylindrical specimen, with a diameter of 96 mm and a height of 96 mm, is placed between two steel plates, and a frictional contact is assumed at the interfaces, with a friction coefficient $\mu_c = 0.30$ between ARC and steel. The bottom steel plate is completely constrained at the base. This modeling technique accounts for the confinement effects caused by the specimen's interaction with the testing machine's loading plates.

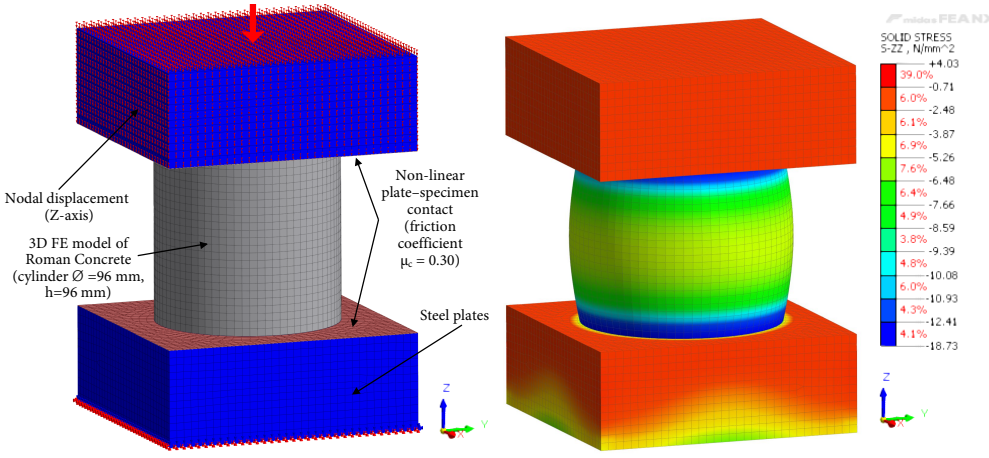

(a) (b)

Figure VI.4: Schematic 3D FE model of cylindrical specimen of ARC: (a) Load and boundary constraints; (b) Stress distribution σ_{zz} during the final step when vertical incremental displacements are applied.

Figure VI.5 shows the envelope of the experimental stress–strain curves obtained from the ARC cylinder compression tests, together with the chosen representative curve (P3-4 CP), which is used as a reference for the numerical calibration.

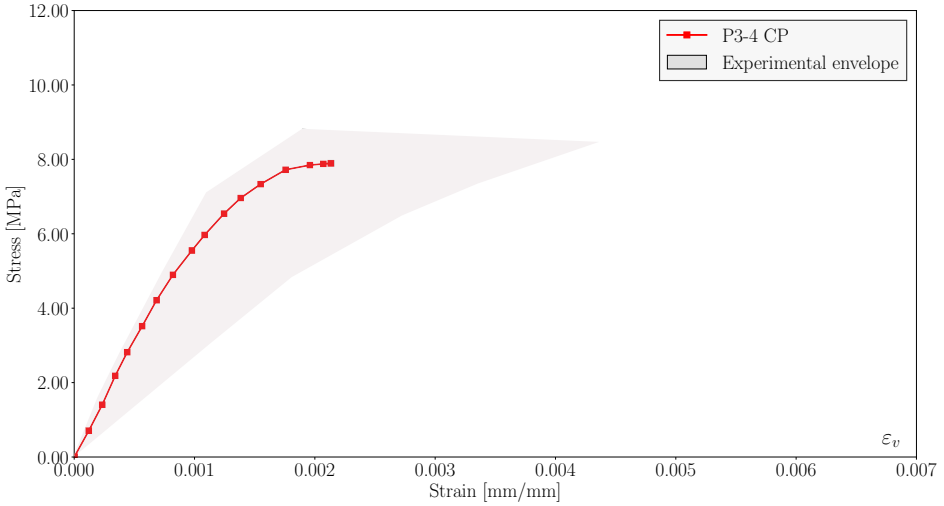

Figure VI.5: ARC core compression tests on cylindrical specimens with diameter-to-height ratio close to 1:1: envelope of the experimental stress–strain curves and the corresponding representative curve.

By analyzing the mechanical properties of the ARC specimens tested in the laboratory and summarized in Table V.5, the elastic modulus E varies between 5,000 and 6,900 MPa, while the compressive strength ranges approximately from 6.00 MPa to 12.20 MPa. As in the case of the brickwork masonry, the numerical curve is calibrated so as to minimize the MSE defined in Eq. (VI.1), which is evaluated between the experimental and numerical compressive stresses at selected strain levels along the monotonic uniaxial loading branch of the P3-4 CP curve.

Specifically, the numerical curve approximates the behavior of the specimens in the range of small and moderate deformations, while it reproduces the average strength of the material at larger strains. The best representation of the variability observed in all tests was achieved by imposing the following set of parameters for ARC: $E = 5,900$ MPa (see the average value in Table V.5), $c = 2.00$ MPa, $\phi = 25°$ and $\psi = 25°$. In the numerical analyses, Poisson's ratio was assumed equal to $\nu = 0.15$. The stress–strain curve obtained on the basis of these parameters provides a good representation of the experimental behavior over the domain of interest.

Figure VI.6(a)–(c) illustrates the sensitivity analyses of the numerical simulations to variations in cohesion, friction angle and dilation angle, as well as the resulting best-fit curve for the representative specimen (see Figure VI.6(d)).

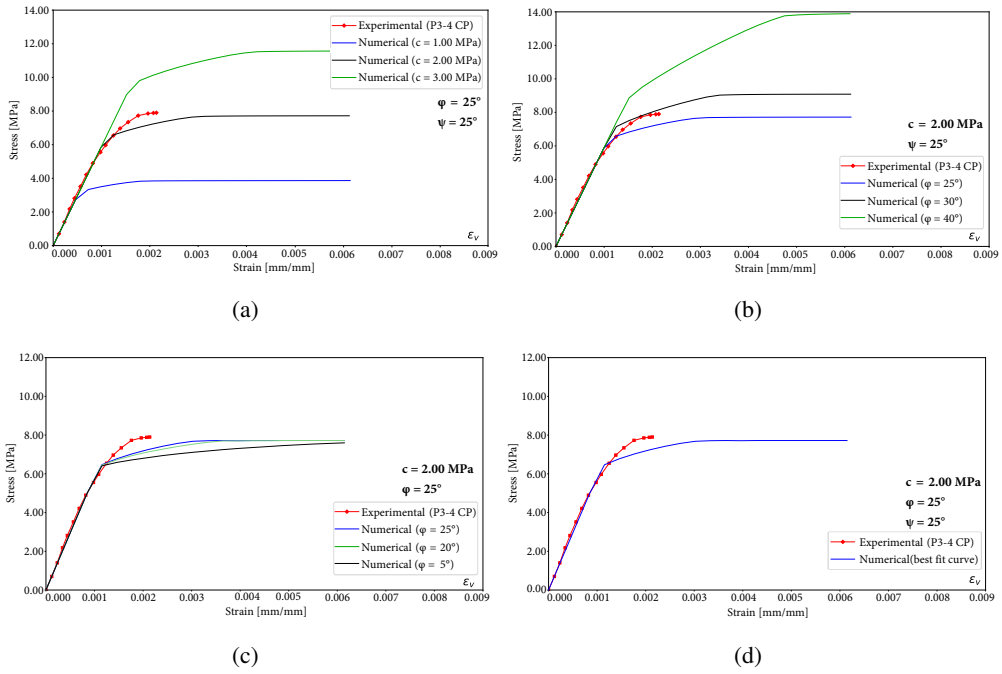

Figure VI.6: Sensitivity analyses for calibrating D–P parameters in the ARC cylinder compression simulations: (a) Variation in c; (b) Variation in ϕ; (c) Variation in ψ; (d) Best-fit curve.

VI.4 Summary of deterministic D-P material parameters

Table VI.1 outlines the mechanical parameters used for the materials in the 3D FE model. Young's modulus, Poisson's ratio, and D-P parameters for brickwork masonry and ARC core were obtained from calibration procedures described in Sections VI.2 and VI.3, based on 3D NLFE simulations of in situ double flat-jack tests and laboratory compression tests on cylindrical ARC specimens, respectively.

The third material, referred to as *incoherent infill*, is added to simulate the presence of a localized weak, weakly bonded material that is recognized by the four core drilling specimens extracted inside the Atrium walls. In the absence of direct experimental data, its mechanical properties were conservatively assumed to represent a very deformable, low-strength material: a low Young's modulus and cohesion were assigned, as well as a relatively high Poisson's ratio, and the friction and dilation angles were chosen to reflect a loose granular infill with limited shear resistance. This conservative assumption reduces the global stiffness and strength of the masonry walls. In this way, the incoherent

infill does not artificially increase the load-bearing capacity of the walls, but its effect on the system's local deformability is still considered.

Table VI.1: Linear elastic and non-linear D-P parameters of the model materials.

	Parameter	Brickwork masonry	ARC core	Incoherent infill
Linear	Young's modulus [MPa]	850	5,900	200*
	Poisson's ratio [-]	0.20	0.15	0.40*
Non-linear	Cohesion [MPa]	0.25	2.00	0.02*
	Friction angle [°]	45	25	35*
	Dilation angle [°]	30	25	15*

* Assumed values to account for very low property values.

The calibrated parameters for brickwork masonry and ARC structural materials, together with the assumed properties of the incoherent infill, provide a deterministic characterization of the materials adopted in the next numerical analyses, as described in Sections VI.5. In particular, these D–P parameters are used as input data to homogenize the multi-leaf walls of St. Peter's Basilica by means of 3D NLFEAs and are intended as preliminary, since the global reliability-based structural assessment of the Basilica is performed adopting the CDP model, with a probabilistic calibration of its parameters.

VI.5 3D FE-based homogenization of multi-leaf masonry walls

VI.5.1 Homogenization under uniaxial compression

Based on the stratigraphies identified within the Basilica, a series of numerical simulations under uniaxial compression were performed in order to calibrate an equivalent single-layer wall panel for homogenization purposes.

Two different configurations were explored. Model A assumes a fully compact inner core of ARC (see Figure VI.7(a)), whereas Model B assumes an inner core composed of 50% compact ARC and 50% incoherent infill material (see Figure VI.7(b)). The 3D FE models represent a multi-leaf wall measuring 9.80 m length, 9.80 m height, and 3.10 m thick.

Endoscopic surveys and core stratigraphies indicated that, at times, the inner core might be substantially heterogeneous, with a compact ARC band adjacent to lower-quality, fragmented material. The lower-bound configuration used here is designed

to replicate the negative local condition and quantify its impact on the homogenized structural behavior.

However, the general information from the diagnostic campaign indicates that these discontinuous or damaged core regions are limited rather than widespread. In the following probabilistic studies and global reliability-based assessment (see Chapters VII and IX), the core will be idealized as fully compact ARC, while the mixed-core configuration discussed in this chapter is primarily used to explore the sensitivity of the homogenized response to local core degradation.

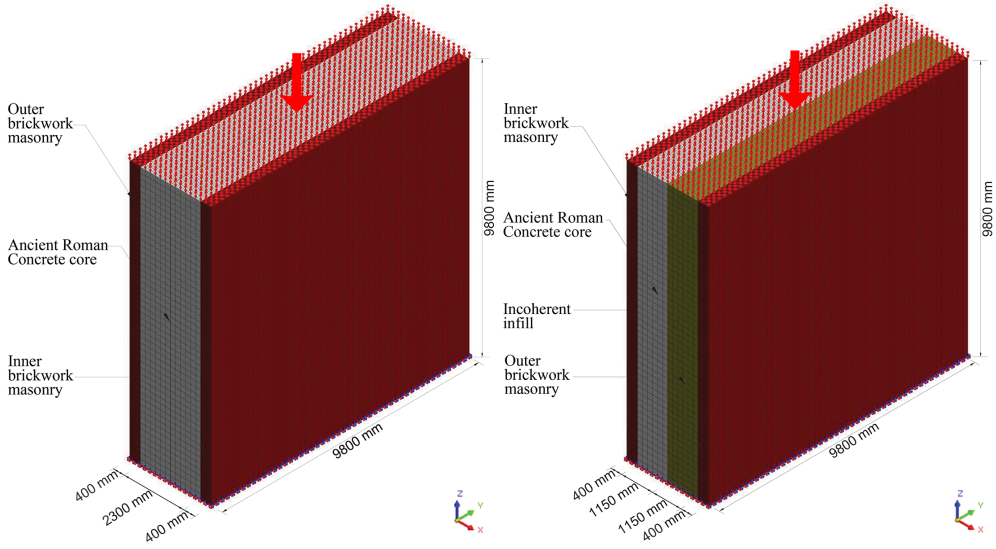

Figure VI.7: Schematic 3D FE model of multi-leaf masonry wall in compression simulation: (a) Multi-leaf masonry panel with 100% compact internal core (Model A); (b) Multi-leaf masonry panel with 50% compact internal core (Model B).

Both 3D FE multi-layer models consists of 38,666 four-node hexahedral FE, with an average structured mesh size of 200 mm. The wall's base is completely constrained, and non-linear frictional contacts exist between the layers' interfaces. Under these assumptions, the top cross-section is free in the vertical plane (with faces orthogonal to the Y-axis). A progressively increasing vertical displacement in the Z-direction is applied to all nodes on the top surface of each layer, simulating a uniaxial compression test at the wall panel scale. The results of these simulations are discussed in Section VI.6.

VI.5.2 Homogenization under in-plane shear condition

In a second stage, the same multi-leaf wall structures were subjected to combined in-plane bending moment and axial load to evaluate the structural behavior of the homogenized material under a different load conditions. The 3D FE models are similar to those used for uniaxial compression simulations, but they have different boundary conditions and load paths.

The Model A configuration assumes a fully compact inner core (see Figure VI.8(a)), whereas the Model B configuration involves an inner core composed of 50% compact ARC and 50% incoherent infill material. The wall dimensions and discretization (9.80 m in length and height, 3.10 m in thick, 38,666 hexahedral elements with an average size of 200 mm) remain unaltered. Both models have fixed constraints at the base.

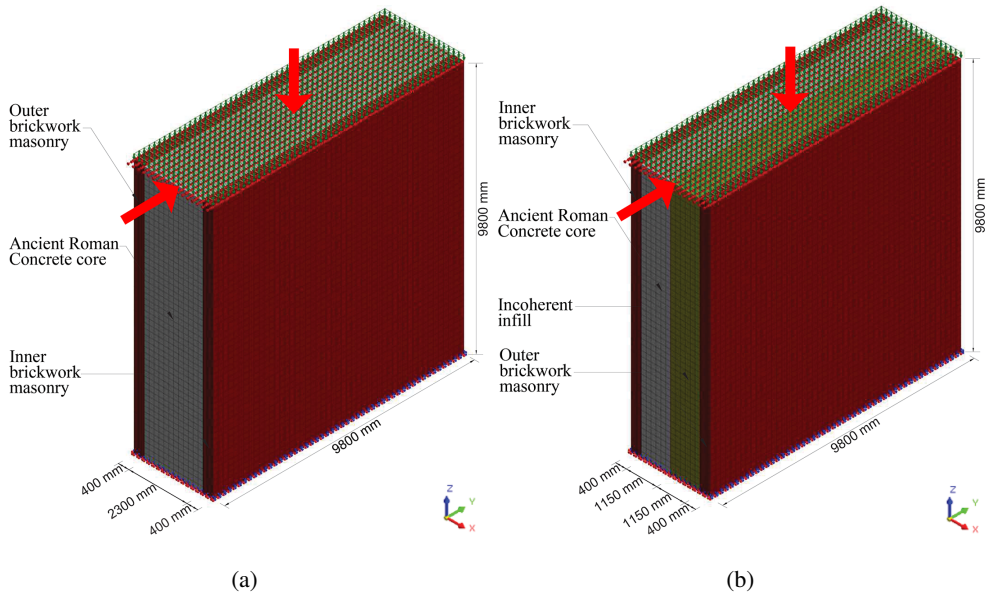

Figure VI.8: Schematic 3D FE model of multi-leaf masonry wall in in-plane shear simulation: (a) Multi-leaf masonry panel with 100% compact inner core (Model A); (b) Multi-leaf masonry panel with 50% compact inner core (Model B).

In the first phase of the NLSAs, a uniform vertical pressure of 0.60 MPa is applied on the top surface of the masonry panel in the Z-direction. This corresponds to the average vertical stress measured by single flat-jack testing in situ. In the second phase, all nodes at the top of the panel are subjected to progressively increasing horizontal displacement in the Y direction, resulting in in-plane shear and bending moment at the base. The resulting base shear and horizontal displacement at a control node at the top of the

panel are measured and compared to those obtained from a single-layer homogenized wall. The simulation results are reported in Section VI.6.

VI.6 Discussion of the results and limitations

This section analyzes and discusses the main conclusions of the numerical simulations reported in Section VI.5, with a focus on the strengths and limits of both the adopted constitutive model and the homogenization approach.

Figure VI.9 shows stress-strain curves generated from uniaxial compression analyses for two multi-leaf configurations. In particular, the study compares elastic modulus and peak stress in a fully compact core (Model A) versus a core with 50% incoherent infill material (Model B). In particular, in the Model A, the stress-strain curves were extracted for each layer across the wall thickness (see Figure VI.9(a)), whereas the corresponding curves for the Model B are illustrated in Figure VI.9(b).

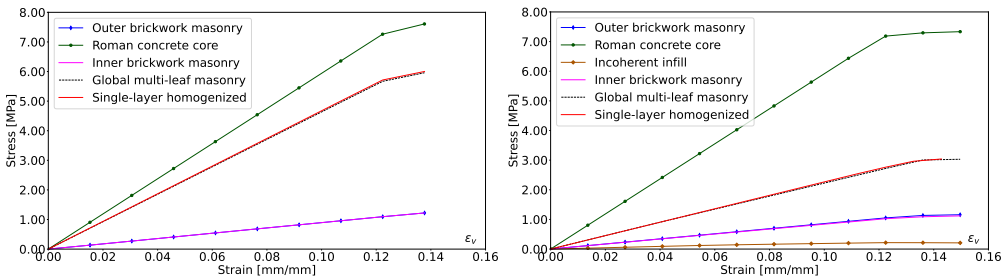

(a) (b)

Figure VI.9: Results of numerical analyses under uniaxial compression: (a) Stress–strain curves for multi-leaf masonry (Model A); (b) Stress–strain curves for multi-leaf masonry (Model B).

Given the variability of the studied stratigraphies and the alternation of zones where the core is either totally made of ARC or partially replaced by lower-quality infill material, a single-layer equivalent panel was calibrated by averaging the structural responses of the two extreme situations. Figure VI.10 shows the intermediate stress-strain curve (red line).

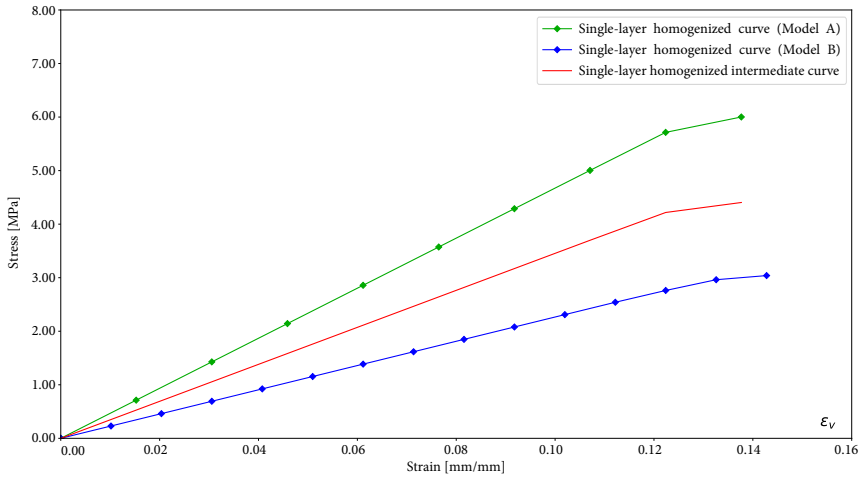

Figure VI.10: Results of numerical analyses under uniaxial compression: stress–strain curves for single-layer homogenized masonry (intermediate curve).

The mechanical properties of this single-layer homogenized material are characterized by the following values: $E = 3{,}400$ MPa, $\nu = 0.20$, $c = 1.20$ MPa, $\phi = 30°$ and $\psi = 30°$. In this configuration, plastic strains were limited to about 0.15% in order to ensure an initial, controlled excursion into the plastic range of the material during calibration.

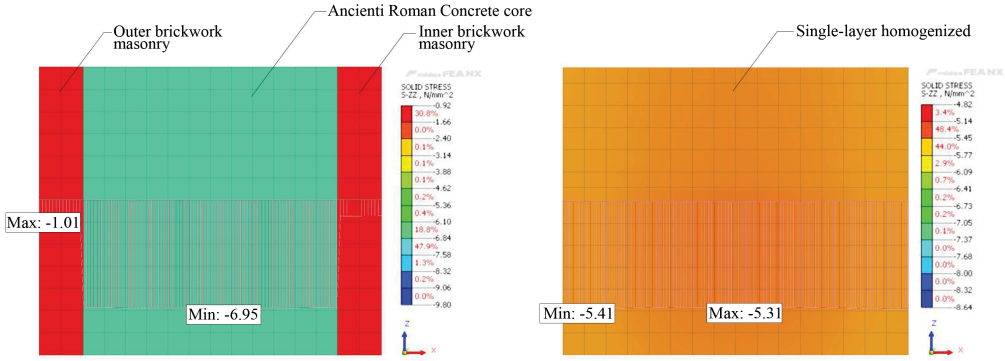

(a) (b)

Figure VI.11: Results of numerical analyses in uniaxial compression: (a) Stress distribution σ_{zz} in multi-leaf masonry wall (Model A); (b) Stress distribution σ_{zz} in single-layer homogenized masonry wall (Model A).

Figure VI.11(a) shows a transverse cross-section of the multilayer wall corresponding to the Model A. The vertical stress distribution σ_{zz} among the different layers clearly indicates that the stiffer inner ARC core attracts higher compressive stresses, whereas

the two external brickwork leaves carry approximately 14% of the total compressive load. This percentage is consistent with the ratio between the elastic moduli of the brickwork masonry and the ARC core. Figure VI.11(b) illustrates the corresponding stress distribution in the equivalent single-layer homogenized wall at the same analysis step.

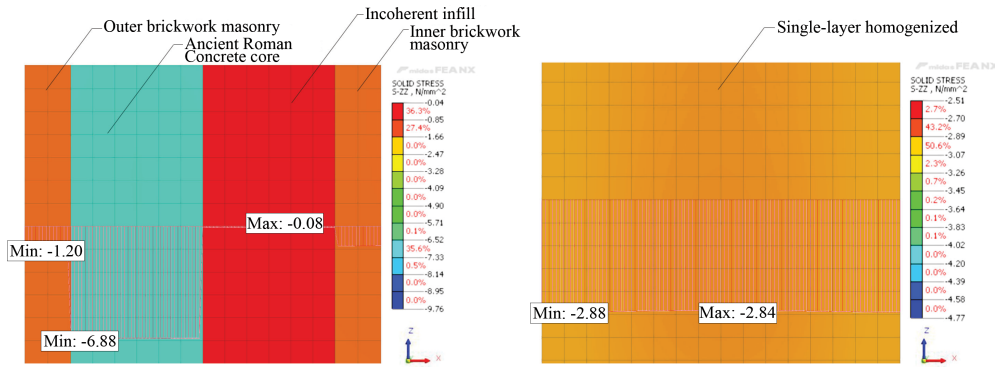

(a) (b)

Figure VI.12: Results of numerical analyses under uniaxial compression: (a) Stress distribution σ_{zz} in multi-leaf masonry wall (Model B); (b) Stress distribution σ_{zz} in single-layer homogenized masonry wall (Model B).

Similarly, Figure VI.12(a) shows the transverse cross-section of the multilayer wall for the Model B, where the inner core consists of alternating compact ARC and incoherent infill. In this case, the stress distribution is more irregular and the presence of the incoherent layer significantly reduces the load-bearing contribution of the core, leading to a lower global stiffness and strength for the equivalent single-layer material (see Figure VI.12(b)).

When compared to the multi-layer case, the homogenized single-layer model has an underestimation of peak compressive stresses in the ARC core and an overestimation in the external brickwork leaves, as expected. Nonetheless, the average stress over the entire wall thickness is globally uniform. This demonstrates one of the homogenization approach's inherent limitations: while it replicates global stiffness and strength, it necessarily smoothed out through-thickness stress gradients and may underestimate local concentrations and damage in the core [24].

In the second calibration phase, the behavior of the same wall panel, described by a homogenized material with the parameters identified in uniaxial compression, was investigated under combined shear and axial load. For this purpose, the multi-leaf walls (Model A and Model B) and the single-layer equivalent wall were analyzed under a

vertical pressure of 0.60 MPa and increasing in-plane displacement, as described in Section VI.5.2. The load–displacement curve was evaluated in terms of base shear and horizontal displacement at a control node located at the top of the panel.

As shown in Figure VI.13(a), a good agreement is obtained between the load–displacement curves of the multi-leaf wall with a fully compact core and those of the equivalent single-layer wall, indicating that the homogenized material calibrated under uniaxial compression can also capture the global in-plane shear behavior in this configuration. It is worth noting that in this case the outer leaves contribute only marginally to the global stiffness, while the ARC core governs the structural response.

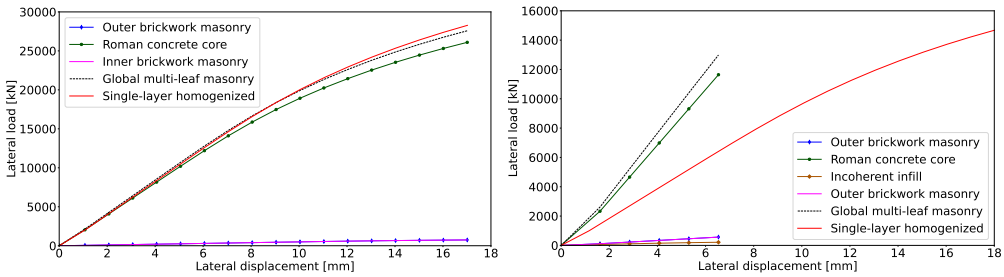

(a) (b)

Figure VI.13: Results of numerical analyses subjected to shear with a vertical pressure of 0.60 MPa: (a) Load–displacement curves for multi-leaf masonry (Model A); (b) Load–displacement curves for multi-leaf masonry (Model B).

In contrast, Figure VI.13(b) shows that, for the Model B configuration with 50% incoherent infill, a significant discrepancy emerges between the behavior of the multi-leaf wall and that of the homogenized single-layer wall, even when using the same set of material parameters. This difference is mainly due to the presence of the highly deformable, incoherent layer, which limits the capacity of the multi-leaf wall to develop large horizontal displacements and induces an asymmetric stratigraphy with respect to the mid-plane of the wall. Such asymmetry generates parasitic effects and complex local mechanisms that cannot be fully captured by the homogenized continuum model.

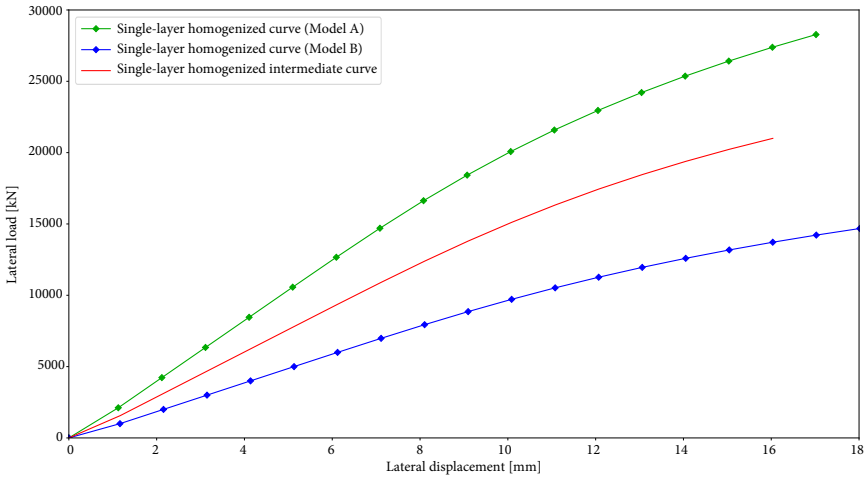

Figure VI.14: Results of numerical analyses subjected to shear with a vertical pressure of 0.60 MPa: load–displacement curves for single-layer homogenized masonry.

Finally, the same shear test was performed on the single-layer panel calibrated under uniaxial compression, adopting intermediate mechanical properties obtained by averaging the two extreme stratigraphic configurations. The corresponding load–displacement curve is shown in Figure VI.14 (red line). Also in this case, plastic strains were limited to about 0.15%, in order to maintain the calibration within a range of moderate non-linearity.

Basically, the results confirm that the proposed homogenization strategy provides a reasonable compromise between accuracy and computational efficiency for the global modeling of the Basilica. At the same time, the analyses highlight the main limitations of the approach: (i) the inability to fully reproduce local stress concentrations and damage patterns associated with degraded or incoherent core regions; and (ii) the sensitivity of the homogenized structural behavior to the assumed stratigraphy, which is partly reconstructed on the basis of local investigations. These aspects motivate the probabilistic treatment of material properties and core configurations adopted in the next chapters, where the uncertainties identified at the material and panel scale are explicitly propagated into the reliability-based assessment of the entire structure.

It should be noted that the analyses conducted so far are preliminary, focusing on calibrating a D-P model to gain initial insights into the material response. For the global reliability-based structural assessment of the Basilica (illustrated in Chapter IX), a more refined constitutive law, the CDP model, is adopted. This choice is motivated by CDP's capability to capture the inelastic behavior of masonry under combined compression and tension, providing a more accurate representation of the structure's global response.

VI.7 References

[1] Aldreghetti, I., Baraldi, D., Boscato, G., Cecchi, A., Massaria, L., Pavlovic, M., Reccia, E., and Tofani, I. (2017). Multi-leaf masonry walls with full, damaged and consolidated infill: experimental and numerical analyses. *Key Engineering Materials*, 747:488–495.

[2] Alecci, V., De Stefano, M., Luciano, R., Marra, A., and Stipo, G. (2021). Numerical investigation on the use of flat-jack test for detecting masonry deformability. *Journal of Testing and Evaluation*, 49(1):537–549.

[3] Alejano, L. R. and Bobet, A. (2014). Drucker–prager criterion. In *The ISRM Suggested Methods for Rock Characterization, Testing and Monitoring: 2007-2014*, pages 247–252. Springer.

[4] Amer, O., Aita, D., Bompa, D. V., Torky, A., Hussein, Y. M., Ali, A. H., et al. (2023). Behavior of unreinforced multi-leaf stone masonry walls under axial compression: Experimental and numerical investigation. *Engineering structures*, 293:116621.

[5] Boscato, G., de Carvalho Bello, C. B., and Cecchi, A. (2021). Multi-leaf masonry walls: Load transfer mechanisms sensitivity to mechanic and geometric parameters. In *Structures*, volume 31, pages 540–557. Elsevier.

[6] D'Altri, A. M., Sarhosis, V., Milani, G., Rots, J., Cattari, S., Lagomarsino, S., Sacco, E., Tralli, A., Castellazzi, G., and de Miranda, S. (2020). Modeling strategies for the computational analysis of unreinforced masonry structures: review and classification. *Archives of computational methods in engineering*, 27:1153–1185.

[7] Guadagnuolo, M., Aurilio, M., Basile, A., and Faella, G. (2020). Modulus of elasticity and compressive strength of tuff masonry: Results of a wide set of flat-jack tests. *Buildings*, 10(5):84.

[8] Hodson, T. O., Over, T. M., and Foks, S. S. (2021). Mean squared error, deconstructed. *Journal of Advances in Modeling Earth Systems*, 13(12):e2021MS002681.

[9] Lourenço, P. B., Zucchini, A., Milani, G., and Tralli, A. (2006). Homogenisation approaches for structural analysis of masonry buildings. *International Journal of Mechanical Sciences*.

[10] Lubliner, J., Oliver, J., Oller, S., and Onate, E. (1989). A plastic-damage model for concrete. *International Journal of solids and structures*, 25(3):299–326.

[11] MIDAS Information Technology, Co., Ltd. (2022). *MIDAS FEA NX Manual*. CSP FEA, Este (PD), Italy.

[12] Miedziałowski, C. and Walendziuk, A. (2023). Description of material properties of degraded and damaged segments of multi-leaf masonry in analyses of large three-dimensional structures. *Materials*, 16(11):4076.

[13] Moayedian, S. M. and Hejazi, M. (2024). Estimating the modulus of elasticity and the compressive strength of brick, mortar and masonry at different scales. In *Structures*, volume 61, page 106116. Elsevier.

[14] Nastri, E. and Todisco, P. (2022). Macromechanical failure criteria: Elasticity, plasticity and numerical applications for the non-linear masonry modelling. *Buildings*, 12(8):1245.

[15] Pinheiro, P., Fernandes, P., Santos, P., and Rodrigues, H. (2017). Mechanical characterisation of masonry walls with flat-jack tests. In *Nondestructive Techniques for the Assessment and Preservation of Historic Structures*, pages 53–73. CRC Press.

[16] Rusticano, G., Daró, P., and Mendola, L. L. (2024). Homogenization techniques for multi-leaf masonry wall analysis: Fem strategies for historical structures. In *International Brick and Block Masonry Conference*, pages 63–75. Springer.

[17] Segura, J., Pelà, L., Roca, P., and Cabané, A. (2019). Experimental analysis of the size effect on the compressive behaviour of cylindrical samples core-drilled from existing brick masonry. *Construction and building materials*, 228:116759.

[18] Simões, A., Bento, R., Gago, A., and Lopes, M. (2016). Mechanical characterization of masonry walls with flat-jack tests. *Experimental Techniques*, 40(3):1163–1178.

[19] Stavroulaki, M. and Papalou, A. (2014). Parametric analysis of old multi-leaf masonry walls. *International Journal of Conservation Science*, 5(4).

[20] Tiberti, S. and Milani, G. (2019). Simple homogenized numerical model for the analysis of multi-leaf masonry walls. In *Structural Analysis of Historical Constructions: An Interdisciplinary Approach*, pages 992–999. Springer.

[21] Valluzzi, M. R., da Porto, F., and Modena, C. (2004). Behavior and modeling of strengthened three-leaf stone masonry walls. *Materials and structures*, 37:184–192.

[22] Viale, N., Ventura, G., Lourenço, P. B., and Ortega, J. (2021). Linear and non-linear fem analyses to assess a shear flat-jack test for masonries. *Journal of Building Engineering*, 43:103169.

[23] Vintzileou, E. (2011). Three-leaf masonry in compression, before and after grouting: a review of literature. *International Journal of Architectural Heritage*, 5(4-5):513–538.

[24] Witzany, J., Brožovský, J., Čejka, T., Kubát, J., and Zigler, R. (2021). Stabilization and consolidation of historical multi-leaf masonry. In *12th International Conference on Structural Analysis of Historical Constructions (SAHC)*.

[25] Zucchini, A. and Lourenco, P. B. (2007). Mechanics of masonry in compression: Results from a homogenisation approach. *Computers & structures*, 85(3-4):193–204.

CHAPTER VII

Probabilistic material characterization: Concrete damage plasticity model

"Ora, con l'aiuto di Dio, avendo deposto l'obelisco a terra…"

("Now, having with God's help set the obelisk down on the ground…")

– Domenico Fontana

VII.1 Introduction

This chapter presents the probabilistic material characterization framework used for NLFEAs of St. Peter's Basilica's historical masonry, focusing on the calibration of the CDP constitutive model [30, 32, 33]. Based on the experimental data described in the previous chapter, a Bayesian updating framework is implemented to reduce the epistemic uncertainties associated with the limited available data [4, 7, 29]. The aim is to create probability distributions for the essential CDP parameters, which can then be used in reliability-based NLFEAs [8, 34].

The chapter begins with a description of the uniaxial stress–strain behavior of historical masonry in compression and tension, focusing on the empirical formulations derived from literature used to assemble the elastic and inelastic regions required by the CDP formulation [22].

The implementation of the CDP model is then presented, along with the processes needed to create the uniaxial compression and tension curves in MIDAS FEA NX. On this basis, the probabilistic characterization of the CDP parameters is presented. The identification of deterministic and random variables is first outlined, accompanied by the rationale for choosing the stochastic parameters [21].

The Bayesian updating then combines experimental evidence and prior information to generate physically comparable posterior distributions tailored to NLFE simulations [11, 23]. To ensure readability within the main chapter, in Appendix A the detailed statistical formulations and graphical outputs behind this method are reported.

The chapter ends by showing how 3D Stochastic Non-Linear Finite Element Analyses (S-NLFEAs) [2, 31], in combination with the LHS technique [19, 24], can be used to homogenize a multi-leaf masonry wall into an equivalent single-layer material [27]. In this framework, such numerical simulations are one technique to translate the probabilistic characterization of material behavior into similar macroscopic features, ensuring that the stochastic variability observed experimentally can be systematically transferred to the structural scale.

It should be noted that the probabilistic approach adopted in this work primarily addresses uncertainties in material properties, rather than discrepancies arising from the simplified representation of shear behavior with a single-layer equivalent material. Consequently, some local deviations, such as those in shear stress distribution, may persist.

VII.2 Stress–strain behavior of historical materials: CDP Model

VII.2.1 Uniaxial compressive law

Under compression, the assembled uniaxial stress–strain law is described by a three-branch piecewise relationship based on literature-derived empirical formulations: (i) a linear-elastic region, (ii) a non-linear ascending branch up to the peak strength governed by a shape parameter α, and (iii) a post-peak softening branch governed by a ductility parameter A_d (see Figure VII.1).

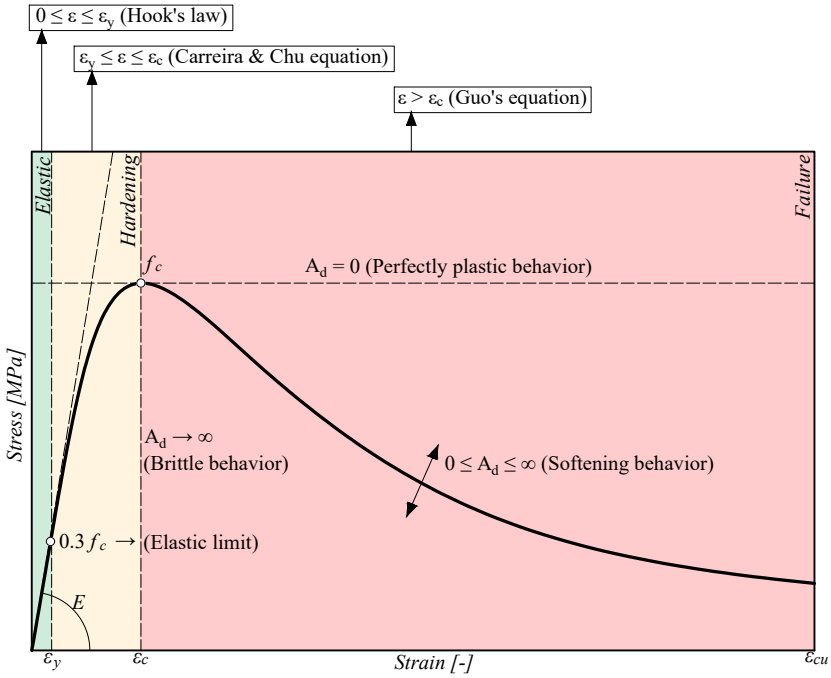

Figure VII.1: Schematic stress–strain curve in uniaxial compression based on literature-derived empirical formulations.

Let ε denote the total axial strain, E the initial tangent elastic modulus, f_c the peak compressive strength, and ε_c the strain at peak stress.

From a mathematical point of view, the global law is defined as

$$\sigma_c(\varepsilon) = \begin{cases} E\,\varepsilon & 0 \le \varepsilon \le \varepsilon_y \\ f_c \dfrac{\alpha\, x}{\alpha - 1 + x^{\alpha}} & \varepsilon_y < \varepsilon \le \varepsilon_c \\ f_c \dfrac{x}{A_d\,(x-1)^2 + x} & \varepsilon > \varepsilon_c \end{cases} \tag{VII.1}$$

More in detail, the initial branch is assumed purely elastic and follows Hooke's law

$$\sigma_c(\varepsilon) = E\,\varepsilon \tag{VII.2}$$

up to a conventional yield strain ε_y defined at 30% of the peak stress,

$$\sigma_y = 0.3\,f_c, \qquad \varepsilon_y = \frac{\sigma_y}{E} = \frac{0.3\,f_c}{E} \tag{VII.3}$$

The non-linear ascending branch is described by the Carreira & Chu equation [6]

$$\sigma_c(\varepsilon) = f_c \frac{\alpha\, x}{\alpha - 1 + x^{\alpha}}, \qquad x = \frac{\varepsilon}{\varepsilon_c} \tag{VII.4}$$

where the shape parameter α is linked to the initial stiffness through

$$\alpha = \frac{E\,\varepsilon_{cu}}{E\,\varepsilon_{cu} - f_c} \tag{VII.5}$$

In practice, the obtained curve is truncated at ε_y and smoothly connected to the elastic branch so that the assembled curve remains continuous in both stress and stiffness at the transition.

The post-peak softening branch is described by Guo's equation [17]

$$\sigma_c(\varepsilon) = f_c \frac{x}{A_d\,(x-1)^2 + x}, \qquad x = \frac{\varepsilon}{\varepsilon_c} \tag{VII.6}$$

where A_d represents a dimensionless parameter that governs the ductility of the materials and the shape of the softening post-peak curve. For $x > 1$, increasing A_d reduces the stress level and produces a sharper post-peak decay, (i.e., a more brittle response). Conversely, decreasing A_d leads to a more gradual softening (i.e., a more ductile response), and in the limit $A_d \to 0$ the curve tends to a perfectly plastic plateau with $\sigma_c \approx f_c$.

In this modified formulation, in order to link A_d to physically meaningful quantities, a target residual stress ratio

$$r = \frac{\sigma_r}{f_c} \in [0.10, 0.20] \tag{VII.7}$$

is assumed at an ultimate strain ε_{cu} (equal to 3.5% in this study). Introducing

$$x_u = \frac{\varepsilon_{cu}}{\varepsilon_c} \tag{VII.8}$$

and imposing $\sigma_c(\varepsilon_{cu}) = \sigma_r = r\, f_c$, one obtains

$$r = \frac{\sigma_r}{f_c} = \frac{x_u}{A_d\,(x_u - 1)^2 + x_u} \tag{VII.9}$$

from which the corresponding value of A_d follows as

$$A_d = \frac{x_u}{(x_u - 1)^2}\left(\frac{1}{r} - 1\right) \tag{VII.10}$$

This calibration strategy ensures that the softening branch reaches a residual stress between 10% and 20% of the peak strength at a strain level, while allowing the parameter A_d to directly control the ductility of the post-peak response.

Within the adopted CDP formulation, the uniaxial compression law is implemented in terms of stress versus inelastic strain rather than total strain. For each point of the continuous law $\sigma_c(\varepsilon)$ in Eq. (VII.1), the inelastic strain is computed as

$$\varepsilon_c^{\text{inel}} = \varepsilon - \varepsilon^{\text{el}} = \varepsilon - \frac{\sigma_c(\varepsilon)}{E} \tag{VII.11}$$

so that the input to the CDP material in FE software consists of tabulated pairs $(\sigma_c,\, \varepsilon^{\text{inel}})$ for the compression law. In parallel, the evolution of the compressive damage variable $d_c(\varepsilon_c^{\text{inel}})$ is defined as

$$d_c = 1 - \frac{\sigma}{\sigma_c} \tag{VII.12}$$

where $\sigma = \sigma_c(\varepsilon)$ is the nominal (damaged) compressive stress and σ_c is the corresponding undamaged effective stress at the peak compressive strength. In this definition, $d_c \approx 0$ in the elastic and hardening ranges (no stiffness degradation), while d_c increases monotonically along the post-peak branch as σ decreases, close to unity when the residual strength is reached, ensuring that the stiffness degradation and softening behavior governed by the parameter A_d are properly reproduced in the global 3D NLFE simulations.

VII.2.2 Uniaxial tensile behavior

Under uniaxial tension, the material response is idealized by a two-branch piecewise law, also based on literature-derived empirical formulations: (i) a linear elastic region up to cracking, and (ii) a post-cracking softening region described by a Thorenfeldt's equation exponential law [35]. In line with common observations for concrete-like materials, the peak tensile strength is assumed equal to one tenth of the compressive strength (see Figure VII.2).

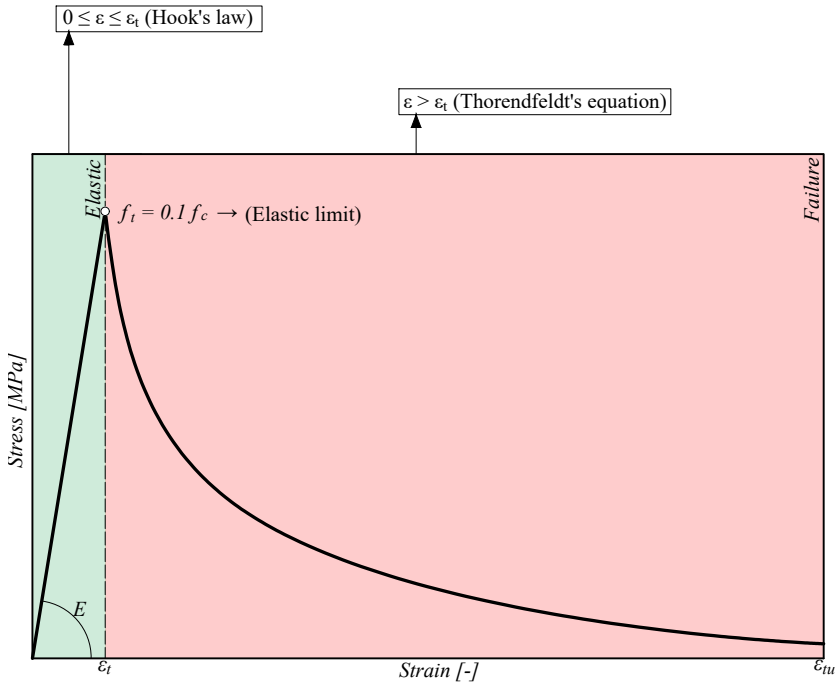

Figure VII.2: Schematic stress–strain curve in uniaxial tension based on literature-derived empirical formulations.

Assuming the same Young's modulus E in tension and compression, the strain at first cracking is given by

$$\varepsilon_t = \frac{f_t}{E} \tag{VII.13}$$

From a mathematical point of view, the global uniaxial tensile stress–strain relationship is expressed as

$$\sigma_t(\varepsilon) = \begin{cases} E\,\varepsilon & 0 \le \varepsilon \le \varepsilon_t \\ f_t \left(\dfrac{\varepsilon_t}{\varepsilon}\right)^{0.7+1000\,\varepsilon} & \varepsilon > \varepsilon_t \end{cases} \tag{VII.14}$$

where σ_t is the nominal tensile stress.

Within the CDP formulation, the uniaxial tensile law is implemented in terms of stress versus inelastic strain. For each point of the continuous law $\sigma_t(\varepsilon)$ in Eq. (VII.14), the tensile inelastic strain is computed as

$$\varepsilon_t^{\text{inel}} = \varepsilon - \varepsilon^{\text{el}} = \varepsilon - \frac{\sigma_t(\varepsilon)}{E} \tag{VII.15}$$

so that the input to the CDP material in FE software consists of tabulated pairs $(\sigma_t, \varepsilon^{\text{inel}})$ for the tension law.

In parallel, the evolution of the tensile damage variable $d_t(\varepsilon^{\text{inel}})$ is defined consistently with the same curve by

$$d_t = 1 - \frac{\sigma}{\sigma_t} \tag{VII.16}$$

where $\sigma = \sigma_t(\varepsilon)$ is the nominal (damaged) tensile stress and σ_t is the corresponding undamaged effective stress at the peak tensile strength. With this definition, $d_t \approx 0$ in the purely elastic range (no stiffness degradation), whereas d_t increases monotonically along the softening branch as σ_t decreases, tending to unity as the tensile stress approaches its residual value at ε_u. In this way, the degradation of tensile stiffness associated with cracking is properly reproduced in the 3D NLFE simulations.

VII.3 Probabilistic characterization of CDP parameters: a Bayesian approach

VII.3.1 Identification of deterministic and random parameters

Within the CDP formulation implemented in FE software, not all input parameters are treated as random. A first group of parameters is assumed deterministic, either because they have a minor influence on the global structural response or because they are poorly identifiable from the available experimental data. These include the plasticity parameters governing the shape of the yield surface and the rate effects, which are fixed to calibrated values and kept constant throughout the Bayesian updating procedure. The adopted deterministic plasticity parameters, taken from the literature [5], are summarized in Table VII.1.

Table VII.1: Deterministic plasticity parameters adopted for the CDP model of materials in FE software.

Variable	Symbol	Unit	Value
Dilation angle	ψ	[°]	31
Eccentricity	ζ	[–]	0.10
Compressive strength ratio	f_{b0}/f_{c0}	[–]	1.16
Triaxiality	K	[–]	0.67
Viscosity parameter	μ	[–]	0.0001

In addition, some basic material properties are also taken as deterministic, such as the unit weight and Poisson's ratio of the different constituents, which are defined from typical values for historical brickwork masonry, ARC and travertine stone that are not included in the Bayesian updating. These parameters are reported in Table VII.2.

Table VII.2: Deterministic material parameters adopted in the numerical model.

Material	Variable	Symbol	Unit	Value
Brickwork masonry	Unit weight	γ_m	[kN/m^3]	18
	Poisson's ratio	ν_m	[–]	0.20
ARC	Unit weight	γ_c	[kN/m^3]	16
	Poisson's ratio	ν_c	[–]	0.20
Travertine	Unit weight	γ_t	[kN/m^3]	25
	Poisson's ratio	ν_t	[–]	0.20

Conversely, the main parameters that directly govern the uniaxial compression and tension laws of Section VII.2.1 and Section VII.2.2 are treated as random variables. For each material, the vector of random parameters is defined as $\theta = (E, f_c, \varepsilon_c)$.

The updating of the PDF and its corresponding Cumulative Density Function (CDF) of the uncertain CDP parameters θ in light of the experimental data is performed within a Bayesian framework and is governed by Bayes' theorem:

$$p(\theta \mid data) = \frac{p(data \mid \theta)\, p(\theta)}{p(data)} \tag{VII.17}$$

where each term has the following probabilistic interpretation:

- **Posterior** $p(\theta \mid data)$: PDF (updated state of knowledge) of the parameter vector θ given the experimental data. In this work, θ collects the random CDP parameters, and $p(\theta \mid data)$ represents their calibrated distribution after accounting for the test data.

- **Likelihood** $p(data \mid \theta)$: PDF of observing the experimental data conditional on a given parameter set θ. It quantifies how well a candidate set of CDP parameters reproduces the measured stress–strain response.
- **Prior** $p(\theta)$: PDF of the parameters before observing the data. It includes the initial information on the CDP parameters, derived from the literature and standards.
- **Evidence** $p(data)$: marginal probability of the evidence, obtained by integrating the numerator over all admissible parameter values

$$p(data) = \int p(data \mid \theta)\, p(\theta)\, \mathrm{d}\theta \tag{VII.18}$$

This decomposition (posterior = likelihood $\times$ prior evidence) follows the standard Bayesian interpretation adopted in the literature [26] and provides the backbone of the probabilistic calibration procedure illustrated in Figure VII.3.

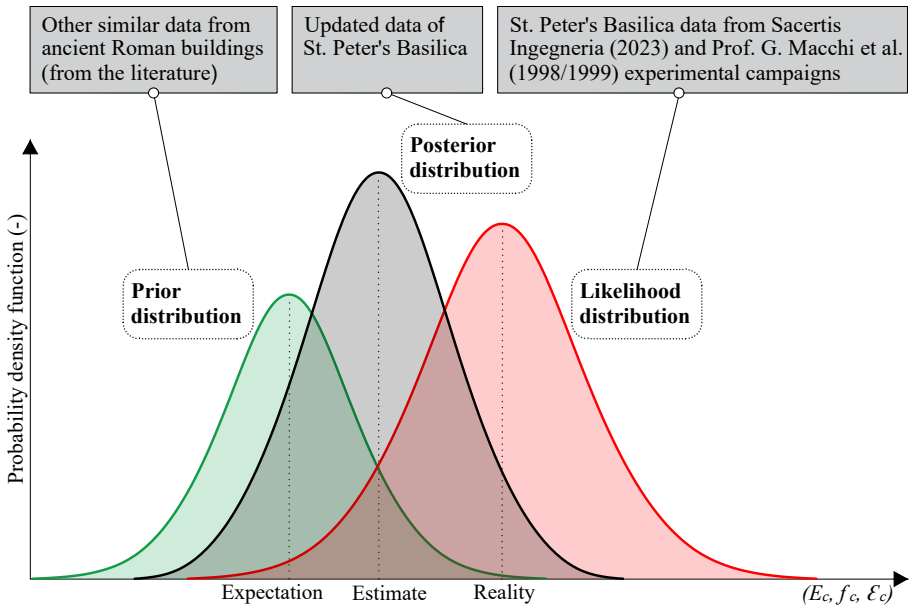

Figure VII.3: Bayesian inference framework for St. Peter's Basilica data.

In this work, the Bayesian updating is carried out by means of the Metropolis–Hastings algorithm [18, 28], a Markov Chain Monte Carlo (MCMC) [15] sampling method used to generate representative samples from the posterior distribution $p(\theta \mid \text{data})$, which are then used to estimate the uncertainty of the CDP parameters under analysis.

Due to the limited sample size, a non-parametric bootstrap resampling procedure with 5,000 synthetic samples with replacement is applied to the available data [12].

In this approach, the variable of interest is modeled using a lognormal distribution , and the bootstrap samples are used to quantify and stabilize the sampling uncertainty affecting the estimates of the mean μ and coefficient of variation V.

The outcome of the Bayesian updating is, for each CDP parameter, a posterior PDF that reflects both the prior information and the experimental data and is described by three main statistical descriptors: (i) the mean value μ_X of the generic property X, (ii) its standard deviation σ_X, and (iii) the corresponding coefficient of variation $V_X = \sigma_X/\mu_X$.

VII.3.2 Bayesian updating of the random material parameters

Brickwork masonry

In order to define the prior distribution, the mechanical characteristics of the investigated brickwork masonry are assumed to be comparable to those of solid brick masonry with lime mortar, as reported in [10]. Furthermore, in accordance with [9], these values are reduced by a factor of 0.7 for $f_{c,m}$ and 0.8 for E_m to account for the presence of thick mortar joints (joint thickness greater than 13 mm, as in the present study). The reduced values are used as input for the probabilistic characterization of the prior.

The current literature provides only limited data for the probabilistic characterization of $\varepsilon_{c,m}$ in this type of historic masonry. In this study, the experimental results reported in [3] are used as the main quantitative reference to estimate its mean value and coefficient of variation in the prior model.

Finally, the likelihood functions are constructed from the experimental data described in Chapter VI. Since no direct in-situ tests of the compressive strength of the historic brickwork masonry are available, the double flat-jack tests carried out in the Basilica provide only an estimate of E_m. In this study $f_{c,m}$ is indirectly related to E_m through empirical formulas predicting the modulus of elasticity as a linear function of compressive strength [13].

$$E_m = k\, f_{c,m} \quad \Rightarrow \quad f_{c,m} = \frac{E_m}{k} \tag{VII.19}$$

This approach is in accordance with several experimental studies on existing masonry that report coefficients k typically in the range 400–1000 [16, 20]. To be in line with the lower bound of this range and to represent the expected low stiffness and strength of the investigated historic brickwork masonry, a relatively low value of the coefficient, $k = 420$, is used in this study. Adopting this lower-bound value leads to a conservative estimate of the reliability; a more rigorous assessment could also include the upper-bound value of k to explore material property uncertainty. However, this was not

carried out here, because, when treating the multi-leaf masonry wall as a homogeneous single-layer material, the mechanical properties of the external layers have a limited influence on the overall structural behavior.

The results of the Bayesian updating for the three CDP parameters, E_m, $f_{c,m}$ (according to Eq. (VII.19)), and $\varepsilon_{c,m}$, are shown in Figures VII.4, VII.5 and VII.6.

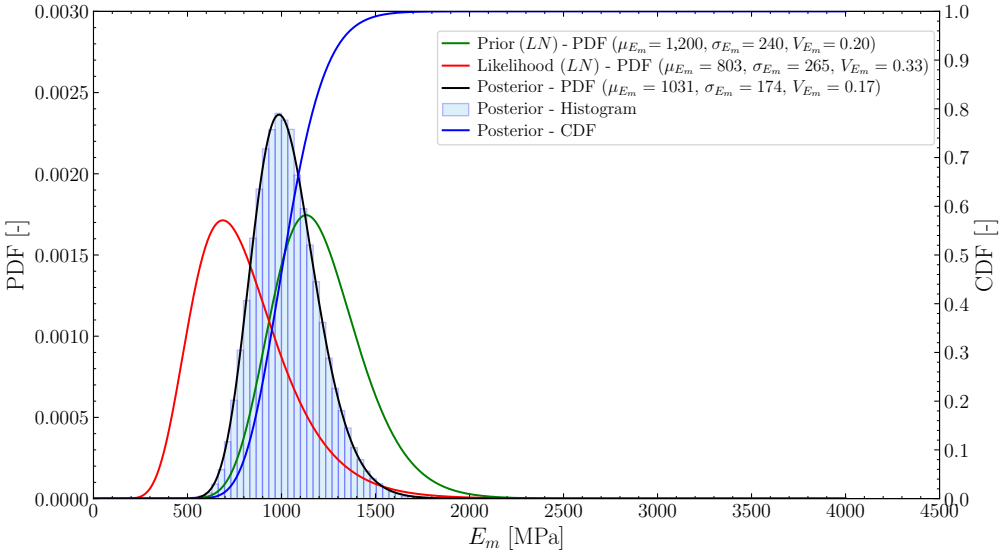

Figure VII.4: Prior, likelihood and posterior distributions for E_m of brickwork masonry (Bayesian updating results).

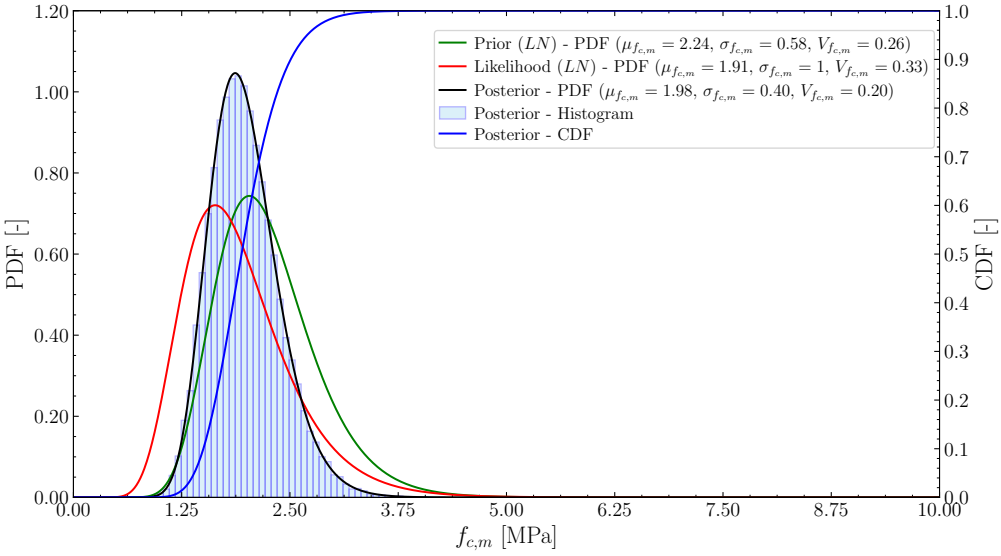

Figure VII.5: Prior, likelihood and posterior distributions for $f_{c,m}$ of brickwork masonry (Bayesian updating results).

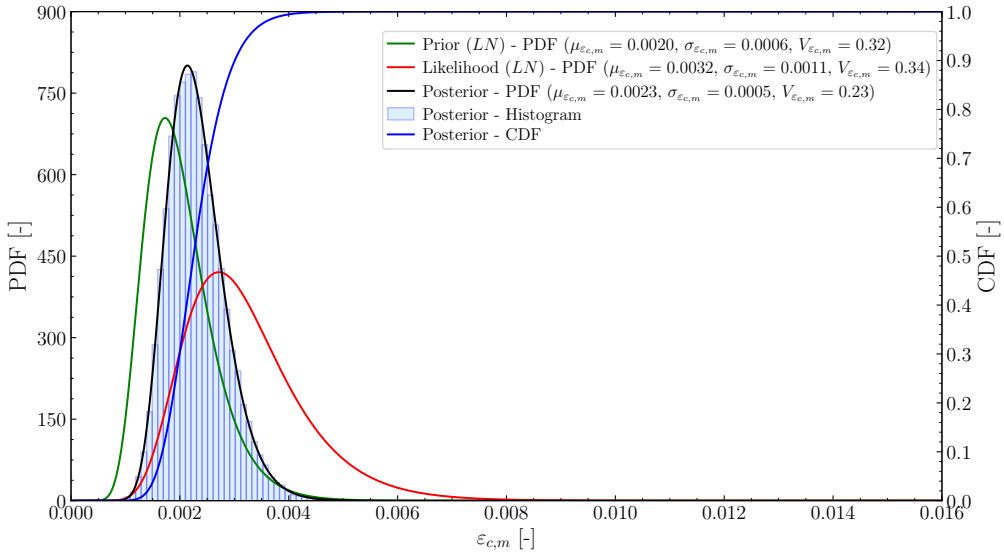

Figure VII.6: Prior, likelihood and posterior distributions for $\varepsilon_{c,m}$ of brickwork masonry (Bayesian updating results).

Each plot shows the prior and likelihood PDFs, together with the posterior PDF and its corresponding CDF. For additional information on the data used in this statistical study, see Sections A.1 and A.2 in Appendix A.

Ancient Roman Concrete

The current literature provides only limited data for the probabilistic characterization of E_c, $f_{c,c}$ and $\varepsilon_{c,c}$. In order to define the prior distribution, the mechanical characteristics of the investigated ARC core are derived from the study by [14], in which similar material typologies were investigated in Ancient Roman monumental buildings located in the same area.

Furthermore, the likelihood functions are constructed from the experimental data described in Chapter VI and are complemented by the results of a previous experimental diagnostic campaign conducted by EniTecnologie S.p.A. in 1998–1999, with laboratory testing performed at the Department of Structural Mechanics of the University of Pavia and subsequently processed by Prof. G. Macchi et al. The results of the Bayesian updating for the three CDP parameters are shown in Figures VII.7, VII.8 and VII.9.

Particularly, each plot shows the prior and likelihood PDFs, together with the posterior PDF and its corresponding CDF. Also here, for additional information on the data used in this statistical study, see Sections A.1 and A.2 in Appendix A.

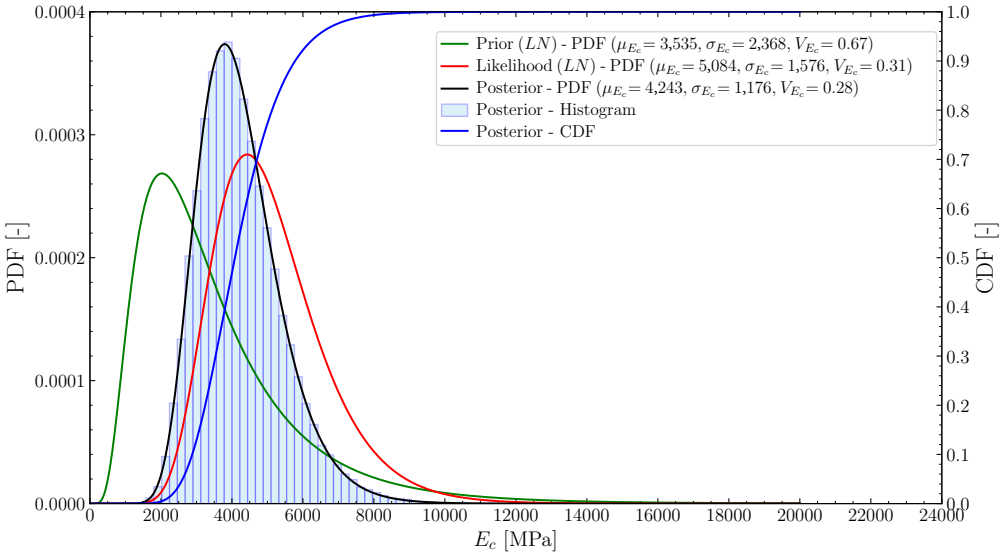

Figure VII.7: Prior, likelihood and posterior distributions for E_c of ARC core (Bayesian updating results).

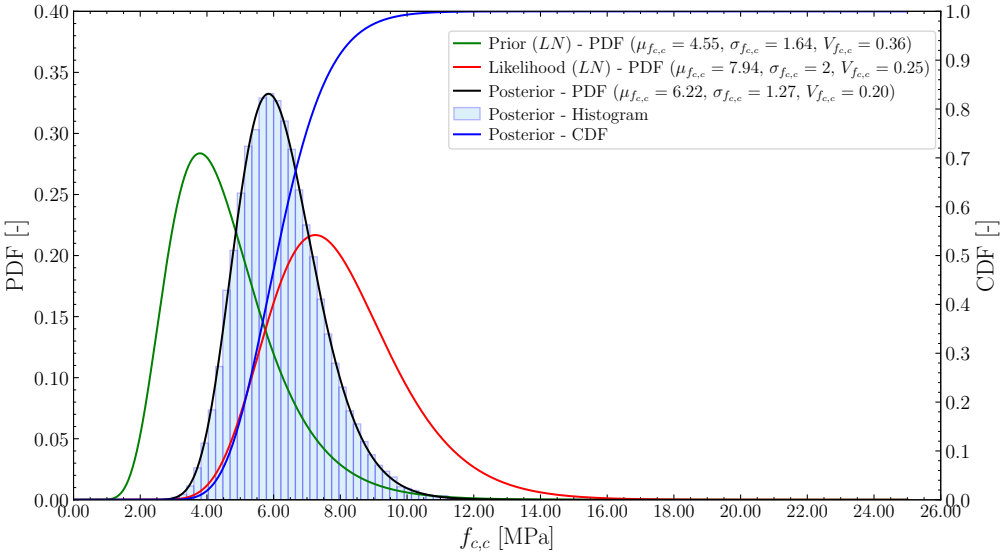

Figure VII.8: Prior, likelihood and posterior distributions for $f_{c,c}$ of ARC core (Bayesian updating results).

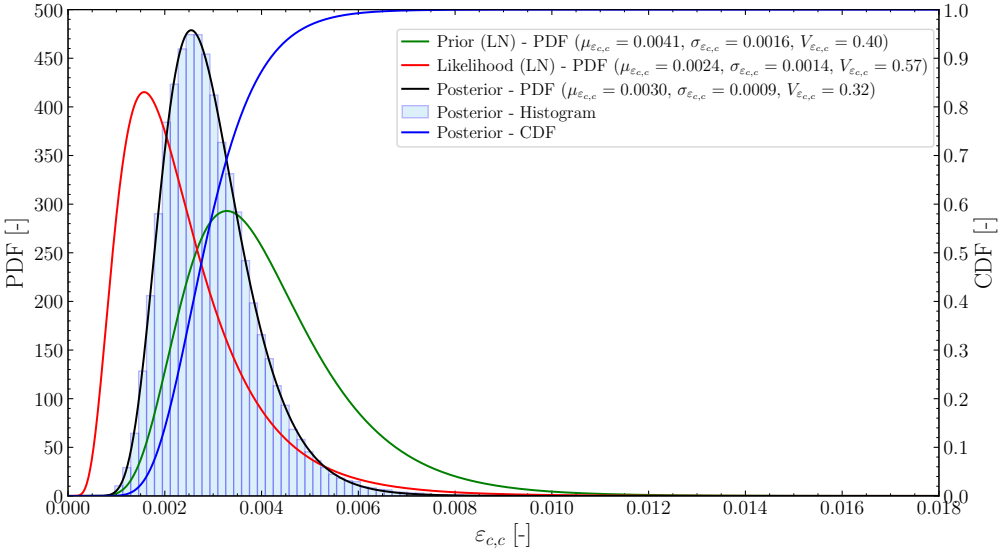

Figure VII.9: Prior, likelihood and posterior distributions for $\varepsilon_{c,c}$ of ARC core (Bayesian updating results).

Travertine

In the case of travertine, the available experimental database is extremely limited. Only one core specimen, extracted from the main Façade of St. Peter's Basilica, was tested during the experimental diagnostic campaign conducted by EniTecnologie S.p.A. in 1998–1999, with laboratory uniaxial compression test performed at the Department of Structural Mechanics of the University of Pavia. Such a small number of tests does not allow for a meaningful statistical inference based on a single data.

For this reason, the probabilistic characterization of travertine is restricted to the definition of a "posterior" distribution, without performing a Bayesian updating step. The posterior distribution is obtained by directly combining the limited experimental evidence available, specifically the single test on the Basilica specimen and the experimental results reported in [25], which refer to Lapis Tiburtinus travertine extracted in the *Acque Albule Basin*, west of Tivoli (about 30 km east of Rome, in the same region as St. Peter's Basilica).

In this way, the posterior distribution includes both the in-situ measurement provided by the core extracted from the Façade and the experimental evidence available in the literature. It is important to emphasize that travertine is a natural stone, characterized by a highly heterogeneous texture and a wide variability in its mechanical properties. Consequently, the aim the data processing is not to provide a precise statistical cali-

bration, but rather to obtain a reasonable probabilistic description of the mechanical behavior of travertine to be used in next numerical analyses.

The statistical characteristics for the three CDP parameters are shown in Figures VII.10, VII.11 and VII.12.

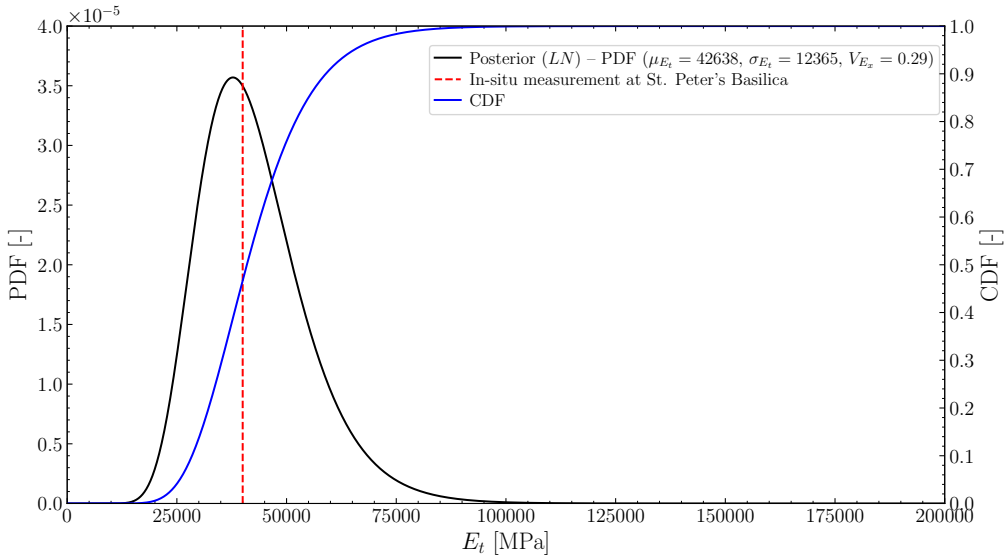

Figure VII.10: PDF and CDF of the posterior distribution of E_t for travertine.

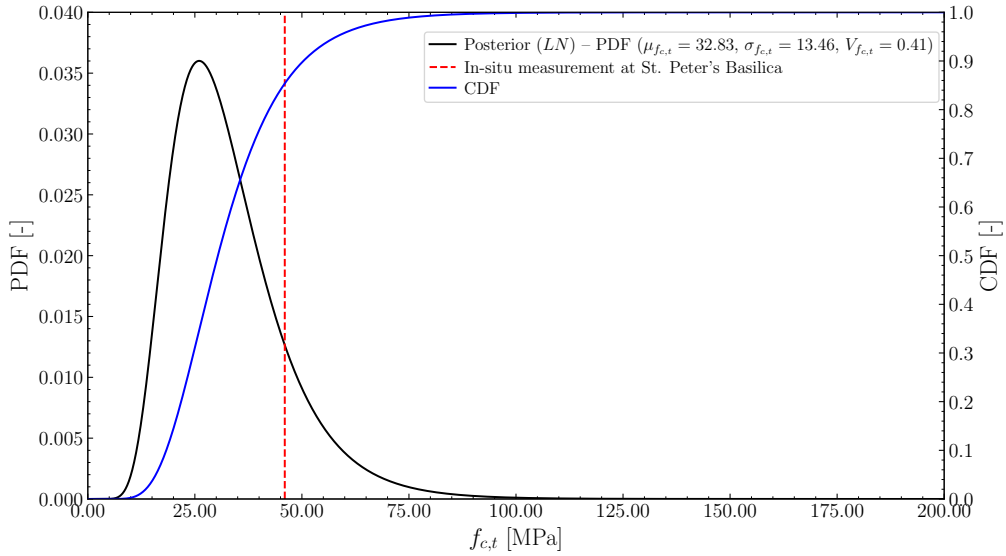

Figure VII.11: PDF and CDF of the posterior distribution of $f_{c,t}$ for travertine.

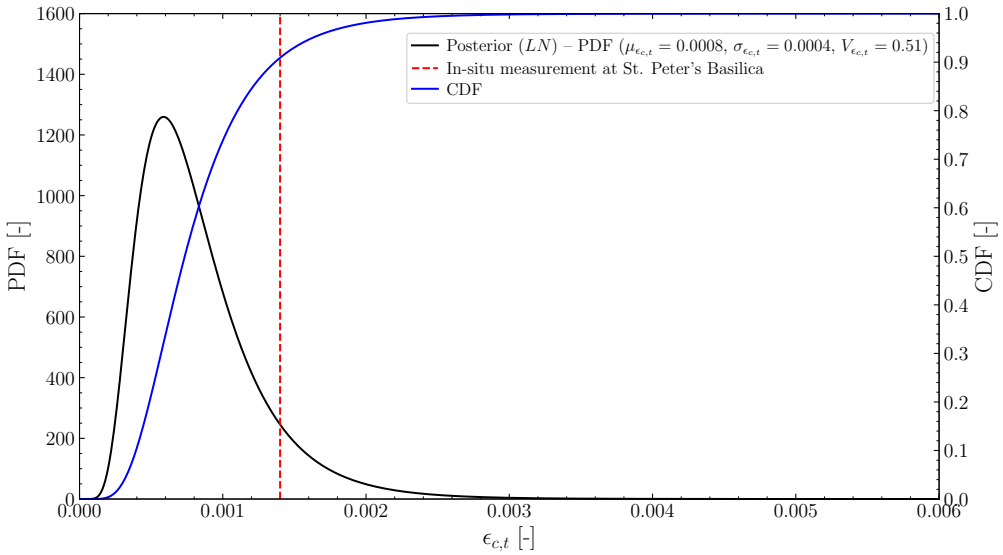

Figure VII.12: PDF and CDF of the posterior distribution of $\varepsilon_{c,t}$ for travertine.

Particularly, each plot shows only the posterior PDFs and its corresponding CDF. For additional information on the data used in this statistical study, see Section A.2.3 in Appendix A.

Summary of the Bayesian updating results

Table VII.3 summarizes the results of the Bayesian updating procedure for all random material parameters of the ARC core, brickwork masonry and travertine stone considered in this chapter. For each parameter, the table reports the resulting posterior distribution in terms of μ and V. These results provide a probabilistic database to be used as input for the S-NLFEAs to homogenize the multi-leaf masonry wall into an equivalent single-layer material, illustrated in the next Section VII.4.

Table VII.3: Random material parameters obtained from Bayesian updating.

Material	Variable	Symbol	Distribution	Unit	μ	V
Brickwork masonry	Elastic modulus	E_m	Lognormal	[MPa]	1,031	0.17
	Compressive strength	$f_{c,m}$	Lognormal	[MPa]	1.98	0.20
	Peak compressive strain	$\varepsilon_{c,m}$	Lognormal	[–]	0.0023	0.23
ARC	Elastic modulus	E_c	Lognormal	[MPa]	4,243	0.28
	Compressive strength	$f_{c,c}$	Lognormal	[MPa]	6.22	0.20
	Peak compressive strain	$\varepsilon_{c,c}$	Lognormal	[–]	0.0030	0.32
Travertine	Elastic modulus	E_t	Lognormal	[MPa]	42,638	0.29
	Compressive strength	$f_{c,t}$	Lognormal	[MPa]	32.83	0.41
	Peak compressive strain	$\varepsilon_{c,t}$	Lognormal	[–]	0.0008	0.51

VII.4 Probabilistic 3D NLFEAs for the homogenization of the multi-leaf masonry wall

In order to homogenize the investigated multi-leaf masonry wall into an equivalent single-layer material, the probabilistic material models obtained from the Bayesian updating procedure (see Table VII.3) are propagated through a set of 3D S-NLFEAs.

The basic idea is to: (i) generate stochastic combinations of CDP parameters for the external brickwork masonry leaves and the ARC core; (ii) filter out physically inconsistent combinations; (iii) construct admissible stress–strain constitutive laws from the empirical Eqs. VII.1–VII.14; and finally, (iv) perform S-NLFEAs on a representative three-leaf wall specimen under uniaxial compression, from which equivalent homogenized parameters for the multi-leaf system are determined.

VII.4.1 Generation of random CDP parameter sets

Starting from the posterior distributions in Table VII.3, the chosen CDP parameters are treated as random variables for both the brickwork masonry leaves (E_m, $f_{c,m}$, $\varepsilon_{c,m}$) and the ARC core (E_c, $f_{c,c}$, $\varepsilon_{c,c}$).

For each material, a LHS technique is adopted to draw random samples (E, f_c, ε_c) from the CDFs of the corresponding lognormal posterior distributions. In the LHS procedure, the range of each variable is divided into n intervals (stratifications) of equal probability; in this study, a value of $n = 50$ was chosen. In order to provide a more uniform representation of the parameter space than basic random sampling, one value is then chosen at random from each interval.

Nevertheless, when combined with the empirical stress-strain laws, not all sampled triplets are physically admissible in Eqs. VII.1–VII.14.

In particular, the initial tangent modulus E must not be smaller than the secant modulus at peak strength $E_{\text{sec}} \geq f_c/\varepsilon_c$. This condition excludes non-convex constitutive behaviors in compression and unrealistically flat ascending branches. The parameter space is divided into two domains defined as follows:

$$\Omega_s = \left\{ (E, f_c, \varepsilon_c) \ : \ E \geq \frac{f_c}{\varepsilon_c} \right\}, \qquad \Omega_f = \left\{ (E, f_c, \varepsilon_c) \ : \ E < \frac{f_c}{\varepsilon_c} \right\} \tag{VII.20}$$

where Ω_f represents the non-admissible combinations, while Ω_s represents the physically admissible domain.

Figure VII.13 showing the LHS results for brickwork masonry in the $(f_{c,m}/\varepsilon_{c,m}, E_m)$ domain, where the dashed line $E_m = f_{c,m}/\varepsilon_{c,m}$ separates Ω_s and Ω_f (limit condition). In this way, 33 triplets are located within Ω_s, while the other 17 triplets are located within Ω_f. A similar analysis is performed for the ARC material, as shown in Figure VII.14, where 48 out of 50 LHS samples are admissible and only 2 combinations are rejected.

In the next S-NLFEAs, only the admissible triplets in Ω_s are used as input CDP parameters.

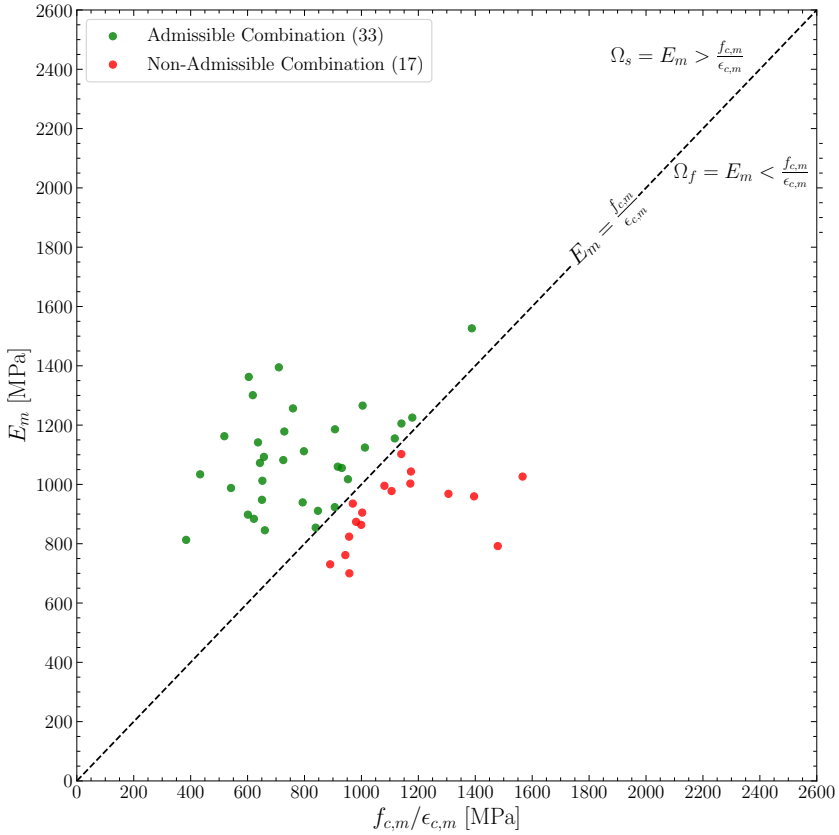

Figure VII.13: Admissible (green) vs non-admissible (red) CDP material-parameter combinations in the $(f_{c,m}/\varepsilon_{c,m}, E_m)$ domain, obtained by LHS for brickwork masonry.

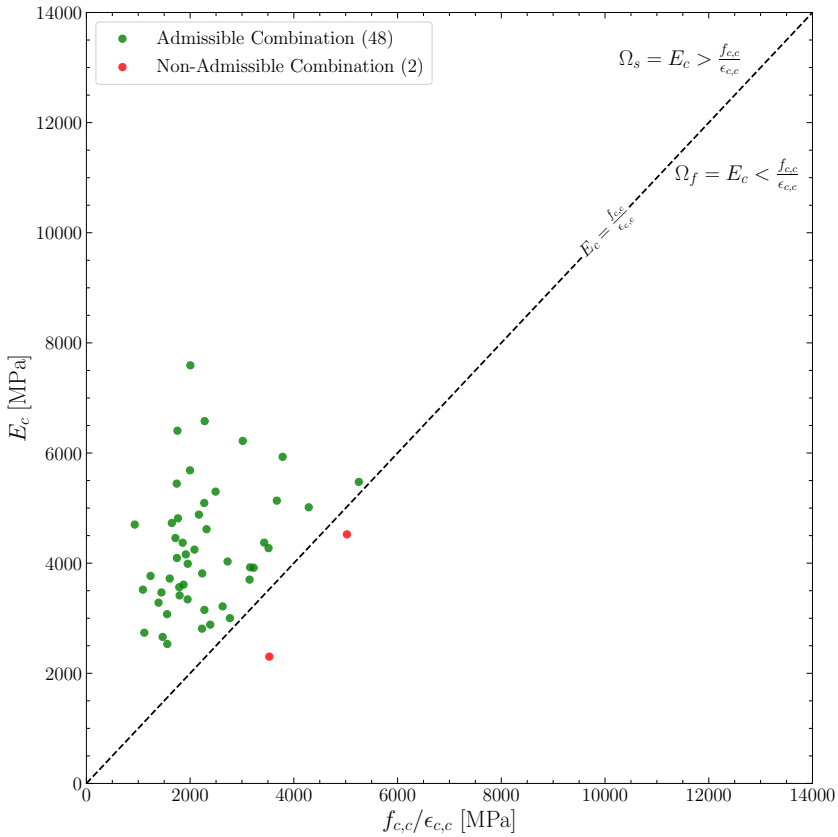

Figure VII.14: Admissible (green) vs non-admissible (red) CDP material-parameter combinations in the $(f_{c,c}/\varepsilon_{c,c}, E_c)$ domain, obtained by LHS for ARC.

VII.4.2 Probabilistic stress–strain laws for brickwork masonry and ARC

For each admissible triplet (E, f_c, ε_c) related to Ω_s, the corresponding random uniaxial stress–strain laws in compression and tension are implemented through Eqs. VII.1–VII.14.

The resulting stress–strain curves for brickwork masonry are reported in Figure VII.15. In particular, Figure VII.15(a) shows the uniaxial compression laws, characterized by an initial non-linear ascending branch, a peak at $(\varepsilon_{c,m}, f_{c,m})$ and a softening descending branch, while Figure VII.15(b) reports the corresponding uniaxial tension laws. Two extremal responses, represented as Curve 1: Min $f_{c,m}$ (in blue) and Curve 2: Max $f_{c,m}$ (in red), are selected from all acceptable curves based on the minimum and maximum compressive strength values. These results provide a plausible envelope of the potential masonry behavior under compression and tension, considering the stochastic uncertainty related to modeling parameters.

An analogous procedure is applied to the ARC material, producing the families of admissible compression and tension curves plotted in Figure VII.16. Also in this case, two representative extremal curves are extracted and identified as Curve 1: Min $f_{c,c}$ (in blue) and Curve 2: Max $f_{c,c}$ (in red).

According to the posterior statistics in Table VII.3, ARC shows significantly higher stiffness and compressive strength than brickwork masonry, with peak strains a little higher on average.

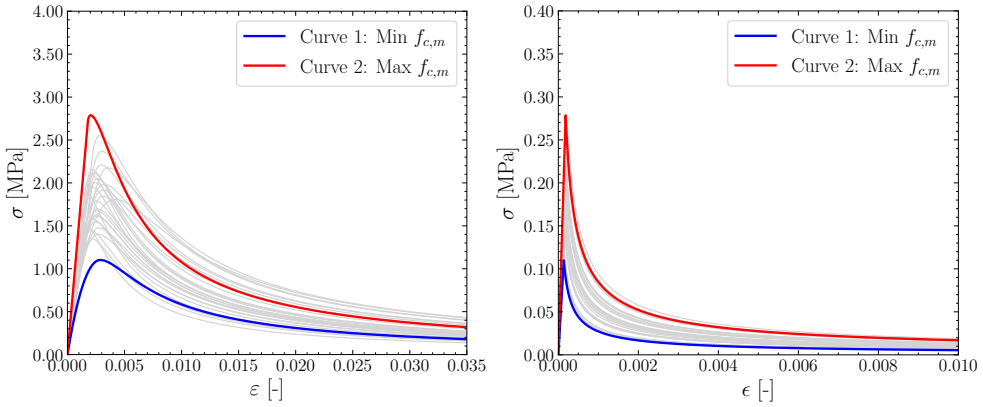

(a) (b)

Figure VII.15: Admissible stress-strain curves for brickwork masonry, obtained by LHS: (a) uniaxial compression; (b) uniaxial tension.

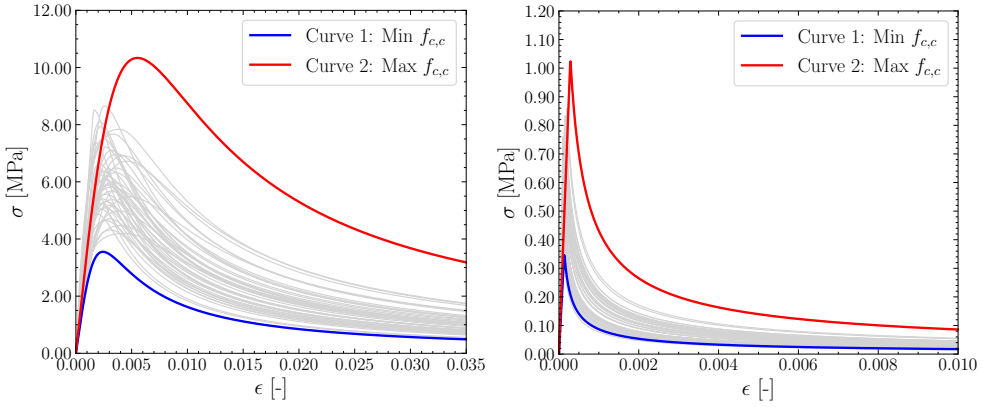

(a) (b)

Figure VII.16: Admissible stress-strain curves for ARC, obtained by LHS: (a) uniaxial compression; (b) uniaxial tension.

VII.4.3 Probabilistic 3D NLFE analyses

The stochastic homogenization procedure is carried out on a three-leaf wall specimen idealized to be representative of the multi-leaf masonry walls investigated in the Atrium of St. Peter's Basilica. In other words, the geometry is assumed fixed, and the thickness ratio is chosen on the basis of endoscopic investigation id. 3 (see Table V.2 in Chapter IV). The adopted geometry, developed in FE software, is schematically illustrated in Figure VII.17.

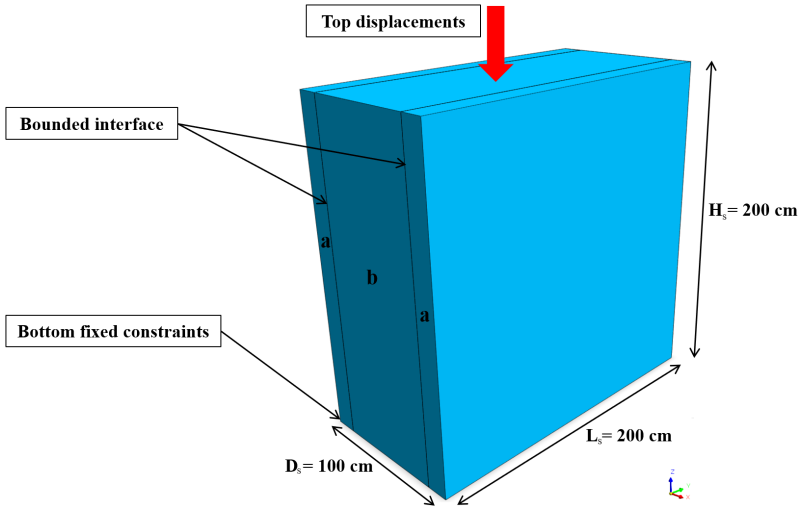

Figure VII.17: Schematic geometry of the multi-leaf masonry wall specimen under uniaxial compression in the numerical simulations.

The specimen has a total height $H_s = 200$ cm, a total length $L_s = 200$ cm and a total depth $D_s = 200$ cm. The two external brickwork masonry leaves have thickness $a = 13$ cm each, while the ARC core has thickness $b = 74$ cm, which results in the thickness ratio $2a/b = 0.35$.

The interface is assumed to be perfectly bonded, with no discontinuity between leaves and a uniform behavior in the out-of-plane direction, because specific knowledge regarding the mechanical connection between brickwork and ARC is unknown.

The 3D NLFE model, shown in Figure VII.18(a), consists of 11,781 four-node hexahedral FE, with an average structured mesh size of 70 mm. The following boundary and load conditions are adopted: (i) a fully fixed constraints are applied at the base of the specimen and (ii) a prescribed vertical displacement (in Z direction) is imposed at the top surface, uniformly applied to all nodes.

Based on the sampled LHS triplets, different CDP material properties are assigned to the ARC core and its outer brickwork masonry leaves.

The S-NLFEAs are structured around the all admissible LHS samples obtained for the ARC core and the Min/Max $f_{c,m}$ curves for the external brickwork masonry (see Section VII.4.2). In this way, for each of the 48 admissible ARC parameter sets, two multi-leaf wall configurations are analyzed: (i) Masonry Upper Bound, in which the ARC core is combined with external leaves modeled with the Max $f_{c,m}$ brickwork masonry curve; and (ii) Masonry Lower Bound, with the same ARC core as above but external leaves modeled with the Min $f_{c,m}$ brickwork masonry curve.

These combinations provide a total of 96 S-NLFEAs for the three-leaf configuration with $2a/b = 0.35$. In addition, for each of the 48 ARC parameter sets, a further analysis is performed on a wall specimen entirely made of ARC (i.e., without external brickwork layers, with $2a/b = 0$). In this case, the same global dimensions $H = D = 200$ cm are assumed, but the full geometry is assigned to the ARC material. These additional S-NLFEAs provide a reference homogeneous model that allows quantifying the error introduced by neglecting the external masonry leaves.

Figure VII.18(b) shows, for a representative set of CDP parameters, the tensile-damage field d_t at the last step of the NLSA performed. The damage pattern is characterized by sub-vertical cracks that develop mainly in the external masonry leaves and propagate into the ARC core, in agreement with the failure mode observed in laboratory uniaxial compression tests on multi-leaf masonry walls [1].

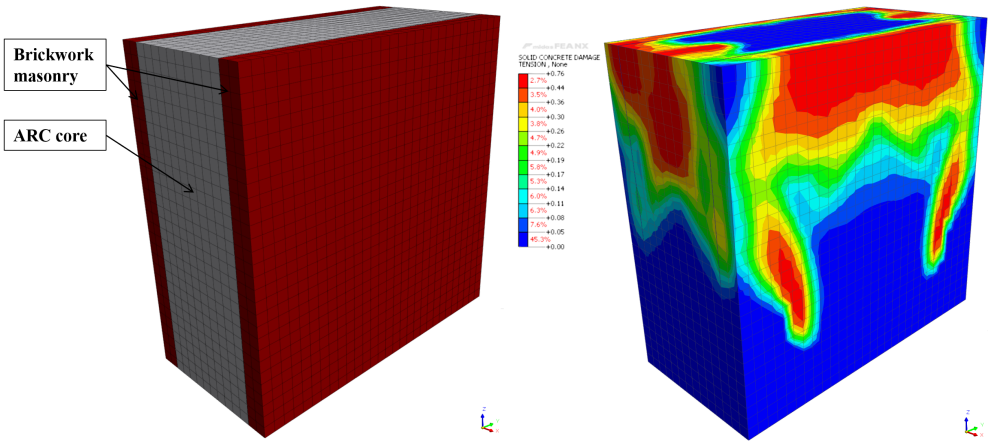

(a) (b)

Figure VII.18: (a) 3D NLFE model with mesh and material assignment; (b) tensile-damage field d_t of the 3D NLFE model at the last step of the NLSA, for a representative CDP parameter set within the range 1–48 (see Figure VII.20).

VII.4.4 Equivalent homogenized material parameters

The global stress-strain curves of multi-leaf masonry wall specimens under uniaxial compression are plotted for each S-NLFEA (see Figure VII.19). In particular, the vertical strains are limited to $\varepsilon_v = 0.6\%$, because this strain level is enough to capture the peak strength and the linear-elastic behavior, which are both essential characteristics needed for the identification of equivalent homogenized parameters.

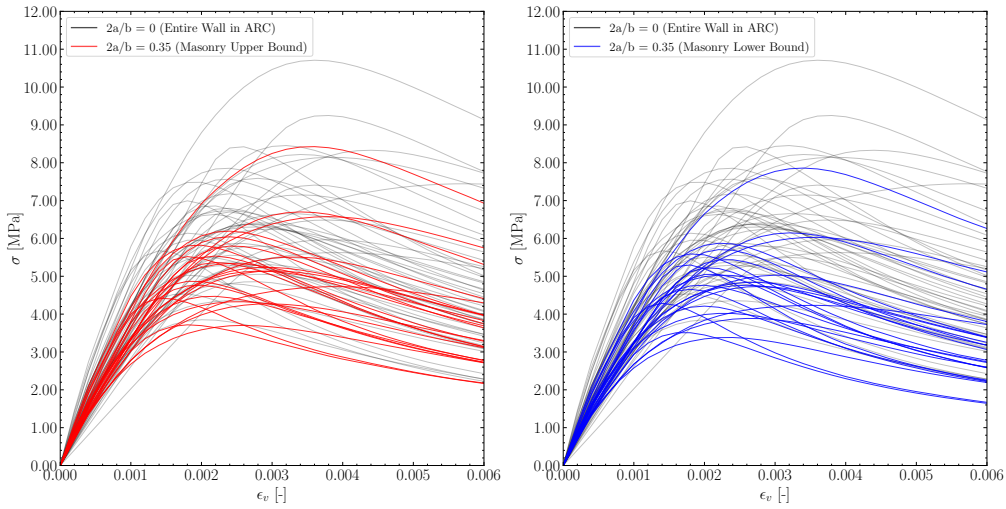

(a) (b)

Figure VII.19: Global stress–strain curves of multi-leaf masonry wall specimens under uniaxial compression, obtained from S-NLFEAs: (a) Entire wall in ARC vs Masonry upper bound; (b) Entire wall in ARC vs Masonry lower bound.

More in detail, the global stress–strain curves correspond to: (i) the entire wall in ARC with $2a/b = 0$; and (ii) the multi-leaf masonry wall with $2a/b = 0.35$ in the masonry upper bound configuration (see Figure VII.19(a)) and (iii) in the masonry lower bound configuration (see Figure VII.19(b)).

The wall made entirely of ARC exhibits the highest compressive strength and stiffness, as expected. However, the presence of the weaker external brickwork leaves causes a reduction of both quantities.

For each analysis, three equivalent homogenized parameters are extracted from the numerical σ–ε_v curve of the multi-leaf masonry wall system: (i) the homogenized elastic modulus E_{h}, obtained as the initial linear-elastic branch of the curve; (ii) the homogenized compressive strength $f_{c,\mathrm{h}}$ is taken at the peak of each curve; and finally (iii) the corresponding peak strain $\varepsilon_{c,\mathrm{h}}$, defined as the strain at which $f_{c,\mathrm{h}}$ is reached. Furthermore, the distributions of the homogenized compressive strengths $f_{c,\mathrm{h}}$ for all 48

ARC parameter sets are summarized in Figure VII.20, where the sets are ordered by increasing $f_{c,c}$ of the ARC core.

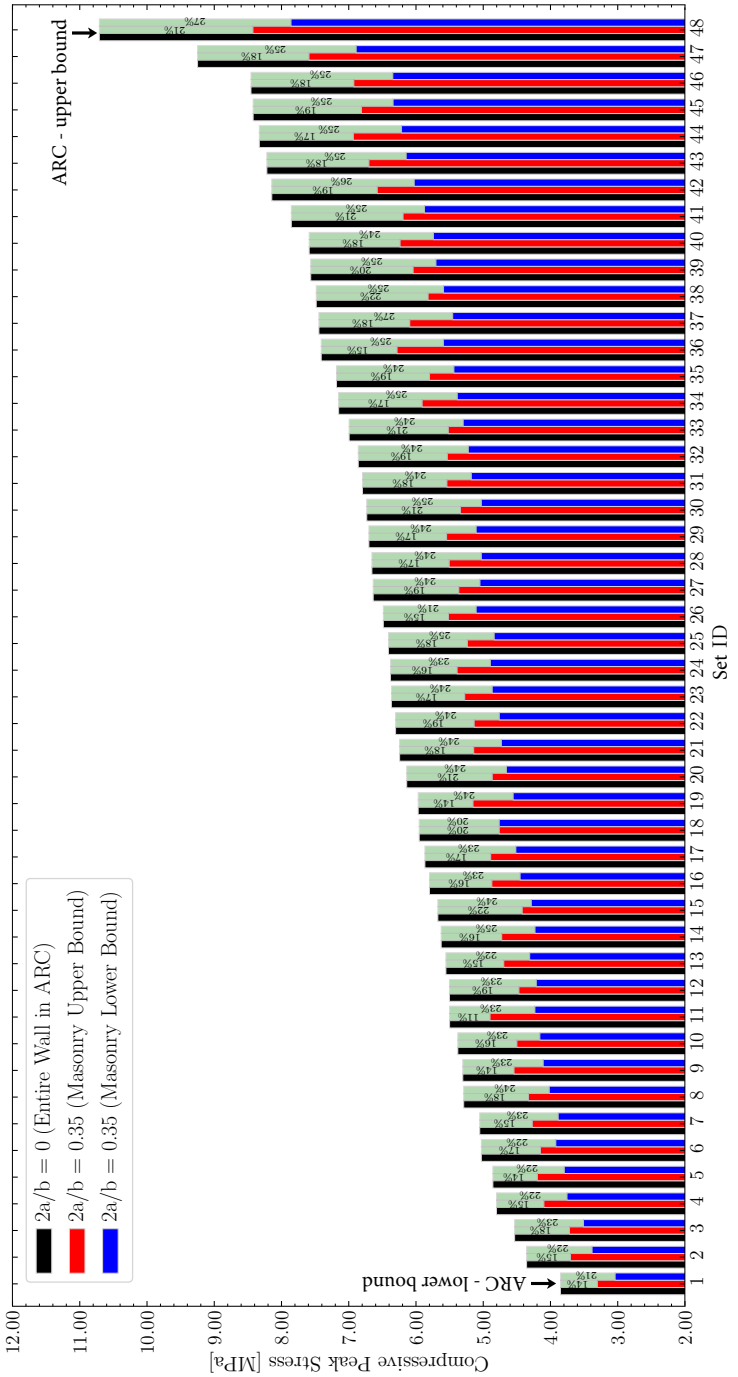

Figure VII.20: Comparison of compressive peak stresses for the three wall specimens configurations under uniaxial compression, obtained from S-NLFEAs.

For each Set ID, three values are reported, corresponding to the configurations described above: black for the wall entirely composed of ARC; red for the masonry upper bound combined with the corresponding ARC properties; and blue for the masonry lower bound combined with the same ARC properties.

The percentage values indicated above the bars quantify the overestimation of the compressive strength that would result from modeling the wall as entirely made of ARC (i.e., by neglecting the external masonry leaves). In this study, this overestimation is estimated to range from 11% to 27%. These results highlight that while the ARC core determines the global stiffness and strength of the wall, and the contribution of the external brickwork leaves is not negligible. Neglecting the masonry leaves in a homogenized macro-scale model would systematically overestimate the compressive capacity and may therefore lead to non-conservative assessments when the model is calibrated to target reliability levels.

Summary of the homogenized material parameters

Table VII.4 summarizes the outcomes of the S-NLFEAs in terms of equivalent homogenized material parameters for the multi-leaf masonry wall.

For each parameter (e.g., E_{h}, $f_{c,\mathrm{h}}$, $\varepsilon_{c,\mathrm{h}}$), the table reports the probabilistic distribution through its mean value and coefficient of variation. The corresponding PDFs are reported in Section A.3 of Appendix A. These results provide a probabilistic database for the homogenized response of the ARC core and brickwork masonry system.

It is worth noting that the material responses discussed here are not strict probabilistic bounds. Extremal curves are selected from admissible realizations based on the observed peak material response (e.g., compressive strength) to define a plausible envelope of the homogenized behavior.

Formally, probabilistic bounds would require response quantiles or pointwise confidence bands through Monte Carlo simulations. Such rigor was considered unnecessary for the current study, where the objective is to identify plausible extremal realizations of the homogenized response.

Table VII.4: Random material parameters obtained from S-NLFEAs for the homogenized multi-leaf masonry wall.

Material	Variable	Symbol	Distribution	Unit	μ	V
Homog. multi-leaf wall	Elastic modulus	E_h	Lognormal	[MPa]	3,352	0.22
	Compr. strength	$f_{c,h}$	Lognormal	[MPa]	5.01	0.20
	Peak compr. strain	$\varepsilon_{c,h}$	Lognormal	[–]	0.0028	0.26

In addition, for the three-layer wall specimen, consisting of two external masonry leaves (thickness $a = 0.13$ m each) and a central ARC core (thickness $b = 0.74$ m), the homogenized unit weight can be taken as $\gamma_{\text{hom}} = 16.52\ \text{kN/m}^3$, obtained from the following volume averaging:

$$\gamma_{\text{hom}} = \frac{\gamma_m V_m + \gamma_c V_c}{V_m + V_c} \tag{VII.21}$$

where γ_m and γ_c denote the unit weights of brickwork masonry and ARC, respectively; V_m and V_c are the corresponding volumes.

VII.5 References

[1] Amer, O., Aita, D., Bompa, D. V., Torky, A., Hussein, Y. M., Ali, A. H., et al. (2023). Behavior of unreinforced multi-leaf stone masonry walls under axial compression: Experimental and numerical investigation. *Engineering structures*, 293:116621.

[2] Arregui-Mena, J. D., Margetts, L., and Mummery, P. M. (2016). Practical application of the stochastic finite element method. *Archives of computational methods in engineering*, 23(1):171–190.

[3] Binda, L., Tedeschi, C., and Baronio, G. (2024). Influence of thick mortar joints on the early and late mechanical behaviour of byzantine constructions. *WIT Transactions on The Built Environment*, 42.

[4] Bracchi, S., Rota, M., Magenes, G., and Penna, A. (2016). Seismic assessment of masonry buildings accounting for limited knowledge on materials by bayesian updating. *Bulletin of Earthquake Engineering*, 14(8):2273–2297.

[5] Brune, P. F. (2010). *The mechanics of imperial Roman concrete and the structural design of vaulted monuments*. University of Rochester.

[6] Carreira, D. J. and Chu, K.-H. (1985). Stress-strain relationship for plain concrete in compression. In *Journal proceedings*, volume 82, pages 797–804.

[7] Caspeele, R., Botte, W., and Vereecken, E. (2025). Bayesian performance assessment of existing concrete structures combining different types of information from inspections and monitoring. *Structure and Infrastructure Engineering*, pages 1–17.

[8] Cervenka, V. (2013). Reliability-based non-linear analysis according to fib model code 2010. *Structural Concrete*, 14(1):19–28.

[9] Circolare n. 7 del 21 gennaio 2019, Consiglio Superiore dei Lavori Pubblici (2019). *Istruzioni per l'applicazione dell'Aggiornamento delle Norme Tecniche per le Costruzioni di cui al Decreto Ministeriale 17 gennaio 2018*. Ministry of Infrastructures and Transportations. (In Italian).

[10] CNR-DT 212/2013 (2013). Istruzioni per la valutazione affidabilistica della sicurezza sismica di edifici esistenti. (In Italian).

[11] Croce, P., Beconcini, M. L., Formichi, P., Landi, F., Puccini, B., and Zotti, V. (2021). Bayesian methodology for probabilistic description of mechanical parameters of masonry walls. *ASCE-ASME Journal of Risk and Uncertainty in Engineering Systems, Part A: Civil Engineering*, 7(2):04021008.

[12] Davison, A. C. and Hinkley, D. V. (1997). *Bootstrap methods and their application*. Number 1. Cambridge university press.

[13] Eurocode 6: (2005). *Design of Masonry Structures – Part 1-1: General Rules for Reinforced and Unreinforced Masonry Structures*. Number EN 1996-1-1. European Committee for Standardization, Brussels, Belgium.

[14] Ferretti, A. S. (1996). Materiali da costruzione e tecnologie costruttive del patrimonio archeologico e monumentale romano. *Unpublished research conductued at Università degli Studi di Roma" La Sapienza*.

[15] Gelman, A., Hwang, J., and Vehtari, A. (2014). Understanding predictive information criteria for bayesian models. *Statistics and computing*, 24(6):997–1016.

[16] Guadagnuolo, M., Aurilio, M., Basile, A., and Faella, G. (2020). Modulus of elasticity and compressive strength of tuff masonry: Results of a wide set of flat-jack tests. *Buildings*, 10(5):84.

[17] Guo, Z. (2014). *Principles of reinforced concrete*. Butterworth-Heinemann.

[18] Hastings, W. K. (1970). Monte carlo sampling methods using markov chains and their applications.

[19] Helton, J. C. and Davis, F. J. (2003). Latin hypercube sampling and the propagation of uncertainty in analyses of complex systems. *Reliability Engineering & System Safety*, 81(1):23–69.

[20] Jafari, S., Rots, J. G., and Esposito, R. (2022). A correlation study to support material characterisation of typical dutch masonry structures. *Journal of Building Engineering*, 45:103450.

[21] Jankowiak, T. and Lodygowski, T. (2005). Identification of parameters of concrete damage plasticity constitutive model. *Foundations of civil and environmental engineering*, 6(1):53–69.

[22] La Mendola, L. and Papia, M. (2002). General stress-strain model for concrete or masonry response under uniaxial cyclic compression. *Structural engineering and mechanics: An international journal*, 14(4):435–454.

[23] Landi, F., Marsili, F., Friedman, N., and Croce, P. (2021). gpce-based stochastic inverse methods: A benchmark study from a civil engineer's perspective. *Infrastructures*, 6(11):158.

[24] Lourenço, P. B., Milani, G., Tralli, A., and Zucchini, A. (2007). Analysis of masonry structures: review of and recent trends in homogenization techniques. *Canadian Journal of Civil Engineering*, 34(11):1443–1457.

[25] Luza Huillca, C. A., Jiménez Pacheco, H. G., Miranda Ramos, L. M., Delgado Sarmiento, P. K., Alvarez Tohalino, V. L., Terrones Diaz, H. E., and Vargas Jr, E. d. A. (2023). Characterization analyzes in the geomechanical behavior of travertine rock. *SN Applied Sciences*, 5(10):267.

[26] MacKay, D. J. (2003). *Information theory, inference and learning algorithms*. Cambridge university press.

[27] Meftah, S. A., Aldosari, S. M., Tounsi, A., Cuong-Le, T., Khedher, K. M., and Alluqmani, A. E. (2024). Simplified homogenization technique for nonlinear finite element analysis of in-plane loaded masonry walls. *Engineering Structures*, 306:117822.

[28] Metropolis, N., Rosenbluth, A. W., Rosenbluth, M. N., Teller, A. H., and Teller, E. (1953). Equation of state calculations by fast computing machines. *The journal of chemical physics*, 21(6):1087–1092.

[29] Nagel, J., Mojsilović, N., and Sudret, B. (2015). Bayesian assessment of the compressive strength of structural masonry. In *Proceedings of the 12th International Conference on Applications of Statistics and Probability in Civil Engineering (ICASP12), Vancouver, Canada, July 12-15*. University of British Columbia.

[30] Nastri, E., Tenore, M., and Todisco, P. (2023). Calibration of concrete damaged plasticity materials parameters for tuff masonry types of the campania area. *Engineering Structures*, 283:115927.

[31] Olsson, A. M. and Sandberg, G. E. (2002). Latin hypercube sampling for stochastic finite element analysis. *Journal of Engineering Mechanics*, 128(1):121–125.

[32] Qasem, M., Hasan, M., Muhamad, R., Chin, C.-L., and Alanazi, N. (2025). Generalised calibration and optimization of concrete damage plasticity model for finite element simulation of cracked reinforced concrete structures. *Results in Engineering*, 25:103905.

[33] Rainone, L. S., Tateo, V., Casolo, S., and Uva, G. (2023). About the use of concrete damage plasticity for modeling masonry post-elastic behavior. *Buildings*, 13(8):1915.

[34] Slobbe, A., Rózsás, Á., Allaix, D. L., and Bigaj-van Vliet, A. (2020). On the value of a reliability-based nonlinear finite element analysis approach in the assessment of concrete structures. *Structural concrete*, 21(1):32–47.

[35] Thorenfeldt, E. (1987). Mechanical properties of high-strength concrete and applications in design. In *Symposium Proceedings, Utilization of High-Strength Concrete, Norway, 1987*.

This page intentionally left blank.

CHAPTER VIII

Global 3D non-linear finite element model

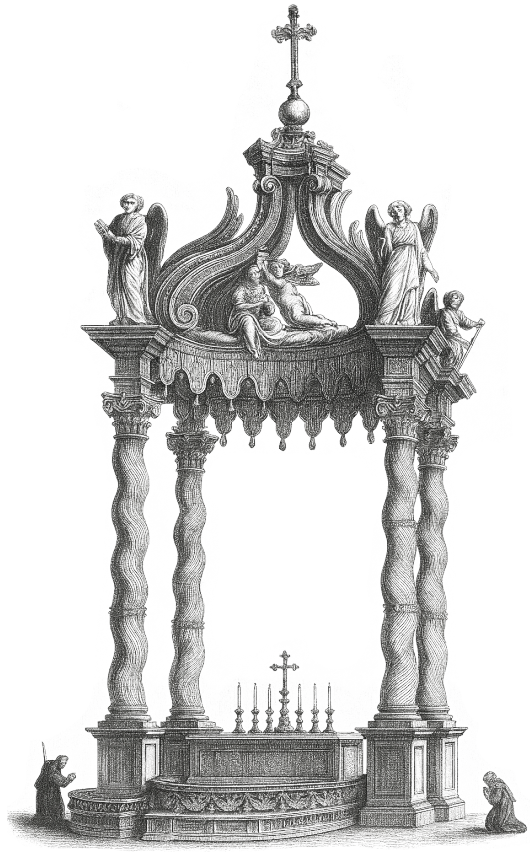

"Chi non si discosta talvolta dalle regole non le supera mai."

("Those who do not sometimes step outside the rules never surpass them.")

– Gian Lorenzo Bernini

VIII.1 Introduction

This chapter presents the development and calibration of the global 3D NLFE model of the 17th-century body of St. Peter's Basilica. Building on the digital twin and historical information discussed in Chapter IV and on the material constitutive models and probabilistic characterization presented in Chapter VII, the aim is to simulate the structural behavior under gravity loads and to assess the global safety levels presented in the next chapter [1, 3].

Since this H-BIM model is primarily intended for documentation and visualization, it cannot be used directly for structural analysis [9]. A dedicated geometric idealization and defeaturing phase is therefore carried out to preserve the main load-bearing components and their spatial interaction while removing non-structural details that would affect mesh generation and numerical convergence.

A large-scale 3D FE discretization is developed on this optimized geometry, employing solid elements for the masonry walls and piers, the vaults, and the travertine blocks, with localized mesh refinements implemented in areas expected to experience stress concentrations and damage localization [11]. The mechanical behavior of the different materials is described through non-linear constitutive laws previously calibrated on experimental and diagnostic data, allowing the simulation of cracking, crushing and stiffness degradation under increasing load levels.

An important aspect of the modeling process is the mechanical interaction between external travertine masonry and the massive multi-leaf walls built regarded as an equivalent single layer material. To investigate its influence on the global response, two alternative global models are developed: the first assumes a fully bonded interface (perfect displacement compatibility), while the second adopts a frictional/contact interface that allows partial interaction, including limited sliding and opening. Apart from the interface assumption, the two models share the same geometry, mesh, material properties, boundary conditions and load conditions, enabling a direct comparison of their structural behavior [7].

Finally, the reliability of the global model is assessed through a dynamic calibration procedure [4]. The numerical model is first analyzed in the linear elastic range to extract its natural frequencies and mode shapes, which are then compared with those identified experimentally through ambient vibration measurements. The stiffness-related parameters are adjusted within physically meaningful ranges to improve the agreement between numerical and experimental modal properties, with particular attention to the role of the boundary constraints with the adjacent structures [2, 10].

VIII.2 Geometric idealization for global 3D NLFE model

The starting point for the global 3D FE model is the geometric survey and digital representation of St. Peter's Basilica presented in Chapter IV.

Starting from the high-resolution point-cloud data, Italferr S.p.A. developed a detailed H-BIM model with an exclusively architectural purpose, which accurately reproduces the volumes and the main internal spaces of the Basilica (see Figure VIII.1).

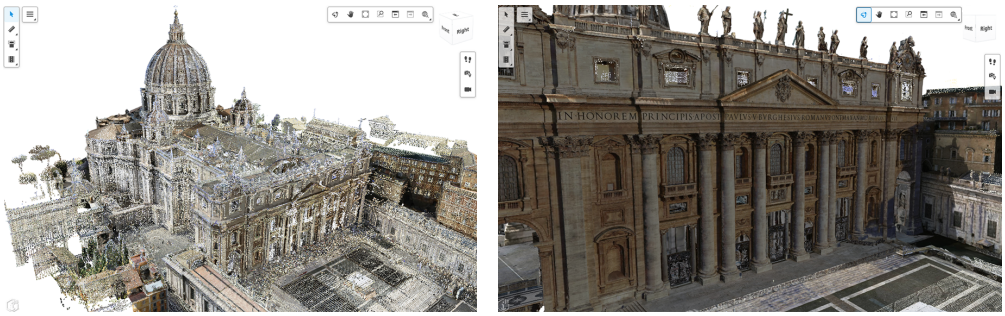

(a) (b)

Figure VIII.1: Point-cloud model of St. Peter's Basilica: (a) global view; (b) detail of the Façade.

This architectural H-BIM model was then imported into MIDAS FEA NX and used as a geometric reference for the construction of the structural FE model (see Figure VIII.2).

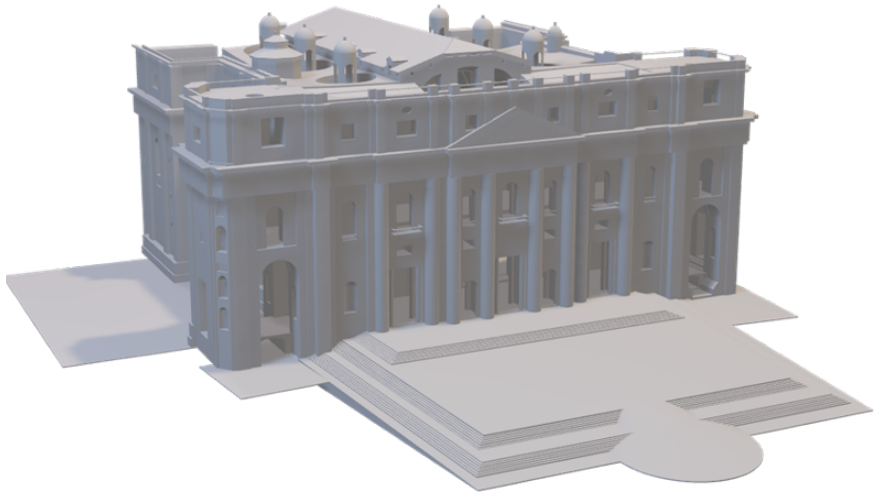

Figure VIII.2: Architectural H-BIM model of the 17th-century body of the Basilica.

A systematic defeaturing process was carried out to reduce the geometric complexity while preserving the main load-bearing components and their interaction.

In this phase, purely decorative elements, very small offsets and fillets, and geometrical irregularities not relevant for the global structural response were removed or regularized, and some curved or highly articulated regions were idealized with simpler surfaces and solids.

The final FE-ready geometry thus retains the essential structural features of the Basilica, such as walls, piers, arches, vaults and domes, while avoiding unnecessary detail, thereby enabling a robust and computationally efficient global 3D analysis.

It is important to note that an architectural H-BIM model cannot be used as input for a structural FE analysis. Architectural models are typically conceived for documentation, visualization and coordination purposes, and therefore contain a large number of non-structural elements, small offsets, overlaps and local gaps between adjacent components. From a numerical point of view, however, a consistent FE mesh requires that all load-bearing parts are perfectly connected to each other, with shared faces, edges and nodes along their interfaces.

In practice, even very small geometric gaps between walls, vaults, piers and slabs may lead to disconnected meshes, spurious mechanisms or the need for an excessive number of artificial constraints. For this reason, a geometric cleaning and defeaturing process is carried out after importing the architectural H-BIM into FE software: interfaces are regularized, gaps are closed, overlapping or redundant solids are removed, and complex shapes are replaced by simpler but mechanically equivalent volumes. This ensures a continuous and conforming mesh, in which adjacent elements exchange internal forces through common nodes.

The model includes the 17th-century body of the Basilica, comprising the central nave, the side aisles, the main piers supporting the central vault of the nave, the Façade body and the lateral towers, as well as the system of barrel and cross vaults. Secondary chapels, minor cavities and local architectural details with negligible structural contribution (e.g., cornices, statues and small shallow niches) are omitted or simplified. Where necessary, local irregularities in wall thickness are regularized so that each wall or pier can be represented by volumes with constant or piecewise constant thickness. This results in a geometrically optimized but structurally representative configuration, appropriate for large-scale NLFEAs.

For numerical analysis, the geometry is idealized to retain the main structural features while removing unnecessary detail, resulting in a computationally efficient global 3D FE model (see Figure VIII.3).

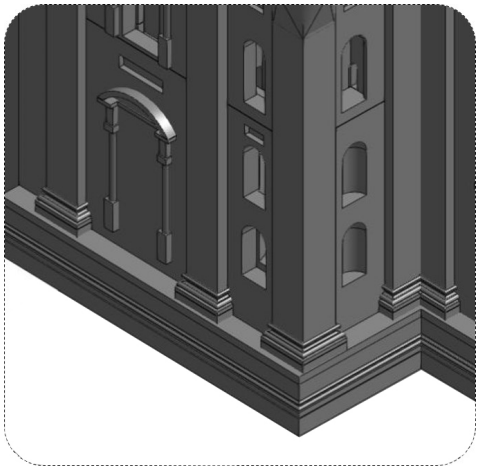

(a)

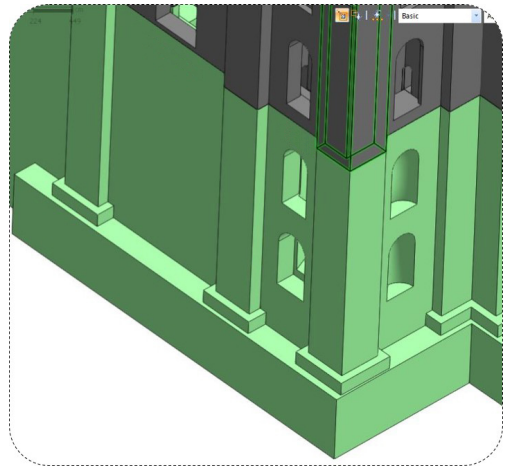

(b)

(c)

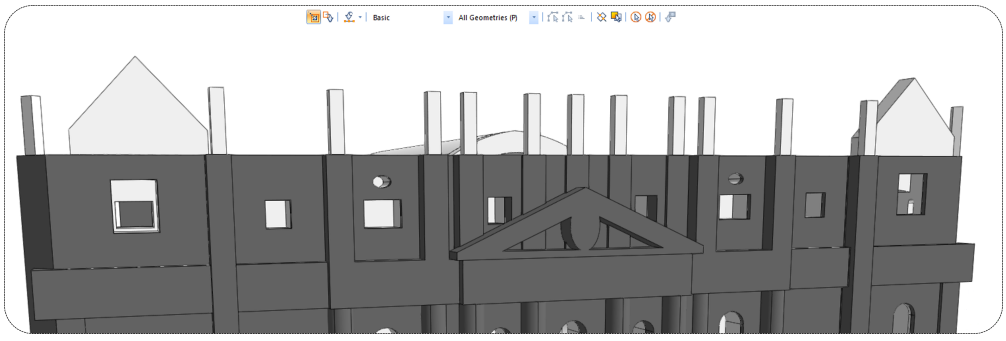

(d)

Figure VIII.3: Example of geometric defeaturing for FE modeling: (a) detail of the H-BIM; (b) corresponding simplified geometry; (c) detail of the Façade statue from the digital twin of the Basilica; (d) corresponding simplified geometry.

The global reference system is defined with the Z-axis aligned with the vertical direction, while the X- and Y-axes lie in the horizontal plane and follow the longitudinal and transverse directions of the Basilica, respectively. This choice ensures that the numerical model is compatible with the architectural system and simplifies the interpretation of the results in terms of global deformation modes and load transfer paths.

Different levels of the structure, such as floor levels, vault imposts and foundation planes, are identified by horizontal reference planes at the corresponding elevations, which provides a clear basis for defining boundary conditions and loading schemes and for organizing the post-processing of numerical outputs.

Figure VIII.4 shows representative global views of the optimized geometry, highlighting the overall spatial configuration of the 17th-century body of the Basilica and the continuity between its main load-bearing components.

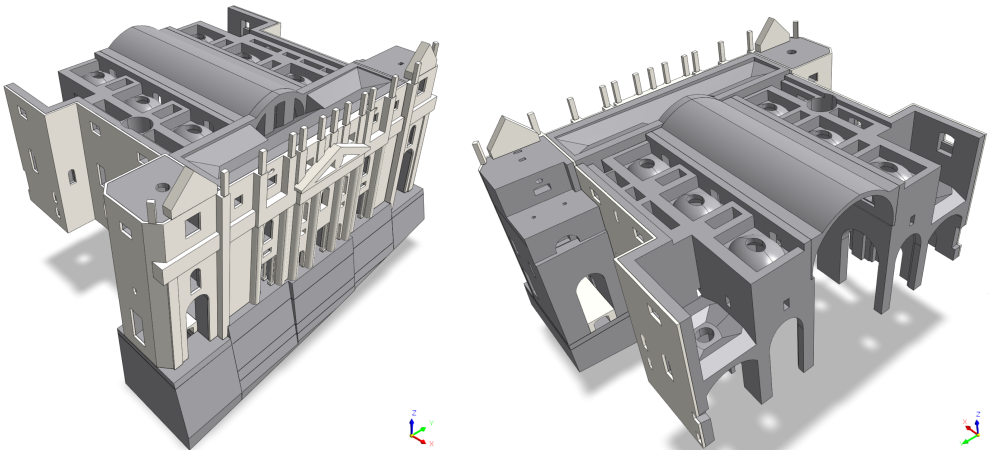

(a) (b)

Figure VIII.4: Global views of the optimized geometry of St. Peter's Basilica in FE software: (a) view from the Façade side; (b) view from the central nave side.

Particular attention is placed to the representation of the massive homogenized multi-leaf walls, which are combined with travertine masonry elements distributed around the Basilica, especially at the Façade and other structurally relevant zones.

In the global model, the homogenized multi-leaf masonry wall and the external travertine facing are represented as separate volumetric layers, in accordance with the stratigraphic information derived from the digital twin of the Basilica combined with the endoscopic surveys and historical documentation. This modeling choice allows the mechanical interaction between the different wall components.

An average travertine thickness of approximately 0.65 m is assumed, in agreement with available historical sources and investigation data [5]. Longitudinal and transverse cross-sections of the optimized geometry are shown in Figure VIII.5. These sections highlight the 3D continuity between walls, piers and vaults, as well as the remarkable thickness of the supporting masonry, which in some zones exceeds 4.0 m. These geometric characteristics play an important role in determining the global stiffness and stress redistribution processes of the Basilica, thus needing the use of a full 3D modeling approach.

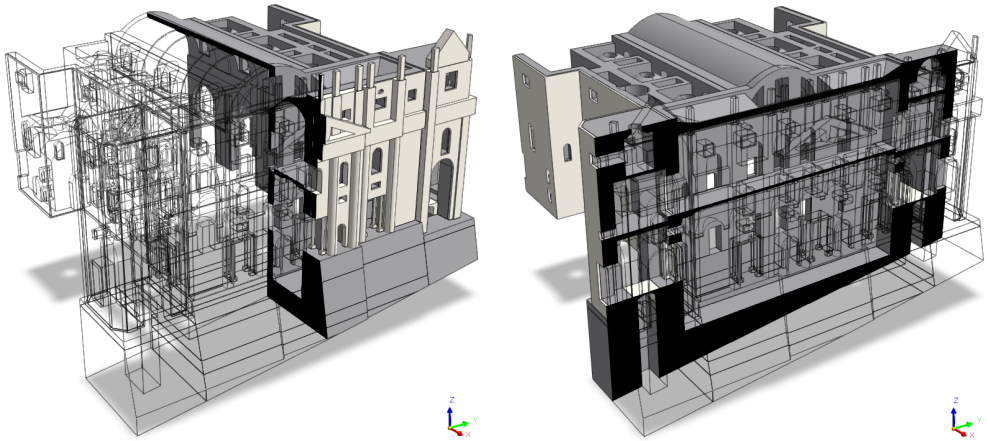

(a) (b)

Figure VIII.5: Cross-sections of the optimized global geometry of St. Peter's Basilica: (a) longitudinal section (X direction); (b) transverse section (Y direction).

From a numerical viewpoint, the above geometric features have direct implications for the discretization strategy adopted in the next phase. The presence of very thick load-bearing members, sharp curvature changes at vault springings, and material transitions requires a mesh capable of preserving geometric conformity and ensuring force transfer through shared interfaces. At the same time, the overall scale of the model imposes the need for a controlled number of degrees of freedom to keep the computational effort compatible with large-scale 3D NLFEAs.

A detailed view of a representative homogenized multi-leaf wall and the travertine facing, is provided in Figure VIII.6. This detail will be particularly relevant for the discussion of the interface modeling strategy in Section VIII.3.2.

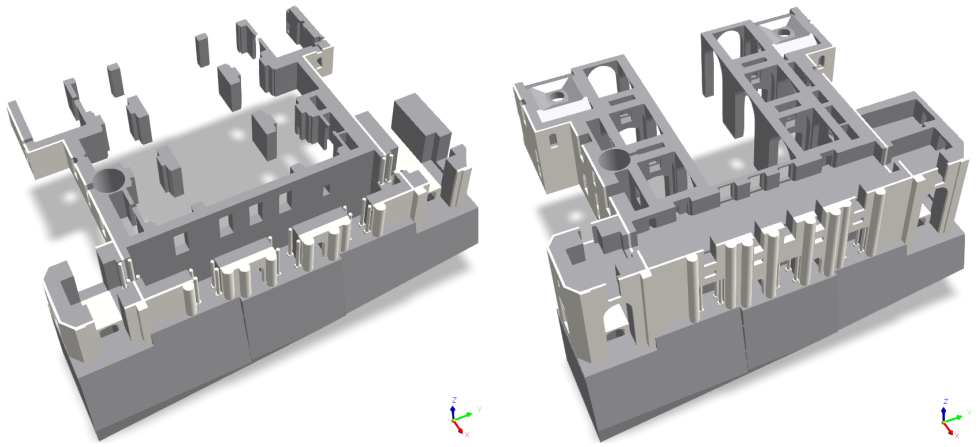

(a) (b)

Figure VIII.6: Cross-sections of the optimized global FE geometry of St. Peter's Basilica (Z direction): (a) Atrium level section ; (b) Hall of Blessings section.

For these reasons, the mesh is designed according to a graded discretization concept: relatively coarse elements are used in the inner portions of massive walls and piers where stress gradients are expected to be smoother, while local refinements are introduced around openings, at the vault imposts, and along the main material interfaces, where stress concentrations and damage localization may develop. The adopted element types and the resulting mesh topology are described in detail in the following section.

VIII.3 Element type and mesh discretization

VIII.3.1 Element type

The main structural components (masonry walls and piers, vaults and arches, travertine masonry, and foundation blocks) are modeled using solid FE.

A hybrid solid discretization is adopted, consisting predominantly of four different type of isoparametric solid elements: (i) four-node tetrahedral elements are used where the geometry is highly irregular or involves curved boundaries; (ii) five-node pyramidal elements are included to accommodate local transitions and ensure mesh compatibility between different element topologies; (iii) six-node prismatic (wedge); (iv) eight-node hexahedral (brick) elements (with reduced integration) in regions with relatively regular geometry (see Figure VIII.7).

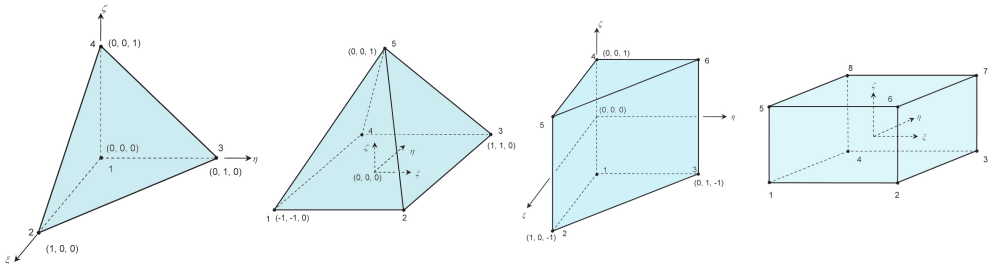

(a) (b) (c) (d)

Figure VIII.7: Type of solid isoparametric elements implemented in the global model of St. Peter's Basilica: (a) 4-node tetrahedron; (b) 5-node pyramidal element; (c) 6-node prismatic (wedge) element; (d) 8-node hexahedral (brick) element (adapted from [8]).

This hybrid element approach provides an accurate geometric representation while controlling mesh density and computational cost. The use of hexahedral-dominant regions, complemented by tetrahedral/prismatic/pyramidal elements only where needed, minimizes the total number of elements; conversely, an all-tetrahedral discretization would have resulted in a substantially larger mesh to achieve comparable accuracy.

Vaults and sub-horizontal diaphragms are also modeled by solid elements, ensuring that the connection between walls, piers, and vaulted systems is accurately represented in 3D space. Steel tie-rods are represented by embedded truss elements, with axial stiffness defined by their cross-sectional properties. The ties are modeled as tension-only members (no compression capacity) and idealized as a linear elastic–perfectly plastic material with yield stress $f_y = 275$ MPa.

The constitutive models assigned to the various FE correspond to those calibrated in Chapters VI and VII. Furthermore, in Table VIII.1 the main structural materials adopted in the 3D FE model are summarized.

Table VIII.1: Main structural materials adopted in the 3D FE model.

Material	E [MPa]	ν [–]	γ [kN/m^3]	Constitutive model
Homogenized multi-leaf masonry	3,352	0.20	16.52	CDP
Travertine masonry	42,338	0.20	25.00	CDP
Higher foundation blocks	3,352	0.20	16.52	LE
Lower foundation blocks	1,000	0.20	16.52	LE
Steel tie-rods	200,000	0.30	76.98	LE–PP

LE: linear elastic; PP: perfectly plastic.

VIII.3.2 Mesh discretization

Two different 3D global FE models are developed, varying in the representation of the interfaces between the external travertine masonry and the homogenized multi-leaf masonry layers. In the absence of detailed evidence on the actual degree of interlocking between the two materials, this study investigates two limiting interface conditions, taken as lower- and upper-bound assumptions.

A Model A, in which fully bonded interface is assumed. In particular, the adjacent solid FE share common nodes along the interface surfaces, with perfect displacement compatibility and preventing any relative sliding or opening. From a numerical point of view, no interface elements are implemented, as continuity is directly imposed through mesh connectivity during the semi-automatic discretization in FE environment.

A Model B, in which the same geometric discretization of the material domains is maintained, but zero-thickness elastic interface elements are introduced along the contact surfaces between the travertine masonry and the homogenized multi-leaf masonry layers. To this end, all nodes shared by the two solid domains are first physically disconnected, so that the interface behavior is governed exclusively by the interface elements.

In a 1D idealization, this can be interpreted as an interface spring acting in series. The interface elements are characterized by a normal stiffness k_n, introduced to prevent interpenetration between the adjacent FE, and by a tangential stiffness k_t, set to allow only very limited relative sliding and opening under shear and tensile actions.

The interface parameters are calibrated by adopting a very low, yet non-zero, $k_t = 0.0001$ N/mm^3, to avoid numerical instabilities, whereas $k_n = 0.97$ N/mm^3 is obtained from the following empirical expression adapted from [6]:

$$k_n = \frac{E_t E_h}{(D_h + D_t)(E_t - E_h)} \tag{VIII.1}$$

where E_h is the elastic modulus of the homogenized multi-leaf masonry, E_t is the elastic modulus of travertine, D_h is the representative thickness of the homogenized multi-leaf masonry wall ($D_h = 3.10$ m), and D_t is the mean travertine thickness ($D_t = 0.65$ m).

Furthermore, a mesh sensitivity analysis was performed on a portion of Basilica (specifically, on the south tower) by progressively refining the element size and monitoring key response quantities (e.g., the vertical displacement at a representative control point). The NLSAs were performed using the constitutive models reported in Table VIII.1, adopting the mean compressive and tensile strengths of the materials. Only self-weight was applied, with fixed constraints imposed at the bottom faces.

The results shown in Figure VIII.8 indicate that the chosen average mesh size (i.e., 70 cm) provides a satisfactory compromise between accuracy and computational effort, with variations below a few percent under further refinement.

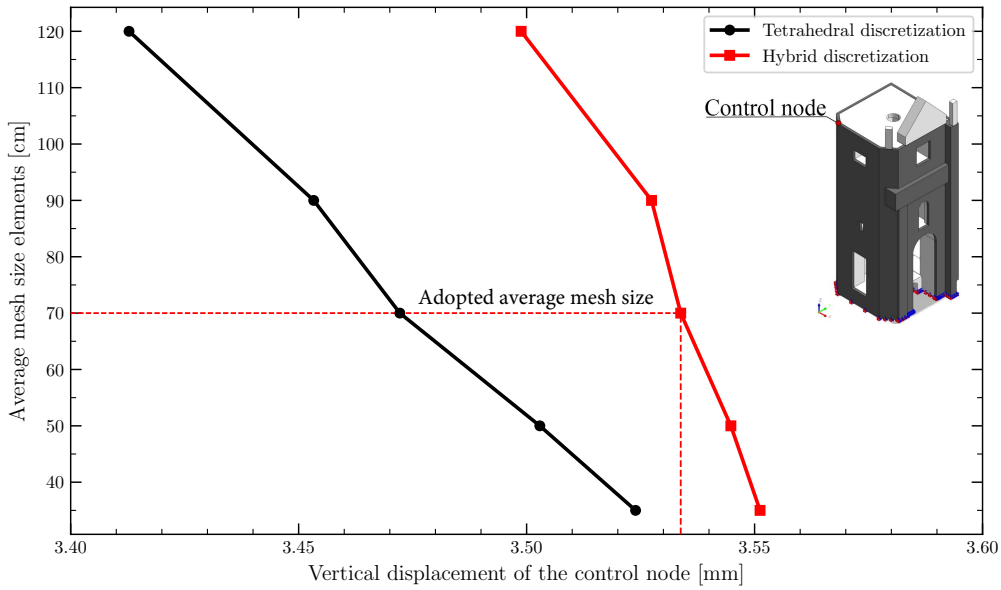

Figure VIII.8: Results of the mesh sensitivity analysis performed on a portion of the 3D FE model of St. Peter's Basilica (south tower). The control node is a corner node on the top face, as indicated in the figure.

Finally, Table VIII.2 compares the two solid-element discretization approaches adopted for the global 3D FE model of the Basilica, reporting the total numbers of nodes and elements. For the same target mesh size, the hybrid solid-element strategy reduces the overall number of finite elements by approximately 75% compared with an equivalent tetrahedral discretization.

Table VIII.2: Comparison between the two solid-element discretization approaches.

FE discretization	Average mesh element size* [cm]	Total nodes [-]	Total FE [-]
Tetrahedral solid elements	70	686,000	3,110,000
Hybrid solid elements	70	498,000	758,000

* Average mesh element size excluding the foundation blocks.

Accordingly, this mesh is adopted for the reliability-based NLSAs presented in Chapter IX and for the linear dynamic calibration described in Section VIII.5. In practical terms, the average element size h_{mesh} adopted in most walls and piers is approximately 70 cm; it is reduced to about 40 cm near large openings and at wall–vault junctions,

and increased to approximately 150 cm in the foundation blocks. A transition zone with gradually reducing element sizes is used to minimize sudden stiffness changes and improve numerical performance.

Figure VIII.9 shows a global view of FE mesh of the Basilica, consisting of approximately 758,000 hybrid solid-elements, together with detailed views of representative areas highlighting the refined discretization around arches and columns.

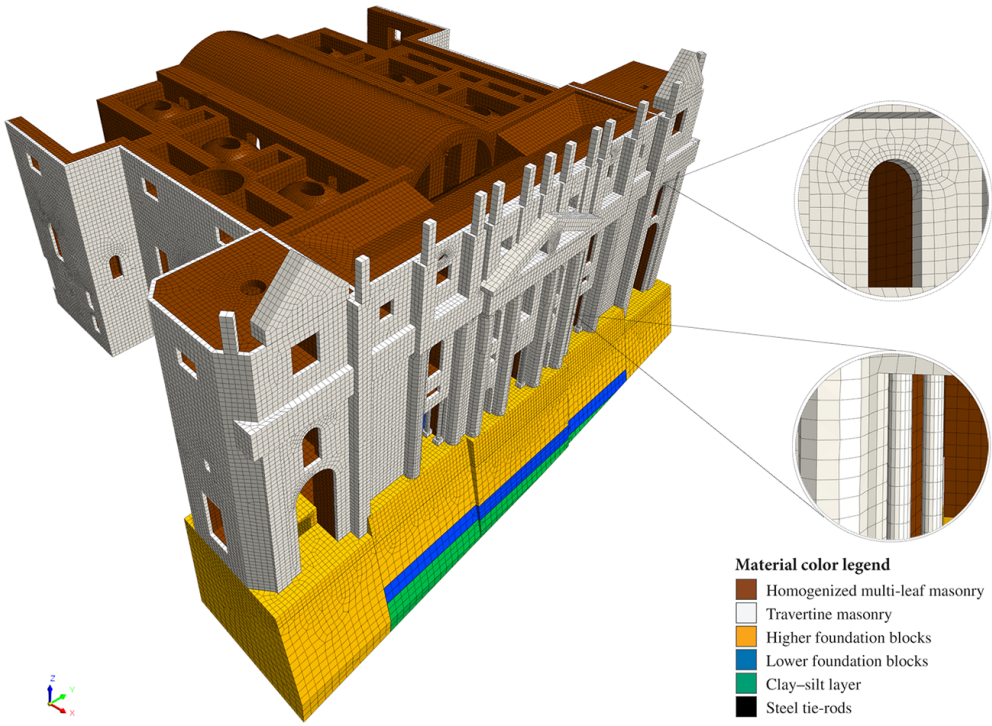

Figure VIII.9: Global view of the 3D FE model of St. Peter's Basilica, highlighting the hybrid solid-element discretization and the material color legend.

VIII.4 Boundary and load conditions

The boundary and load conditions adopted for the global 3D NLFE models are defined to represent, in a simplified yet realistic manner, the support and interaction conditions of the Basilica under self-weight. Model A and Model B share the same global constraints and loading, differing only in the mechanical representation of the travertine–homogenized multi-leaf masonry interfaces (Section VIII.3).

St. Peter's Basilica rests on a complex historical substructure interacting with the surrounding soil and adjacent buildings (Chapter IV). In the numerical model, this is represented through a combination of fixed supports and linear elastic translational

springs. Under the main Façade foundations, a preliminary assumption of perfectly fixed supports is adopted, fully restraining the foundation-level nodes in translation.

By contrast, the longitudinal extension is supported by discrete nodal springs in the three global directions (x, y, and z), introduced at the foundation level to provide a Winkler-type representation of soil–structure interaction. In the absence of detailed geotechnical investigations, the same stiffness is assumed in all directions, $K_x = K_y = K_z = 0.1\ \mathrm{N/mm^3}$.

Additional nodal springs in x, y, and z are assigned along the interfaces between the modeled 17th-century body and the adjacent, non-modeled portion of the Basilica (i.e., the 16th-century body), and along the contact surfaces between the north tower and the adjacent building aggregate. Figure VIII.10 highlights the adopted boundary conditions.

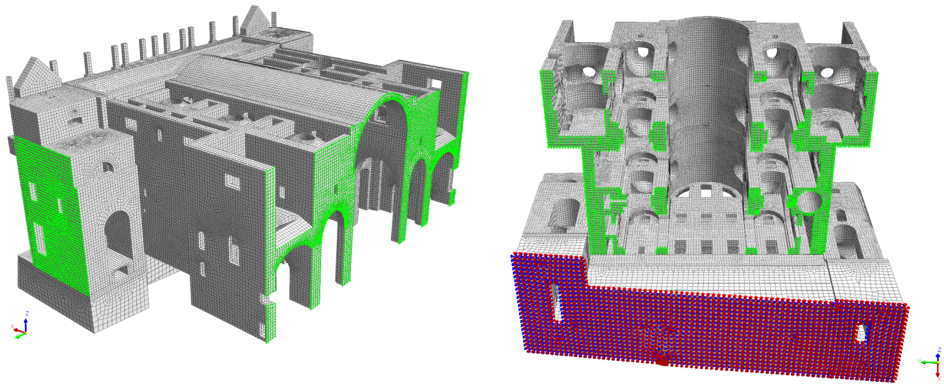

(a) (b)

Figure VIII.10: Global view of the 3D FE model of St. Peter's Basilica with the adopted boundary conditions: (a) interfaces between the 17th-16th-century bodies and between the north tower-adjacent building aggregate (in green, nodal springs); (b) foundations (in green, nodal springs and in blue/red, fixed constraints).

These springs offer an elastic constraint that takes into account the surrounding structure, allowing for realistic force transfer while preventing unnaturally free lateral deformations at the model boundaries.

Particularly, the following Section VIII.5 covers only the calibration of nodal springs associated with vertical interfaces against adjacent structures.

In this chapter, only permanent gravitational actions are considered. The self-weight of the structure is applied by assigning to each material domain its specific unit weight

and by activating a uniform gravity field in the Z direction. The adopted unit weight for the structural materials correspond to the values reported in the previous Table VIII.1.

Some non-structural components and secondary structural elements (e.g., the timber roof system supported by small brick columns above the central nave vault, see Figure VIII.11) are accounted for through an equivalent distributed load.

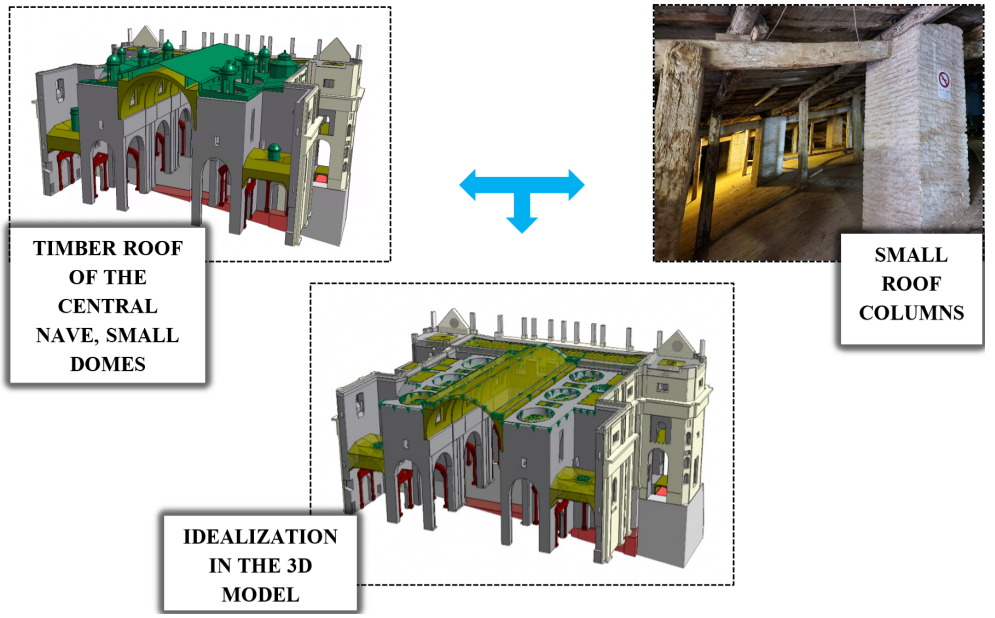

Figure VIII.11: Schematic idealization of secondary loads in the 3D model of St. Peter's Basilica.

No additional live loads, or seismic effects are included in the present phase of the analysis.

This choice is motivated by the objective of isolating the contribution of permanent actions and material nonlinearity to the global stress state and safety levels of the Basilica. The gravity load is applied incrementally, starting from an unloaded configuration and gradually increasing the load factor.

At each load step, the non-linear equilibrium equations are solved accounting for the evolution of damage and plasticity in the homogenized multi-leaf masonry and travertine materials.

A full Newton–Raphson method is adopted, with convergence assessed through displacement and work criteria, set to 0.01 and 0.0001, respectively. In general, the NLSAs are performed using 50 load increments; up to three bisection levels are enabled in case of convergence difficulties, with a maximum of 100 iterations per level. If convergence is not achieved within these limits, the analysis is terminated.

VIII.5 Dynamic model calibration

The validity of the global 3D FE model is first assessed by comparing its dynamic properties with those identified experimentally on the Basilica. The dynamic identification campaign, described in Chapter V, provides estimates of the natural frequencies associated with the most significant global vibration modes. These experimental modal parameters are used here as a benchmark for the calibration of the numerical model.

To improve the agreement between the experimental and numerical modal properties, a model-updating procedure is carried out by performing several linear eigenvalue analyses on the global FE configuration (Model A only), using the mean elastic properties reported in Table VIII.1.

The results of the calibrated models are summarized in Table VIII.3, which reports the experimental and numerical frequencies, together with the numerical mode shapes, for the first significant modes.

Table VIII.3: Main results from model updating and comparison with frequency values extracted from the experimental CSDs reported in Section V.3.2.

Mode ID	Position	f_{FEM} [Hz]	f_{CSD} [Hz]	Mode Shape	Direction
1	16th /17th -century body intersection	1.62	1.63	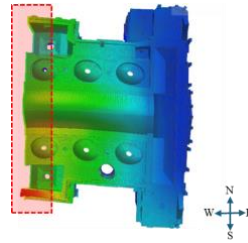	S-N
3	Façade body	2.04	2.00	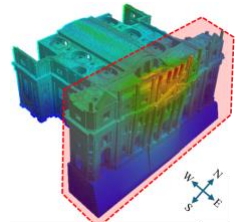	E-W
4	16th /17th -century body intersection	2.43	2.27	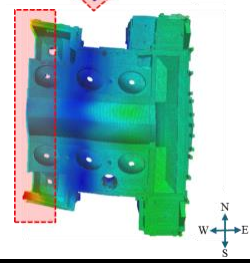	S-N

The parameters selected for calibration include the nodal translational springs (K_x, K_y, and K_z) introduced at the lateral interfaces, as discussed in Section VIII.4. These parameters are changed within specified limits based on engineering judgements.

In other words, the calibration process is based on an iterative model-updating procedure aimed at minimizing the relative error between numerical and experimental frequencies for the first set of global modes, while preserving a realistic distribution of stiffness among the various structural components.

Finally, for each trial set of parameters, a new eigenvalue analysis is performed and the resulting modal frequencies are compared with the experimental targets.

The comparison confirms that the calibrated model, under normal condition, is able to reproduce not only the global frequency levels but also the qualitative distribution of deformation in the main structural components.

VIII.6 References

[1] Angjeliu, G., Coronelli, D., and Cardani, G. (2020). Development of the simulation model for digital twin applications in historical masonry buildings: The integration between numerical and experimental reality. *Computers and Structures*, 238:106282.

[2] Boscato, G., Russo, S., Ceravolo, R., and Fragonara, L. Z. (2015). Global sensitivity-based model updating for heritage structures. *Computer-Aided Civil and Infrastructure Engineering*, 30(8):620–635.

[3] Camus, A. (2024). Preserving historic st. peter's basilica with a digital twin. *GIM International*.

[4] Darò, P., Iacussi, L., Turrisi, S., Rusticano, G., Chiariotti, P., Zappa, E., Cigada, A., and Mancini, G. (2025). Dynamic characterization of monumental building for shm purpose: The case of the papal basilica of st peter. In *International Conference on Experimental Vibration Analysis for Civil Engineering Structures*, pages 84–93. Springer.

[5] Giunta, G. and Calloni, G. (2000). Ground penetrating radar applications on the facade of st. peter's basilica in vatican. In *Proc. 15 World Conference on Non Destructive Testing, Rome*, pages 172–176.

[6] Lourenco, P. B. and Gaetani, A. (2022). *Finite element analysis for building assessment: Advanced use and practical recommendations*. Routledge.

[7] Macorini, L. and Izzuddin, B. A. (2011). A non-linear interface element for 3d mesoscale analysis of brick-masonry structures. *International Journal for numerical methods in Engineering*, 85(12):1584–1608.

[8] MIDAS Information Technology, Co., Ltd. (2022). *MIDAS FEA NX Manual*. CSP FEA, Este (PD), Italy.

[9] Pocobelli, D. P., Boehm, J., Bryan, P., Still, J., and Grau-Bové, J. (2018). Bim for heritage science: a review. *Heritage Science*, 6(1):1–15.

[10] Shabani, A., Feyzabadi, M., and Kioumarsi, M. (2022a). Model updating of a masonry tower based on operational modal analysis: The role of soil-structure interaction. *Case Studies in Construction Materials*, 16:e00957.

[11] Shabani, A., Skamantzari, M., Tapinaki, S., Georgopoulos, A., Plevris, V., and Kioumarsi, M. (2022b). 3d simulation models for developing digital twins of heritage structures: Challenges and strategies. *Procedia structural integrity*, 37:314–320.

This page intentionally left blank.

CHAPTER IX

Reliability-based structural assessment

"Un architetto dimostra la sua abilità trasformando i difetti di un sito in vantaggi."

("An architect proves his skill by turning the defects of a site into advantages.")

– Gian Lorenzo Bernini

IX.1 Introduction

This chapter presents a reliability-based safety assessment of the 17th-century building of St. Peter's Basilica under gravity actions. The historic materials, including multi-leaf Roman concrete, brickwork masonry and travertine stone, are probabilistically characterized from experimental evidence [17].

The assessment is carried out using the semi-probabilistic PFM [5, 16] formulated through the DVM in accordance with the *fib* Bulletin 80 [10, 12] and the *fib* Model Code 2020 [9].

Reliability-based PSFs [3, 7, 18, 19] are introduced for materials and resistance modeling, and for permanent actions and the modeling of load effects under gravity loads. These factors are expressed as functions of the annual reliability index [13, 14].

The calibrated format is then applied to the global model under self-weight by means of NLFEAs [11].

Further, in order to try to explain the possible interaction between homogenized multi-leaf masonry and travertine stone, two different interface hypotheses are considered: (i) the first with perfect bond (bounded interface) and (ii) the second one with tangential slip (unbounded interface). Three control nodes are placed at the intrados crowns of the main vaults to monitor a response that is both representative and damage-sensitive.

The CDP model for compression and tension behavior is used, and the stress-strain relationships resulting from this are provided in the design for both structural materials. The spatial evolution of tensile damage can be observed in chosen areas of the Basilica, indicating the initiation and localization of cracking, with a focus on the development of possible load-carrying mechanisms in the main vaults.

The global verification is based on the ULS. The chapter ends with a global reliability assessment based on the most critical vault and analyzes how the results compare to the chosen annual target reliability index, as well as how the existing methods can be extended to include additional actions or further parts of the Basilica (e.g., 16th-century body of the Basilica and its related substructures) in future development phases.

IX.2 Reliability-based calibration of partial safety factors

IX.2.1 Definition of partial factor for material properties

The evaluation of the material partial factor γ_m is based on the probabilistic characterization of the historic materials obtained from the experimental campaign and Bayesian inference (see Chapter V and Chapter VII).

Assuming a lognormal statistical model for the strength of the material X, the adjusted partial factor associated with the uncertainty of the material is calculated for a reference period of one year by adopting a resistance sensitivity factor $\alpha_R = 0.7$ (favorable actions). Denoting by X_k the characteristic value and by X_d the design value, the partial factor γ_m can be obtained as follows:

$$\gamma_m = \frac{X_k}{X_d} = \frac{\mu_X \exp\left(-1.645\, V_X\right)}{\mu_X \exp\left(-\alpha_R\, \beta\, V_X\right)} \tag{IX.1}$$

where μ_X and V_X are the mean and coefficient of variation of X, and $\beta = \Phi^{-1}(1 - P_f)$ is the annual reliability index corresponding to the probability of failure P_f.

Based on Eq. (IX.1), the resulting reliability–based curves of γ_m for homogenized multi-leaf masonry and travertine are presented as a function of P_f and are reported in Figure IX.1. The coefficients of variation used in the plots, based on the compressive strengths of the structural materials, are as follows: $V_{\text{hom}} = 0.20$ for the homogenized multi-leaf masonry and $V_{\text{trav}} = 0.41$ for travertine.

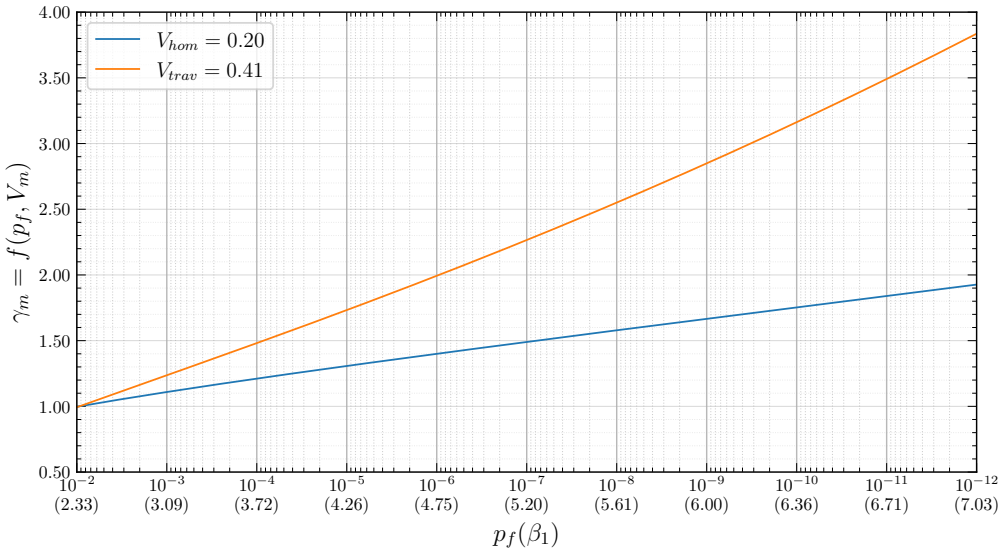

Figure IX.1: Evolution of the material partial factor γ_m versus failure probability P_f for homogenized multi–leaf masonry and travertine.

The resistance model's uncertainties are represented by the random variable θ_R, which is assumed to be normally distributed, with mean $\mu_{\theta R}$ and coefficient of variation $V_{\theta R}$.

In this study, in the absence of building-specific validation data for the present NLFEAs, a representative value of $V_{\theta R} = 0.20$ is used, based on engineering judgment. A resistance sensitivity factor $\alpha_R = 0.7$ (favorable actions) accounts for the ultimate resistance's sensitivity to the basic underlying factors, resulting in an effective factor $\tilde{\alpha}_R = 0.4\,\alpha_R$ for a one-year reference.

Under these assumptions (normal model factor and FORM), the adjusted resistance-model partial factor can be obtained as follows:

$$\gamma_{Rd} = \frac{\mu_{\theta R}}{\theta_{Rd}} = \frac{1}{1 - \tilde{\alpha}_R\,\beta\,V_{\theta R}} \tag{IX.2}$$

Based on Eq. (IX.2), the curves $\gamma_{Rd}(P_f)$ for different coefficients of variation are shown in Figure IX.2.

In general, $V_{\theta R}$ should be derived by: (i) assembling a representative validation set (tests or high-fidelity simulations) for the same class of structural response; (ii) computing the model factor $\theta_R = R_{\text{exp}}/R_{\text{model}}$ under consistent loading and boundary conditions; (iii) estimating $\mu_{\theta R}$ and $V_{\theta R}$; and (iv) performing posterior predictive checks as well as mesh and parameter sensitivity analyses to ensure that the estimated dispersion is robust and not dominated by numerical artifacts.

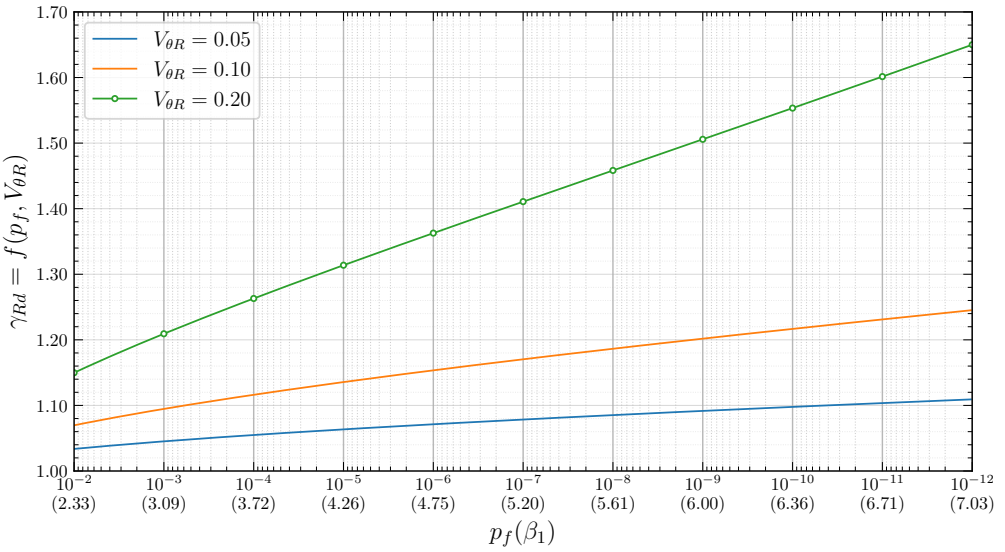

Figure IX.2: Evolution of the resistance model uncertainties partial factor γ_{Rd} versus failure probability P_f for homogenized multi–leaf masonry and travertine (green curve).

Values of $V_{\theta R}$ in reliability formats and semi-probabilistic frameworks typically range between 0.05 and 0.30, depending on the model complexity and the type of failure mechanism considered [6].

Considering the additional uncertainties associated with historic multi-leaf masonry (ARC core) and interface behavior, this value is regarded as a reasonable estimate based on engineering judgment, while it may be refined in future validation studies.

For the assessment of existing structures, the partial factor applied to NLFEAs resistance when material strengths are taken as representative (mean) values is obtained by a separate factor approach according to DVM as the product of the material partial factor γ_m and the resistance model partial factor γ_{Rd}:

$$\gamma_M = \gamma_m \gamma_{Rd} \tag{IX.3}$$

with γ_m and γ_{Rd} defined in Eq. (IX.1) and Eq. (IX.2), respectively.
Based on Eq. (IX.3) and on the statistical parameters adopted for γ_{Rd} and γ_m described above, the resulting reliability–based curves of γ_M for homogenized multi-leaf masonry and travertine are shown as a function of the probability of failure P_f in Figure IX.3.

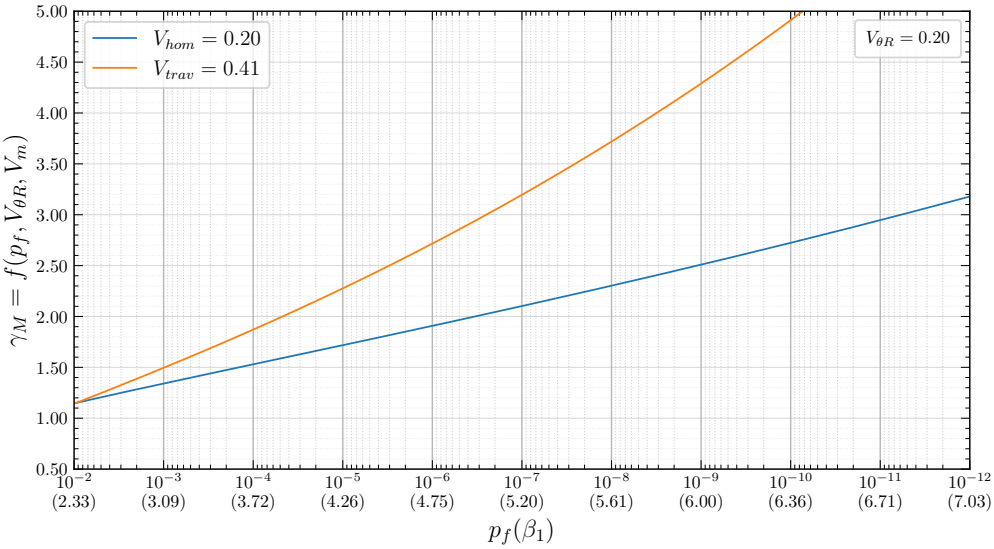

Figure IX.3: Evolution of the material partial factor γ_M versus failure probability P_f for homogenized multi–leaf masonry and travertine.

IX.2.2 Definition of partial factor for effects of actions

The reliability-based partial factor γ_g accounts for the variability of the permanent action G. In addition to the structural self-weight (G_1), other permanent non-structural

actions (G_2) were considered in the present study. These include architectural elements such as pilasters, cornices, and roof components, which were converted into equivalent permanent loads acting on the structure (see Chapter VIII). In particular, a normal distribution is assumed, and two representative values of the coefficient of variation are considered:
(i) self–weight, $V_{g1} = 0.04$; (ii) other permanent non–structural loads, $V_{g2} = 0.10$.

Using a load-effect sensitivity factor $\alpha_E = -0.8$ (unfavorable actions) for a one-year reference period, the design value of permanent action is $G_d = \mu_g - \alpha_E\,\beta\,\sigma_g$. Taking the representative value as $G_k = \mu_g$, the resulting partial factor can be obtained as follows:

$$\gamma_g = \frac{G_d}{G_k} = \frac{\mu_g - \alpha_E\,\beta\,\sigma_g}{\mu_g} = 1 - \alpha_E\,\beta\,V_g \tag{IX.4}$$

Based on Eq. (IX.4), the resulting curves of γ_g as a function of the probability of failure P_f are presented in Figure IX.4.

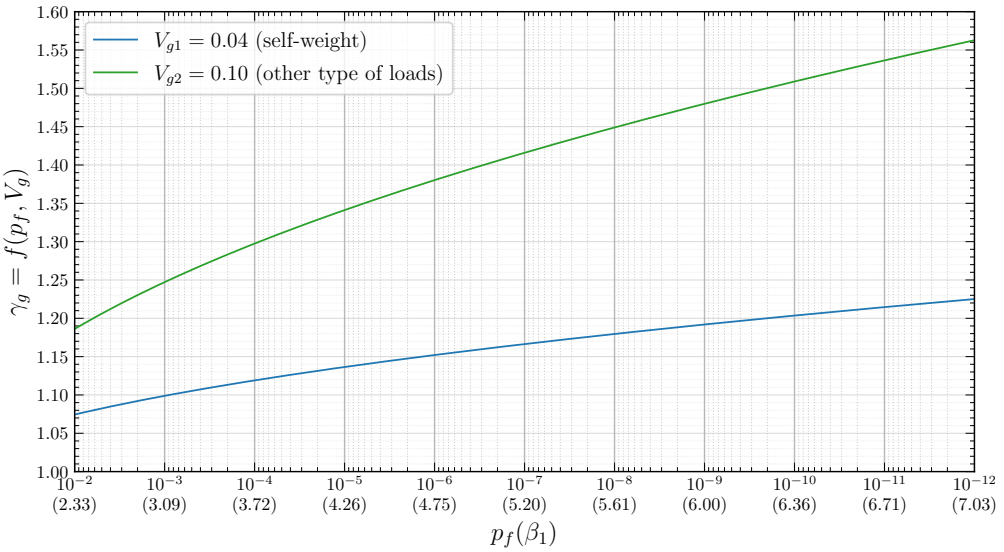

Figure IX.4: Evolution of the permanent–action partial factor γ_g versus failure probability P_f for self-weight and other type of loads.

Uncertainties in the modeling of load effects under gravity are represented by the random model factor θ_E, assumed to be normally distributed with mean $\mu_{\theta E}$ (taken as 1.0) and coefficient of variation $V_{\theta E} = \sigma_{\theta E}/\mu_{\theta E}$. These uncertainties stem from idealized boundary conditions, discretization/regularization choices, interface–contact modeling, and non-linear solver settings, all of which affect the internal forces computed under permanent loads.

Within a FORM over a one-year reference period and adopting a load–effect sensitivity factor $\alpha_E = -0.8$ (unfavorable actions), the corresponding reliability-based partial factor can be obtained as follows:

$$\gamma_{Ed,G} = 1 - 0.4\,\alpha_E\,\beta\,V_{\theta E} \tag{IX.5}$$

Using Eq. (IX.5) with $V_{\theta E} = 0.10$ for bending and shear, the resulting $\gamma_{Ed,G}(P_f)$ curve is shown in orange in Fig. IX.5.

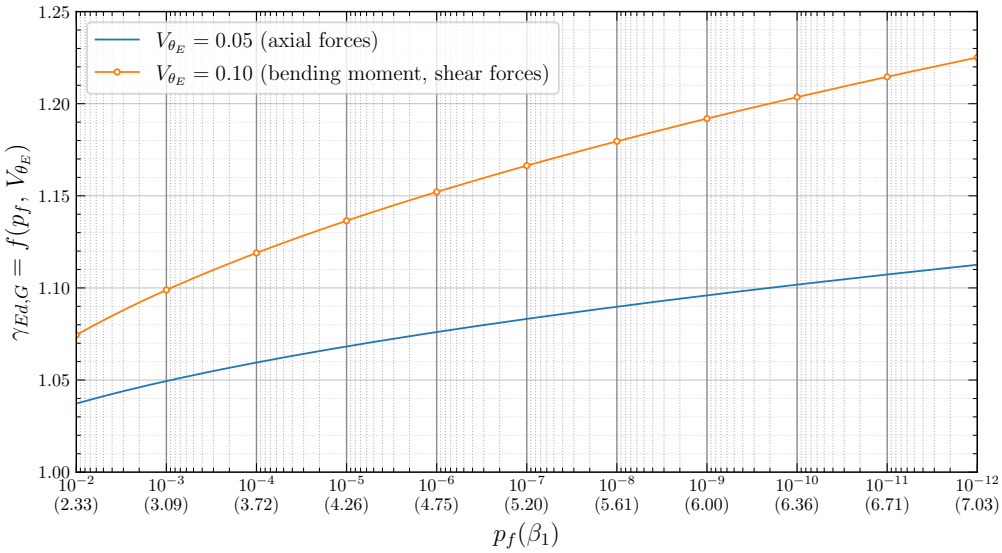

Figure IX.5: Evolution of the load–effect modeling partial factor $\gamma_{Ed,G}$ versus failure probability P_f for bending moment and shear-force effects (orange curve).

For the assessment of existing structures within separate–factor approach of the DVM, the design action effect due to permanent loads is obtained by applying a combined factor as follows:

$$\gamma_G = \gamma_g\,\gamma_{Ed,G} \tag{IX.6}$$

with γ_g and $\gamma_{Ed,G}$ defined in Eq. (IX.4) and Eq. (IX.5), respectively.

Based on Eq. (IX.6) and on the statistical parameters adopted for γ_g and $\gamma_{Ed,G}$ described above, the resulting reliability–based curves of γ_G as a function of the probability of failure P_f are presented in Figure IX.6. In particular, separate curves are reported for γ_{G1} (self-weight, in blue) and γ_{G2} (other permanent non-structural loads, in orange).

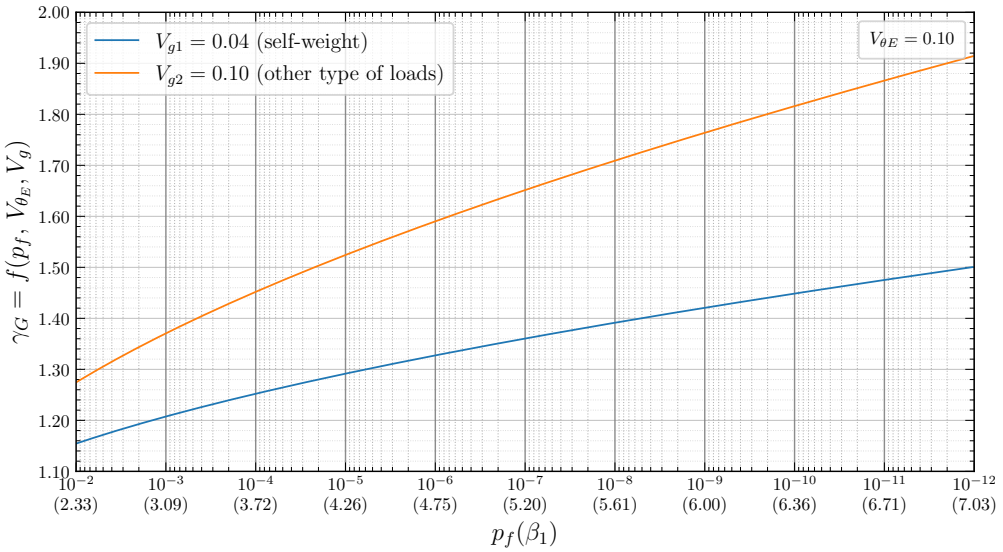

Figure IX.6: Evolution of the permanent action factor γ_G versus failure probability P_f for self-weight and other type of loads.

Table IX.1 summarizes the reliability-based PSFs for actions and resistances adopted in the 3D FE models of St. Peter's Basilica, expressed as functions of the annual reliability index β with a failure probability P_f ranging from 10^{-2} to 10^{-12}.

Table IX.1: Summary of the reliability-based PSFs for loads and resistances as functions of annual reliability index β.

β_1	P_f	γ_{G1}	γ_{G2}	γ_{Rd}	$\gamma_{m,\text{hom}}$	$\gamma_{m,\text{trav}}$	$\gamma_{M,\text{hom}}$	$\gamma_{M,\text{trav}}$
2.33	1.00×10^{-2}	1.15	1.27	1.15	1.00	1.00	1.15	1.15
2.73	3.16×10^{-3}	1.18	1.32	1.18	1.05	1.12	1.24	1.32
3.09	1.00×10^{-3}	1.21	1.37	1.21	1.11	1.24	1.34	1.50
3.42	3.16×10^{-4}	1.23	1.41	1.24	1.16	1.36	1.44	1.68
3.72	1.00×10^{-4}	1.25	1.45	1.26	1.21	1.48	1.53	1.87
4.00	3.16×10^{-5}	1.27	1.49	1.29	1.26	1.61	1.62	2.07
4.26	1.00×10^{-5}	1.29	1.52	1.31	1.31	1.73	1.72	2.27
4.52	3.16×10^{-6}	1.31	1.56	1.34	1.35	1.86	1.81	2.50
4.75	1.00×10^{-6}	1.33	1.59	1.36	1.40	1.99	1.91	2.71
4.98	3.16×10^{-7}	1.34	1.62	1.39	1.45	2.13	2.00	2.95
5.20	1.00×10^{-7}	1.36	1.65	1.41	1.49	2.27	2.10	3.20
5.41	3.16×10^{-8}	1.38	1.68	1.43	1.53	2.41	2.20	3.45
5.61	1.00×10^{-8}	1.39	1.71	1.46	1.58	2.55	2.30	3.72
5.81	3.16×10^{-9}	1.41	1.74	1.48	1.62	2.70	2.41	4.00
6.00	1.00×10^{-9}	1.42	1.76	1.51	1.67	2.85	2.51	4.29
6.18	3.16×10^{-10}	1.43	1.79	1.53	1.71	3.00	2.61	4.59
6.36	1.00×10^{-10}	1.45	1.82	1.55	1.75	3.16	2.72	4.91
6.54	3.16×10^{-11}	1.46	1.84	1.58	1.80	3.33	2.84	5.25
6.71	1.00×10^{-11}	1.48	1.87	1.60	1.84	3.49	2.95	5.60
6.87	3.16×10^{-12}	1.49	1.89	1.63	1.88	3.66	3.06	5.95
7.03	1.00×10^{-12}	1.50	1.91	1.65	1.93	3.83	3.18	6.32

IX.3 Safety assessment: application of the partial factor method

In standard practice, the PFM in its Level-I formulation, as implemented in *fib* Model Code 2020 [9] and EN 1990 [8], is applied by means of local linear-elastic checks in the most stressed sections (component level), by following the inequality:

$$E_d \leq R_d \quad \text{(local, linear checks)}.$$

Following a global safety format [1, 4], the structural capacity is assessed through 3D NLFEAs, and the safety condition is verified at the system level by comparing the design value of external actions with the global design resistance, according to the following inequality:

$$F_d \leq R_d \quad \text{(global, NLFEAs-based check)}.$$

In the present study, the safety verification is not expressed through a direct comparison between action effects and resistance values. Instead, the design actions are applied to the global NLFE model, and the ULS is assessed by verifying the absence of collapse mechanisms, identified through the accumulation and localization of damage in critical regions.

In particular, the ULS is associated with the onset of a collapse mechanism. This mechanism is identified by the formation of extended damaged zones and kinematically admissible mechanisms in the non-linear response of the masonry vaults.

Accordingly, the limit state function may be expressed in a generalized form as

$$g(X) = R(X) - E(X) \tag{IX.7}$$

where X denotes the set of basic random variables.

In the present framework, the resistance term $R(X)$ is associated with a critical threshold value Φ_{crit} defining the activation of a collapse mechanism, while the action effect $E(X)$ is associated with a global response indicator $\Phi_{\text{NLFEA}}(X)$ obtained from the NLFEAs.

Specifically, the indicator Φ_{NLFEA} is defined in terms of the tensile damage variable d_t of the CDP model, which is used to characterize the accumulation and localization of tensile damage in the structure. The variable d_t ranges between 0 (undamaged material) and 1 (fully damaged material) and provides a physically meaningful measure of crack initiation and propagation.

In the present study, the verification at the ULS is not performed locally, but rather at the global system level: what matters is not the peak tensile damage in a single FE, but the development and propagation of an extended crack that could potentially activate a collapse mechanism. The design value of the structural resistance is evaluated with NLFEAs by the following equations:

$$R_d(\beta) = \frac{R_{\mathrm{NLFEA}}(f_d)}{\gamma_{Rd}(\beta)}; \qquad f_d(\beta) = \frac{f_m}{\gamma_m(\beta)} \tag{IX.8}$$

where f_m denotes the representative mean strengths (both in compression and tension) of ancient homogenized multi-leaf masonry and of travertine stone, estimated probabilistically through Bayesian inference of the experimental data (see Chapter VII for details on the probabilistic characterization of the principal parameters of structural materials).

The design value of the external actions are obtained by applying the appropriate PSFs only to the permanent actions:

$$F_d(\beta) = \gamma_G(\beta) \sum_k G_k \tag{IX.9}$$

where G_k denotes the representative mean value of the actions (i.e., self-weight, other type of loads), estimated deterministically in this study based on nominal values.

A multi-level assessment is carried out using NLSAs on the global 3D NLFE model under gravity loads. For a set of annual reliability levels β, permanent actions are factored into $\gamma_G(\beta)$, and the material strengths (in compression and in tension) are reduced to the design values f_d through $\gamma_M(\beta) = \gamma_m(\beta)\,\gamma_{Rd}(\beta)$.

Two 3D FE models with different interface hypotheses are considered: (i) Model A — bounded interface, with perfect bond between homogenized multi-leaf masonry and travertine; and (ii) Model B — unbounded interface in which the two materials are separated by an interface allowing tangential slip (see Chapter VIII for detailed modeling assumptions).

For masonry vaults, the failure is typically global rather than isolated component failure: a system mechanism forms when a sufficient number of plastic hinges (typically four) develop in distinct sections. Due to the non-linear nature of the problem, a closed-form limit-state function is not generally available; the reliability assessment is carried out by simulation with 3D NLFEAs, using a mechanism-based failure criterion [2].

This global, mechanism-based approach, combined with the PFM with calibrated PSFs, provides a consistent and practicable framework for assessing the safety of the monumental masonry building under gravity loads.

IX.3.1 Design strengths

To obtain the design strengths f_d, the global 3D FE model adopts the non-linear CDP model. For each target reliability index β, the peak compressive and tensile strengths $\{f_c, f_t\}$ are reduced by the combined material factor $\gamma_M(\beta)$ calibrated through the DVM (ref. Eq. (IX.8)).

The reduction is applied directly at the material level: stiffness parameters (E) and strain measures (at peak and at maximum point) are kept unchanged, while only the stress ordinates at the peaks are scaled. This assumption was adopted as a simplification: it allows lowering the design capacity without modifying the overall shape of the stress–strain response, preserving pre-peak stiffness and post-peak softening behavior.

Formally, $f_{c,d} = f_c/\gamma_M(\beta)$ and $f_{t,d} = f_t/\gamma_M(\beta)$, resulting in the design stress–strain curves $\sigma_d(\varepsilon)$ obtained by scaling the strength-governed portions of $\sigma(\varepsilon)$ by $\gamma_M(\beta)$.

The resulting design stress–strain curves and the solver's CDP stress–inelastic-strain and damage–strain laws for the structural materials (for representative values of β) are shown below.

(i) homogenized multi-leaf masonry, uniaxial compressive and tensile behavior in Figures IX.7 and IX.8, respectively;

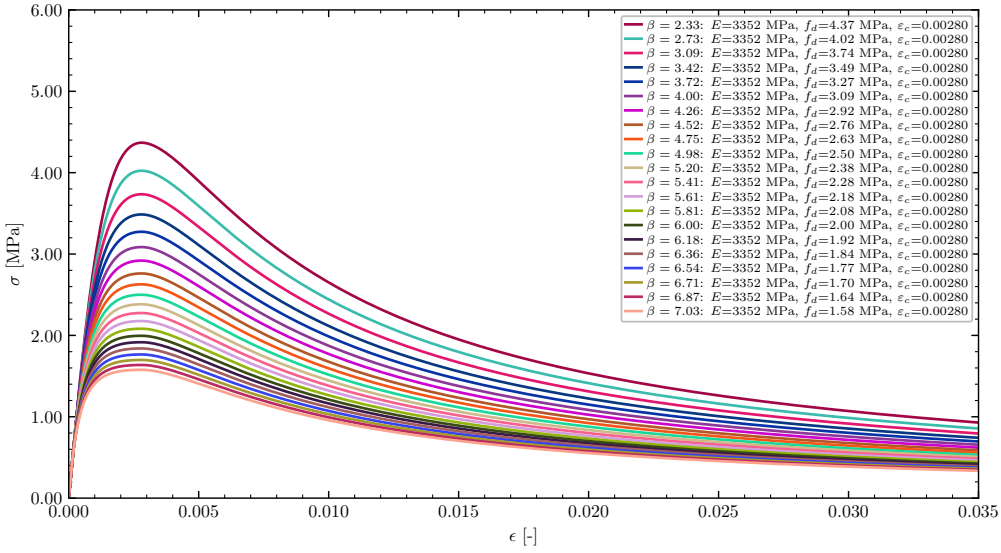

Figure IX.7: Reliability-based stress-strain curves: Uniaxial compression for the homogenized multi-leaf masonry.

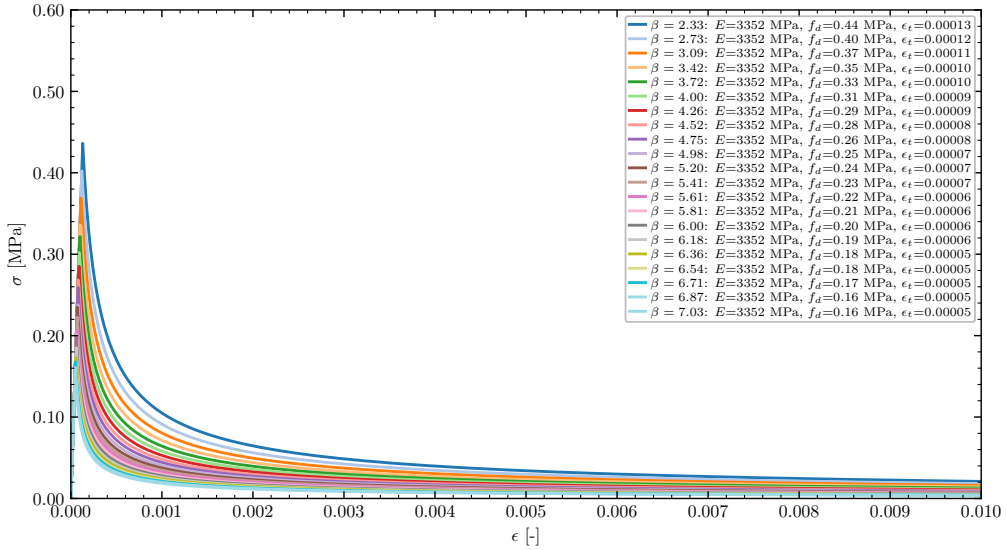

Figure IX.8: Reliability-based stress-strain curves: Uniaxial tension for the homogenized multi-leaf masonry.

(ii) Travertine stone, uniaxial compression and tension in Figures IX.9 and IX.10;

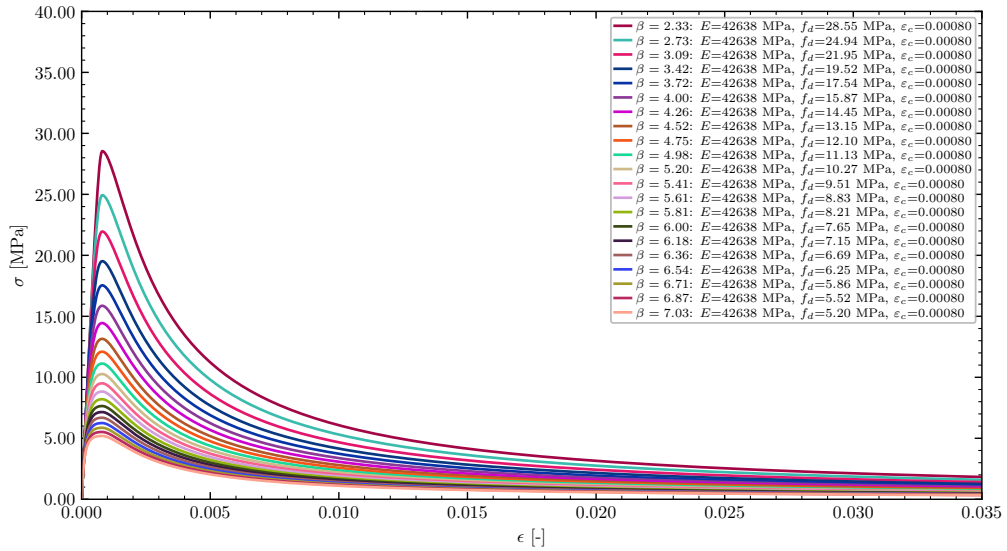

Figure IX.9: Reliability-based stress-strain curves: Uniaxial compression for the travertine stone.

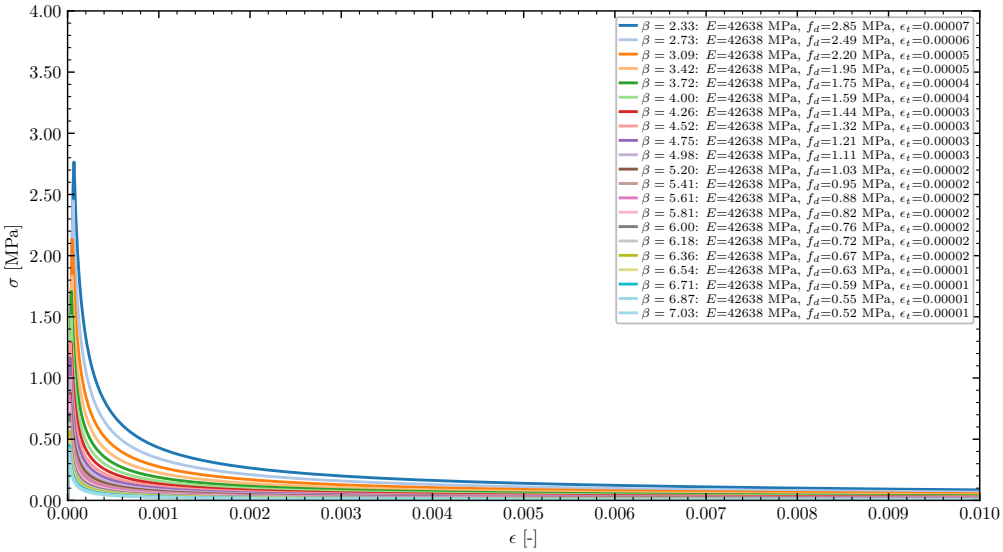

Figure IX.10: Reliability-based stress-strain curves: Uniaxial tension for the travertine stone.

Further, the CDP curves are reported for (i) the homogenized multi-leaf masonry in compression (Figs. IX.11 and IX.12);

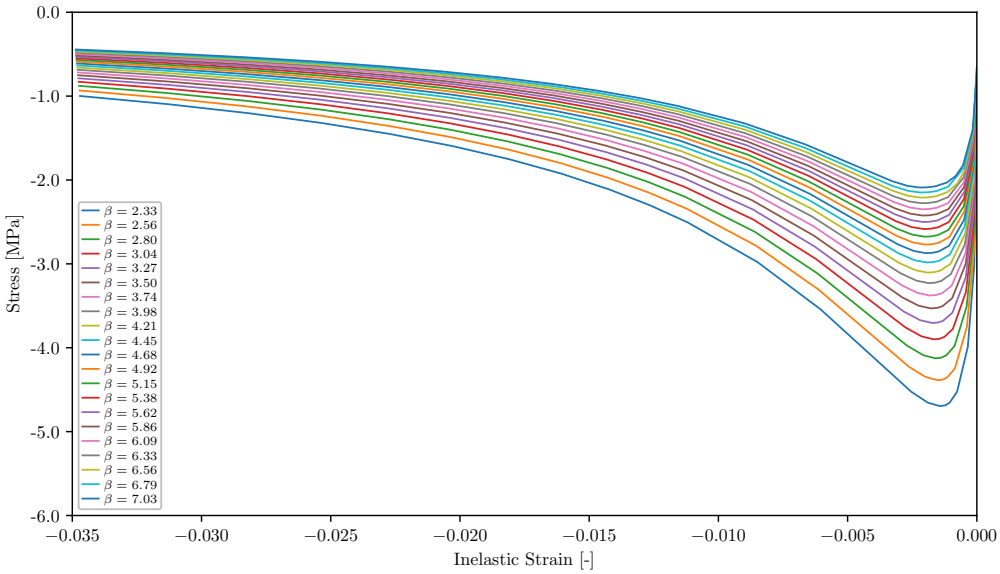

Figure IX.11: Reliability-based CDP in FE software, inelastic strain-stress curves: Uniaxial compression for the homogenized multi-leaf masonry.

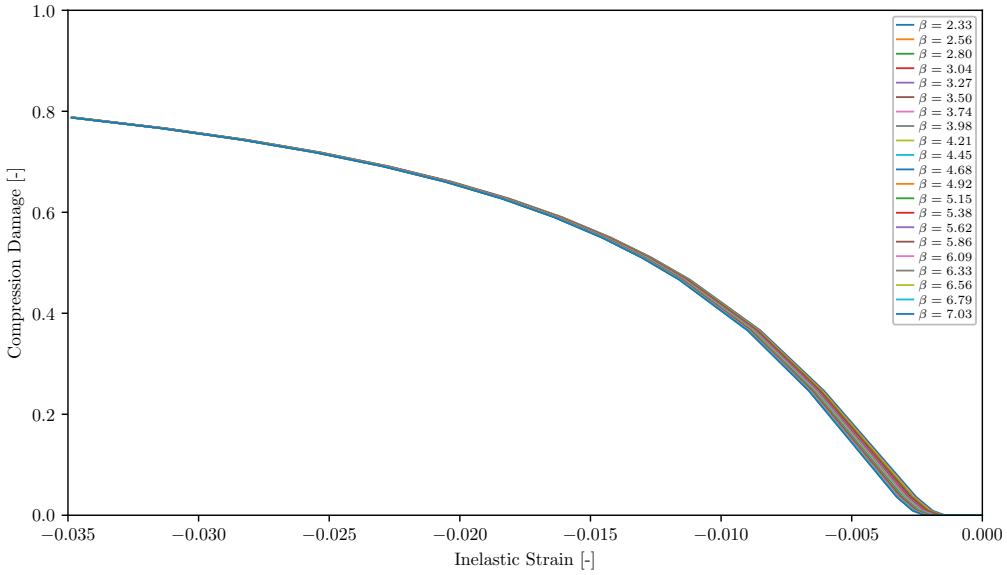

Figure IX.12: Reliability-based CDP in FE software, inelastic strain-compression damage curves: Uniaxial compression for the homogenized multi-leaf masonry.

(ii) homogenized multi-leaf masonry in tension, Figures IX.13 and IX.14;

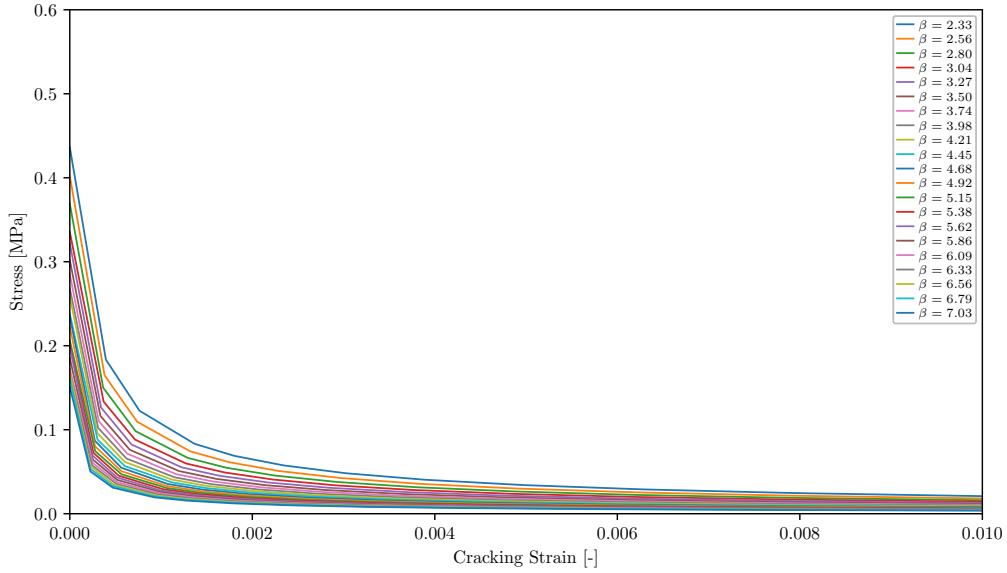

Figure IX.13: Reliability-based CDP in FE software, cracking strain-stress curves: Uniaxial tension for the homogenized multi-leaf masonry.

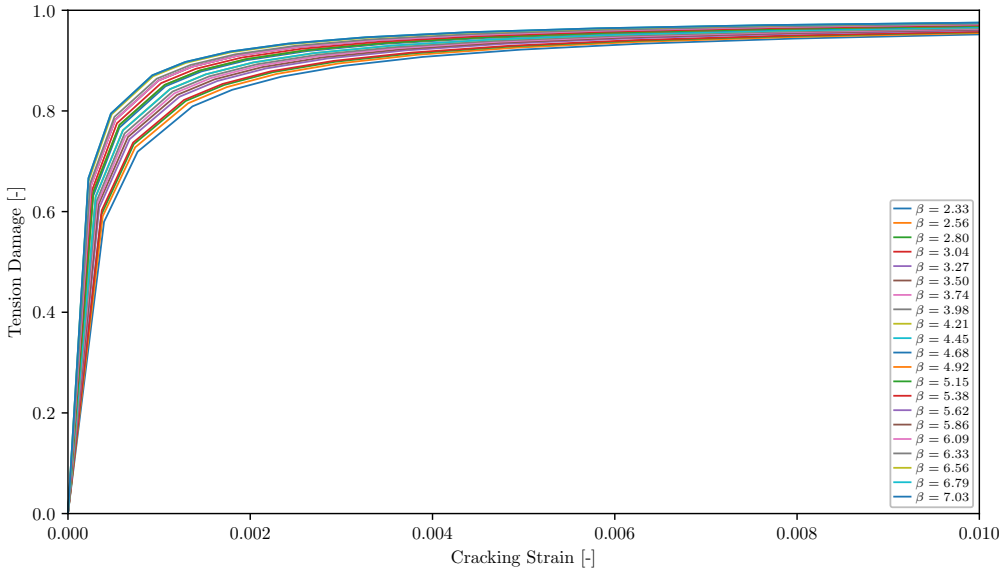

Figure IX.14: Reliability-based CDP in FE software, cracking strain-tension damage curves: Uniaxial tension for the homogenized multi-leaf masonry.

(iii) travertine in compression, Figures IX.15 and IX.16;

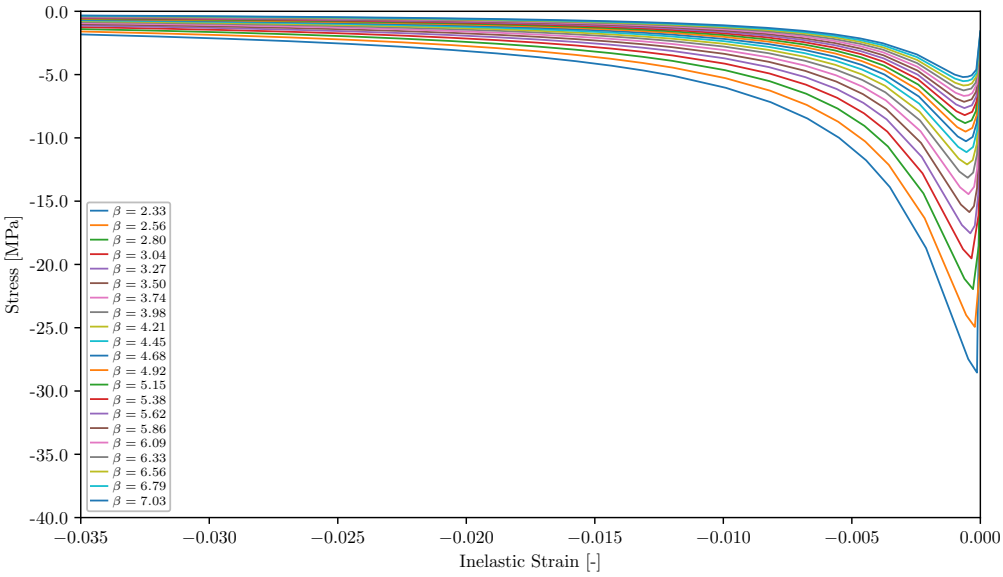

Figure IX.15: Reliability-based CDP in FE software, inelastic strain-stress curves: Uniaxial compression for the travertine stone.

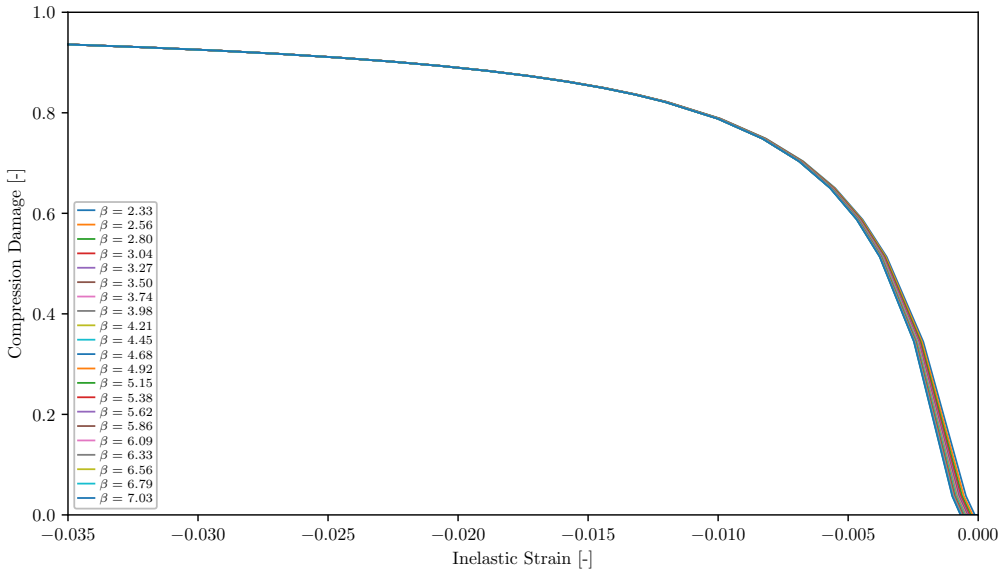

Figure IX.16: Reliability-based CDP in FE software, inelastic strain-compression damage curves: Uniaxial compression for the travertine stone.

(iv) travertine in tension, Figures IX.17 and IX.18.

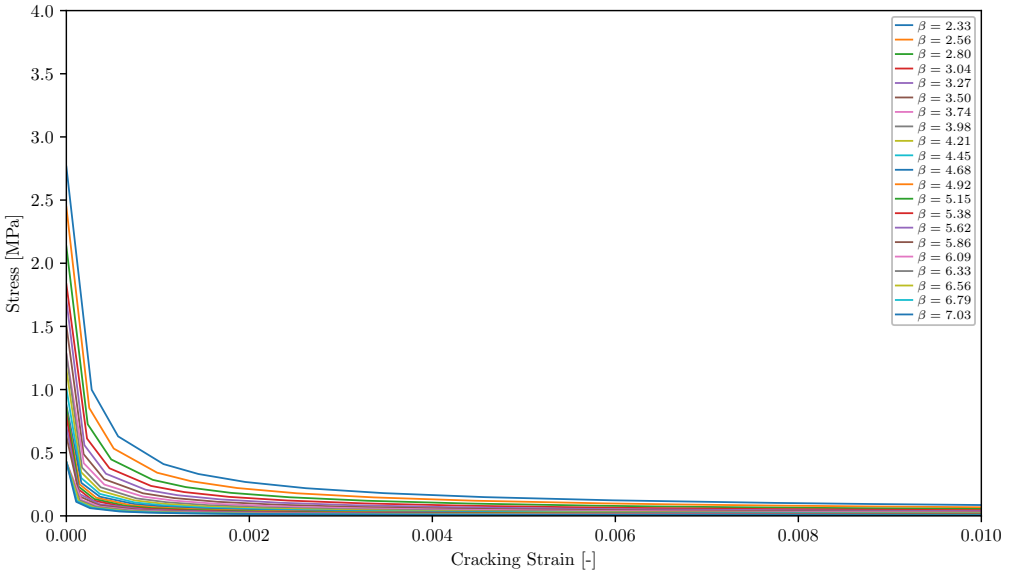

Figure IX.17: Reliability-based CDP in FE software, cracking strain-stress curves: Uniaxial tension for the travertine stone.

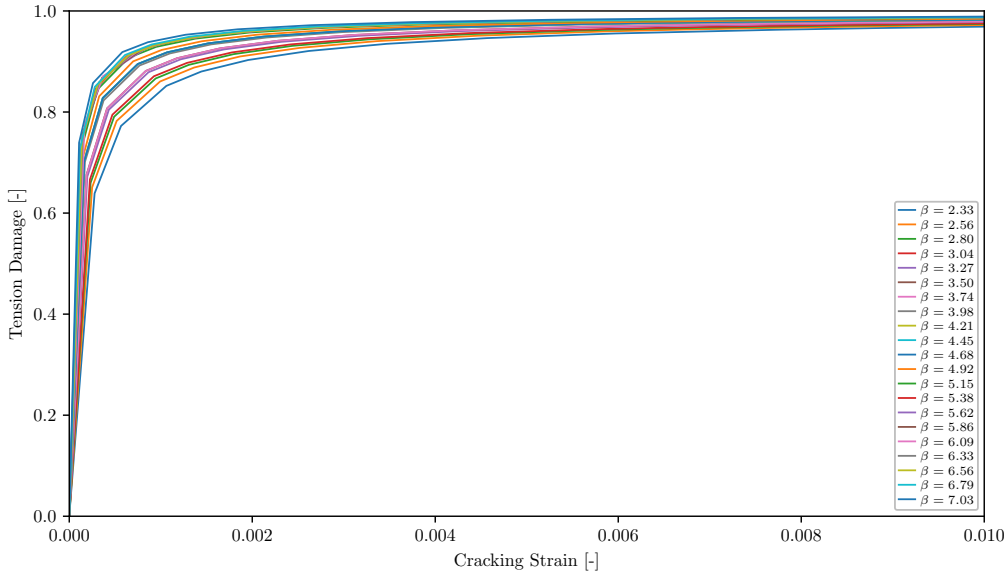

Figure IX.18: Reliability-based CDP in FE software, cracking strain-tension damage curves: Uniaxial tension for the travertine stone.

IX.3.2 Reliability index assessment

As shown in Figure IX.19, three control nodes were selected in the crown (mid-span) of the main masonry vaults of the Basilica extrados to track the evolution of the structural response. Those control nodes are chosen: node 1 - central nave vault, node 2 - Hall of Blessings vault, and node 3 - Atrium vault.

The mid-span crowns were chosen as control points because they are kinematically critical: (i) they coincide with the position of maximum deformation bending under self-weight, (ii) their vertical response is highly sensitive to global stiffness degradation (cracking/damage), thus providing early warning signs of hinge formation and mechanism development, and (iii) they are less affected by local boundary artifacts, allowing consistent comparison across 3D NLFE models and β levels.

In the case of monumental masonry structures such as St. Peter's Basilica, the global structural behavior under ordinary conditions is predominantly governed by permanent actions. Assuming no explicit modeling of material degradation processes, both the load effect associated with permanent actions and the structural resistance may be considered time-invariant. As a result, the limit state function is not time dependent, and the related reliability index remains constant across the reference period (see Figure II.5 in Chapter II).

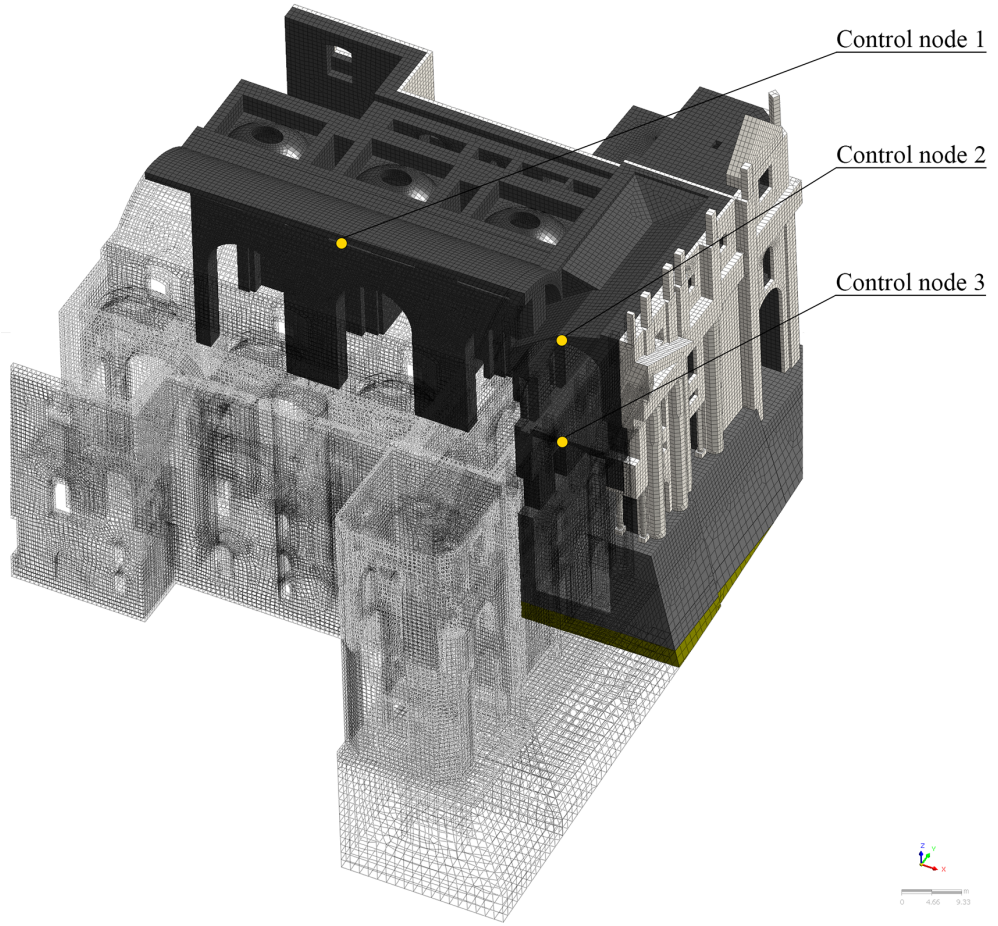

Figure IX.19: Schematic of the control-node locations in the global 3D NLFE model of St. Peter's Basilica.

Figures IX.20, IX.21 and IX.22 report the gravity load–displacement curves, P, at Control Node 1 (central nave vault), Control Node 2 (Hall of Blessings), and Control Node 3 (Atrium), respectively, for the two interface hypotheses (Model A and Model B).

The comparison isolates the role of the masonry–travertine interface: Model A (bounded interface) exhibits a higher initial stiffness and a delayed departure from linearity, whereas Model B (unbounded interface) shows larger vertical displacements and an earlier non-linear response due to tangential slip along the interface.

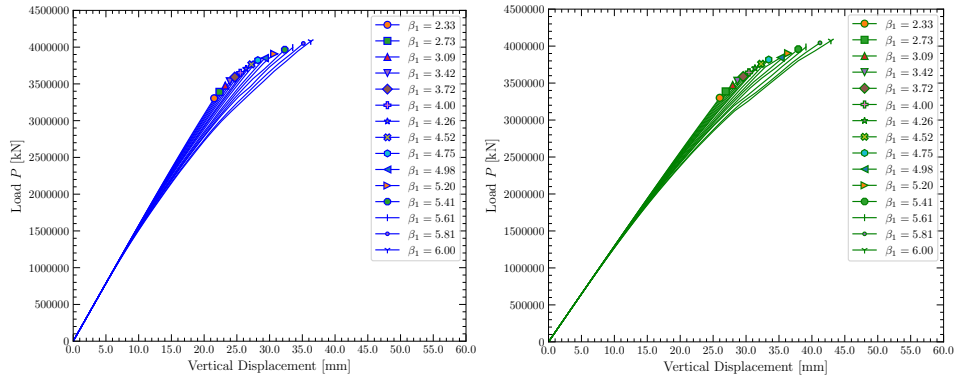

(a) (b)

Figure IX.20: Load–displacement curves — Control node 1 (central nave vault): (a) Reliability-based curve for Model A; (b) Reliability-based curve for Model B.

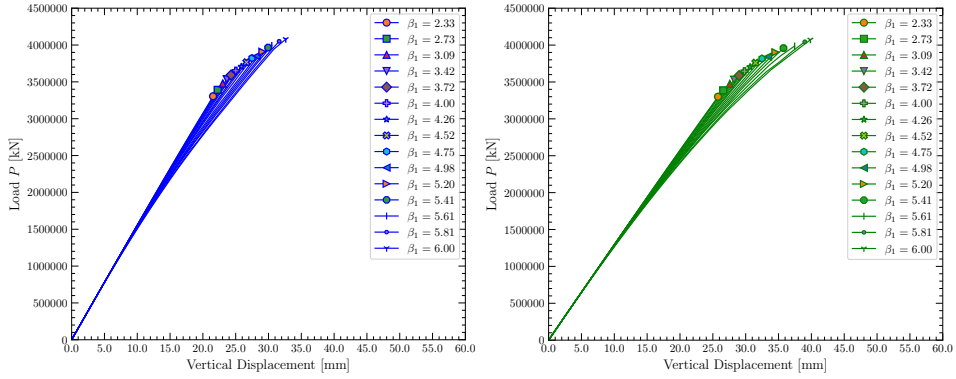

(a) (b)

Figure IX.21: Load–displacement curves — Control node 2 (Hall of Blessings vault): (a) Reliability-based curve for Model A; (b) Reliability-based curve for Model B.

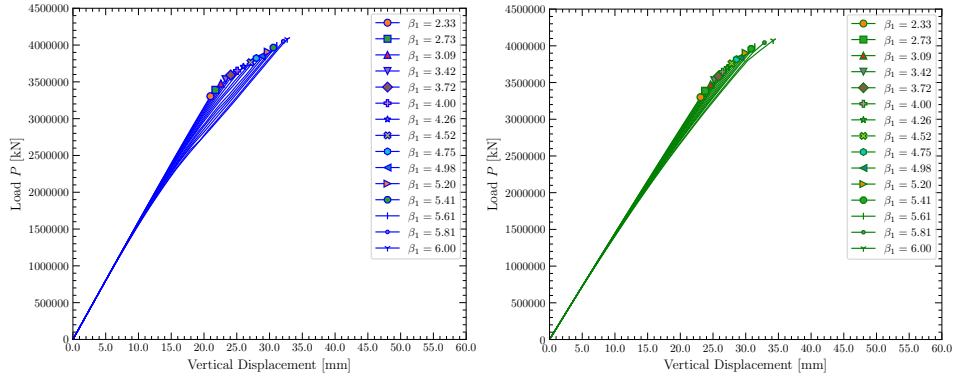

(a) (b)

Figure IX.22: Load–displacement curves — Control node 3 (Atrium vault): (a) Reliability-based curve for Model A; (b) Reliability-based curve for Model B.

Figures IX.23, IX.24 and IX.25 show, for the same control nodes, the vertical displacement at the design gravity level as a function of the annual reliability index β for both models. As β increases (i.e., as more conservative partial factors are adopted), only the peak strengths f_d are reduced while the elastic moduli remain unchanged; accordingly, the vaults become more compliant and the displacements tend to increase monotonically with β.

For reference, a target reliability index $\beta_t = 4.2$ is adopted, in accordance with international recommendations for structures with high societal and cultural importance [15], [9].

The reliability index $\beta_{\text{assessment}}$ was evaluated for both Model A and Model B at the onset of plastic hinge formation in the main investigated vaults. For each vault, a representative value was defined as the average of the two estimates obtained from the considered models:

$$\beta_{\text{assessment}}^{(i)} = \frac{1}{2}\left(\beta_A^{(i)} + \beta_B^{(i)}\right) \tag{IX.10}$$

where i denotes the i-th vault investigated.

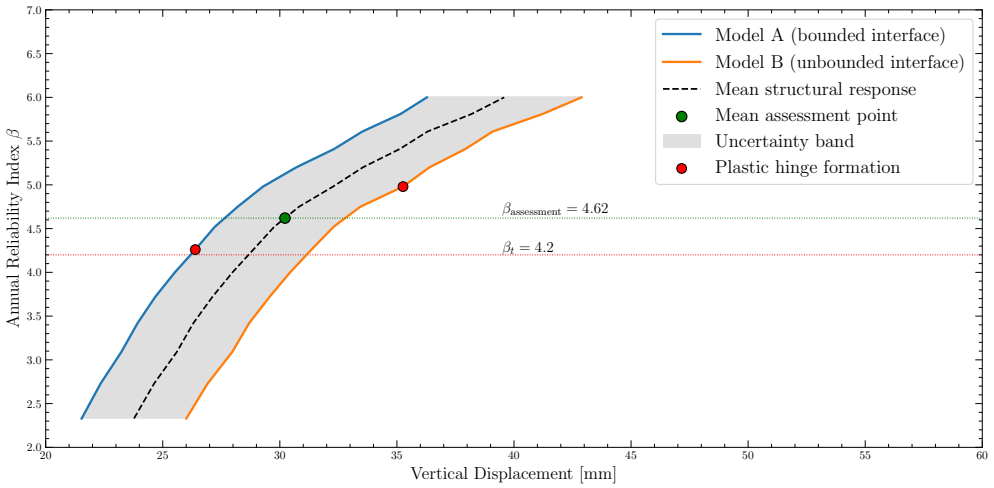

Figure IX.23: Displacement vs Annual reliability index curves: Control node 1 (central nave vault).

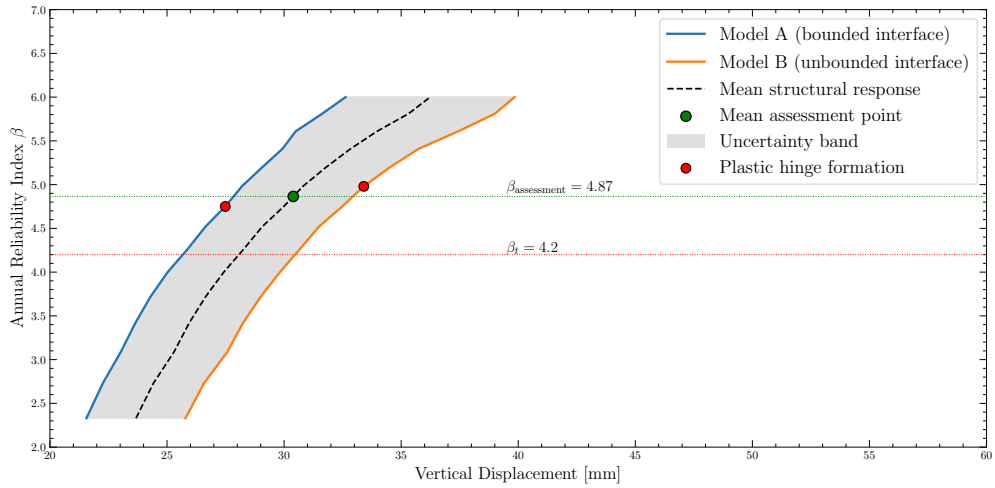

Figure IX.24: Displacement vs Annual reliability index curves - Control node 2 (Hall of Blessings vault).

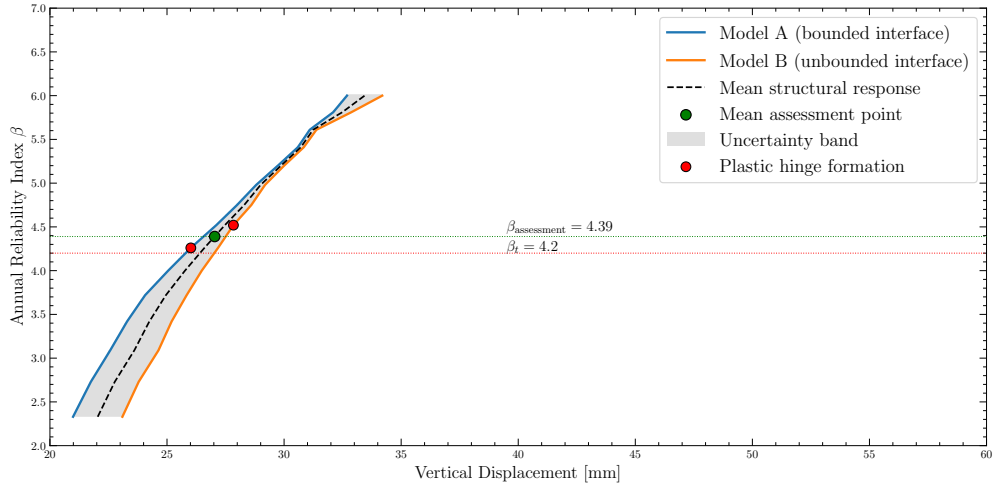

Figure IX.25: Displacement vs Annual reliability index curves - Control node 3 (Atrium vault).

Table IX.2 summarizes the reliability indices evaluated at the onset of plastic hinge formation in the principal investigated vaults.

Table IX.2: Summary of the reliability assessment in terms of annual reliability index β and corresponding vertical displacement.

	Model A		Model B		Mean value	
Control node	δ_v [mm]	$\beta_{\text{assessment}}$	δ_v [mm]	$\beta_{\text{assessment}}$	δ_v [mm]	$\beta_{\text{assessment}}$
1	26.39	4.26	35.26	4.98	30.22	4.62
2	27.49	4.75	33.40	4.98	30.39	4.87
3	23.38	4.26	27.84	4.52	25.68	4.39

The global reliability index for the entire structure can be conservatively defined as the minimum value among the average indices of the analyzed vaults, namely:

$$\beta_{\text{assessment}}^{\text{global}} = \min_i \left(\beta_{\text{assessment}}^{(i)} \right) \tag{IX.11}$$

In particular, a global value of $\beta_{\text{assessment}} = 4.39$ (corresponding to an annual failure probability of approximately $p_f \approx 5 \times 10^{-6}$) is obtained at the system level by considering the most critical condition.

This minimum value corresponds to the Atrium vault, which exhibits the earliest formation of continuous hinge lines under tensile damage, indicating the potential activation of a global failure mechanism.

The following figures illustrate the evolution of the tensile damage field d_t under gravity loads, showing the increase of the annual reliability index from $\beta = 2.33$ to the estimated $\beta_{\text{assessment}}$ at the attainment of the considered ULS.

For the bounded-interface configuration (3D NLFE Model A), see Figures IX.26, IX.28, and IX.30; for the unbounded-interface configuration (3D NLFE Model B), see Figures IX.27, IX.29, and IX.31.

The plots report $d_t \in [0, 1]$ on representative cross sections, where higher d_t values indicate greater crack opening and stiffness degradation. As β increases (i.e., as more conservative PSFs are adopted), earlier cracking and progressive localization are observed, with damage concentrating in kinematically critical locations such as the crown and adjacent high-curvature regions.

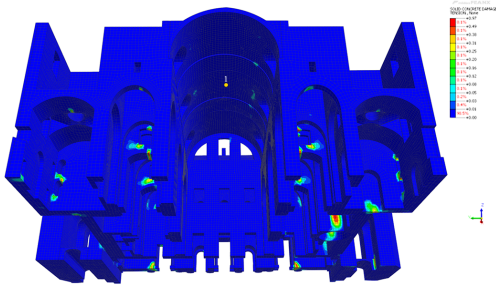

(a) $\beta = 2.33$

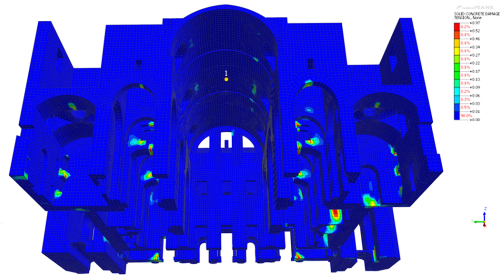

(b) $\beta = 2.73$

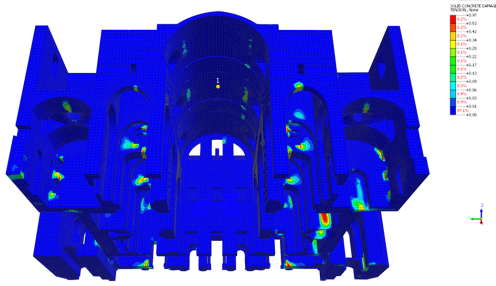

(c) $\beta = 3.09$

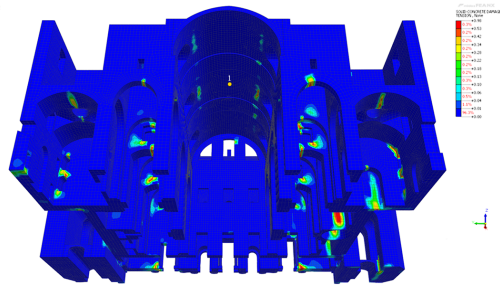

(d) $\beta = 3.42$

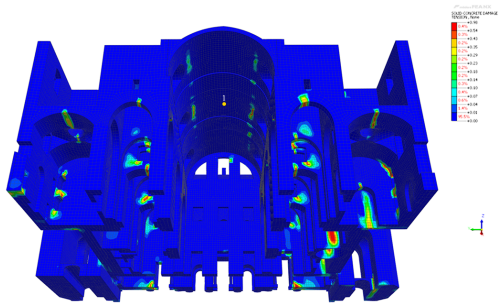

(e) $\beta = 3.72$

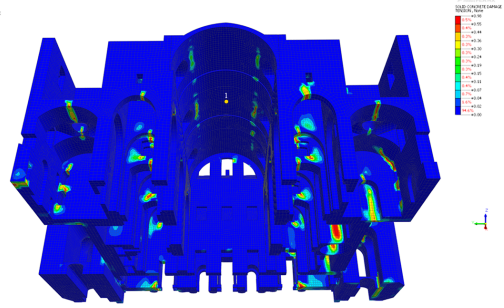

(f) $\beta = 4.00$

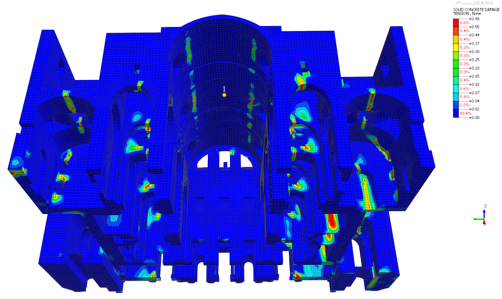

(g) $\beta = 4.26$

Figure IX.26: Reliability-based tensile-damage maps d_t on a cross-section of 3D NLFE model A: (a)–(g) β ranging from 2.33 to 4.26 for the central nave vault.

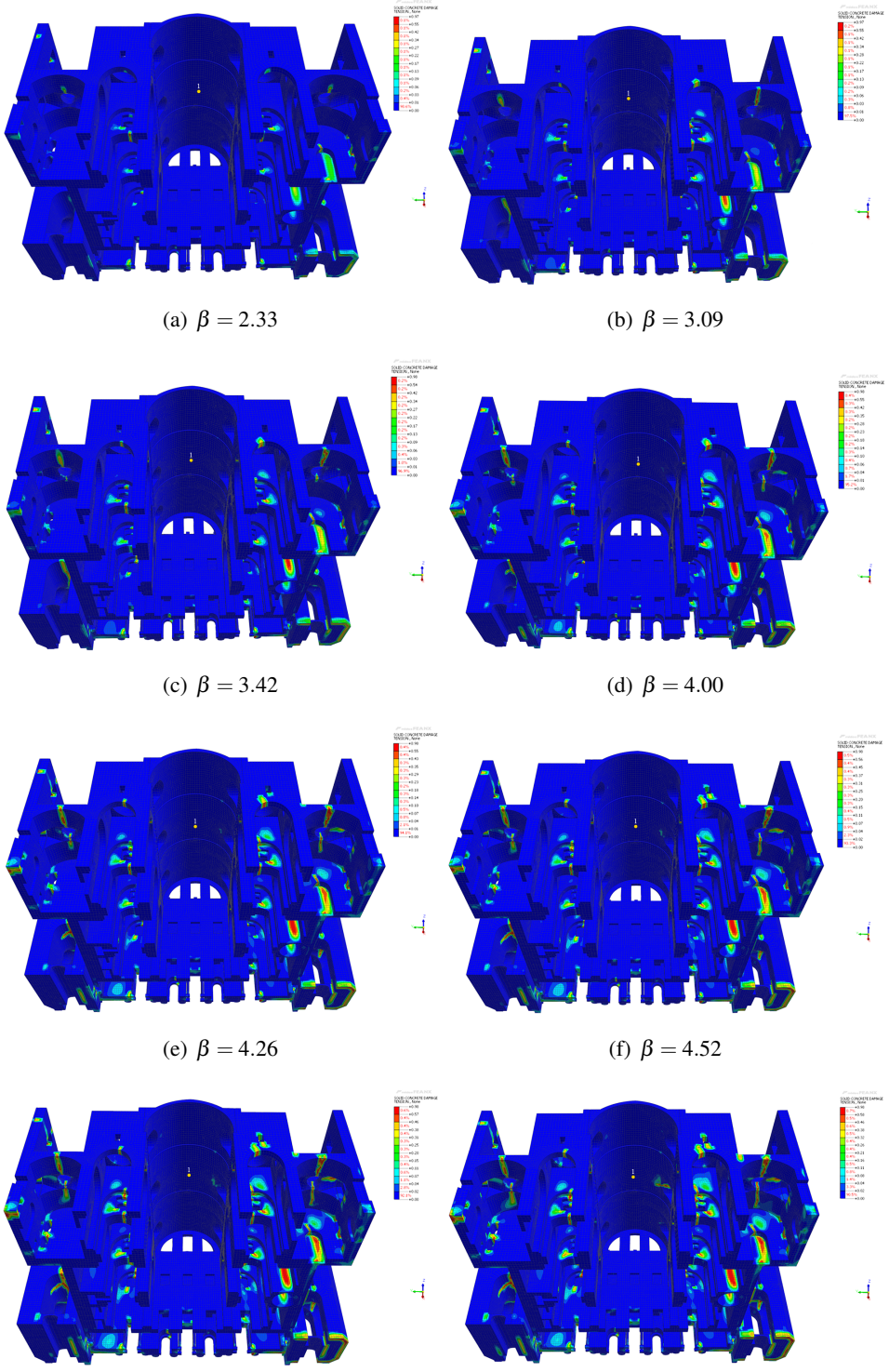

(a) $\beta = 2.33$ (b) $\beta = 3.09$

(c) $\beta = 3.42$ (d) $\beta = 4.00$

(e) $\beta = 4.26$ (f) $\beta = 4.52$

(g) $\beta = 4.75$ (h) $\beta = 4.98$

Figure IX.27: Reliability-based tensile-damage maps d_t on a cross-section of 3D NLFE model B: (a)–(h) β ranging from 2.33 to 4.98 for the central nave vault.

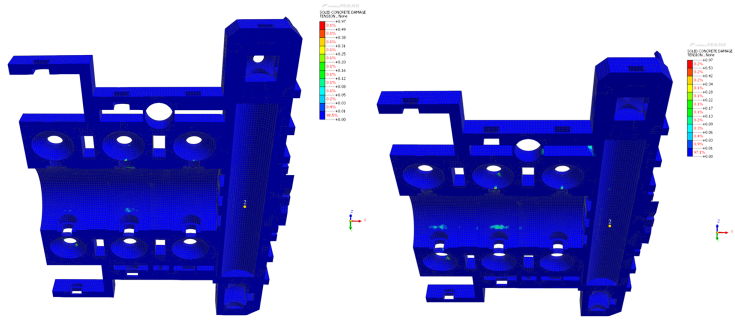

(a) $\beta = 2.33$ (b) $\beta = 3.09$

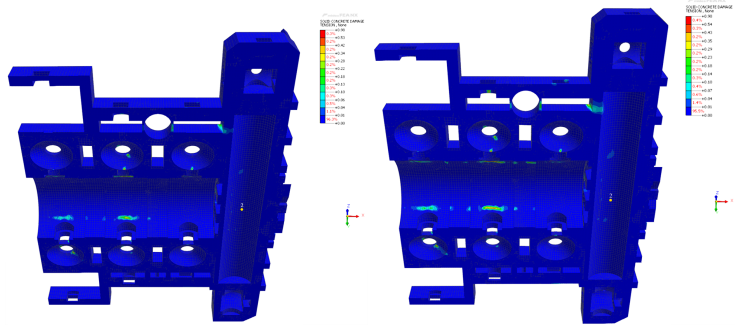

(c) $\beta = 3.42$ (d) $\beta = 3.72$

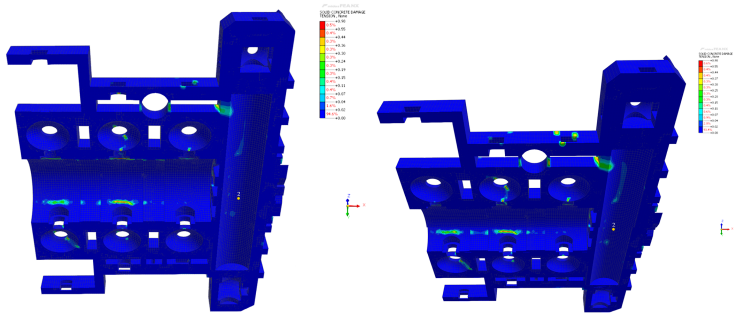

(e) $\beta = 4.00$ (f) $\beta = 4.26$

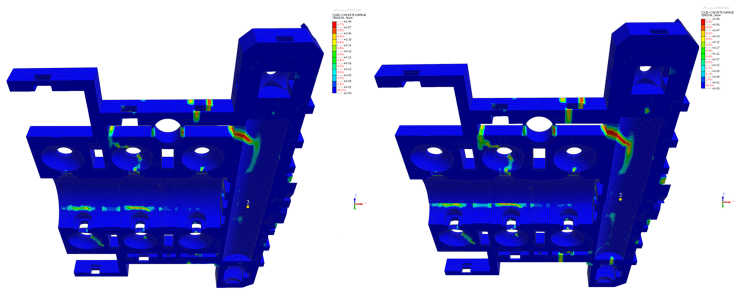

(g) $\beta = 4.52$ (h) $\beta = 4.75$

Figure IX.28: Reliability-based tensile-damage maps d_t on a cross-section of 3D NLFE model A: (a)–(h) β ranging from 2.33 to 4.75 for the Hall of Blessings vault.

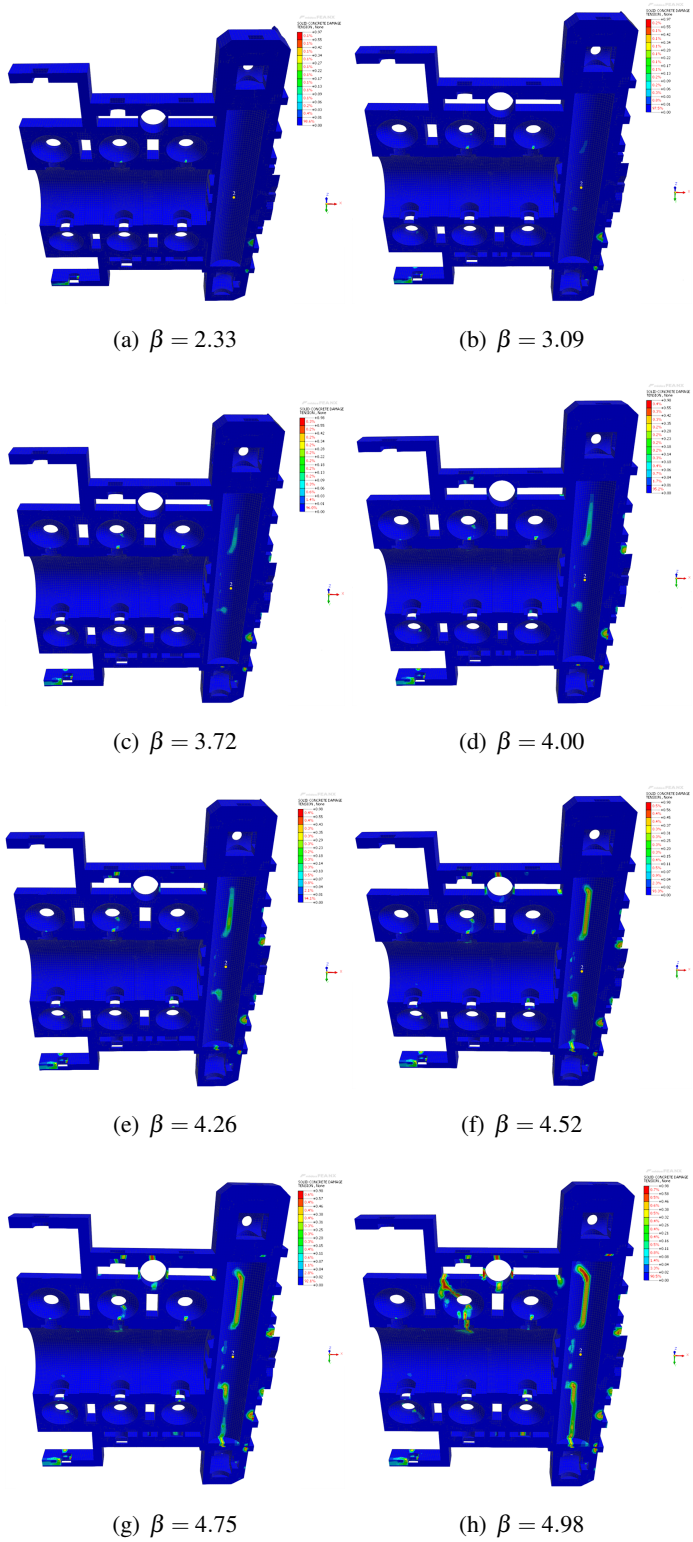

(a) $\beta = 2.33$ (b) $\beta = 3.09$

(c) $\beta = 3.72$ (d) $\beta = 4.00$

(e) $\beta = 4.26$ (f) $\beta = 4.52$

(g) $\beta = 4.75$ (h) $\beta = 4.98$

Figure IX.29: Reliability-based tensile-damage maps d_t on a cross-section of 3D NLFE model B: (a)–(h) β ranging from 2.33 to 4.98 for the Hall of Blessings vault.

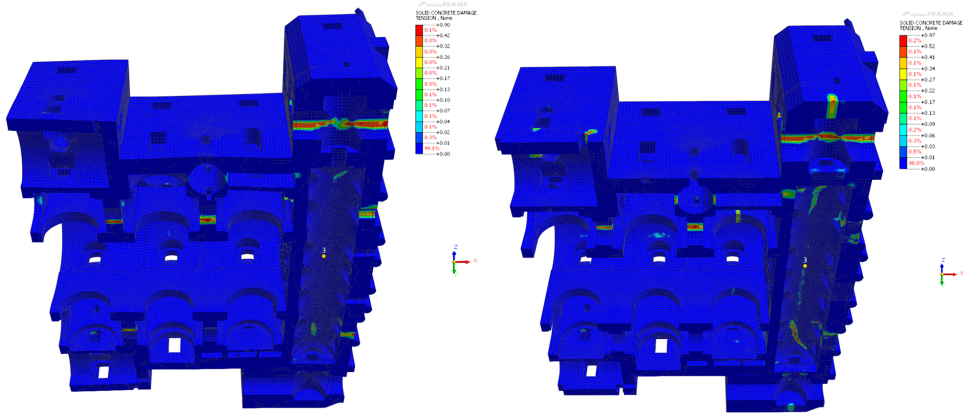

(a) $\beta = 2.33$ (b) $\beta = 2.73$

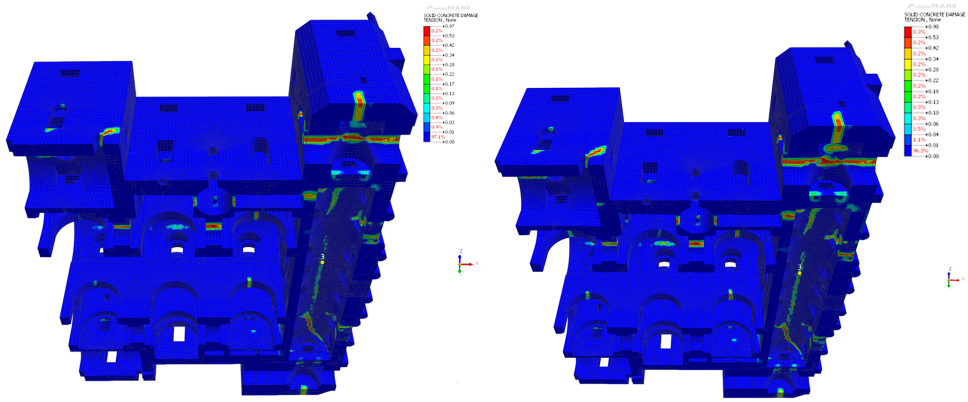

(c) $\beta = 3.09$ (d) $\beta = 3.42$

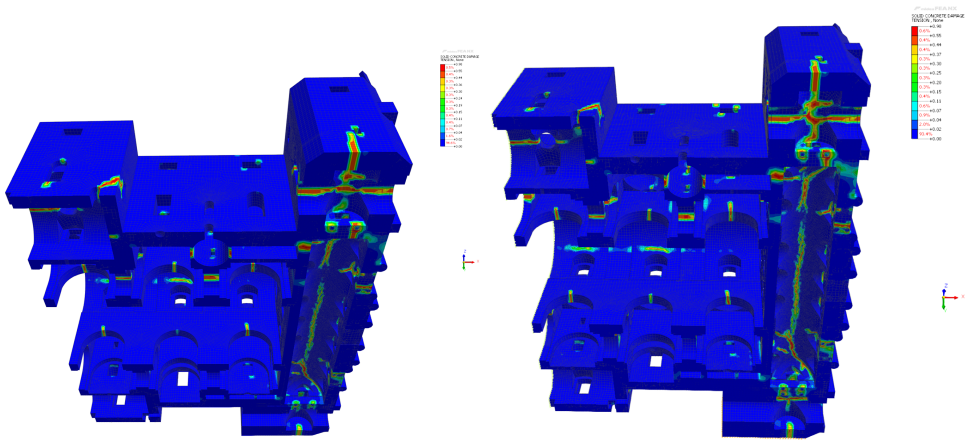

(e) $\beta = 4.00$ (f) $\beta = 4.26$

Figure IX.30: Reliability-based tensile-damage maps d_t on a cross-section of 3D NLFE model A: (a)–(f) β ranging from 2.33 to 4.26 for the Atrium vault.

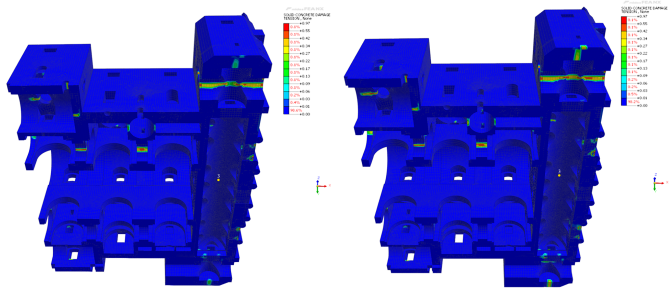

(a) $\beta = 2.33$ (b) $\beta = 2.73$

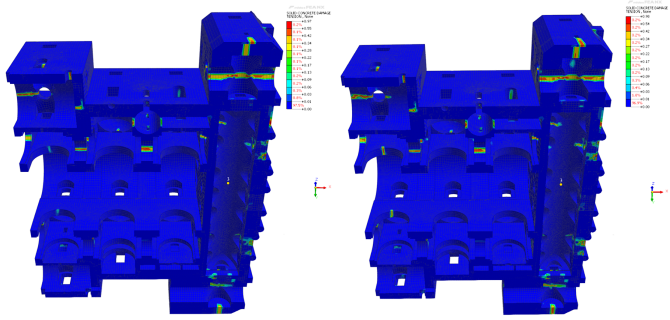

(c) $\beta = 3.09$ (d) $\beta = 3.42$

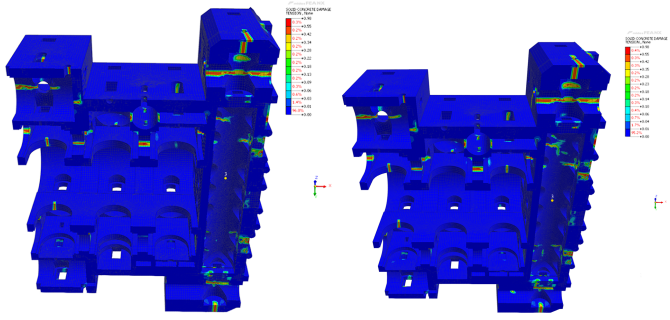

(e) $\beta = 3.72$ (f) $\beta = 4.00$

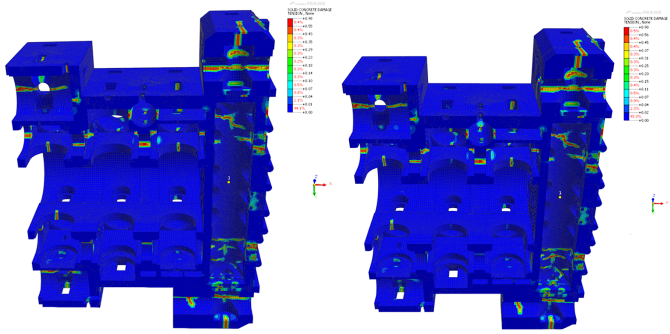

(g) $\beta = 4.26$ (h) $\beta = 4.52$

Figure IX.31: Reliability-based tensile-damage maps d_t on a cross-section of 3D NLFE model B: (a)–(h) β ranging from 2.33 to 4.52 for the Atrium vault.

IX.4 References

[1] Allaix, D. L., Carbone, V. I., and Mancini, G. (2013). Global safety format for non-linear analysis of reinforced concrete structures. *Structural concrete*, 14(1):29–42.

[2] Casas, J. R. (2011). Reliability-based assessment of masonry arch bridges. *Construction and Building Materials*, 25(4):1621–1631.

[3] Caspeele, R. and Van Den Hende, K. (2023). Validation of the harmonized partial factor method for design and assessment of concrete structures as proposed for fib model code 2020. *Structural Concrete*, 24(4):4368–4376.

[4] Castaldo, P., Gino, D., and Mancini, G. (2019). Safety formats for non-linear finite element analysis of reinforced concrete structures: discussion, comparison and proposals. *Engineering Structures*, 193:136–153.

[5] Castro, P. M., Delgado, R. M., and de Sá, J. M. C. (2005). A partial factors methodology for structural safety assessment in non-linear analysis.

[6] Cervenka, V. (2013). Global safety formats in fib model code 2010 for design of concrete structures. In *Proceeding of the 11th International Probabilistic Workshop, Brno*, pages 27–31.

[7] Croce, P., Beconcini, M. L., Formichi, P., Landi, F., Puccini, B., and Zotti, V. (2021). Evaluation of partial safety factors for the structural assessment of existings masonry buildings. In *International Probabilistic Workshop*, pages 341–352. Springer.

[8] EN.1990.Eurocode (2002). Basis of structural design.

[9] fib, 2020 – International Federation for Structural Concrete (2023). *fib Model Code 2020 for Concrete Structures*. fib, Lausanne, Switzerland.

[10] fib. Bulletin No. 80 (2016). Partial safety factor methods for existing concrete structures.

[11] Franck, S. A., Bretschneider, N., and Slowik, V. (2020). Safety analysis of existing masonry arch bridges by nonlinear finite element simulations. *International journal of damage mechanics*, 29(1):126–143.

[12] Gino, D., Castaldo, P., Bertagnoli, G., Giordano, L., and Mancini, G. (2020). Partial factor methods for existing structures according to fib bulletin 80: Assessment of an existing prestressed concrete bridge. *Structural Concrete*, 21(1):15–31.

[13] Holicky, M. and Sykora, M. (2012). Structural assessment of heritage buildings. *WIT Trans. Built. Environ*, 123:69–80.

[14] Isfeld, A. C., Stewart, M. G., and Masia, M. J. (2023). Structural reliability and partial safety factor assessment of unreinforced masonry in vertical bending. *Australian Journal of Structural Engineering*, 24(3):191–205.

[15] JCSS – Joint Committee on Structural Safety (2001). *Probabilistic Model Code*. JCSS, Zurich, Switzerland.

[16] Mancini, G. (2019). Partial factor methods for existing structures according to fib bulletin 80: Assessment of an existing prestressed concrete bridge. *Structural Concrete*.

[17] Moreira, V. N., Matos, J. C., and Oliveira, D. V. (2017). Probabilistic-based assessment of a masonry arch bridge considering inferential procedures. *Engineering Structures*, 134:61–73.

[18] Orcesi, A., Diamantidis, D., O'connor, A., Palmisano, F., Sykora, M., Boros, V., Caspeele, R., Chateauneuf, A., Mandić Ivanković, A., Lenner, R., et al. (2024). Investigating partial factors for the assessment of existing reinforced concrete bridges. *Structural engineering international*, 34(1):55–70.

[19] Zięba, J., Skrzypczak, I., and Buda-Ożóg, L. (2021). Calibration of partial safety factors of sample masonry structures. *Materials*, 14(17):5003.

CHAPTER X

Conclusions and future perspectives

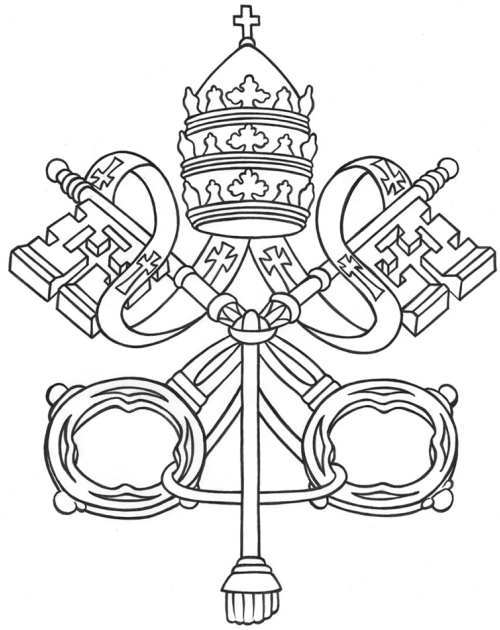

"Come pietre viventi, fatevi costruire in una casa spirituale."

("Like living stones, let yourselves be built into a spiritual house.")

– 1 Peter 2:5

X.1 Conclusions

This thesis has implemented, and critically examined an integrated framework for the probabilistic reliability assessment of complex monumental masonry buildings, with specific application to the 17th-century body of St. Peter's Basilica in Vatican City. The effort was inspired by the need to create a connection between the high level of complexity and uncertainty that characterizes monumental masonry heritage, and the probabilistic concepts and safety formats that drive current structural design and assessment. Within this context, the Basilica was used as a special case study due to its exceptional historical, architectural, and structural significance, as well as a model for analyzing other massive churches and cathedrals with multi-leaf walls and vaulted systems.

The research objectives formulated in Chapter I have been addressed in a systematic stepwise manner, combining historical-structural knowledge, diagnostic investigations, advanced 3D numerical modeling, and structural reliability concepts.

First, a set of mechanical parameters for the different components of the multi-leaf masonry (brickwork leaves, ARC core, travertine stone facing) has been derived by integrating in-situ NDT and MDT with laboratory tests on extracted cores and supporting numerical simulations at the material and wall scales. This led to a homogenized representation of the multi-leaf walls appropriate for global 3D NLFEAs, while preserving the key features of the original stratigraphy and the associated sources of uncertainty.

Second, the thesis has extended the material modeling from a purely deterministic viewpoint to a probabilistic description based on the CDP model. The constitutive parameters governing the compressive and tensile stress–strain behavior were identified as random variables, and prior probabilistic models were formulated from literature data and standards. These priors were further updated using Bayesian approach and resulting in posterior distributions that explicitly account for the information gathered over the 2023 diagnostic campaign carried out by SACERTIS INGEGNERIA S.R.L. In this way, the calibrated probabilistic CDP model provides a statistically consistent link between experimental observations, material variability, and the NLFEAs at the global scale.

Third, a detailed 3D NLFE macro-model of the 17th-century body of St. Peter's Basilica has been developed, including the principal structural components (homogenized multi-leaf walls, piers, barrel and groin vaults, minor domes, and foundations under the main Façade body) and realistic boundary conditions informed by the historical-structural analysis. The model has been set up using the homogenized material properties and calibrated constitutive parameters, and it has been checked and

tuned against available dynamic identification results, which confirmed the globally coherent behavior of the Basilica and the strong interaction between the Façade body and the longitudinal nave. NLSAs under gravity loads allowed the identification of the main load paths, the location of critical regions in the vault system, and the global deformation patterns under self-weight.

Fourth, the probabilistic material models and the global 3D NLFEAs have been embedded in a reliability-based safety format tailored to monumental masonry structures. PSFs for material properties, model uncertainties, and permanent actions have been calibrated as functions of the annual reliability index β_1, following the principles of the DVM in accordance with the international recommendations for target reliability levels. These reliability-based PSFs have then been applied to the 3D NLFE model of the Basilica to assess the ULS under gravity loads. Two alternative hypotheses for the interface between homogenized multi-leaf masonry and travertine have been considered (perfect bond and tangential slip), highlighting the influence of interface behavior on stiffness, damage evolution, and load–displacement response of the main vaults.

From the structural point of view, the analysis indicates that the 17th-century body of St. Peter's Basilica exhibits a high level of safety with respect to the adopted annual target reliability index under gravity actions. The global assessment index obtained from one of the most significant vault (Atrium) is significantly above the chosen target level, corresponding to an annual probability of failure that is lower than the reference threshold. The evolution of tensile-damage fields and the formation of kinematically admissible hinge patterns confirm that the collapse mechanism is associated with a limited number of critical vaults rather than with a diffuse loss of capacity throughout the entire 17th-century building. The comparison between the bounded and unbounded interface configurations shows that interface slip tends to increase displacements and to anticipate the onset of nonlinearity, but it does not compromise the global reliability level within the investigated range of parameters and load combinations.

More generally speaking, the thesis illustrates that the combination of knowledge-based diagnostics, homogenized constitutive modeling, probabilistic parameter identification, and reliability-driven PFM provides a rational and transparent framework for the safety assessment of monumental masonry buildings. The outlined workflow explains how epistemic and aleatory uncertainty spread from the material scale to the structural response, and then to the reliability indices and safety checks. It also illustrates how the calibrated PSFs for existing monumental structures may differ from those used for ordinary buildings, especially when structure-specific diagnostic information is available and explicitly incorporated into the assessment.

Finally, while the investigation has focused on gravity loads and the 17th-century body of the Basilica, the methodology has been specifically generalized. It may be applied to other complex heritage structures with appropriate adaptations, so allowing the incorporation of probabilistic analysis into conservation practice and decision making. The outcomes highlight the importance of combining advanced numerical tools with reliability concepts not only to quantify current safety levels, but also to prioritize future investigations, guide monitoring strategies, and evaluate potential strengthening or risk-mitigation measures.

X.2 Future perspectives

The study presented in this thesis should be regarded as a first step toward a comprehensive reliability-based structural assessment of St. Peter's Basilica and, more generally, of monumental masonry buildings. However, different improvements and developments are possible, both at the level of the case study and in terms of the methodological framework.

A natural first direction concerns the extension of the numerical and probabilistic modeling to the 16th-century body of the Basilica, including the central Greek-cross core, the four colossal piers, the drum, and the main dome designed by Michelangelo.

In the present work, these elements have been considered primarily as part of the historical-structural context and as boundary conditions for the 17th-century body; however, their behavior is crucial for the global stability of the monument. Future studies should therefore aim at constructing a unified global 3D NLFE model that encompasses both the 16th- and 17th-century structures, allowing the interaction between the main dome, the surrounding vaults, and the Façade–nave system to be captured explicitly. This would require additional efforts in terms of geometric idealization, material characterization for the older construction phases, and careful treatment of the interfaces between different construction stages.

A related line of research concerns the foundations, substructures and underground cavities under the Basilica. In this thesis, the support conditions have been modeled in a simplified way, based on the currently available information and with the focus on gravity loads.

Future studies could develop a more detailed representation of the foundation system by combining archival documentation, borehole investigations, geophysical surveys and the geometric data provided by the digital twin. On this basis, more refined soil–structure interaction models could be built, explicitly accounting for the soil

stratigraphy, the presence of crypts and service corridors, and possible local variations in stiffness. Such models would provide a clearer picture of how vertical and horizontal thrusts are transmitted to the ground and would be essential for assessing the response of the Basilica under exceptional actions and potential long-term degradation processes.

Another significant improvement is the integration of additional load conditions than gravity. For instance, the seismic response of the Basilica needs focused consideration, considering the high vulnerability of historic masonry structures to horizontal actions and the presence of large-span vaults and domes.

Future studies could employ the probabilistic material models and global FE models developed in this thesis as a basis for non-linear dynamic analyses under realistic ground motions, leading to the construction of seismic fragility curves and risk measures for selected limit states (e.g., damage of key vaults, activation of global mechanisms in the dome–nave system, or loss of support in critical piers). Wind actions, thermal effects, and possible differential settlements could also be explored, especially in a multi-hazard perspective where different actions may interact over the remaining service life of the structure.

From a methodological point of view, the probabilistic framework could be improved by introducing additional random variables and more advanced reliability methods. In the present work, the focus has been placed on a limited number of material parameters and on the calibration of PSFs through the DVM.

Future study should concern spatial variability in material characteristics, correlations between structural elements, and model uncertainties. This could require the use of surrogate models or advanced safety formats (e.g., EcoV, GRF and GSF) to keep the computational cost at an acceptable level while preserving accuracy in the estimation of low P_f that are relevant for monumental heritage.

A further promising avenue is the tighter integration between the reliability-based numerical models and SHM. The dynamic tests carried out during the 2023 diagnostic campaign already provide a valuable baseline for model calibration and for the identification of global dynamic properties. In forthcoming phases, the global 3D NLFE model and the probabilistic material descriptions could be embedded within a digital twin framework for the Basilica, supporting: (i) the optimal placement of sensors based on information-theoretic criteria; (ii) the continuous updating of mechanical parameters and boundary conditions using monitoring data; and (iii) the detection and localization of damage through probabilistic model updating. In this perspective, the reliability-based assessment would evolve from a one-off exercise into a living process, where safety indicators and risk measures are periodically revisited as new data become available.

The implemented framework could also be used as a decision-support tool to assess potential intervention and risk-mitigation measures. Future work could compare alternative strengthening schemes (e.g., additional tie-rods, local consolidations of vaults, improvement of interfaces or foundations) in terms of their effect on reliability indices, PSFs, and expected damage under different scenarios.

Finally, although the application has focused on St. Peter's Basilica, the underlying concepts are widely transferable. Furthermore, future study could replicate and adapt this methodology framework to other complex monumental masonry buildings. Comparative study using several case studies could help in generalizing the results, identifying common patterns and key features, and refining the recommended target reliability levels and PSFs for cultural heritage.

In an extended perspective, the work presented here is intended not only as a contribution to the understanding of a single unique monument, but also as a step toward a more systematic and probabilistically informed approach to the preservation of monumental masonry heritage.

APPENDICES

This page intentionally left blank.

Appendix A:

Input data and results of 3D NLFEAs

A.1 Prior knowledge from literature and standards

A.1.1 Brickwork masonry

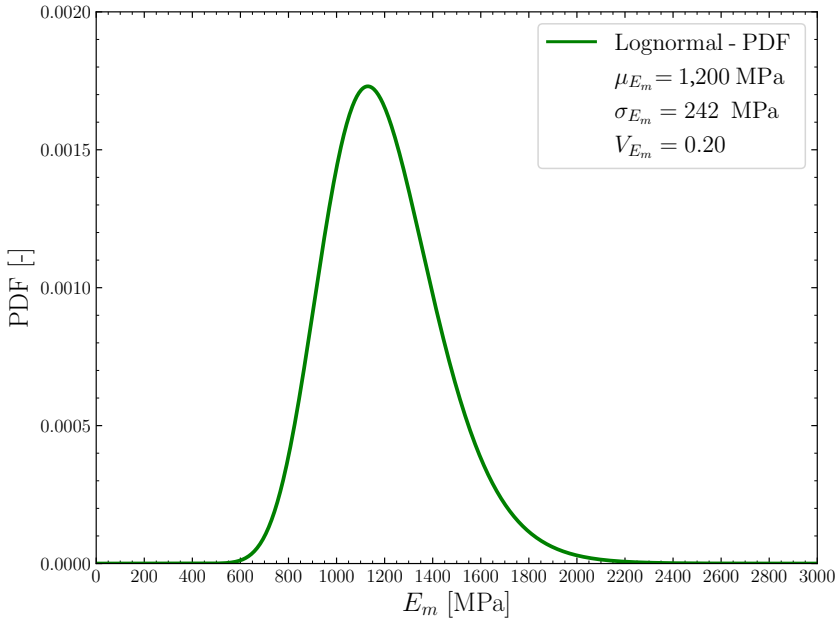

Figure A.1: PDF of the prior distribution of elastic modulus E_m for brickwork masonry.

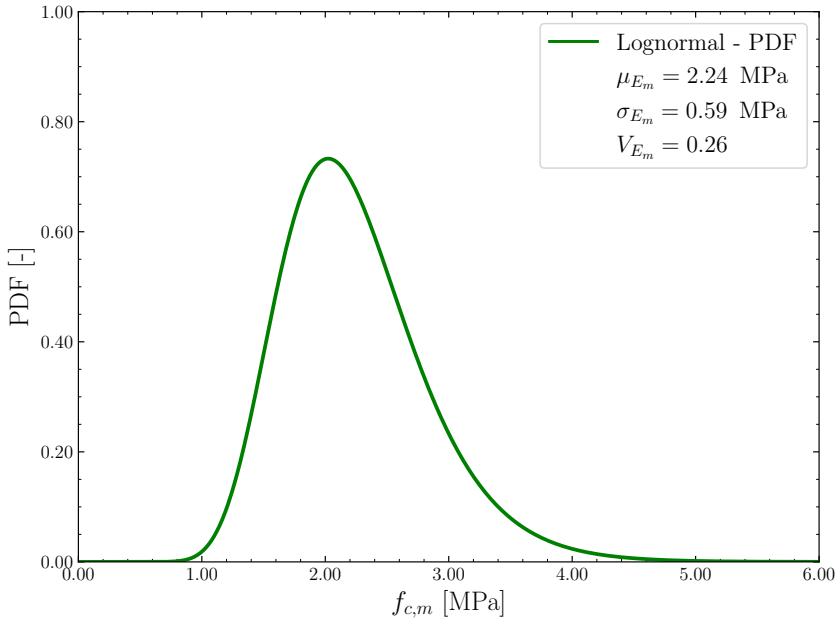

Figure A.2: PDF of the prior distribution of compressive strength $f_{c,m}$ for brickwork masonry.

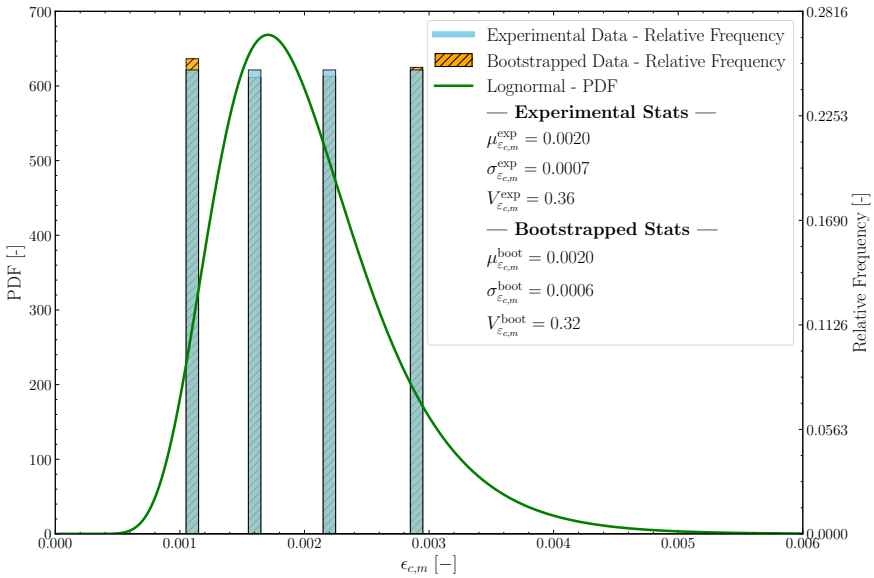

Figure A.3: PDF of the prior distribution of the peak compressive strain $\varepsilon_{c,m}$ for brickwork masonry.

A.1.2 Ancient Roman Concrete

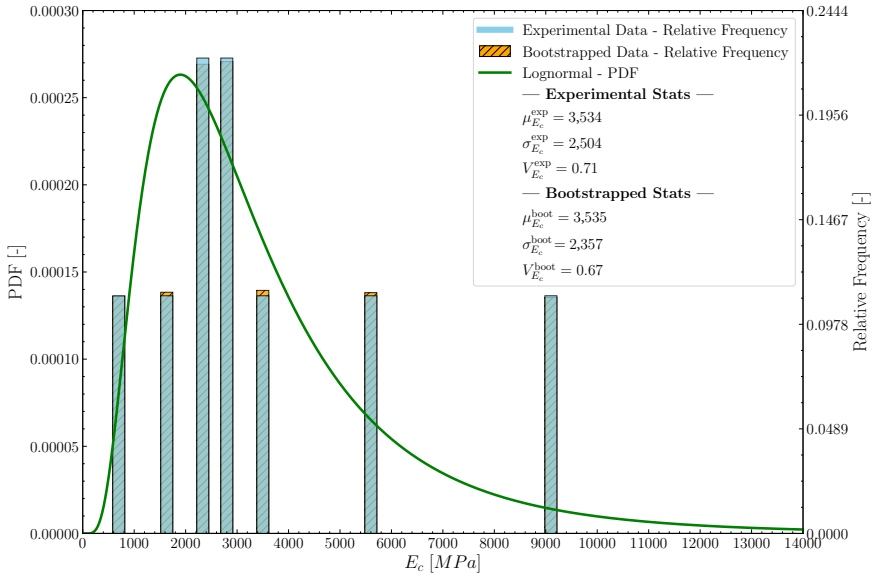

Figure A.4: PDF of the prior distribution of the elastic modulus E_c for ARC.

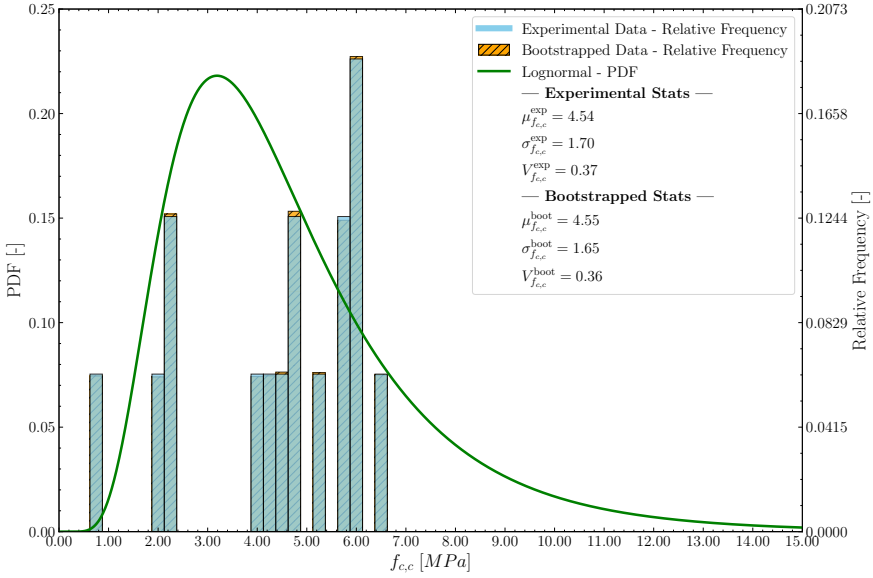

Figure A.5: PDF of the prior distribution of the compressive strength $f_{c,c}$ for ARC.

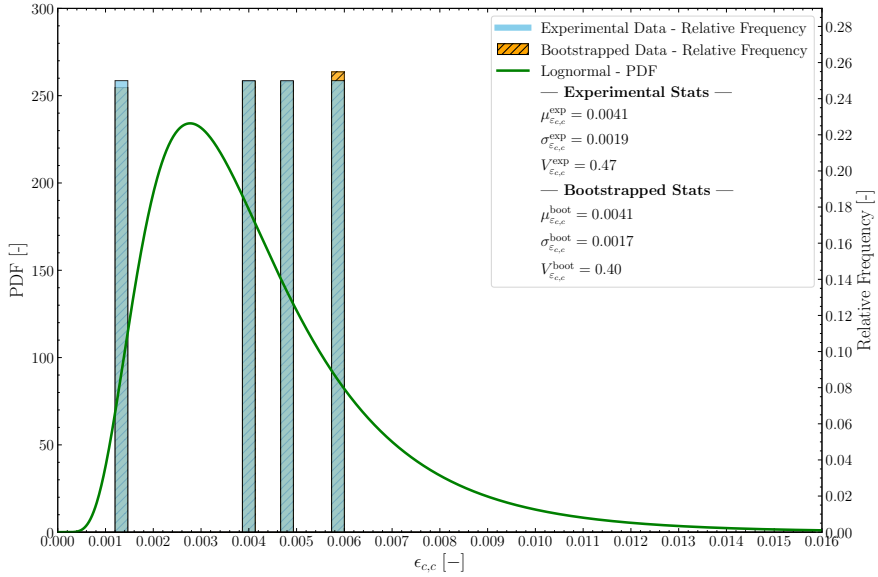

Figure A.6: PDF of the prior distribution of the peak compressive strain $\varepsilon_{c,c}$ for ARC.

A.1.3 Travertine

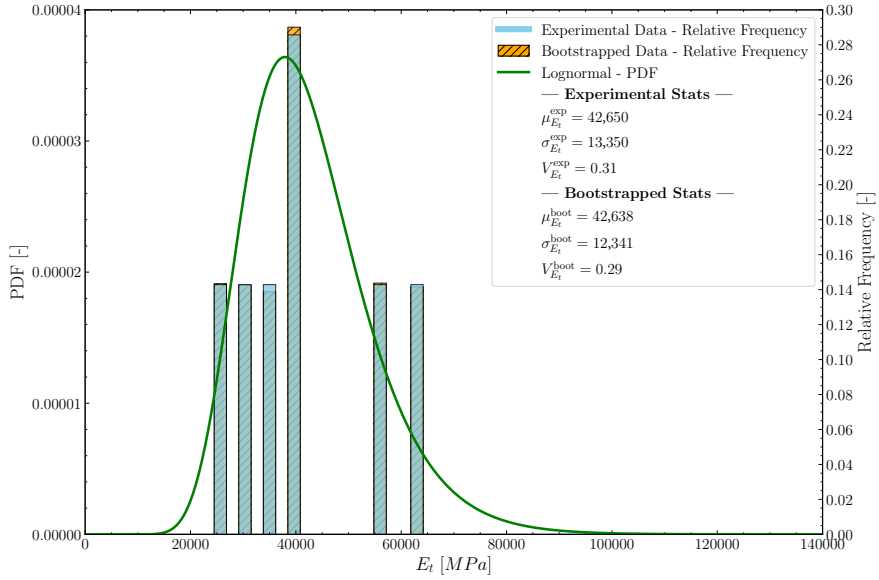

Figure A.7: PDF of the prior distribution of the elastic modulus E_t for travertine.

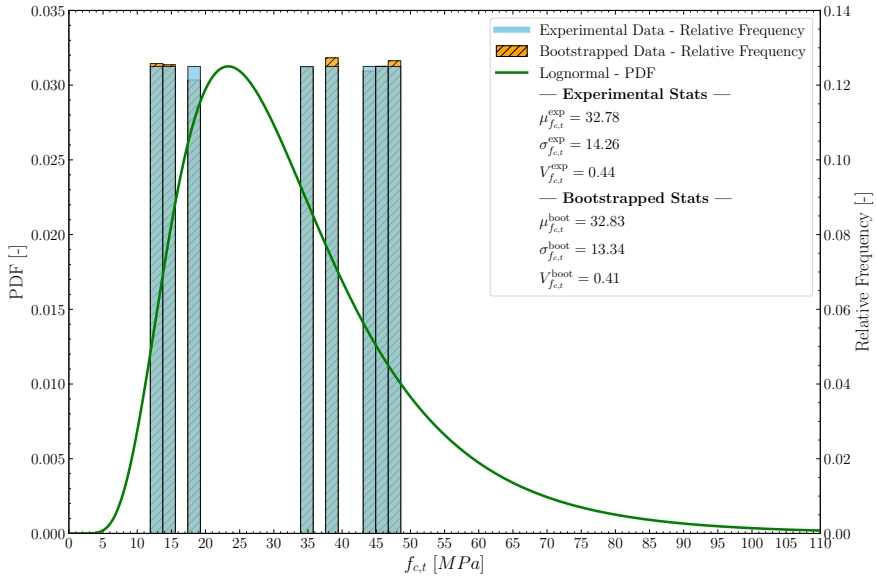

Figure A.8: PDF of the prior distribution of the compressive strength $f_{c,t}$ for travertine.

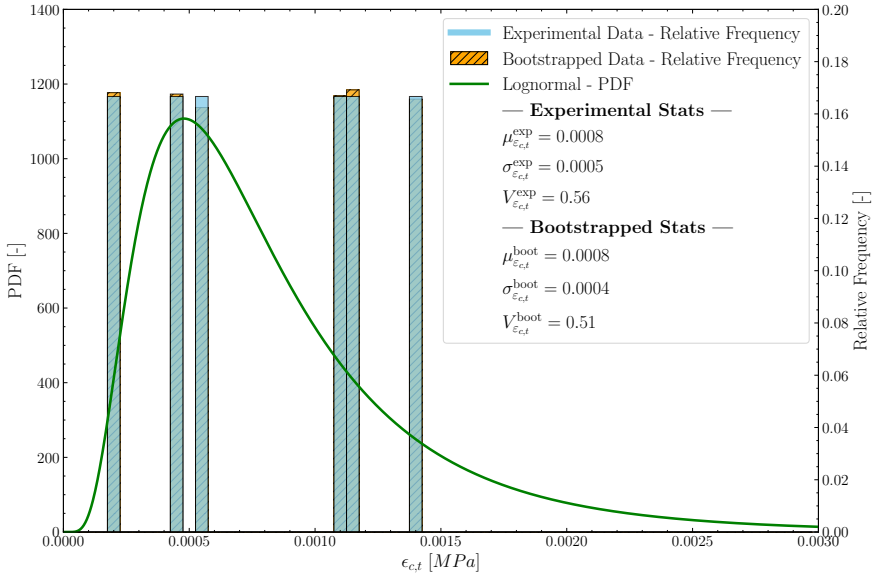

Figure A.9: PDF of the prior distribution of the peak compressive strain $\varepsilon_{c,t}$ for travertine.

A.2 Likelihood of experimental data from St. Peter's Basilica

A.2.1 Brickwork masonry

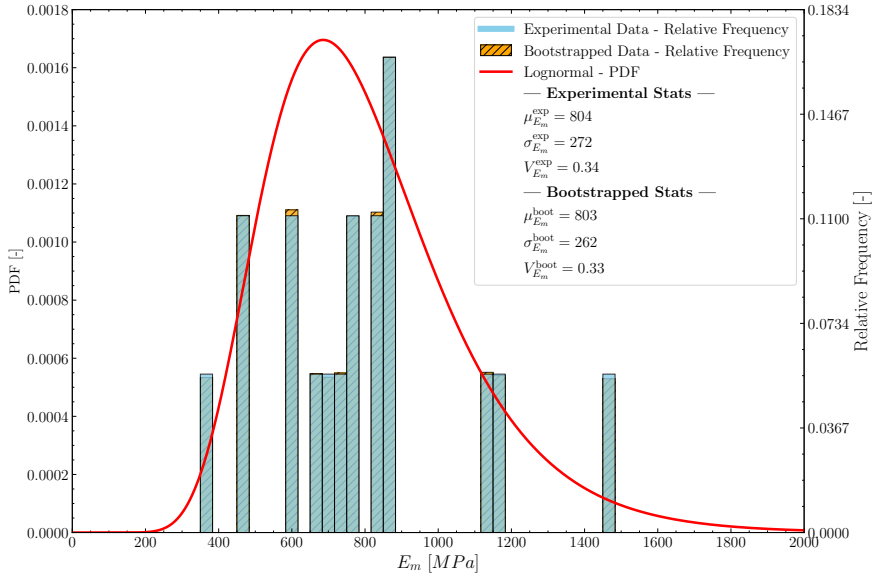

Figure A.10: PDF of the likelihood distribution of the elastic modulus E_m for brickwork masonry.

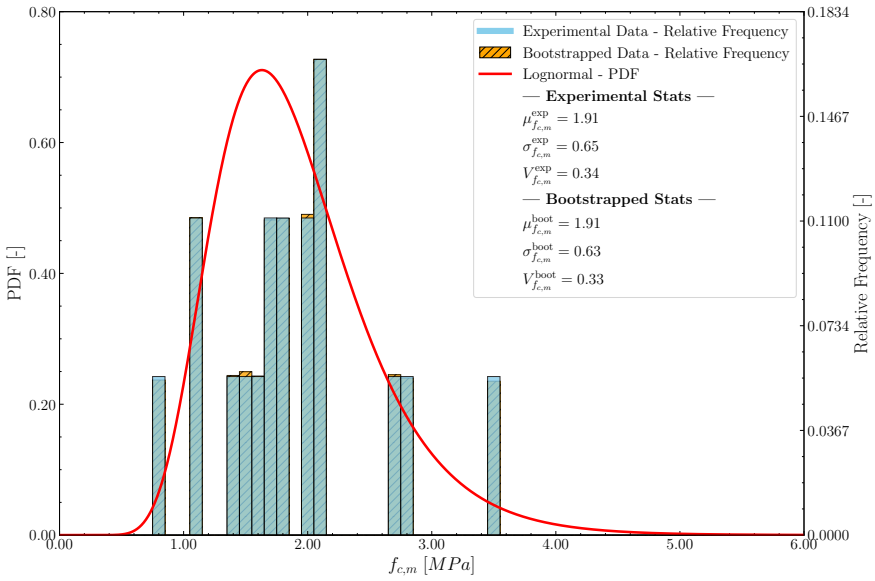

Figure A.11: PDF of the likelihood distribution of the compressive strength $f_{c,m}$ for brickwork masonry.

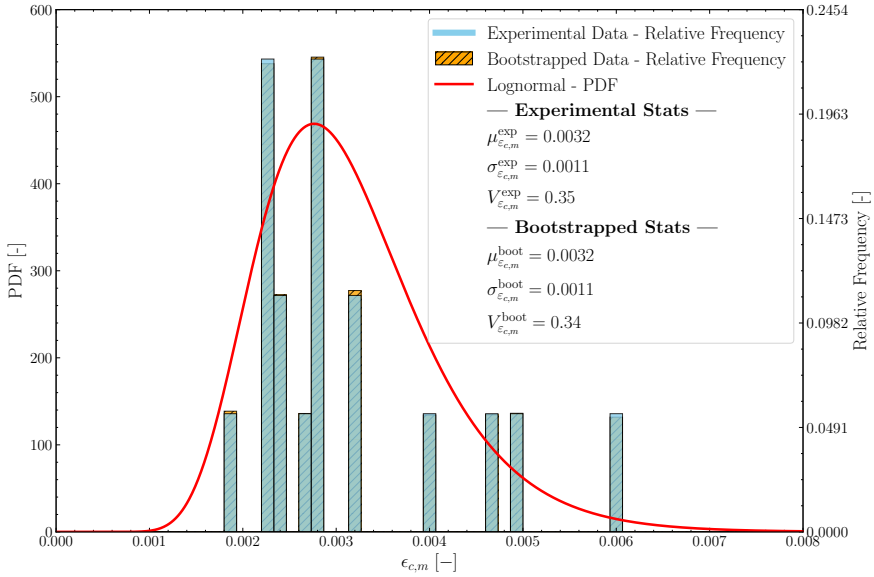

Figure A.12: PDF of the likelihood distribution of the peak compressive strain $\varepsilon_{c,m}$ for brickwork masonry.

A.2.2 Ancient Roman Concrete

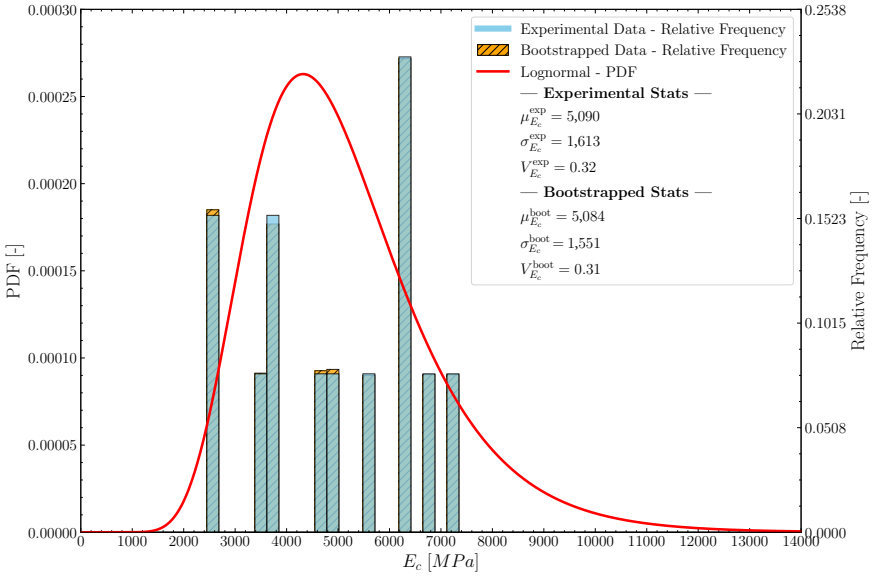

Figure A.13: PDF of the likelihood distribution of the elastic modulus E_c for ARC.

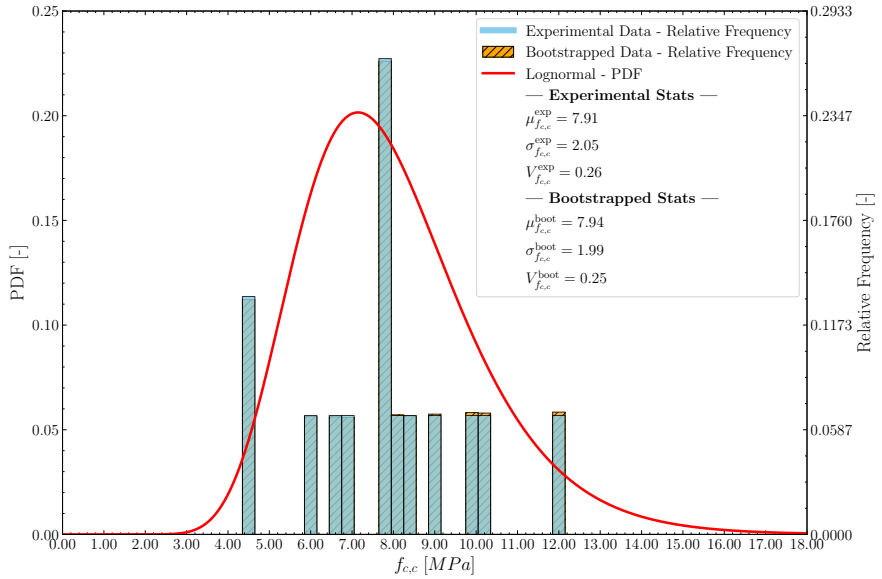

Figure A.14: PDF of the likelihood distribution of the compressive strength $f_{c,c}$ for ARC.

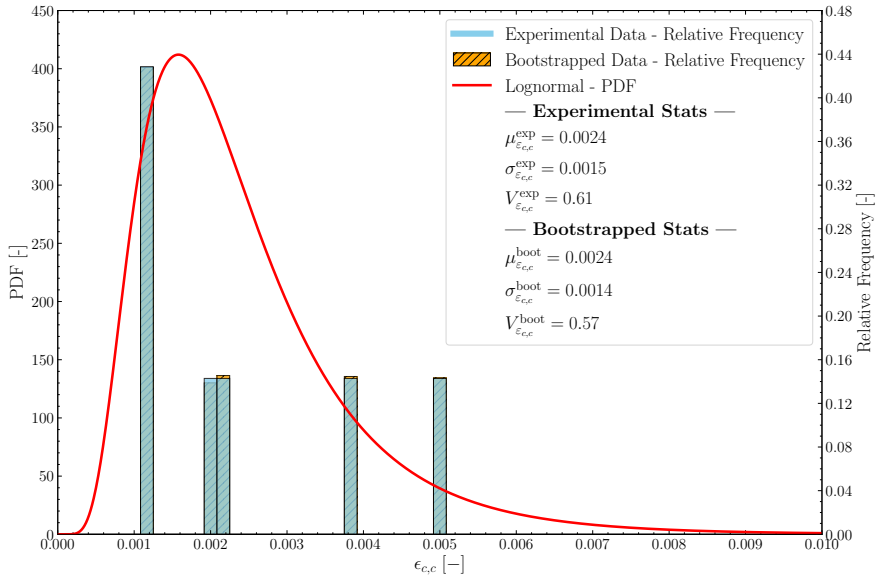

Figure A.15: PDF of the likelihood distribution of the peak compressive strain $\varepsilon_{c,c}$ for ARC.

A.2.3 Travertine

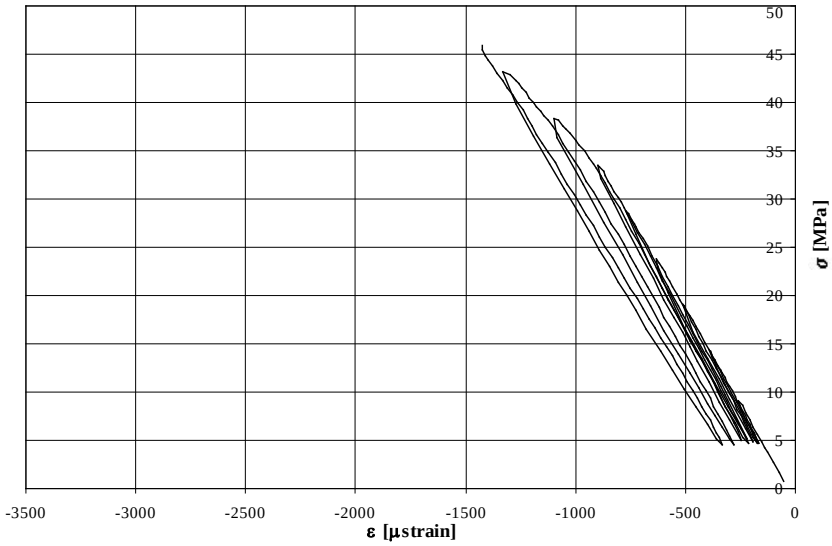

Figure A.16: Stress–strain curve of a travertine specimen from the 1998–1999 experimental campaign by EniTecnologie S.p.A.

A.3 Probabilistic 3D NLFEAs data from the homogenization of the multi-leaf masonry walls

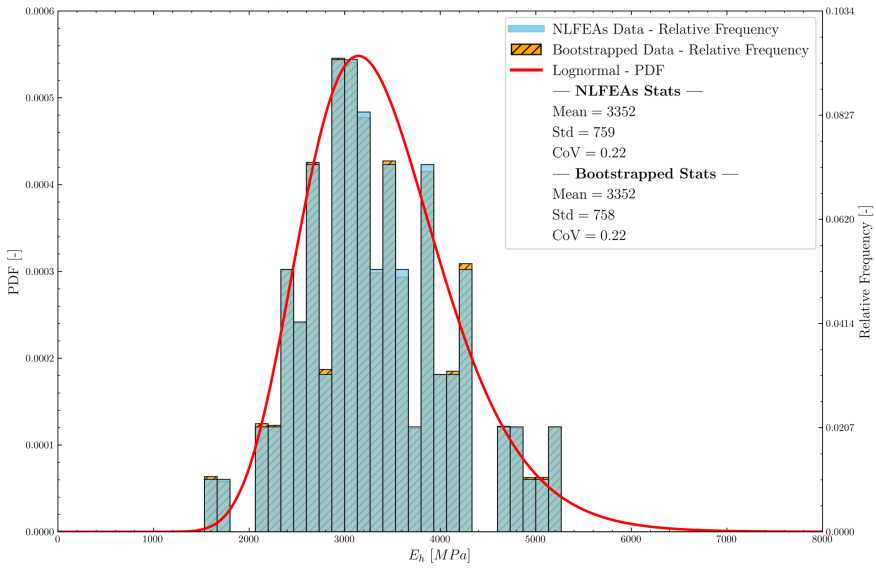

Figure A.17: PDF of the elastic modulus E_c for ARC, derived from S-NLFEAs data.

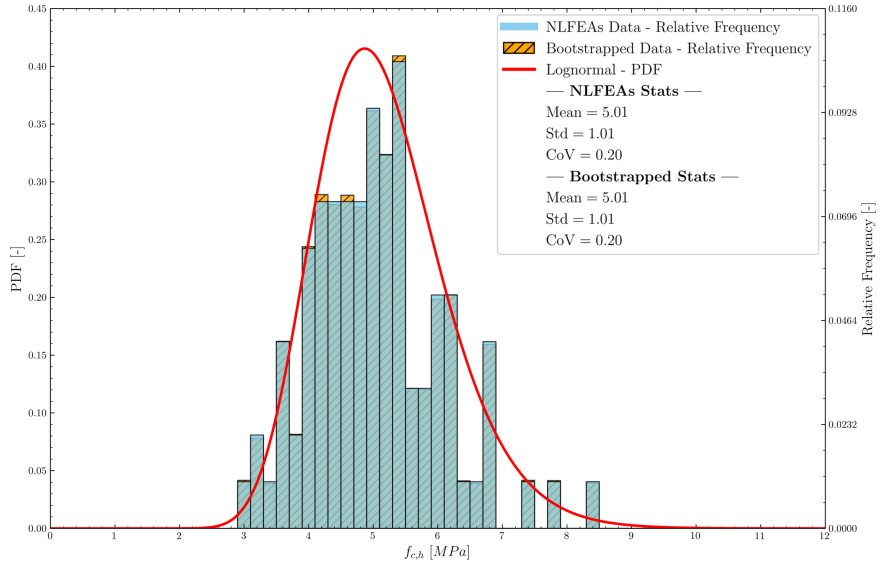

Figure A.18: PDF of the compressive strength $f_{c,c}$ for ARC, derived from S-NLFEAs data.

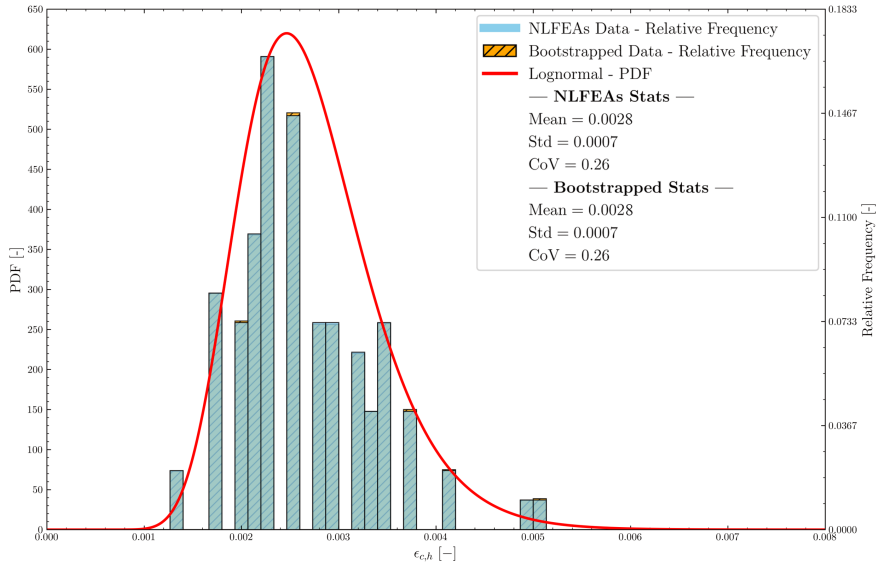

Figure A.19: PDF of the peak compressive strain $\varepsilon_{c,c}$ for ARC, derived from S-NLFEAs data.

Appendix B:

In-situ diagnostic test location plans

TYPES OF INVESTIGATIONS PERFORMED:

	Single flat-jack tests
	Double flat-jack tests
C	Core drilling test (diameter = 100 mm; max depth = 300 cm)
	Endoscopic investigations
	Sonic pulse velocity tests
	Openings for inspection of the masonry texture

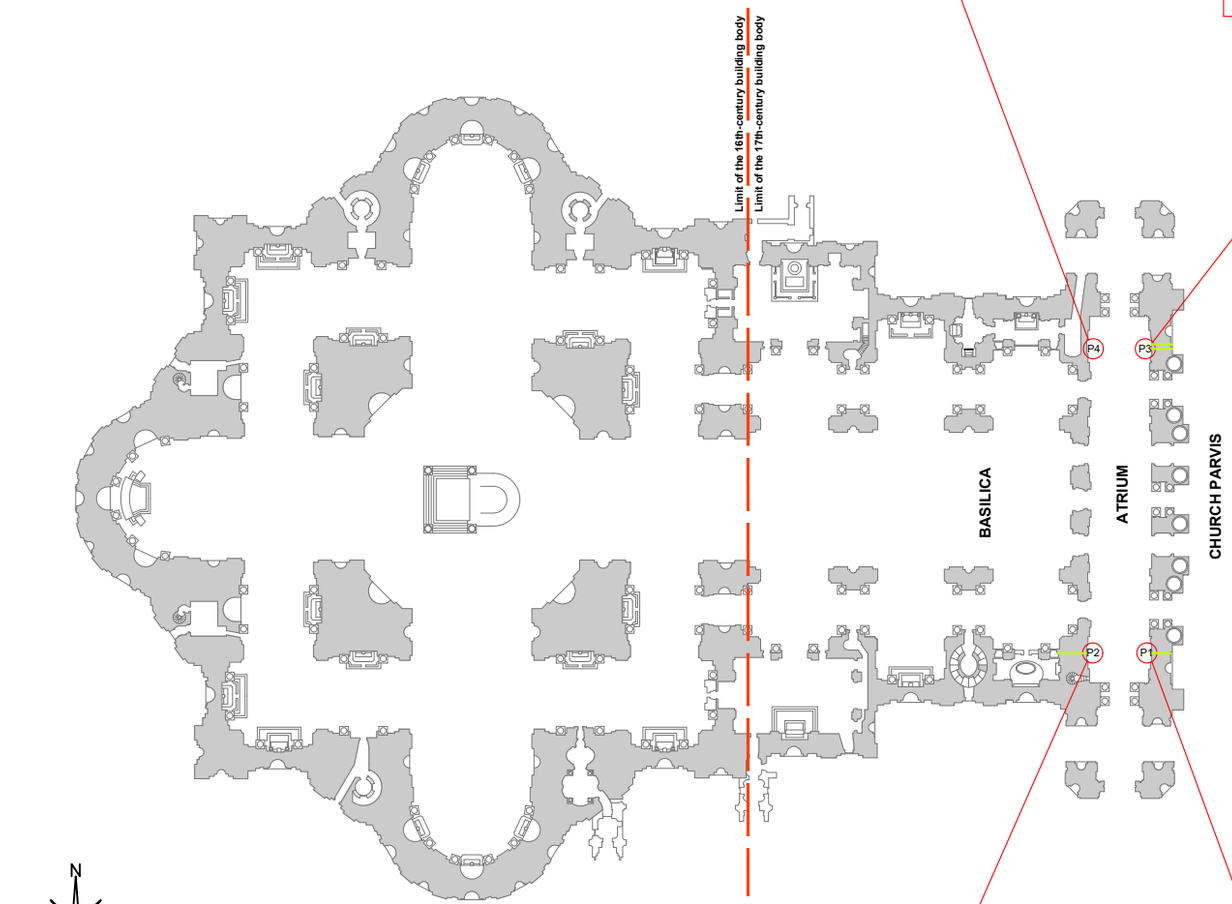

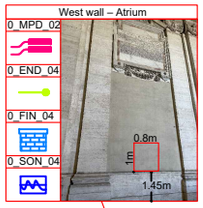

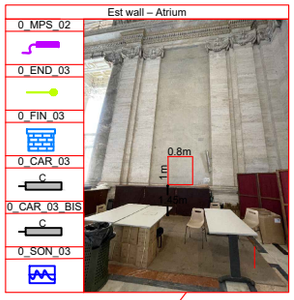

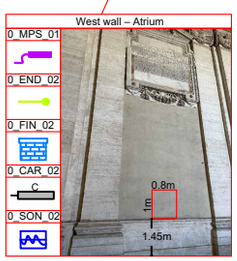

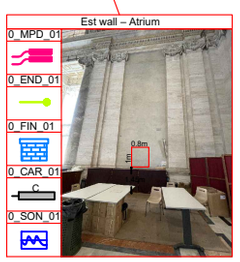

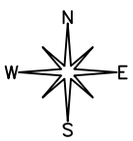

Graphic scale

0 10 20 30 40 50 60 70 80 90 100 m

SACERTIS Ingegneria S.r.l.
Via Isonzo, 34 - 00198 Roma - Italy
sacertisingegneriasrl@legalmail.it

STATIC AND DYNAMIC MONITORING OF ST. PETER'S BASILICA

INVESTIGATION PLAN

BASILICA FLOOR PLAN

Date 28.02.23

Scale Graphic

SHEET **01**

TYPES OF INVESTIGATIONS PERFORMED:

	Single flat-jack tests
	Double flat-jack tests
	Endoscopic investigations
	Sonic pulse velocity tests
	Openings for inspection of the masonry texture

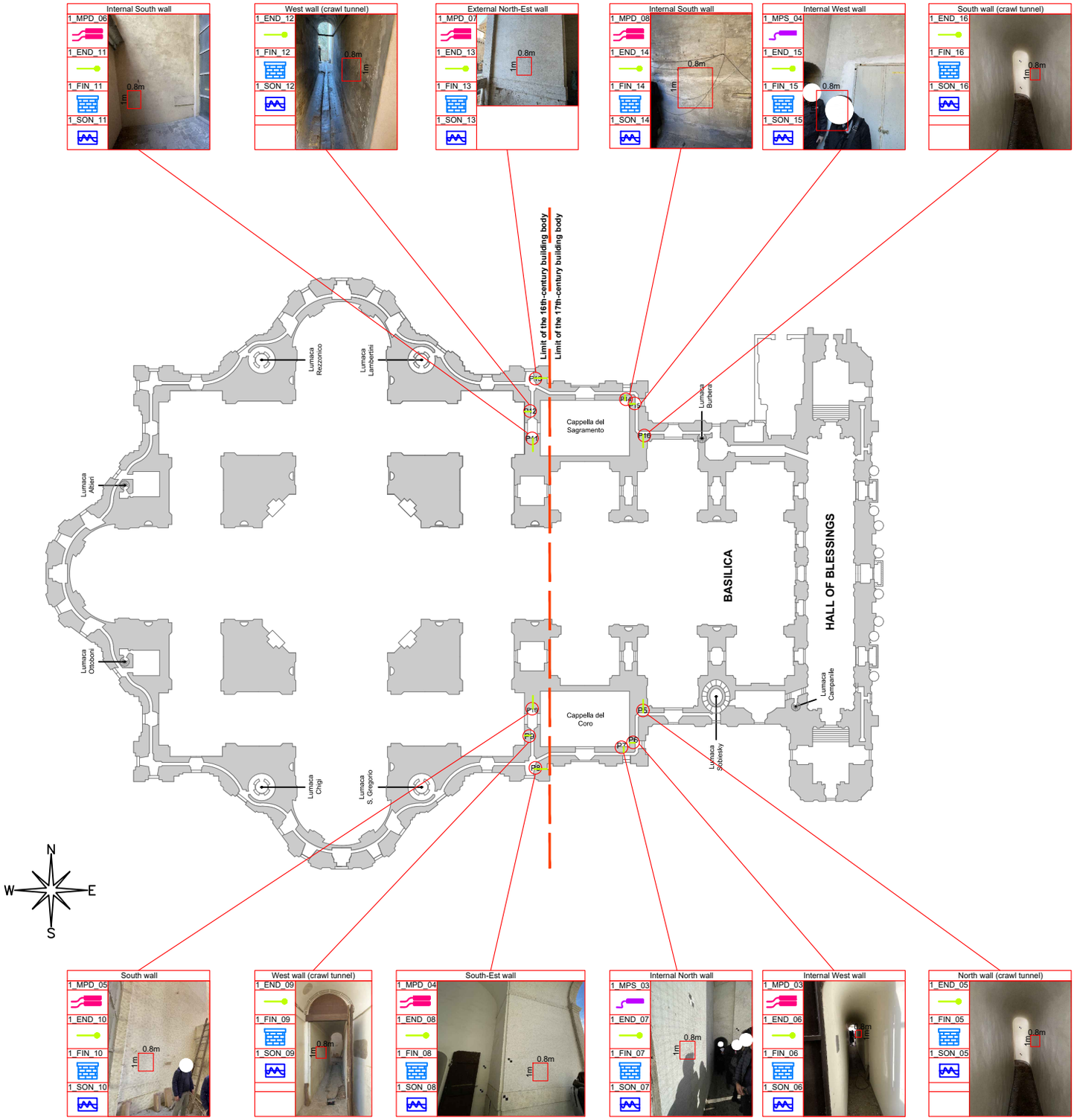

Graphic scale

0 10 20 30 40 50 60 70 80 90 100 m

SACERTIS INGEGNERIA

SACERTIS Ingegneria S.r.l.
Via Isonzo, 34 - 00198 Roma - Italy
sacertisingegneriasrl@legalmail.it

STATIC AND DYNAMIC MONITORING OF ST. PETER'S BASILICA

INVESTIGATION PLAN

FIRST CORRIDOR – FIRST FLOOR PLAN

Date 28.02.23

Scale Graphic

SHEET 02

TYPES OF INVESTIGATIONS PERFORMED:

	Single flat-jack tests
	Double flat-jack tests
	Endoscopic investigations
	Sonic pulse velocity tests
	Openings for inspection of the masonry texture

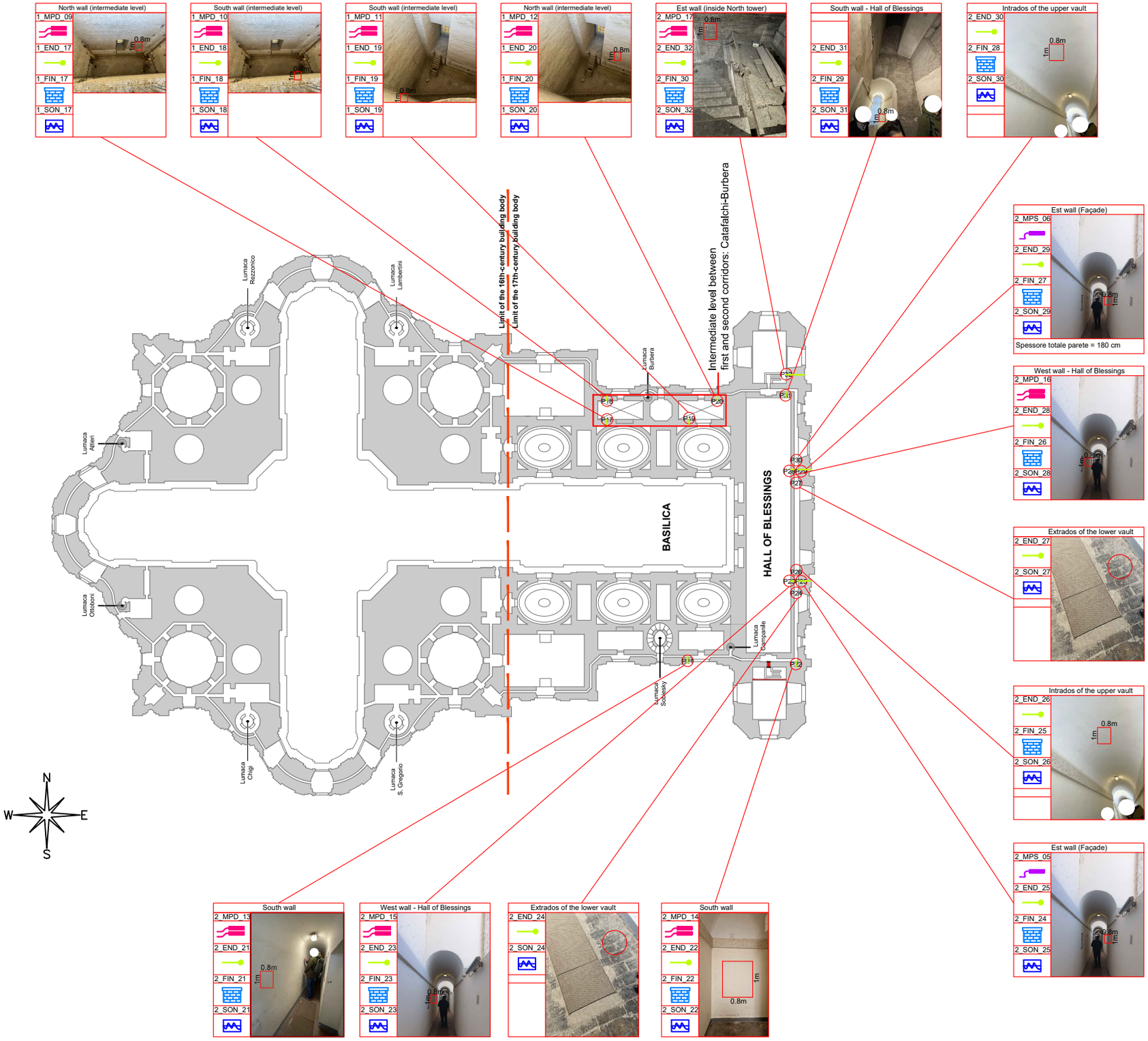

SACERTIS Ingegneria S.r.l.
Via Isonzo, 34 - 00198 Roma - Italy
sacertisingegneriasrl@legalmail.it

STATIC AND DYNAMIC MONITORING OF ST. PETER'S BASILICA

INVESTIGATION PLAN

SECOND CORRIDOR – SECOND FLOOR PLAN

Date 28.02.23

Scale Graphic

SHEET 03

TYPES OF INVESTIGATIONS PERFORMED:

	Double flat-jack tests
	Endoscopic investigations
	Sonic pulse velocity tests
	Openings for inspection of the masonry texture

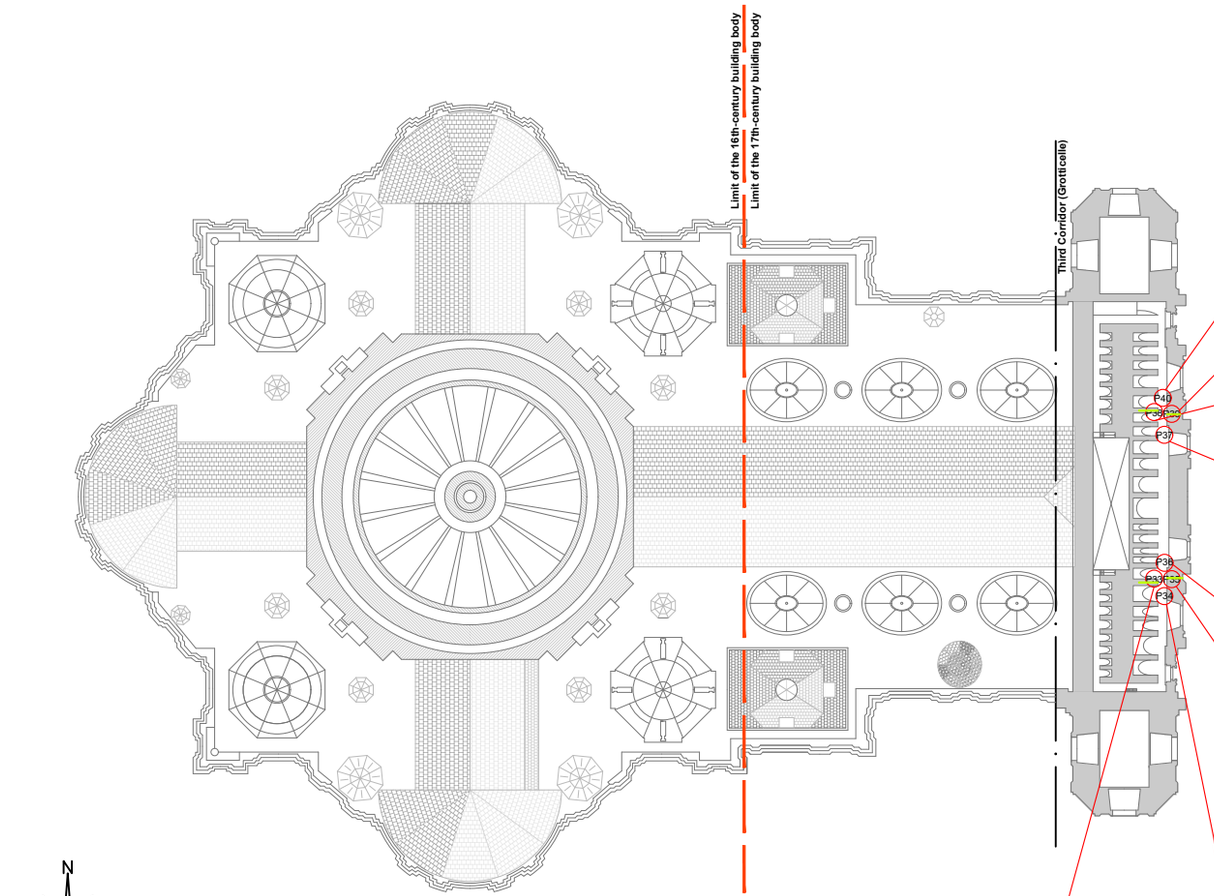

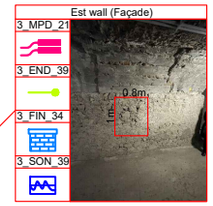

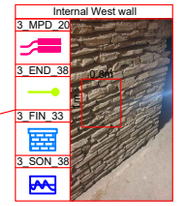

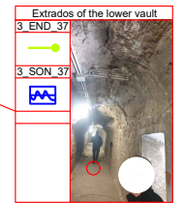

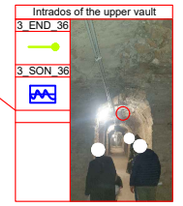

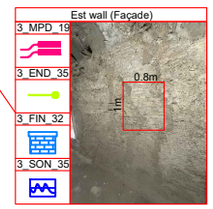

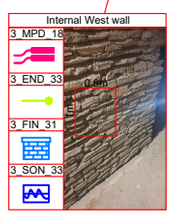

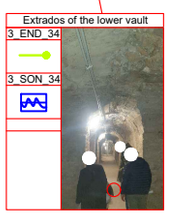

Graphic scale

0 10 20 30 40 50 60 70 80 90 100 m

SACERTIS Ingegneria S.r.l.
Via Isonzo, 34 - 00198 Roma - Italy
sacertisingegneriasrl@legalmail.it

STATIC AND DYNAMIC MONITORING OF ST. PETER'S BASILICA

INVESTIGATION PLAN

THIRD CORRIDOR (GROTTICELLE) - PLAN SCHEME

Date 28.02.23

Scale Graphic

SHEET 04

This page intentionally left blank.